Universidade de Aveiro Departamento de Electrónica, Telecomunicações e Informática,
2014

Rogério Pais Dionísio

Modulação e Conversão de Formatos Óticos Avançados

Advanced Optical Modulation and Format Conversion

Universidade de Aveiro
2014

Departamento de Electrónica, Telecomunicações e Informática

Rogério Pais Dionísio

Modulação e Conversão de Formatos Óticos Avançados

Advanced Optical Modulation and Format Conversion

Dissertação apresentada à Universidade de Aveiro para cumprimento dos requisitos necessàrios à obtenção do grau de Doutor em Engenharia Electrotécnica, realizada sob a orientação científica do Professor Doutor António Luís Jesus Teixeira, Professor Associado com Agregação do Departamento de Electrónica, Telecomunicações e Informática da Universidade de Aveiro, e do coorientador Professor Doutor Rogério Nunes Nogueira, Investigador Principal do Instituto de Telecomunicações (IT).

Apoio financeiro do Instituto Politécnico de Castelo Branco — IPCB através da bolsa de formação avançada de docentes do IPCB.

Instituto Politécnico de Castelo Branco

Apoio financeiro da Fundação para a Ciência e Tecnologia — FCT através da bolsa SFRH / PROTEC / 50015 / 2009.

FCT
Fundação para a Ciência e a Tecnologia
MINISTÉRIO DA EDUCAÇÃO E CIÊNCIA

o júri / the jury

presidente / president

Doutor Armando da Costa Duarte
Professor Catedrático da Universidade de Aveiro

vogais / examiners committee

Doutor António Luís Jesus Teixeira
Professor Associado com Agregação da Universidade de Aveiro (**Orientador**)

Doutora Maria do Carmo Raposo de Medeiros
Professora Associada da Faculdade de Ciências e Tecnologia da Universidade de Coimbra

Doutor Paulo Sérgio de Brito André
Professor Associado do Instituto Superior Técnico

Doutor Mário José Neves de Lima
Professor Auxiliar da Universidade de Aveiro

Doutor Rogério Nunes Nogueira
Investigador do Instituto de Telecomunicações de Aveiro (**Coorientador**)

Doutora Giorgia Parca
Investigadora do Instituto de Telecomunicações de Aveiro

Doutora Berta Maria Barbosa Neto
Optical System Verification and Testing Engineer Coriant, Portugal

agradecimentos

Quero começar por agradecer ao meu orientador, o Professor Doutor António Teixeira, e ao meu co-orientador, o Professor Doutor Rogério Nogueira. Ao Professor Doutor António Teixeira, agradeço todo o apoio prestado, as inúmeras contribuições para este trabalho e a partilha da sua visão e génio científicos. Aos dois, agradeço as discussões científicas e o árduo trabalho de revisão desta dissertação.

Aos meus colegas de grupo, e em particular Claudia Reis, Giorgia Parca, Berta Neto, Ana Rocha, Ali Shapari e Zoran Vujicic, agradeço as suas valiosas contribuições para o trabalho aqui apresentado.

Ao Instituto Politécnico de Castelo Branco (IPCB), pela dispensa parcial de serviço docente, concedida ao abrigo do Programa de Formação Avançada de docentes do IPCB.

Ao Instituto de Telecomunicações (IT), por ter disponibilizado os laboratórios que permitiram a realização do trabalho experimental.

À Fundação para a Ciência e Tecnologia (FCT), pelo suporte específico dado a esta dissertação, através da Bolsa (SFRH/PROTEC/50015/2009) e pelo financiamento providenciado através dos projectos MOTION (PTDC/EEA-TEL/73529/2006), THRONE (PTDC/EEA-TEL/66840/2006), TOMAR-PON (PTDC/EEA-TEL/108412/2008) e CONTACT (PTDC/EEA-TEL/114144/2009). Às redes de excelência europeias BONE e EURO-FOS, pelo suporte à minha participação em actividades científicas internacionais.

Uma palavra especial a todos os meus colegas e amigos do grupo de comunicações óticas do IT, cujo apoio, camaradagem e amizade em muito contribuíram para o bom desenrolar deste meu desafio.

À minha família, por estar sempre presente, à Gena, pelo amor e apoio incondicional, à Eva e à Rute, a alegria das nossas vidas.

Bem-hajam todos.
Rogério Dionísio

palavras-chave

Interferómetro Mach-Zehnder baseado em amplificadores ópticos de semicondutor (MZI-SOA), algoritmo genético, conversão de comprimento de onda, processamento óptico, conversão de formato, modulação de fase e de amplitude.

resumo

Nos últimos anos, a crescente procura e troca de informação tem levado ao aumento de tráfego nas redes de comunicação óticas actuais. As comunicações coerentes, com recurso à amplitude e fase do sinal, ressurgem como uma das técnicas de transmissão capazes de aumentar a eficiência espectral e o rendimento dos canais óticos.

Nesse âmbito, este trabalho apresenta um estudo sobre a conversão de formatos de modulação de sinais, usando técnicas exclusivamente no domínio ótico, através de conversão de comprimento de onda, com base no MZI-SOA. Esta técnica, aplicada em nós óticos que interligam redes óticas com débitos binários distintos, permite uma maior escalabilidade e eficiência da rede.

A tese começa por apresentar uma caracterização experimental detalhada das propriedades estáticas e dinámicas do MZI-SOA.

É depois proposto um modelo semi-analítico que descreve a evolução da amplitude e fase do sinal ótico à saída do MZI-SOA. Os coeficientes do modelo são obtidos recorrendo a um algoritmo genético multi-objectivo. O modelo é validado experimentalmente, explorando a dependência do sinal ótico com os parâmetros operacionais do MZI-SOA.

Segue-se a proposta de uma técnica de conversão de formato de modulação de amplitude para modulação de fase contínua.

Finalmente, é feito um estudo das potencialidades do MZI-SOA para conversão de formato de modulação de amplitude para modulação QPSK e QAM. Mostra-se a depedência da constelação do sinal com o desvio dos parâmetros operacionais, em torno do valor ótimo. A técnica é validada experimentalmente para modulação QPSK.

keywords Mach-Zehnder interferometer based on semiconductor optical amplifiers (MZI-SOA), genetic algorithm, wavelength conversion, optical processing, format conversion, phase and amplitude modulation.

abstract Over the years, the increased search and exchange of information lead to an increase of traffic intensity in todays optical communication networks. Coherent communications, using the amplitude and phase of the signal, reappears as one of the transmission techniques to increase the spectral efficiency and throughput of optical channels.

In this context, this work present a study on format conversion of modulated signals using MZI-SOAs, based exclusively on all-optical techniques through wavelength conversion. This approach, when applied in interconnection nodes between optical networks with different bit rates and modulation formats, allow a better efficiency and scalability of the network.

We start with an experimental characterization of the static and dynamic properties of the MZI-SOA.

Then, we propose a semi-analytical model to describe the evolution of phase and amplitude at the output of the MZI-SOA. The model's coefficients are obtained using a multi-objective genetic algorithm. We validate the model experimentally, by exploring the dependency of the optical signal with the operational parameters of the MZI-SOA.

We also propose an all-optical technique for the conversion of amplitude modulation signals to a continuous phase modulation format.

Finally, we study the potential of MZI-SOAs for the conversion of amplitude signals to QPSK and QAM signals. We show the dependency of the conversion process with the operational parameters deviation from the optimal values. The technique is experimentally validated for QPSK modulation.

"Jamais te perderás
nos trilhos traçados.
Porém, nunca as sensações
dos ímpetos libertadores
habitarão o teu corpo acomodado
enquanto não ousares desbravar
o caminho que tanto temes
para além da fronteira."
Do modo anómalo de Existir
João Mendes Rosa

À Gena.

À Rute e à Eva.

Contents

List of Acronyms

Notation	Description
ADC	Analog to Digital Conversion
AMI	Alternate Mark Inversion
APSK	Amplitude Phase Shift Keying
ASE	Amplifier Spontaneous Emission
ASK	Amplitude Shift Keying
AWGN	Average White Gaussian Noise
BER	Bit Error Rate
BERT	Bit Error Rate Tester
BPF	Bandpass Filter
BPSK	Binary Phase Shift Keying
CD	Chromatic Dispersion
CPFSK	Continuous Phase FSK
CPM	Continuous Phase Modulation
CROW	Coupled Ring-resonator Optical Waveguide
CSRZ	Carrier-Suppressed Return-to-Zero
CW	Continuous Wave
DBPSK	Differential Binary Phase Shift Keying
DFB	Distributed Feed-Back
DGD	Differential Group Delay
DI	Delay Interferometer
DISC	Delay-Interferometer-Signal wavelength Conversion
DPQPSK	Dual Polarization Quadrature Phase Shift Keying
DPSK	Differential Phase Shift Keying
DQPSK	Differential Quadrature Phase Shift Keying
DSP	Digital Signal Processing
DUT	Device Under Test
ECL	External Cavity laser

Notation	Description
EDFA	Erbium Doped Fiber Amplifier
EO	Electro-optical
EO-DAC	Electro-Optical Digital to Analog Converter
EOE	Electrical to Optical to Electrical
ER	Extinction Ratio
EVM	Error Vector Magnitude
FPGA	Field Programmable Gate Array
FSK	Frequency Shift Keying
FWM	Four-wave Mixing
GA	Genetic Algorithm
GMSK	Gaussian Minimum Shift Keying
HD	High Definition
HNLF	Highly Non-Linear Fiber
I	In-phase
IM	Intensity Modulator
IP	Internet Protocol
IQM	IQ Modulator
ISI	Inter Symbol Interference
LN	Lithium Niobate ($LiNbO_3$)
LO	Local Oscillator
M2M	Machine–to–Machine
MAN	Metropolitan Area Network
MOGA	Multi-Objective Genetic Algorithm
M-PSK	M-ary Phase Shift Keying
MSK	Minimum Shift Keying
MZDI	Mach Zehnder Delay Interferometer
MZI	Mach-Zehnder Interferometer
MZI-SOA	Mach-Zehnder Interferometer with Semiconductor Optical Amplifier
MZM	Mach-Zehnder Modulator
NoE	Network of Excellence
NOLM	Nonlinear Optical Loop Mirror
NRZ	Non-Return-to-Zero
NRZ-OOK	Non-Return-to-Zero On-Off Keying

Notation	Description
OADM	Optical Add-Drop Multiplexer
OCSA	Optical Complex Spectrum Analyzer
ODL	Optical Delay Line
O-E	Optical to Electrical
OFDM	Orthogonal Frequency Division Multiplexing
OLT	Optical Line Terminal
OMFCS	Optical Modulation Format Conversion System
ONU	Optical Network Unit
OOK	On-Off Keying
OSA	Optical Spectrum Analyzer
OSNR	Optical Signal-to-Noise Ratio
OTDM	Optical Time Division Multiplexing
PBS	Polarization Beam Splitter
PC	Polarization Controller
PLC	Planar Lightwave Circuit
PM	Power Meter
PMD	Polarization Mode Dispersion
PMod	Phase Modulator
POL-MUX	Polarization Multiplexing
PolSK	Polarization Shift Keying
PON	Passive Optical Network
PPLN	Periodically Poled Lithium Niobate
PRBS	Pseudo Random Bit Sequence
PS	Phase Shifter
PSK	Phase Shift Keying
Q	Quadrature
QAM	Quadrature Amplitude Modulation
QoT	Quality of Transmission
QPSK	Quadrature Phase Shift Keying
Quasi-CPM	Quasi-Continuous Phase Modulation
RAM	Random Access Memory
RefSOA	Reflective Semiconductor Optical Amplifier
RMS	Root Mean Squared
RMSE	Root Mean Squared Error
RoF	Radio over Fiber
RTS	Real-time Scope
RZ	Return-to-Zero

Notation	Description
RZ-BPSK	Return-to-Zero Binary Phase Shift Keying
RZ-OOK	Return-to-Zero On-Off Keying
RZ-QPSK	Return-to-Zero Quadrature Phase Shift Keying
SA	Saturable Absorber
Si	Silicon
SNR	Signal-to-Noise Ratio
SOA	Semiconductor Optical Amplifier
SOP	State of Polarization
SPM	Self Phase Modulation
VOA	Variable Optical Attenuator
WDM	Wavelength Division Multiplexing
WGN	White Gaussian Noise
XAM	Cross-Absorption Modulation
XGC	Cross Gain Compression
XGM	Cross Gain Modulation
XOR	Exclusive OR
XPM	Cross Phase Modulation

Note: Each acronym is defined the first time it appears in a Chapter.

List of Symbols

Notation	Description
α	Linewidth enhancement factor of a SOA
$\alpha_{1,2,3,4}$	Coupling factors
A_s	Amplitude of the electrical field
d	Euclidean distance between adjacent symbols in the constellation diagram
δ	Phase mismatch
Δf	Linear frequency deviation
$\Delta\omega$	Angular frequency deviation
$\Delta\phi$	Phase difference between MZI-SOA outputs
E	Electrical field
E_s	Energy per symbol
G_0	Unsaturated gain of a SOA
I_{SOA}	SOA current
k_r	Power ratio between two polarization components
L	Number of modulation levels
λ_P	Pump wavelength
λ_S	Signal wavelength
M	Number of symbols in the constellation diagram
P	Power of an optical signal
p	Linear coefficient between SOA gain and bias current
P_0	Mean power
P_b	Bit error rate probability
P_{CW}	Probe signal power
φ	Phase contribution from a SOA
φ_s	Phase of the electrical field
P_l	Pattern length
P_s	Saturation power of a SOA
R	Responsivity of a photodiode
R_b	Bit Rate
R_s	Symbol Rate
σ_n^2	Noise power spectral density

Notation	Description
V_{PS}	Voltage of a phase shifter
ω_0	Angular frequency of the optical carrier

List of Figures

List of Tables

Chapter 1

Introduction

1.1 Background and Motivation

From the unprecedented popularity of Internet and its derived new services, today's established networks should be able to provide more data throughput than ever. On a recent study [1], CISCO has estimated that global Internet traffic has increased eightfold over the past 5 years, and will increase nearly fourfold over the next 5 years, with an annual global Internet Protocol (IP) traffic above the zettabyte threshold by the end of 2016. Bandwidth intensive content and peer-to-peer applications consume the great majority of bandwidth in most broadband networks today. High Definition (HD) streaming video is considered by many as the ultimate bandwidth-hungry application. When one adds the bandwidth requirements of Internet browsing, social networking, or online gaming, telecommunication service providers have to deliver an increasingly larger amount of bandwidth. Besides human-made Internet traffic, Machine–to–Machine (M2M) communications [2], fostered by smart metering applications [3] and the opening of new radio spectral opportunities [4], are spreading worldwide. This so-called "Internet of Things" [5] will contribute even more to increase the quantity of information exchanged in communication networks, and specially on the optical networks, used both by fixed and wireless communications.

Since their introduction thirty years ago, photonics technologies have largely contributed to the massive development of communication networks and it can be easily predicted they will serve as grounds for most of the network revolutions ahead. An analysis of the drivers of photonics suggests that its future expansion will be made along four paths [6]:

- Make networks faster;
- Make networks more transparent;
- Make networks more dynamic;
- Make networks greener.

These paths correspond to four research areas that pull simultaneously, each one in their own direction, as illustrated in Figure 1.1. Therefore, a successful approach on all topics is a difficult challenge. It now falls within the responsibility of researchers to devise solutions that allow the development of optical systems capable of operating on all four directions.

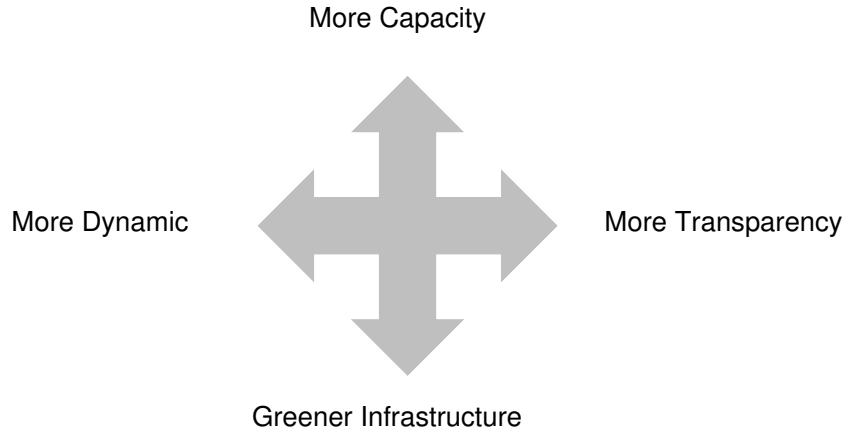

Figure 1.1: The four paths of expansion of future optical networks.

1.1.1 More transparent optical networks

Many Electrical to Optical to Electrical (E/O/E) conversions are performed in today's optical networks, from transport to access networks. The signal in the optical domain is converted to the electric domain using a photodetector, being processed, amplified and then re-injected into the optical fiber by a transmitter. One advantage of this technology is that the transmission impairments such as noise, dispersion and nonlinearities do not accumulate along the link. However, system upgrades, such as bit rates and modulation formats are expensive and difficult to implement because all the regenerators of the link have to be replaced. Besides that, the huge bandwidth of the optical fiber cannot be exploited properly. Increasing optical transparency is obtained by removing these conversions as much as possible. It will benefit to the transport but also to the access networks, by allowing several bit-rates, several modulation formats, or several radio standards to travel across the same generic fibre infrastructure. In particular, transparency will make possible the cost-effective convergence of some networks, e.g. radio and fixed access, or metro and access.

The ongoing introduction of transparency through optical cross-connects based on wavelength selective switches has already removed some limitations to the development of network capacity. In the ideal scenario, an optical data stream enters the network though the input node, possibly travel across several intermediate nodes, and reaches its destination node without conversion to electronics along the route. However, numerous challenges remain to be solved in order to create fully meshed optically transparent networks or subnetworks. The all-optical processing techniques for signal regeneration or for wavelength conversion are also promising techniques. They could not only help to expand transparency further, but also to bring about wavelength agility and, hence, further save on the number of terminals. All-optical processing functions have been mainly achieved by exploiting non-linear effects on both fibers and semiconductors. The Semiconductor Optical Amplifier (SOA) stands out from other all-optical processing devices since it is integrable, provides gain and requires small optical input powers for non-linear operation.

Due to the SOA integrability, interferometric structures have been proposed, which have stable operation when compared to their fiber-based counterparts. The integrated SOA structures allow more optical processing functions than the SOA alone. In particular, the Mach-Zehnder Interferometer (MZI) with a SOA in each arm, and moreover, MZI-SOA integrated arrays have been used to demonstrate several all-optical functions. Therefore, both the SOA and the MZI-SOA are considered key elements for all-optical processing subsystems and consequently for future generation optical networks. For this and other reasons explained in the following subsection, the MZI-SOA was chosen to be the main system of the optical processing study here presented.

1.1.2 More capacity optical networks

The capacity performance is characterized through the information spectral efficiency, expressed in bit/s/Hz. Transmission systems under development are proposing a 4 bits/s/Hz information spectral efficiency, achieved through 100 Gbit/s and more advanced modulation formats with advanced detection techniques using Digital Signal Processing (DSP) [7]. Recent progress have set new records on transmission capacities in optical networks, from laboratory experiments [8] or under real-world conditions [9]. Within the next five to ten years, advanced techniques and engineering must be identified and developed to prepare future networks with an information spectral density increased at least by a factor of ten [6, 10]. The work of this thesis will also focus on this aspect, using the MZI-SOA as all-optical carrier aggregation system, to increase the spectral efficiency of transmitted signals and consequently, the capacity of optical channels.

1.1.3 More dynamic optical networks

Up to now, the traffic increase is supported by optical networks providing the requested capacity thanks to Wavelength Division Multiplexing (WDM) and transport of several high speed optical channels through a single fibre. The very key point is to still better exploit the available bandwidth of optical fibers; this can be obtained by packing channels closer to each other while simultaneously increasing their individual bit rate. However, recent research advancements propose new transmission schemes for the future core networks to cope with the high-capacity requirements. Networks migrate from the fixed WDM single line rate systems to systems with improved and heterogeneous transmission characteristics [11], commonly defined in the literature as "Mixed-Rate/Format networks" [12], or to networks that implement an "Elastic or Flexible-Rate/Format" architecture that has the ability to vary the emitted rate per transmitter [13, 14]. A proposal that has gained significant momentum recently, utilizes Orthogonal Frequency Division Multiplexing (OFDM)-based solution that offers very fine granularity and manages to vary the aggregate network capacity on demand [14]. These techniques requires flexible optical transmitters with the ability to dynamically adapt to different line-rates [13]. In Chapter 5, we propose an optical generator based on MZI-SOAs, with flexible modulation format conversion and baud rate, to focus on this aspect.

1.1.4 Greener infrastructure

This clear and challenging objective is mandatory to cope with the traffic increase, while maintaining the cost and energy of the transported bit at an acceptable level. In the frame of high traffic, studies have shown that it is less efficient to process all packets in all nodes [15]. In effect, it is estimated that 80 % of traffic entering a node is a pass-through traffic, with a destination located in another node. It is then particularly efficient to keep that part of the traffic in the optics domain, without electronic conversion or packet processing. Transparency has the advantage of contributing to more energy-efficient networking without decreasing flexibility and agility. Overall, optical transparency is a useful feature for decreasing cost (cost/bit) and energy consumption (J/bit).

Given this analysis, one may infer that with current technology, it may be difficult to follow simultaneously all four path illustrated in Figure 1.1, which is a main constrains towards implementing the new generation of optical networks. Furthermore, these constrains may be relieved by developments in the fields of all-optical processing, wavelength conversion and flexible techniques for the generation of optical signals with advanced modulation formats. Hence the principal motivation in this thesis is to contribute in these three areas, which hold the promise of being the right technology to build larger capacity, more energy efficient, more dynamic and more transparent optical networks.

1.2 Thesis Outlook

The goal of this thesis is the study of format conversion techniques in all-optical networks. The MZI-SOA shows very attractive capabilities and therefore the objective is to investigate its potential as an optical node for the dynamic generation of optical signals. In doing so, two techniques to implement all-optical modulation format conversion are investigated by means of simulations and experimental studies.

The following structure in six chapters was adopted to describe the thesis:

Chapter 1 exposes the social and technological context of the thesis, as well as the motivation and objectives behind the work here presented. It is expected to motivate the reader for the next chapters where the deeper and more arduous content lies.

Chapter 2 introduces the reader to the devices used for all-optical format conversion and, particularly to the SOA and MZI-SOA fundamentals. The state of the art of SOA based optical format conversion, SOA interferometers and, particularly, of MZI-SOA is overviewed, whilst contextualizing them in the work presented on the following chapters.

Chapter 3 starts off with the experimental characterization of MZI-SOA devices and focus on the evaluation of MZI-SOA devices for phase modulation, exploiting co and counter propagation schemes. Rules of operation are derived for advanced modulation format conversion.

Chapter 4 concerns itself with a semi-analytical static model, optimized by a genetic algorithm, for simulation and performance estimation of MZI-SOA devices.

Chapter 5 present two configurations for advanced format conversion: One uses two MZI-SOAs used in a tandem configuration for all-optical format conversion from Non-Return-to-Zero On-Off Keying (NRZ-OOK) to continuous phase modulation. The other uses the same MZI-SOAs, but in a parallel configuration for all-optical format conversion from NRZ-OOK to multi-level and multi-phase amplitude modulation.

The main conclusions of the work are summarized in the final chapter. Future work following from the work presented in the thesis is also suggested in the concluding paragraphs.

The bibliographic references are listed at the end of each chapter.

1.3 Main Achievements

This thesis has been carried out at *Instituto de Telecomunicações* (IT), in the Optical Communications and Photonics research group, in partnership with the *University of Aveiro* (UA).

The work has been mainly developed within the scope of four National funded research activities (three by FCT and one by QREN-Adi). The TOMAR-PON project (Techniques Of Modulation And Remodulation for PON) is targeted to investigate the optimum modulation and remodulation techniques using Reflective Semiconductor Optical Amplifiers (RSOAs), to improve the capacity and reach for Passive Optical Networks (PONs). In the frame of the project CONTACT (Components and techniques for high capacity optical communications), part of the investigations studying phase modulation with active optical devices have been carried out. In the THRONE project (Devices and techniques for optical processing in high bit-rate networks), optical processing techniques for the generation of advanced modulation formats were addressed, with the aim of improving the spectral efficiency. Finally, the project PANORAMA, funded by QREN-Adi, aimed to develop an advanced optical and microwave platform with integrated management, for core, access and metro networks.

Furthermore, some activities have been realized in the scope of two Networks of Excellence (NoEs), funded by the European Commission, which are mainly devoted on collaborative research, sharing research activities, results and know-how. Within the frame of BONE (Building the Future Optical Network in Europe), the experimental verification of phase modulation based on Cross Phase Modulation (XPM) in MZI-SOA have been carried out. Additionally, through EURO-FOS (Europe's Research Network on Photonics Systems), investigation has been carried out on Quadrature Phase Shift Keying (QPSK) and QAM generator based on XPM in MZI-SOA.

In the author's opinion, the most important results accomplished from this thesis are:

- Experimental study of a phase modulator using a MZI-SOA with co and counter propagation [16–18] schemes (Chapter 3).
- Development of an analytical model for the characterization of the static properties of MZI-SOAs, considering the inherent fabrication yields and asymmetries [19] and numerical validation supported on a Multi-Objective Genetic Algorithm (MOGA) [20,

21] (Chapter 4).

- Development, numerical simulation and experimental demonstration of an all-optical format conversion from two NRZ-OOK sequences to one Quasi-Continuous Phase Modulation (Quasi-CPM) sequence [22], using two cascaded MZI-SOAs (Chapter 5).

- Development and numerical simulation of an all-optical format conversion from NRZ-OOK sequences into a m-QAM signal. The proposed method may accommodate a variable number of input wavelength to create different m-QAM signals. The impact of non-ideal values of operational parameters on the performance of the system is numerically accessed [23]. Experimental demonstration is achieved for NRZ-OOK sequences into a QPSK (4-QAM) signal (Chapter 5).

1.4 List of Publications

The work accomplished during the elaboration of this thesis resulted in 6 papers published in internationally peer reviewed journals and 7 conference proceedings. In addition to these contributions, 4 book chapters were also written within the frame of the EURO-FOS NoE. The work has also originated collaborations with other researchers of the Optical Communications and Photonics research group, which were also published. The publications are listed bellow.

1.4.1 Journal Articles

6. Z. Vujicic, **R. Dionísio**, A. Shapari, N. Pavlovic and A. Teixeira, "Efficient Dynamic Modeling of Reflective Semiconductor Optical Amplifier," *IEEE Journal of Selected Topics on Quantum Electronics*, vol. 19, no. 5, pp. 1–10, 2013.

5. **R. Dionísio**, G. Parca, C. Reis, R. Nogueira and A. Teixeira, "2x10Gbit/s NRZ-OOK to 10Gbaud Quasi Continuous Phase Modulation All-Optical Conversion Using Cascaded MZI- SOAs," *Microwave and Optical Technology Letters*, vol. 54, no. 5, pp. 1240–1242, 2012.

4. **R. Dionísio**, G. Parca, C. Reis, and A. Teixeira, "Operational parameter optimisation of MZI-SOA using multi-objective genetic algorithms," *Electronics Letters*, vol. 47, no. 9, pp. 561–562, 2011.

3. C. Reis, L. Costa, A. Bogoni, A. Maziotis, A. Teixeira, C. Kouloumentas, D. Apostolopoulos, D. Erasme, G. Berrettini, G. Meloni, G. Parca, H. Brahmi, I. Tomkos, L. Poti, M. Bougioukos, P.S. André, P. Zakynthinos, **R. Dionísio**, T. Chattopadhyay, and H. Avramopoulos, "Evolution of All-Optical Flip-Flops and Their Applications in Optical Communications Networks," *IET Optoelectronics*, vol. 6, no. 6, pp. 263–276, 2012.

2. C. Reis, A. Maziotis, C. Kouloumentas, C. Stamatiadis, M. Bougioukos, N. Calabretta, P. André, **R. Dionísio**, B. Neto, H. J. S. Dorren, H. Avramopoulos, and A. Teixeira, "All-optical clocked D flip-flop memory using a hybrid integrated S-R latch," *Microwave and Optical Technology Letters*, vol. 53, no. 6, pp. 1201–1204, 2011.

1. C. Reis, A. Maziotis, C. Kouloumentas, C. Stamatiadis, M. Bougioukos, N. Calabretta, P. André, **R. Dionísio**, B. Neto, H. J. S. Dorren, H. Avramopoulos, and A. Teixeira,"All-optical synchronous S-R flip-flop based on active interferometric devices," *Electronics Letters*, vol. 46, no. 10, pp. 709–710, 2010.

1.4.2 National and International Conferences

7. **R. Dionísio**, R. Nogueira and A. Teixeira,"Numerical Evaluation of Parallel MZI-SOAs for All-Optical 16QAM and 64QAM Generation," in *10th Symposium on Enabling Optical Networks and Sensors (SEON)*, June 2012.

6. **R. Dionísio**, C. Reis, P. André, R. Nogueira and A. Teixeira,"Experimental study of a phase modulator using an active interferometric device," in *15th IEEE Mediterranean Electrotechnical Conference (MELECON)*, pp. 1142–1146, April 2010.

5. **R. Dionísio**, C. Reis, N. Pavlovic, R. Nogueira and A. Teixeira,"Dual MZI-SOA with serial configuration for quadrature phase modulation," in *15th European Conference on Networks and Optical Communications (NOC)*, June 2010.

4. G. Parca, **R. Dionísio**, C. Reis, S. Betti, G. T. Beleffi, and A. Teixeira, "Inherent fabrication yields and asymmetries impacts on MZI-SOA static modelling," in *12th International Conference on Transparent Optical Networks (ICTON)*, pp. 1–4, June 2010.

3. C. Reis, **R. Dionísio**, B. Neto, P. André and A. Teixeira, "All-optical phase modulation using MZI-SOA," in *15th European Conference on Networks and Optical Communications (NOC)*, June 2010.

2. C. Reis, P. André, **R. Dionísio**, B. Neto, A.Teixeira, A. Maziotis, C. Kouloumentas, C. Stamatiadis, M. Bougioukos, H. Avramopoulos, N. Calabretta, and H. J. S. Dorren, "Experimental evaluation of all-optical asynchronous and synchronous memories," in *International Computer Engineering Conference (ICENCO)*, pp. 26–28, December 2010.

1. C. Reis, **R. Dionísio**, B. Neto, A. Teixeira, and P. André, "All-optical XOR based on integrated MZI-SOA with co and counter-propagation scheme," in *3rd ICTON Mediterranean Winter Conference, ICTON-MW*, pp. 1–4, 2009.

1.4.3 Book Chapters

4. **R. Dionísio**, G. Parca, C. Reis, A. Klingler, B. Neto and A. Teixeira, "MZI-SOA with hybrid integration," *Book chapter to appear in the EURO-FOS scientific Handbook of Experimental Fiber-optic Systems for Telecommunications.*

3. **R. Dionísio**, C. Reis and A. Teixeira, "Optical Complex Spectrum Analyzer for phase and power measurements," *Book chapter to appear in the EURO-FOS scientific Handbook of Experimental Fiber-optic Systems for Telecommunications.*

2. C. Reis, **R. Dionísio**, B. Neto, P André, R. Nogueira and A. Teixeira, "Balancing a Mach-Zehnder Interferometer with Semiconductor Optical Amplifiers," *Book chapter to appear in the EURO-FOS scientific Handbook of Experimental Fiber-optic Systems for Telecommunications.*

1. C. Reis, A. Maziotis, C. Stamatiadis, C. Kouloumentas, M. Bougioukos, N. Calabretta, P André, **R. Dionísio**, B. Neto, H. Dorren, H. Avramopoulos and A. Teixeira, "Optical Clocked Flip-Flops based on Active Interferometric Devices," *Book chapter to appear in the EURO-FOS scientific Handbook of Experimental Fiber-optic Systems for Telecommunications.*

1.4.4 Other contributions

Below are other contributions by the author which are not included in this thesis, due to the unrelated content with this research.

17. **R. Dionísio**, J. Ribeiro, P. Marques and J. Rodriguez, "Implementation of a Communication Protocol between a Geo-location Database and TV White Space Devices," in *The 4th Workshop of COST Action IC0902 Cognitive Radio and Networking for Cooperative Coexistence of Heterogeneous Wireless Networks*, October 2013.

16. **R. Dionísio**, "On-Light: Optical Social Network," in *12th International Conference on Education Training in Optics and Photonics (ETOP)*, July 2013.

15. **R. Dionísio**, J. C. Ribeiro, P. Marques and J. Rodriguez, "Evaluation of Blind Sensing Techniques in Multiple Wireless Microphones Environments," in *9th edition of the Conference on Telecommunications (Conftele)*, P1.2, May 2013.

14. J. C. Ribeiro, **R. Dionísio**, H. Esteves, P. Duarte, J. Ribeiro, P. Marques and J. Rodriguez, "Testbed for Combination of Local Sensing with Geo-location Database in Real Environments," *Wireless Communications, IEEE*, vol. 19, no. 4, pp. 59–66, August 2012.

13. **R. Dionísio**, P. Marques and J. Rodriguez, "Evaluation of Sensing Techniques for Wireless Microphone Signals in the TV White Spaces," *Romanian Review Precision Mechanics, Optics & Mechatronics*, no. 41, pp. 90–96, June 2012.

12. **R. Dionísio**, J. C. Ribeiro, J. Ribeiro, P. Marques and J. Rodriguez, "Cross-platform Demonstrator Combining Spectrum Sensing and a Geo-location Database," in *21st ICT Future Network & Mobile Summit (FUNEMS)*, pp. 1–9, June 2012.

11. **R. Dionísio**, P. Marques and J. Rodriguez, "Interference Study between Wireless Microphone Systems and TV White Space Devices," in *IEEE International Conference on Communication (ICC)*, pp. 1874–1878, June 2012.

10. J. P. Girão, B. Neto, A. M. Rocha, C. Reis, **R. Dionísio**, S. Chatzi, F. Bonada, J. Lazaro, A. L. J. Teixeira, and P. S. André, "C + L band extended reach amplified next generation access networks," *Microwave and Optical Technology Letters*, vol. 53, no. 10, pp. 2414–2418, 2011.

9. **R. Dionísio**, P. Marques and J. Rodriguez, "TV White Spaces Maps Computation through Interference Analysis," in *20th ICT Future Network & Mobile Summit (FUNEMS)*, pp. 1–9, June 2011.

8. H. Esteves, P. Duarte, P. Marques and **R. Dionísio**, "Plataforma de agendamento de espectro para equipamentos profissionais," in *5th Congress URSI - ANACOM*, November 2011.

7. B. Neto, **R. Dionísio**, A. M. Rocha, C. Reis, S. Chatzi, F. Bonada, J. Lazaro, A. L. J. Teixeira, and P. S. André, "C+L band extended reach next generation access networks through Raman amplification: Assessment in rural scenario," in *15th International Conference on OptoeElectronics and Communications Conference (OECC)*, pp. 22–23, 2010.

6. B. Neto, A. M. Rocha, J. P. Girão, **R. Dionísio**, C. Reis, , S. Chatzi, F. Bonada, J. Lazaro, A. Teixeira, and P. S. André, "C+L band gain equalization for extended reach WDM-ring PON using hybrid Raman / in line EDFA amplification," in *12th International Conference on Transparent Optical Networks (ICTON)*, pp. 1–3, June 2010.

5. B. Neto, A. M. Rocha, J. P. Girão, **R. Dionísio**, C. Reis, J. Lazaro, A. Teixeira, and P. S. André, "Comparative analysis of hybrid in line EDFA / Raman with simple Raman amplification in WDM ring PON for C+L band," in *15th European Conference on Networks and Optical Communications (NOC)*, June 2010.

4. B. Neto, C. Reis, **R. Dionísio**, J. M. Ferreira, J. A. Lazaro, G. Tosi-Beleffi, A. N. Pinto, R. Nogueira, A. Teixeira, J. Prat, and P. S. André, "Assessment and mitigation of erbium-doped fibre amplifiers (EDFA) gain transients in hybrid wavelength division multiplexing/time division multiplexing passive optical network (WDM/TDM PON) in the presence of packet-based traffic," *IET Optoelectronics*, vol. 4, no. 6, pp. 219–225, 2010.

3. B. Neto, A. Klingler, C. Reis, **R. Dionísio**, R. Nogueira, A. L. J. Teixeira and P. S. André, "Enhanced optical gain clamping for upstream packet based traffic on hybrid WDM/TDM-PON using fiber Bragg grating," *Optics Communications*, vol. 284, no. 5, pp. 1354–1356, 2010.

2. **R. Dionísio**, "Módulo Expositivo e Interactivo sobre Fenómenos Ópticos," in *Actas da 4ªConferência Ibérica de Sistemas e Tecnologias da Informação (CISTI)*, pp. 585–590, June 2009.

1. C. Reis, B. Neto, **R. Dionísio**, G. Incerti, G. Tosi-Beleffi, D. Forin, A. Rocha, A. Teixeira, and P. André, "Transience analysis of bursty traffic with erbium doped

fiber amplifiers," in *11th International Conference on Transparent Optical Networks (ICTON)*, pp. 1–3, June 2009.

References

[1] (2012, May) The Zettabyte Era. [Online]. Available: http://www.cisco.com

[2] G. Wu, S. Talwar, K. Johnsson, N. Himayat, and K. Johnson, "M2M: From mobile to embedded internet," *Communications Magazine, IEEE*, vol. 49, no. 4, pp. 36 –43, april 2011.

[3] Z. Fadlullah, M. Fouda, N. Kato, A. Takeuchi, N. Iwasaki, and Y. Nozaki, "Toward intelligent machine-to-machine communications in smart grid," *Communications Magazine, IEEE*, vol. 49, no. 4, pp. 60 –65, april 2011.

[4] H. Karimi, M. Fenton, G. Lapierre, and E. Fournier, "European Harmonized Technical Conditions and Band Plans for Broadband Wireless Access in the 790-862 MHz Digital Dividend Spectrum," in *New Frontiers in Dynamic Spectrum, 2010 IEEE Symposium on*, april 2010, pp. 1 –9.

[5] (2012, July) Internet of Things. [Online]. Available: http://www.internet-of-things.eu/

[6] (2012, March) Purple Book - Celtic Plus Programme of possible and recomended research items. [Online]. Available: http://www.celtic-initiative.org/PurpleBook+/Purplebook.asp

[7] P. J. Winzer, "High-Spectral-Efficiency Optical Modulation Formats," *J. Lightwave Technol.*, vol. 30, no. 24, pp. 3824–3835, Dec 2012. [Online]. Available: http://jlt.osa.org/abstract.cfm?URI=jlt-30-24-3824

[8] D. Qian, M.-F. Huang, E. Ip, Y.-K. Huang, Y. Shao, J. Hu, and T. Wang, "High Capacity/Spectral Efficiency 101.7-Tb/s WDM Transmission Using PDM-128QAM-OFDM Over 165-km SSMF Within C- and L-Bands," *J. Lightwave Technol.*, vol. 30, no. 10, pp. 1540–1548, May 2012. [Online]. Available: http://jlt.osa.org/abstract.cfm?URI=jlt-30-10-1540

[9] (2012, July) Deutsche Telekom researchers break transmission speed record. [Online]. Available: http://www.telekom.com/media/company/105388

[10] J. Yu, "System solutions toward terabit/s per channel," in *OptoeElectronics and Communications Conference (OECC), 2011 16th*, july 2011, pp. 220 –221.

[11] C. Meusburger and D. A. Schupke, "Optimizing the Migration of Channels with Higher Bit-Rates," in *Optical Fiber Communication Conference*. Optical Society of America, 2009, p. PDPD3. [Online]. Available: http://www.opticsinfobase.org/abstract.cfm?URI=OFC-2009-PDPD3

[12] A. Nag, M. Tornatore, and I. Biswanath Mukherjee, Fellow, "Optical Network Design With Mixed Line Rates and Multiple Modulation Formats," *J. Lightwave Technol.*, vol. 28, no. 4, pp. 466–475, Feb 2010. [Online]. Available: http://jlt.osa.org/abstract.cfm?URI=jlt-28-4-466

[13] O. Rival, G. Villares, and A. Morea, "Impact of Inter-Channel Nonlinearities on the Planning of 25–100 Gb/s Elastic Optical Networks," *J. Lightwave Technol.*, vol. 29, no. 9, pp. 1326–1334, May 2011. [Online]. Available: http://jlt.osa.org/abstract.cfm?URI=jlt-29-9-1326

[14] B. Kozicki, H. Takara, Y. Tsukishima, T. Yoshimatsu, K. Yonenaga, and M. Jinno, "Experimental demonstration of spectrum-sliced elastic optical path network (SLICE)," *Opt. Express*, vol. 18, no. 21, pp. 22 105–22 118, Oct 2010. [Online]. Available: http://www.opticsexpress.org/abstract.cfm?URI=oe-18-21-22105

[15] Y. Zhang, P. Chowdhury, M. Tornatore, and B. Mukherjee, "Energy Efficiency in Telecom Optical Networks," *Communications Surveys Tutorials, IEEE*, vol. 12, no. 4, pp. 441 –458, quarter 2010.

[16] R. Dionisio, C. Reis, P. Andre, R. Nogueira, and A. Teixeira, "Experimental study of a phase modulator using an active interferometric device," in *MELECON 2010*, 2010, pp. 1142–1146.

[17] C. Reis, R. P. Dionisio, B. Neto, A. Teixeira, and P. Andre, "All-optical XOR based on integrated MZI-SOA with co- and counter-propagation scheme," in *ICTON Mediterranean Winter Conference,2009. ICTON-MW 2009. 3rd*, 2009, pp. 1–4.

[18] C. Reis, R. Dionisio, L. Neto, P. André, and A. Teixeira, "All-Optical Phase Modulation using MZI-SOA," in *15th European Conference on Networks and Optical Communications (NOC)*, Faro, Portugal, 2010.

[19] G. Parca, R. Dionisio, C. Reis, S. Betti, G. T. Beleffi, and A. Teixeira, "Inherent fabrication yields and asymmetries impacts on MZI-SOA static modelling," in *Transparent Optical Networks (ICTON), 2010 12th International Conference on*, 2010, pp. 1–4.

[20] R. P. Dionisio, G. Parca, C. Reis, and A. L. Teixeira, "Operational parameter optimisation of MZI-SOA using multi-objective genetic algorithms," *Electronics Letters*, vol. 47, no. 9, pp. 561–562, 2011.

[21] Z. Vujicic, R. Dionisio, A. Shapari, N. Pavlovic, and A.Teixeira, "Efficient Dynamic Modeling of Reflective Semiconductor Optical Amplifier," *IEEE Journal of Selected Topics on Quantum Electronics*, 2013.

[22] R. P. Dionísio, G. Parca, C. Reis, R. Nogueira, and A. L. Teixeira, "2 x 10 Gbit/s NRZ-OOK to 10 Gbaud quasicontinuous phase modulation all-optical conversion using cascaded MZI-SOAs," *Microwave and Optical Technology Letters*, vol. 54, no. 5, pp. 1240–1242, 2012. [Online]. Available: http://dx.doi.org/10.1002/mop.26783

[23] R. Dionisio, R. Nogueira, and A. Teixeira, "Numerical Evaluation of Parallel MZI-SOAs for All-Optical 16QAM and 64QAM Generation," in *10th Symposium on Enabling Optical Networks and Sensors - SEON*, June 2012.

Chapter 2

Optical Modulation and Format Conversion: State of the Art

2.1 Introduction

Format conversion of optical signals started their application with the appearance of optical fiber systems in the 1980s [1], when coherent systems were under investigation world-wide [2]. Coherent detection using advanced optical modulation formats was widely discussed in the context of unamplified systems [3–5], where attenuation-limited single-span transmission required utmost receiver sensitivity. With the advent of efficient optical amplifiers (such as the Erbium Doped Fiber Amplifier (EDFA)), allowing for comparable direct-detection receiver sensitivities [5,6], and despite the fact that coherent optical systems foster spectrally efficient modulation schemes [7], coherent systems research decayed in the early 1990s.

However, in the last decade, we assist to an exponential increase of Internet connections worldwide. With high-bandwidth and on-demand applications continuing to emerge, next-generation optical networks will likely require significant improvements in reconfigurability and ultra-fast operations [8]. The evolution of the optical transmission technologies, towards data rates above 100 Gbit/s, demands a next-generation optical systems with coherent transmission techniques. The next-generation transmitters are required to address the needs to generate various spectrally-efficient modulation formats, such as QPSK, QAM and OFDM, those receiving much attention as candidate modulation formats for 100 Gbit/s transmission [9]. Reduced power consumption and format agility, as well as high performance, are also important keys in successful deployment of next-generation high data-rate modulator technology [10], as already explained in Chapter 1 and illustrated in Figure 1.1.

This chapter is organized as follows. Section 2.2 presents a general description of optical modulation formats, describing the physical properties of a lightwave that can be used to convey digital information, followed by the description of the most relevant metrics in Section 2.3. Section 2.4 present a proposal for the classification of optical modulation format conversion techniques, and covers various format conversion technologies and systems used to imprint data information onto a laser carrier. Since the design of optical transmitters is intimately related to the capabilities of high-speed optoelectronic hardware, an understanding of modulator technologies is vital to the understanding of optical modulation formats conversion. We briefly describe electro-optical techniques for

signal synthesis in Section 2.5. A special attention is devoted to all-optical techniques in Section 2.6; some of the techniques based on MZI-SOAs (the device used in this thesis for modulation format conversion) are described in detail. Moreover, other all-optical processing functionality using MZI-SOAs are briefly discussed in Section 2.7. The summary in Section 2.8 is complemented with a matrix "from/to", filled up, to the best of my knowledge, with all possible format conversions reported up to now.

2.2 Optical modulation formats

From the first application of fiber optics in the middle of the 1970's until only recently, On-Off Keying (OOK) has been the modulation format of choice for most commercial applications. However, other modulation schemes for optical networks have emerged to cope with the increasing traffic.

The purpose of this subsection is to present a brief description of the main modulation formats employed in optical networks, paying special attention in those which are used in the proposed format conversions techniques discussed in Chapters 3 and 5. Throughout this and the following Chapters, 0 and 1 (set in Typeface font) denote logical bits, while Roman font (e.g., $\{0\ ;\ \pm 1\}$ or $\{0\ ;\ \pi\}$) denotes modulation symbols.

2.2.1 Intensity Modulation

The electric field associated with an optical signal can be written as

$$E\left(t\right) = A_s cos\left[\omega_0 t + \varphi_s\right] \tag{2.1}$$

In the case of Amplitude Shift Keying (ASK) modulation format, it encodes the information in the amplitude A_s of the optical field, while keeping ω_0 and φ_s constant,

$$E\left(t\right) = A_s\left(t\right) cos\left[\omega_0 t + \varphi_s\right] \tag{2.2}$$

OOK is a special case of ASK, and one of the most used due to its simplicity. In OOK, A_s takes one of two fixed values during each bit period, depending on whether 1 or 0 bit is being transmitted. In practical situations, A_s is set to zero during the transmission of 0 bits.

The *constellation diagram* of OOK modulated signals is represented in Figure 2.1. A constellation diagram, also called *State Space Diagram*, is a geometric representation describing a modulated signal set. The horizontal axis of the constellation plane represent the In-phase (I) component of the signal and the vertical axis the Quadrature (Q) component. Thus, the constellation of OOK signals lies in a single axis, with one symbol in the origin (bit 0) and the other on the I axis (bit 1). Also represented in Figure 2.1 is the *vector diagram*. A vector diagram displays the I and the Q components like on an oscilloscope, which reveals the dynamics of the symbol transitions. A void of errors would show direct transition to different symbols, which is not the usual case in operational-implemented systems.

Two kind of line coding may be applied to an OOK signal, Non-Return-to-Zero (NRZ)

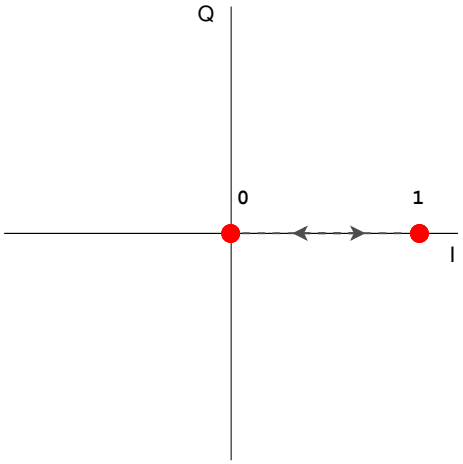

Figure 2.1: Constellation of an OOK signal, with symbols represented by red circles, and ideal vector diagram in grey dashed arrow lines.

or Return-to-Zero (RZ). The lack of timing information of the NRZ format can be overcome by introducing more transitions into the optical waveform. This leads to the RZ formats. However, the bandwidth of a RZ format is wider than that of a NRZ format.

As previously mentioned, one of the most important advantages of OOK is its simplicity and low cost compared with other modulation formats [11, 12]. Otherwise, intensity modulation formats are characterized by a bad nonlinear tolerance due to the presence of a strong optical carrier [12].

2.2.2 Phase Modulation

For Phase Shift Keying (PSK) format, the optical bit stream is generated by modulating the phase φ_s in (2.1) while the amplitude A_s and the angular frequency ω_0 of the optical carrier are kept constant.

$$E(t) = A_s cos[\omega_0 t + \varphi_s(t)] \tag{2.3}$$

For M-ary PSK modulation, the angular aperture between constellation symbols is given by $2\pi/M$, where M is the number of symbols, and the Euclidean distance d can be found to be equal to

$$d = 2A_s sin(\pi/M) \tag{2.4}$$

Thus, for Binary Phase Shift Keying (BPSK), the phase φ_s takes two values, commonly 0 and π, as represented by the constellation in Figure 2.2. For QPSK, each symbol is composed by two bits, and the phase may take one of four values, for example $\{\pi/4; 3\pi/4; 5\pi/4; 7\pi/4\}$, as shown in Figure 2.3.

The use of PSK format requires that the phase of the optical carrier remains stable so that phase information may be extracted at the receiver without ambiguity. This requirement puts a stringent condition on the the laser linewidth tolerance, both for the transmitter and the local oscillator of the coherent receiver. However, the linewidth requirements may be

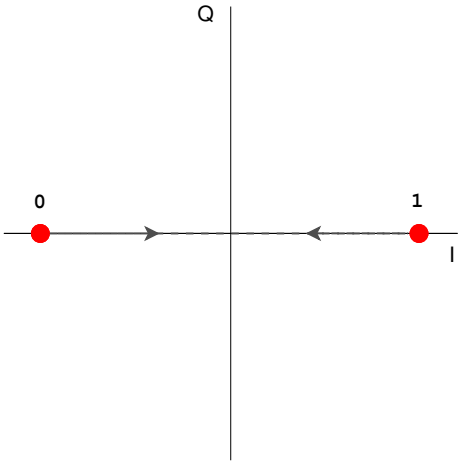

Figure 2.2: Constellation of a BPSK signal.

somewhat relaxed, by using a variant of the PSK format, known as DPSK [11]. In DPSK, the bit stream is previously encoded, so a simpler receiver may be used to recover the information.

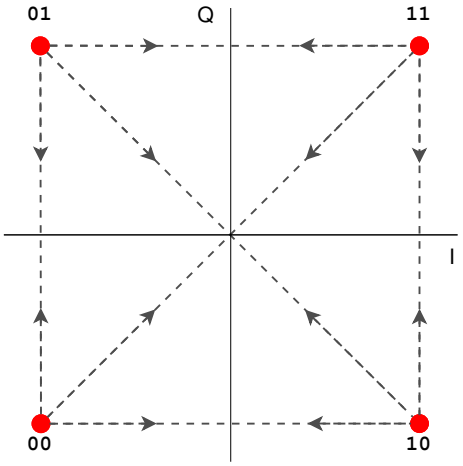

Figure 2.3: Constellation of a QPSK signal. Ideal transitions between symbols are represented buy dashed lines. Each symbol is Gray encoded.

2.2.3 Frequency Modulation

In the case of Frequency Shift Keying (FSK) modulation, data is coded in the optical carrier by shifting the carrier frequency ω_0 itself,

$$E(t) = A_s cos[\omega_0(t)\, t + \varphi_s] \tag{2.5}$$

For binary digital signals, ω_0 takes two values, $\omega_0 - \Delta\omega$ or $\omega_0 + \Delta\omega$, depending on

whether a 0 or a 1 bit is being transmitted. The frequency shift $\Delta f = \Delta\omega/2\pi$ denote the *frequency deviation*. Thus, the optical signal can be written as,

$$E(t) = A_s cos\left[(\omega_0 \pm \Delta\omega)\, t + \varphi_s\right] \tag{2.6}$$

Since the cosine argument of (2.6) can be written as $\omega_0 t + (\varphi_s \pm \Delta\omega t)$, the FSK modulation can also be viewed as a PSK modulation, where the carrier phase increase or decrease linearly over the bit duration, as depicted in Figure 2.4b. A special case is Continuous Phase FSK (CPFSK) [13], where the phase transitions shown in Figure 2.4a are continuous. This kind of FSK modulation is desirable, since discontinuities in waveform (Figure 2.4c) will broaden the signal bandwidth.

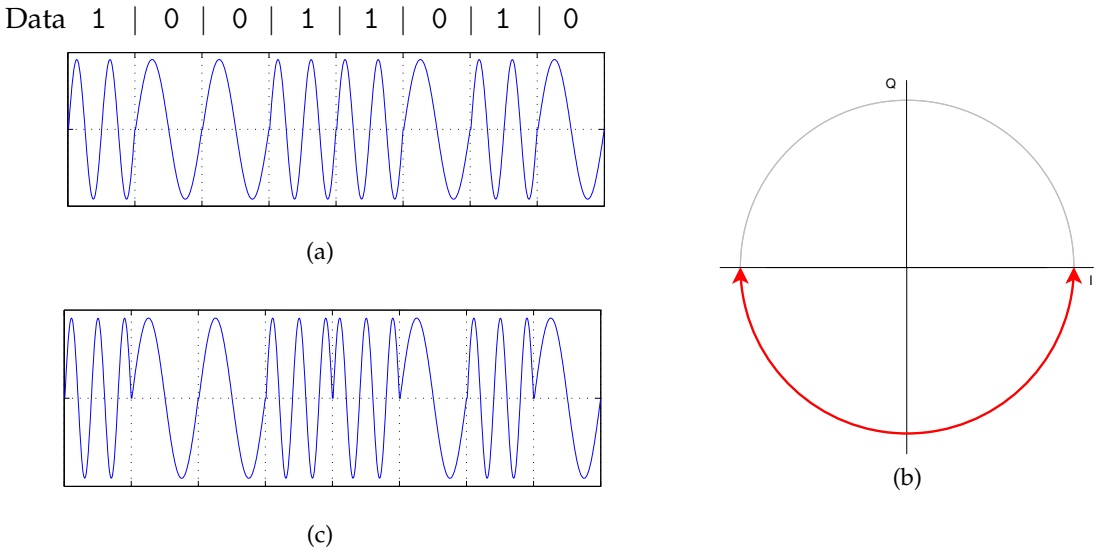

Figure 2.4: Time representation of (a) Continuous phase FSK and (c) FSK signal with phase discontinuities; (b) Constellation diagram.

2.2.4 Hybrid Modulation

In the previous chapters, only one parameter of the optical signal was modified (amplitude A_s, frequency ω_0 or phase φ_s) to produce a modulated signal. Hybrid modulation consider using both amplitude and phase (or frequency) in a single modulation scheme. In the case of QAM, the modulated signal given in (2.7) is generated by modulating the phase and the amplitude of the electric field.

$$E(t) = A_s(t)\, cos\left[\omega_0 t + \varphi_s(t)\right] \tag{2.7}$$

Each constellation point is represented by a symbol made up of several bits. For n bits per symbol, the number of constellation points, or symbols, is $M = 2^n$. Therefore, for 16-QAM, the number of symbols is $M = 2^4 = 16$, where $n = 4$, as depicted in Figure 2.5. By combining intensity and phase modulation, the number of phase states can be reduced for

the same number of symbols, compared to M-PSK modulation, leading to larger Euclidean distances between the symbols.

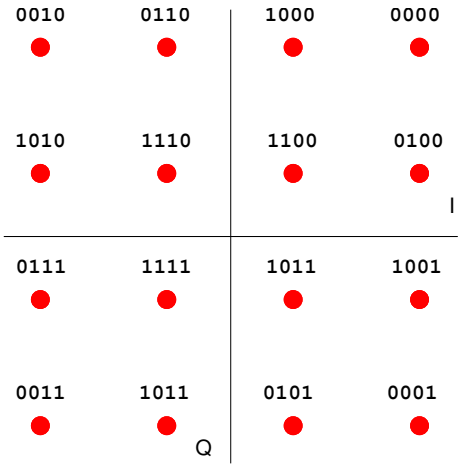

Figure 2.5: Constellation of a 16-QAM signal. Each symbol is Gray encoded.

Using multilevel signaling, $log_2(M)$ data bits are encoded on M symbols, and are then transmitted at a reduced symbol rate of $R_s = R_b/log_2(M)$, where R_b is the bit rate, and higher spectral efficiencies may be obtained due to spectral narrowing. On one hand, multilevel signaling allows for lower symbol rates at a fixed data rate, which is beneficial in the presence of dispersive signal distortions, such as Chromatic Dispersion (CD) [14] or Polarization Mode Dispersion (PMD) [15], and allows for smaller channel spacing. However, these benefits are accompanied by a reduced tolerance to noise [13] and Self Phase Modulation (SPM), and with a higher complexity of components. On the other hand, high-order modulation allows upgrading to higher channel data rates by using existing lower-speed equipment, and thus exceeding the limits of present high-speed electronics and digital signal processing.

Polarization multiplexing

A different approach towards multi-level modulation formats is the use of the polarization dimension of the optical signal. An additional degree of flexibility can be achieved by using Polarization Shift Keying (PolSK) [16] or Polarization Multiplexing (POL-MUX) [17]. PolSK may be used to transmit adjacent WDM channels in alternating polarizations to reduce coherent WDM crosstalk or nonlinear interactions between the channels [18]. POL-MUX is used to increase spectral efficiency, by transmitting two different signals at the same wavelength but in two orthogonal polarizations. In addition, POL-MUX signaling reduces the symbol rate by a factor of two when compared with binary modulation formats at the same total bit rate. This can be useful to increase both linear and nonlinear transmission tolerances. These methods are currently used in commercial systems, but requires complex polarization maintaining system components and polarization sensitive

receiver [12]. These techniques are out of the scope of this thesis and not considered in the remaining Chapters.

2.3 Modulation metrics

2.3.1 Bit Error Rate

The most fundamental and direct metric evaluating the Quality of Transmission (QoT) of every digital communication system is the Bit Error Rate (BER). It is expressed as the ratio of incorrectly received bits to the total number of received bits. Figure 2.6 shows the Signal-to-Noise Ratio (SNR) requirements of the digital modulation formats analyzed in the previous section. The BER curves are computed [13] considering an Average White Gaussian Noise (AWGN) channel with coherent reception, and Gray encoded data bits.

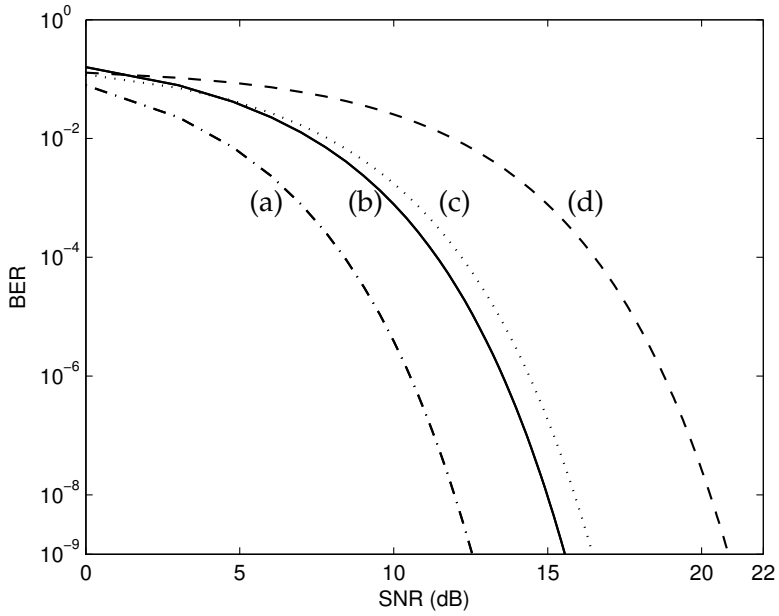

Figure 2.6: Bit Error Rate curves for several modulation format, following [13]. (a) BPSK and QPSK; (b) ASK and FSK; (c) 16-QAM; (d) 64-QAM.

One should keep in mind that performance comparison of digital modulation systems should consider not only error probability, but also transmission bandwidth, spectral spillover and hardware requirements. Several trade-offs exits between those parameters that must be analyzed carefully. Suppose, for example, that we want to keep the error probability to 10^{-9} – A common standard for optical system comparison purposes. The value of SNR needed for BPSK and QPSK is the lowest (12.55 dB), followed by ASK and FSK (15.56 dB), 16-QAM (16.53 dB) and finally 64-QAM with 20.90 dB. However, 16 and 64-QAM allows the transmission of 4 and 8 bits, respectively, in a single symbol time slot, thus increasing

the spectral efficiency of the transmission system compared with binary modulations (ASK, FSK or BPSK).

2.3.2 Error Vector Magnitude

In order to monitor BER it is necessary to demodulate received constellation points. This, however, might not always be possible as the receiver usually does not know the transmitted sequence and is not able to detect bit errors at the physical layer.

Therefore it might be beneficial to define a different QoT figure of merit that corresponds to BER, which gives a tentative estimation of the received signal directly from the constellation points, without resorting to demodulation or information provided by higher layers. One of such metrics is Root Mean Squared (RMS) Error Vector Magnitude (EVM), defined as [19]:

$$EVM_{RMS} = \sqrt{\frac{\frac{1}{N}\sum_{j=1}^{N}\left(\delta I_j^2 + \delta Q_j^2\right)}{P_0}} \times 100\ [\%] \tag{2.8}$$

where δI and δQ are deviations (differences in in-phase and quadrature amplitudes) of received data points with respect to ideal location of those points in the constellation and P_0 is the average power the constellation.

In [19], a relation between Optical Signal-to-Noise Ratio (OSNR) and EVM (under the constraint of a large number of received symbols) is given as:

$$EVM_{RMS} \simeq \frac{1}{\sqrt{SNR}} \tag{2.9}$$

This relation is approximate for non-data-aided receivers due to the fact that only estimates of the transmitted symbols are available [20]. Measured EVM is lower than actual EVM, especially at low SNR, due to the fact that amplitude error variance increases and some received data points are incorrectly assigned to neighboring clusters, thereby reducing measured EVM. For data-aided receiver, on the other hand, relation is exact since the transmitted sequence is known or can be reconstructed without uncertainty as to whether symbols are in the correct decision regions or not.

Bit error rate probability P_b, for an m-QAM modulation under influence of White Gaussian Noise (WGN), can be expressed as [21]:

$$P_b = \frac{2\left(1-\frac{1}{L}\right)}{\log_2(L)} Q\left(\sqrt{\left(\frac{3\log_2(L)}{L^2-1}\right)\left(\frac{2E_s}{N_0\log_2(M)}\right)}\right) \tag{2.10}$$

where L is the number of modulation levels, E_s is the energy per symbol, $\frac{N_0}{2} = \sigma_n^2$ is the noise power spectral density and Q is the Q-function defined as $Q(x) = \frac{1}{\sqrt{(2\pi)}}\int_x^\infty e^{-\frac{u^2}{2}}du$. Combining 2.9 with 2.10 the formula relating BER probability (P_b) to RMS EVM can be found as:

$$P_b \simeq \frac{2\left(1-\frac{1}{L}\right)}{\log_2(L)} Q\left(\sqrt{\left(\frac{3\log_2(L)}{L^2-1}\right)\left(\frac{2}{(EVM_{RMS})^2\log_2(M)}\right)}\right) \tag{2.11}$$

By inserting estimated (or monitored) EVM into the equation, an expected bit error probability can be found. The performance of the modulation format converters described in Chapter 5 uses (2.11) to compute the BER for QPSK, 16-QAM and 64-QAM signals.

2.4 Classification of format conversion techniques

In this section, we start to classify optical modulation formats conversion according to the technique used for the conversion, e.g., if it is an all-optical technique or an electro-optical technique. We also look at the kind of device where the format conversion takes place. Electro-optical techniques employing Phase Modulators (PMods), Mach-Zehnder Modulators (MZMs) and IQ Modulators (IQMods) are briefly presented. Radio over Fiber (RoF) techniques are not considered as format conversion techniques, since the modulation format of the signal is not altered when the signal is converted from the electrical domain to the optical domain. All-optical techniques are classified as using active or passive devices; Recent research on passive devices using Highly Non-Linear Fiber (HNLF) or optical waveguides based devices, such as Coupled Ring-resonator Optical Waveguides (CROWs), Delay Interferometer (DI) or Periodically Poled Lithium Niobate (PPLN) waveguides, will be also presented.

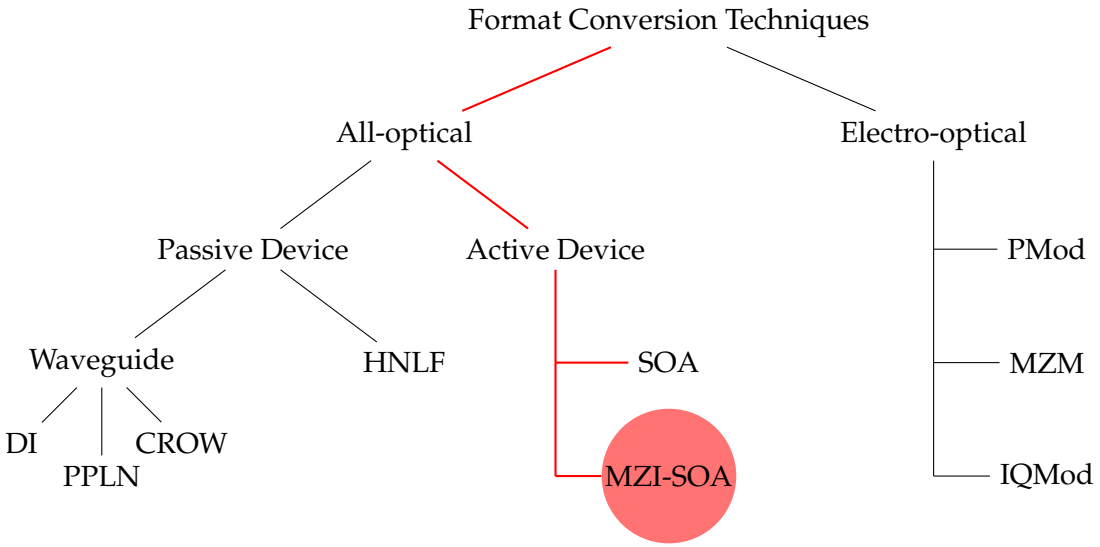

Figure 2.7: Classification of optical modulation format conversion systems. The red path shows the devices used in this thesis.

The individual conversion techniques will be described in more detail in the following sections. Greater insight is given to semiconductor devices, and specially SOA and MZI-

SOAs, which are used throughout this thesis as modulation format conversion devices. To better understand this classification, and to get a comprehensive overview of optical format conversion techniques, Figure 2.7 shows how the most important modulation formats conversion systems discussed today fall into the categories established here.

2.5 Electro-optical format conversion systems

2.5.1 Mach-Zehnder Modulator

A dual-drive MZMs consists of two PMods in both arms that can be operated independently, in contrast to single-drive MZMs. As depicted in Figure 2.8, the incoming light is split into two paths, both equipped with PMods controlled by an electrical drive signal ($u_1(t)$ or $u_2(t)$). After acquiring some phase differences relative to each other, the two optical fields are recombined. The interference varies from constructive to destructive, depending on the relative phase shift.

Generation of arbitrary QAM signals or arbitrary quadrature signals using a dual-drive MZM have been proposed by Ho *et al* [22], with a drive signal having two and three levels. Recently, a 16-QAM signal generation method was successfully demonstrated [23] at 50 Gbit/s (12.5 Gbaud $\times$ 4 bit), using a single dual-drive MZMs and 4-level electrical signals. This method requires the amplitude ratio of two QPSK signals to be adjusted.

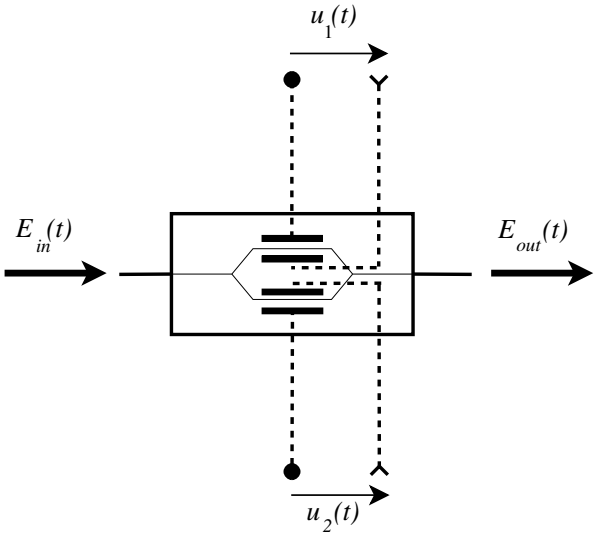

Figure 2.8: Optical dual-drive MZM modulator. Dashed lines are electrical signals.

2.5.2 IQ modulator

An IQMod is a structure usually composed of a PMod and two MZMs. As shown in Figure 2.9, the incoming light is equally split into two arms, the in-phase (I) and the

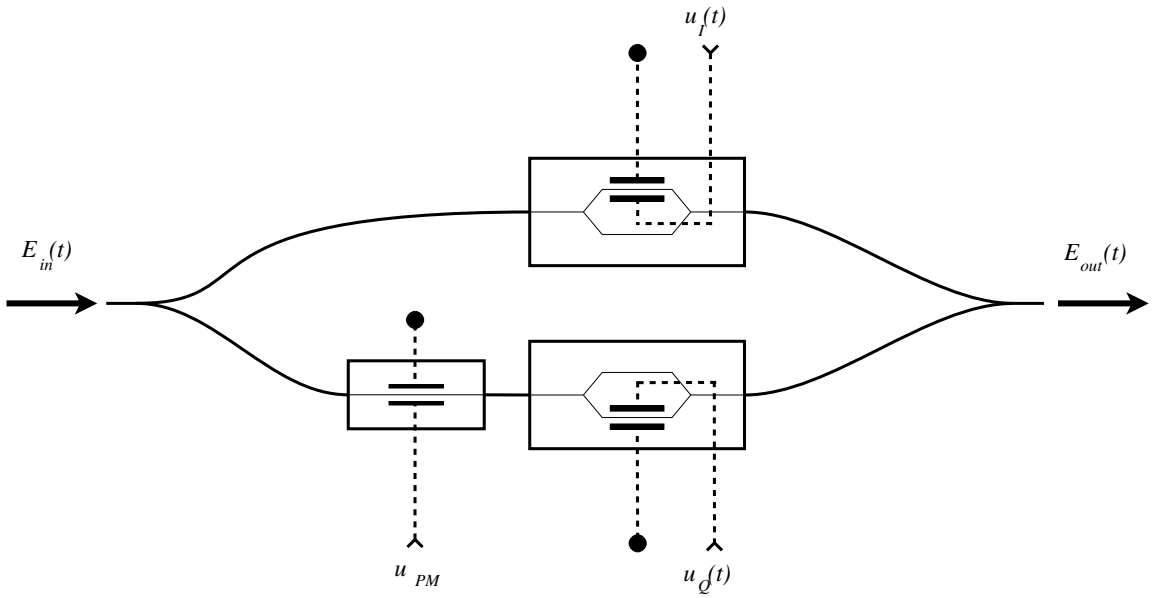

Figure 2.9: Optical IQ modulator. Dashed lines are electrical signals.

quadrature (Q) arm. In both paths, a field amplitude modulation is performed by operating the MZMs in the push-pull mode at the minimum transmission point [24]. Moreover, a relative phase shift of $\pi/2$ is adjusted in one arm, for instance by an additional PMod. This way, any constellation point can be reached in the complex IQ plane after recombining the light of both branches.

Seimetz *et al* [25] have investigated transmitters which require only binary electrical driving signals, using m consecutive PMods in serial configuration, where m is the number of bits per symbol. They have proposed and theoretically analyzed several possible structures of optical M-PSK and m-QAM using IQMods. Differences in the optical transmitter configuration and the electrical driving lead to different properties of the optical multi-level modulation signals [26, 27]. We present a few schemes.

One of the proposed transmitters is shown on Figure 2.10. After the first PMod (180° phase shift), a Differential Binary Phase Shift Keying (DBPSK) signal is obtained; after the second PMod (90° phase shift), a Differential Quadrature Phase Shift Keying (DQPSK) signal is obtained, and so on. Another configuration, proposed by the same authors, is a combination of an optical IQMod and consecutive PMods, shown on Figure 2.11. Here, the IQMod accomplishes a DQPSK modulation, and high-order DPSK formats can be generated by the consecutive PMods. In both schemes, the first MZM is used for RZ pulse carving. Star QAM signals with differentially encoded phases may also be generated by the same scheme as for DPSK transmitters. The DPSK transmitters only have to be extended by an additional MZM for intensity modulation, to be able to place symbols on different intensity rings [24].

Another transmitter also requiring only binary electrical driving signals for Square 16-QAM is composed of an optical IQMod followed by a DQPSK modulator. The latter can be implemented either with one more IQMod, or with two consecutive PMods, as depicted

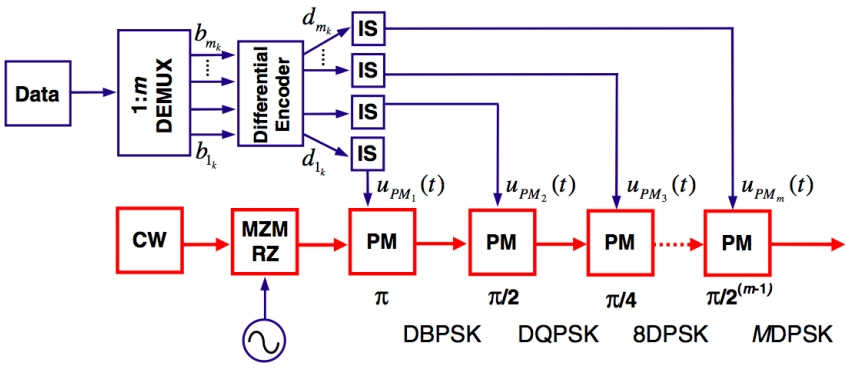

Figure 2.10: DPSK transmitter with binary electrical driving signals, serial configuration [24].

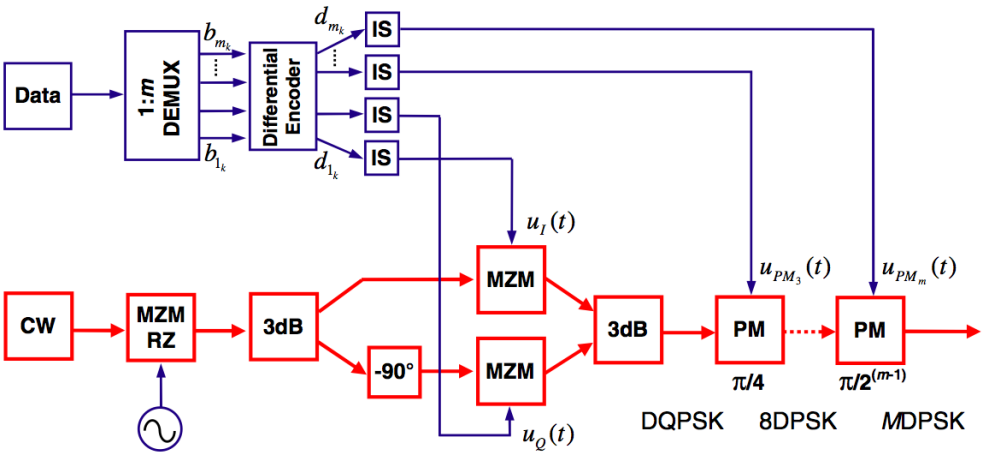

Figure 2.11: Parallel DPSK transmitter with binary electrical driving signals [24].

in Figure 2.12. MZMs within the IQMod achieve modulation in intensity. This way, only positive values on the I and Q axis are addressed. As regards quare 16-QAM, the MZMs are driven by binary electrical signals, and a constellation composed of four symbols in the first quadrant is created. With two consecutive phase modulators which perform phase shifts of π and $\pi/2$, respectively, the three other quadrants can be approached, thus creating a complete square QAM constellation [24]. Yu *et al* [28] also proposed the generation of single-carrier optical signal by format conversion from QPSK to 16-QAM using an IQMod followed by a single arm MZM. Even if the setup was experimentally demonstrated at 432 Gbit/s (without using OFDM or Optical Time Division Multiplexing (OTDM)), the method is limited by a special coding of the electrical binary inputs, so the data sequences cannot be directly used to drive the IQMod.

A different solution to generate QAM signals was proposed by Sakamoto *et al* [29], by using a multi-parallel MZM transmitter. By arranging two IQMod in parallel, a square 16-

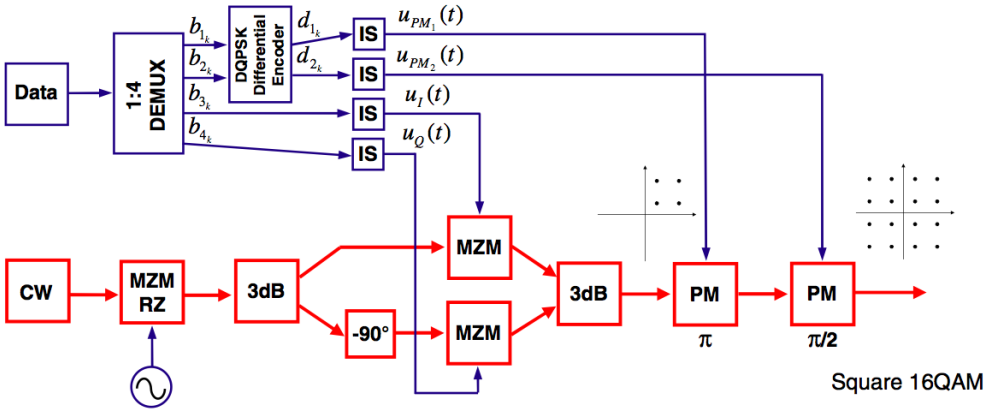

Figure 2.12: Optical Tandem-QPSK transmitter for Square 16-QAM [24].

QAM signal can be synthesized from two QPSK signals, as presented in Figure 2.13.

The square 16-QAM signal is generated by driving MZMs only with binary electrical signals, so that the transmitter is free from handling multi-level electrical driving signals. The same architecture was also used to generate Minimum Shift Keying (MSK) signals by Guo-Wei *et al* [30] and 8-PSK signals [29]. Moreover, m-QAM may be generated by increasing the number of MZMs in parallel. This configuration was called Electro-Optical Digital to

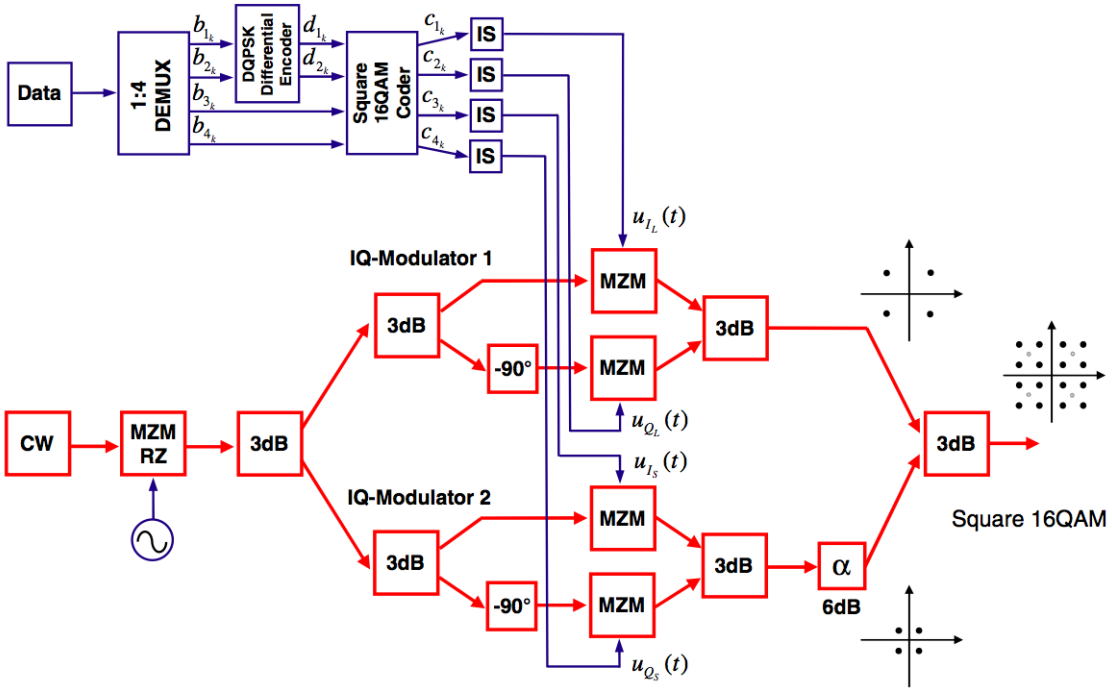

Figure 2.13: Quad-parallel MZM transmitter for generation of square 16-QAM signals [24].

Analog Converter (EO-DAC) [29] and will be discussed in the next section.

Secondini *et al* [31] have proposed an alternative modulation scheme for the generation of 16-QAM optical signals, making use of two-level electrical driving signals and minimum digital precoding. It requires two cascaded IQMods, without any relative phase-stability control.

Recent progress in electronic data processing enables software-defined optical transmission [32]. Freude *et al* have demonstrated multi-format QAM modulation formats and symbol rates set by software-controlled Field Programmable Gate Arrays (FPGAs), using a single IQMod, up to 168 Gbit/s.

2.5.3 EO-DAC

Another approach for the synthesis of optical multilevel signals involves the use of EO-DAC [29]. As illustrated in Figure 2.14, the EO-DAC consists of a Continuous Wave (CW) laser source, a multiparallel modulator, and electrical encoders for driving the modulator.

The multiparallel modulator employs numbers of Electro-optical (EO) modulators integrated in parallel. In the multiparallel modulator, the CW light is divided into n branches with a $1 \times n$ coupler, and in each branch, the CW light divided is EO modulated by a binary data sequence. The amplitude and phase offset of the binary-modulated lightwaves are

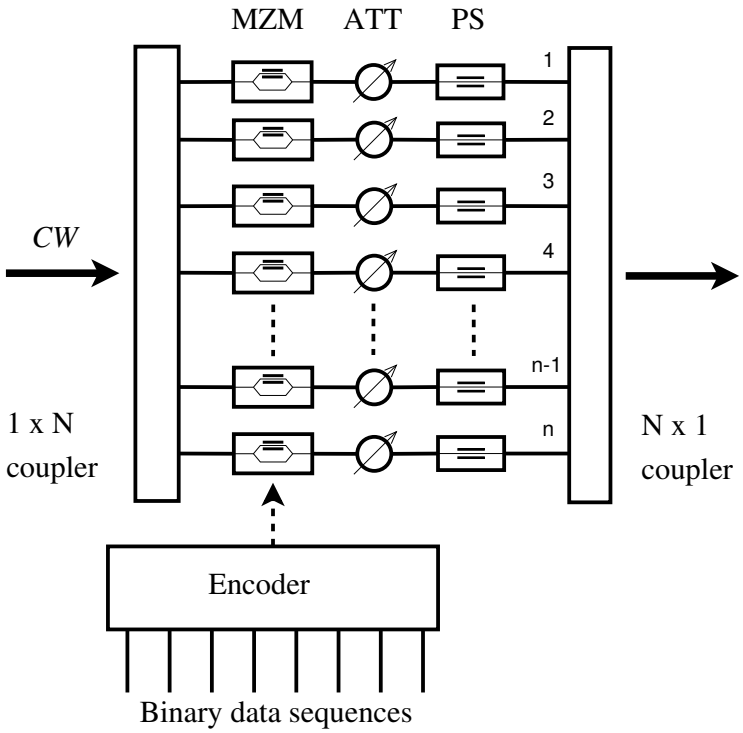

Figure 2.14: Electro-Optical DAC diagram. ATT: Attenuator; PS: Phase shifter; MZM: Mach-Zehnder Modulator; CW: Continuous Wave laser.

appropriately controlled by a parameter controller, i.e., a bias controller. The EO-modulated lightwaves are combined again at the output of the multiparallel modulator by using another $n \times 1$ coupler. By this setup, a BPSK signal is generated by the MZM in each arm of the modulator. Controlling the optical amplitude and the phase offset between the BPSKs correctly, multilevel coherent signals in the 2^n level can be synthesized as a superposition of n sets of BPSK signals. Using this approach, synthesis of QPSK and 16-QAM from BPSK signals were experimentally demonstrated by Sakamoto *et al* [33]. Moreover, Yamazaki *et al* [34] used a combination of a hybrid configuration of silica Planar Lightwave Circuits (PLCs) and a $LiNbO_3$ (LN) PMod array to generate a 64-QAM signal through an optical signal synthesis with three QPSK signals. The modulator was driven by six 10 Gbit/s NRZ binary sequences and was experimentally evaluated for 10 Gbaud (60 Gbit/s) operation.

2.6 All-optical format conversion systems

Recently, the interest in all-optical formats conversion have increased noticeably since all-optical processing is considered one of the most important aspects in future optical networks. Thus, electric to optical and optical to electric converters are likely to become less used, and connection between different networks will become more cost effective. As mentioned in the previous section, a considerable number of advanced modulation formats schemes have been reported in the past few years. They may be selectively employed in future optical networks, depending on the size, bit rate and the system settings. Thus, all-optical conversion techniques applied in network nodes, connecting different networks, will play an important role. The purpose of this section is to describe these techniques; most of them are explained and discussed.

2.6.1 Passive Device Techniques

HNLF

HNLF have become in the past few years a promising technique in order to achieve nonlinear applications. All optical modulation format conversions using these nonlinearities have been studied in several articles, where many researchers have demonstrated a variety of schemes for all-optical conversion. Generally, the principle of operation is based on one HNLF where two or more signals are launched synchronously in order to obtain the desired all optical format conversion. The control signals induce XPM on the optical phase of a RZ clock signal. Thus, the information carried on the amplitude of OOK signals, can be modulated on the phase of another signal. Mishima *et al* [35] propose an all-optical modulation format conversion from NRZ-OOK to RZ multilevel Amplitude Phase Shift Keying (APSK) based on parametric amplification and XPM. The technique requires an RZ pulse sequence and 3 channels NRZ-OOK signals synchronously launched into a HNLF as a probe pulse and control pulses, respectively. The probe pulse is modulated both in its amplitude due to optical parametric amplification and its phase due to XPM, induced by the control pulses. Kitagawa *et al* [36–39] and Wang *et al* [40, 41] used a similar technique to

convert NRZ-OOK signals into RZM-PSK and DPSK signals, respectively, while Bogoni *et al* [42] proposed and experimentally demonstrate binary ASK to quaternary ASK at 160 Gbit/s. Huang *et al* [43] proposed and numerically demonstrated a scheme with two HNLF in a Nonlinear Optical Loop Mirror (NOLM) configuration, to generate 16-QAM signals from OOK at 10 Gbit/s. The 16-QAM signal is generated by the superposition of two QPSK signals with different amplitudes. OOK to QPSK modulation format conversion is achieved by XPM in one HNLF. The amplitude ratio 2:1 of two QPSK signals is realized by parametric amplification. An experimental demonstration of QPSK to a star 16-QAM at 40 Gbit/s was also demonstrated [44].

Non transparency of Four-wave Mixing (FWM) and its application as a format converter technique in HNLFs are also discussed in several papers as well. Lu *et al* [45,46] propose and demonstrate format conversion among optical M-PSK signals, using this technique. They have experimentally demonstrated conversion of DQPSK to DPSK data at 10 and 160 Gbaud, and conversion of RZ-8DPSK to RZ-DQPSK data at 40 Gbaud. In addition, NRZ to RZ format conversion with simultaneous wavelength multicasting, have been reported using a single pump in a HNLF for OOK [47] and DPSK [48] signals, or using an NOLM [49].

In this type of format modulation, where more than one signal is launched into the fiber, group velocity mismatch plays an important role in XPM interaction [33], since it induces walk-off (lost of the synchronism) between signals along the fiber. Walk-off together with FWM induce degradation on the converted signal, such as power differences and unstable phase modulation depending on the bit pattern.

MZDI

Mach Zehnder Delay Interferometer (MZDI) have been used also for modulation format conversion [11]. Lu *et al* [50] presented a study of the intrinsic relations and conversions among different binary modulation formats using MZDI. Conversions between RZ and CSRZ and between Duobinary and AMI can be realized by inverting the sign of the optical field at every bit transition [11], which is represented by arrows with $(-1)^n$ in Figure 2.15. The constructive and destructive ports of an MZDI act as a delay-and-add filter and a delay-and-subtract filter, respectively. A delay-and-subtract filter can convert an NRZ or an RZ to an AMI format [11,51]. Duobinary and AMI can be obtained from DPSK at the constructive and destructive ports of the MZDI, respectively [52]. The periodic frequency characteristic of an MZDI indicates that simultaneous multi-channel format conversions at the same data rate can potentially be implemented.

Groumas *et al* [53] experimentally demonstrated RZ to NRZ conversion of 40 Gbit/s DPSK signals using a MZDI and an optical Bandpass Filter (BPF). Simulations at 40 Gbaud with DPSK, DQPSK and 16-QAM signals have indicated the compatibility of the technique with higher-order modulation formats. Other researchers have demonstrated the feasibility of all-optical conversion from BPSK to QPSK at 12 Gbit/s [54].

All-optical format conversion of 10 Gbit/s NRZ-OOK to Return-to-Zero On-Off Keying (RZ-OOK) has been successfully achieved, utilizing either XPM or FWM, in a Silicon (Si) nanowire [55]. In both cases, the format conversion resulted in a correctly encoded and

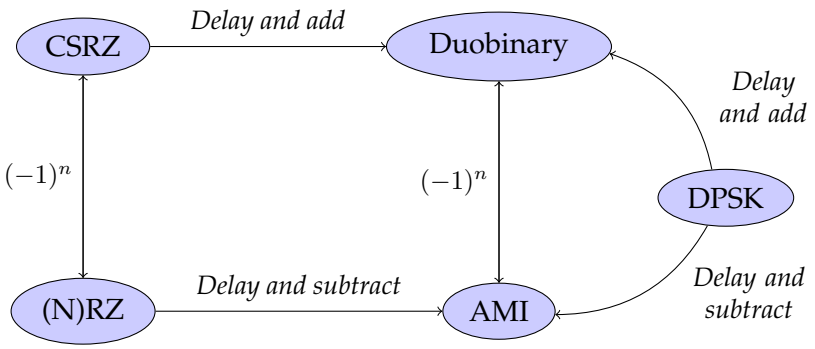

Figure 2.15: Relations among (N)RZ, CSRZ, Duobinary, AMI, and DPSK [50].

polarity-preserved RZ-OOK signal, exhibiting no error floor for BER $< 10^{-10}$. The nanowire is fabricated on silicon-on-insulator unibond wafers, with a buried SiO_2 layer. The buried layer ensures optical isolation for the nanowire from the high-index Si substrate, reducing losses due to leakage modes.

CROW

Recently, researchers have proposed format conversion schemes employing CROWs. Zhou *et al* [56] have experimentally demonstrated and modeled all-optical NRZ to RZ format conversion using CROWs as a notch filters, while Yunhong *et al* [57] use CROW for RZ to NRZ format conversion. Other researchers [58, 59] numerically verified all-optical format conversion from NRZ to BPSK using CROW on a single Si chip. The conversion is based on large phase shift and flattened intensity-response characteristics in the CROW. A CW light experiences different phase shifts controlled by the power of an input NRZ signal, while maintaining approximately constant intensity. Moreover, Ye *et al* [60] verified numerically, also at 160 Gbit/s, the conversion of NRZ, CSRZ, and RZ to PSK, CSRZ-PSK, and RZ-PSK, respectively, by using a set of CROWs with high Q-factors. This scheme possesses several advantages including simplicity, applicability to the ultrahigh speed systems, all-optical signal regeneration [61] and facility of integration. All-optical format conversion from NRZ to QPSK was also numerically demonstrated based on parallel NRZ/BPSK converters in a MZM structure [58].

PPLN waveguide

On the other hand, PPLN-based all-optical format have been reported. Wang *et al* [62, 63] proposed and experimentally demonstrate, all-optical 40 Gbit/s NRZ-to-CSRZ, NRZ-DPSK-to-RZ-DPSK and NRZ-DPSK-to-CSRZ-DPSK format conversions. The obtained theoretical and experimental results indicate that PPLN has a potential to be applied to high-speed all-optical format conversion, which may stimulate future much wider PPLN-based applications in ultra-fast all-optical signal processing.

Other Waveguides

Apiratikul *et al* [64] have demonstrated wavelength and format conversion at 10 Gbit/s, from NRZ-OOK to RZ-OOK based on FWM in a passive GaAs bulk-waveguide. A conversion efficiency of 28 dB over a 48 nm bandwidth was achieved and demonstrates the viability of GaAs waveguides for nonlinear optical signal processing. The conversion of RZ-OOK to Return-to-Zero Binary Phase Shift Keying (RZ-BPSK) signals at 10 Gbit/s in a passive AlGaAs waveguide has been also successfully demonstrated [65]. However, the method suffers from drawbacks due to the presence of residual pattern-dependent Cross-Absorption Modulation (XAM) (along with the requisite XPM) in the probe output by the waveguide, which led to amplitude modulation in the evaluated RZ-BPSK signal, and to an insufficient phase shift resulting from the large coupling loss.

2.6.2 Active Device Techniques

SOA

Several researchers had presented format conversion from NRZ to RZ using a single SOA for OOK signals. One of the proposed conversions scheme is based on a Delay-Interferometer-Signal wavelength Conversion (DISC) configuration, in which an SOA is placed in front of a DI. The inputs to the SOA are an RZ pulse stream (pump) and, at a lower power, the NRZ input data (probe). The pump clock pulses introduce periodic phase shifts to the following NRZ data via XPM in the SOA. This phase modulation is converted into amplitude modulation in the DI, which results in an RZ output signal with a controllable pulse-width (duty-cycle) determined mainly by the offset delay (Δt) of the DI. Yang *et al* [66] used a piece of polarization maintaining fibre with a differential delay (Δt), along with two polarization controllers and a polarizer to form a DI, while Zhao *et al* [67] used a reconfigurable Differential Group Delay (DGD) generator. Other researchers have used the same conversion scheme for multiple wavelength operations, where more than one NRZ input data sequences are converted to RZ format [68, 69], as presented in Figure 2.16. For that case, the SOA is operated in deep saturation to mitigate the undesired Cross Gain Modulation (XGM) between different channels and the DI with a comb-like spectrum is used. The DI transmission peaks are adjusted to be offset from each carrier wavelength with optimal detuning. Thus, the chirp induced on each channel by phase modulation is transmitted, while the original spectrum components are suppressed to some extent. The same format conversion scheme was used not only between OOK signals, but also between OOK and other formats, such as DPSK [70, 71] and BPSK [72]. Marculescu *et al* use two cascaded Delay Interferometers (DIs) and a band-pass filter to produce all-optical conversion from RZ to CSRZ. With this scheme, modulation format conversion, wavelength conversion and regeneration has been experimentally accessed at 42.7 Gbit/s.

A different approach, for NRZ to RZ data format conversion with pulse-width tunability into one by combination of SOA and fiber-based switches, was experimentally demonstrated by Tan *et al* [73]. The SOA-based switch, which employs a delayed Sagnac interferometer using XPM effect in SOA, acts as a pulse-width tunable clock generator. The fiber-based

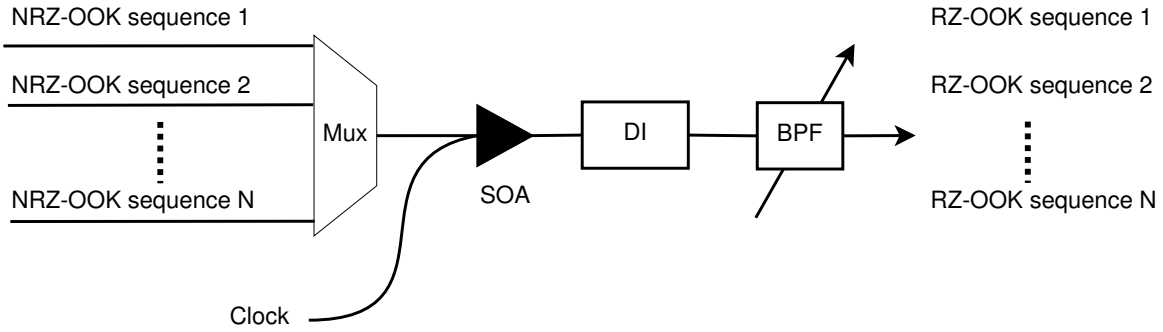

Figure 2.16: Operation principle of the multi-channel format conversions. Mux: Multiplexer; DI: Delay Interferometer (detuned comb filter); BPF: Tunable bandpass filter.

switch using FWM effect in a HNLF performs an AND logic function between input NRZ and the converted RZ clock from the former switch.

Data format conversion from NRZ to RZ was experimentally demonstrated at 40 Gbit/s, using FWM effect of SOA, by injecting synchronously NRZ signal and clock pulses into a single SOA [74]. The study of ASK to FSK format conversion on SOA, based on FWM, was also presented in [75].

On the other hand, RZ to NRZ conversion techniques were also investigated, using XGM effect in a single SOA, combined with an integrated short Saturable Absorber (SA) [76], or using Cross Gain Compression (XGC) effect with a second SOA [77].

In [78], Lu *et al* proposed and experimentally demonstrated an all-optical NRZ to FSK format conversion scheme at an Optical Line Terminal (OLT) to interconnect a Metropolitan Area Network (MAN) and a PON, based on XGM in a SOA. The constant intensity of the converted downstream FSK signal is remodulated at the Optical Network Unit (ONU) to carry upstream data. Error-free conversion has been achieved at 10 Gbit/s.

A scheme that can simultaneously enable modulation format conversion (RZ-to-CSRZ), wavelength conversion and regeneration has been introduced and experimentally accessed at 42.7 Gbit/s. The scheme consists of an SOA followed by two cascaded Delay Interferometers (DIs) and a band-pass filter. The latter enables not only the modulation format conversion but also the suppression of the bit pattern effects [79].

Multi-level all-optical format conversion from NRZ signal to RZ signal, using a SOA and a detuned optical filter, was also demonstrated [80]. The three-level NRZ signal and a synchronous optical clock signal are injected into an SOA, which acts as a nonlinear element and causes the spectrum of the input NRZ signal to be broadened due to XPM effect. A detuned filter is thus used to extract the specific part of the broadened spectrum to obtain three-level RZ signal. The proposed conversion can be achieved with error free at 10 Gbaud.

MZI-SOA

Despite the capabilities of single SOAs for all-optical format conversion, the inclusion of the SOA inside an interferometric structure opens the door for new format conversions,

with added flexibility. In particular, MZI-SOAs has been used in the past decade to generate signals modulated in amplitude, frequency, phase, or a combination of these three domains.

Using one MZI-SOA, all-optical modulation format conversion from NRZ-OOK to RZ-PSK was described and experimentally verified by Mishina *et al* [81]. A diagram of the proposed technique is depicted in Figure 2.17. NRZ-OOK signal pulses with wavelength λ_0 are launched into port #A of the MZI-SOAs as control pulses. The RZ clock pulse sequence at λ_1 and the CW light at λ_2 are launched into ports #B and #C as probe pulses and an assist light, respectively. In SOA1, the carrier density is changed according to the amplitude of the control pulse, and the phase and amplitude of the probe pulse after passing through SOA1 are changed due to XPM and XGM, respectively. The current of SOA2 and the voltage of PS2 on the lower arm of the MZI-SOA are adjusted so that the probe pulse acquire an overall phase shift of π rad. Without the control pulse, after passing through SOA1, the probe pulse has a phase of 0 rad, and the phase of the converted signal that was observed at the output of MZI-SOA is 0 rad, due to the anti-phase interference. When the control pulse is present, the probe pulse after passing through SOA1 has a phase of π rad. The phase of the converted signal that was observed at the output of MZI-SOA is π rad, due to the in-phase interference. Thus, the NRZ-OOK data signal is converted to an RZ-BPSK data signal. The assist light is launched to suppress the rapid change of carriers, which induces frequency chirp and amplitude fluctuations [81].

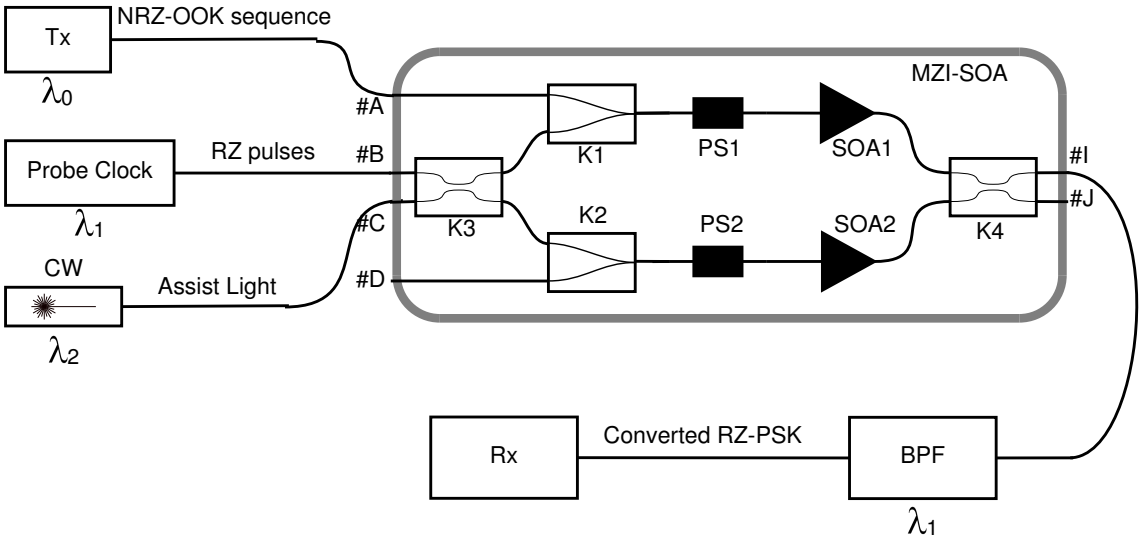

Figure 2.17: Schematic diagram of the proposed format conversion from NRZ-OOK to RZ-BPSK. BPF: Bandpass Filter; Rx: Balanced Receiver.

For higher bitrates conversion, above 10 Gbit/s, the MZI-SOA is usually configured to work in a "push-pull" configuration, in which the control signal are injected in the upper and the lower arms of the of the interferometer (ports #A and #D in Figure 2.17, respectively), with a time delay between them. This techniques greatly helps to increase the operating speed of the format converter by mitigating the impact patterning effects due

to the slow carrier recovery speed of the SOAs [82]. Conversion from RZ-OOK to RZ-PSK at 40 Gbit/s [83], OOK to AMI at 40 Gbit/s [84], or QPSK and OOK to 8PSK [85] at 21.3 Gbaud, were achieved with a single MZI-SOA configured in a "push-pull" configuration. Other experiments, using a dual MZI-SOA for multi-format conversion and spectrum grooming of high-speed channels, were demonstrated in [86], in a flexible and efficient manner. The push-pull technique is described in more detail in Appendix B.

Higher order modulation formats can be generated using the OOK to BPSK format converter of Figure 2.17, as a building block. For example, as shown in Figure 2.18, all-optical OOK to QPSK converter can be constructed with nested OOK to BPSK converter pairs [87]. QPSK is generated when the overall phase difference between the two nested MZI-SOA pairs is set to $\pi/2$ rad. Kang *et al* [82,88] demonstrate the feasibility of this conversion scheme to generate a 173 Gbit/s QPSK signal. Moreover, it is possible to construct a modulator for generating even higher order modulation formats, including 16-QAM or 64-QAM, following a similar method by which the OOK to QPSK format converter is constructed. This topic is subject of further research in Chapter 5 of this thesis.

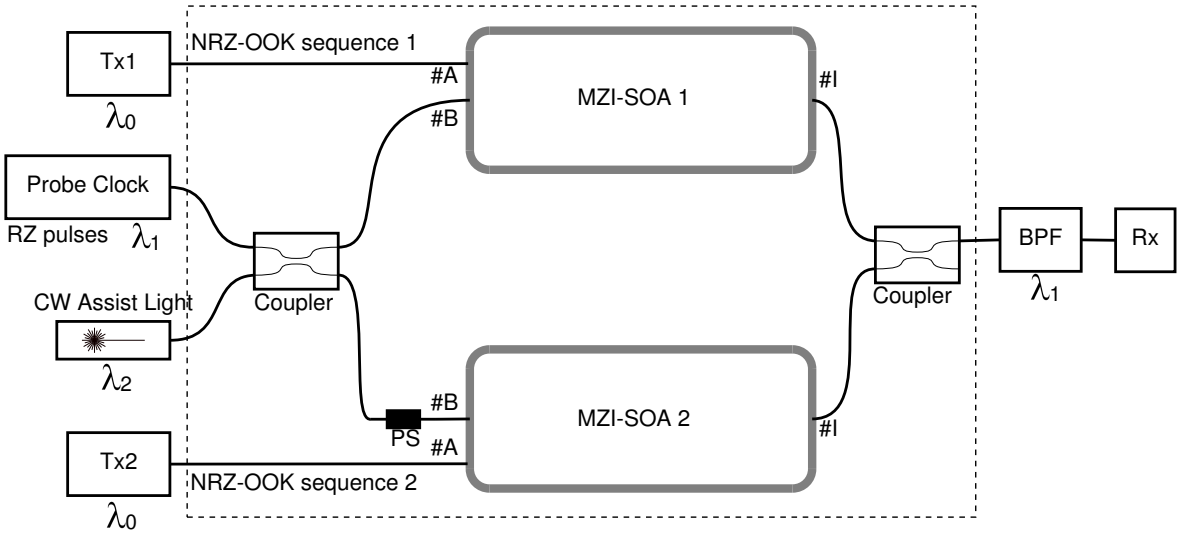

Figure 2.18: Schematic diagram of the format conversion from NRZ-OOK to RZ-QPSK. PS: Phase Shifter; BPF: Bandpass Filter; Rx: Balanced Receiver.

An integrated triple arm MZI-SOA was proposed by Nissanka *et al* [89], to achieve lower power consumption as well as simplicity in operation compared to the solution reported in [87]. An experimental demonstration of format conversion was achieved for two NRZ-OOK signals to one QPSK at 10.7 Gsymbols/s.

2.7 Other optical processing functions with MZI-SOAs

MZI-SOAs are versatile devices, that have been proposed and tested not only for signal generation and modulation format conversion, but also for other important functions in

optical networks. This section present a brief overview of other applications based on all-optical techniques.

2.7.1 Wavelength conversion

The concepts of wavelength conversion has been attracting the interests and efforts of the researchers worldwide in the last decades. System demonstrations of all-optical wavelength conversion started in the late Eighties. The apparent effort was in replacing similar electronic devices by means of all-optical techniques. Several different techniques accomplished by SOAs and MZI-SOAs were introduced to make these functions more effective and robust [90]. XGM was among the first effects to be exploited in order to accomplish all-optical wavelength conversion. As sketched in Figure 2.19, XGM is usually accomplished in an SOA device, where the input signal at λ_S and a CW lightwave pump at λ_P are simultaneously injected (in a co- or counter-propagating scheme): as both signals are within the gain band of the device and the SOA is saturated, the modulation of the overall intensity turns out into a fast modulation of the SOA gain, which is directly transferred to the pump at λ_P. An optical BPF, centered at λ_P, selects the converted signal. In the XGM technique, a critical parameter can be the effective speed of the gain recovery, which practically limits the operating bit rate. However, optimum frequency tuning of the signal, saturation effects, and longer/optimized SOAs were demonstrated to increase the conversion speed, thus leading to up to 40 Gbit/s operation [77]. Recently, high-speed wavelength converter based on FWM in HNLF was demonstrated at 100 Gbit/s/λ [91]. However, the development of high-speed quantum-dot SOA made possible XGM-based all-optical wavelength converter operating up to 160 Gbit/s, thanks to the much shorter lifetime of the carriers [92].

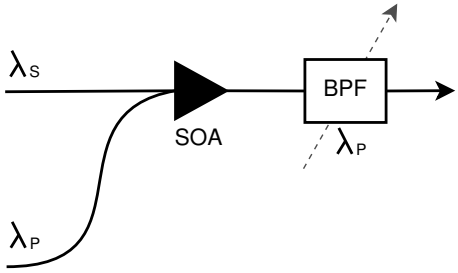

Figure 2.19: Scheme of all-optical wavelength conversion based on XGM in a SOA. BPF: Optical Bandpass filter; SOA: Semiconductor Optical Amplifier; λ_P: pump wavelength; λ_S: Signal wavelength.

The effect of XPM present in SOAs does not simply produce an all-optical wavelength conversion: in order to achieve it, the XPM has to be combined with an interferometric structure, as in MZI-SOAs, where the nonlinear phase change is transformed into an amplitude modulation, as depicted in Figure 2.20. The success of the MZI-SOA has made the XPM effect one of the most competitive solutions for all-optical wavelength conversion. It has good robustness and polarization independence and offers wide tuning range. However,

as in the case of XGM, the technique was originally designed for Intensity Modulator (IM) signals, but recent studies presented new architectures for wavelength conversion of phase modulated signals [93].

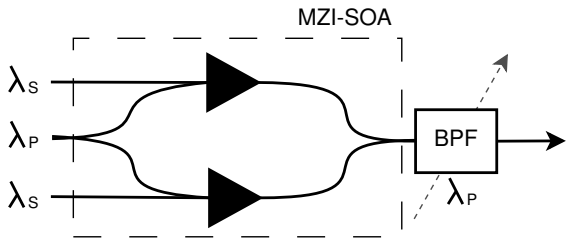

Figure 2.20: Scheme of all-optical wavelength conversion based on XPM in a MZI-SOA. BPF: Optical Bandpass filter; SOA: Semiconductor Optical Amplifier; λ_P: pump wavelength; λ_S: Signal wavelength (The signal λ_S can be injected into one or both SOAs).

2.7.2 Regeneration

All-optical regeneration is usually indicating an optical process that removes most of the distortions and noise from an input signal. If it is acting only on the noise / intersysmbol interference, the regenerator is 2R: reamplify and reshaping [94–96]. If it also performs a jitter removal, as shown in Figure 2.21, it is 3R: 2R and retiming [97]. In many cases, all-optical regeneration schemes come with embedded all-optical wavelength conversion functionality, which makes the two functions directly linked [90]. Other examples of all-optical regeneration may be found using MZI-SOA [93], with two optical amplifiers [98] or using FWM in SOA [99].

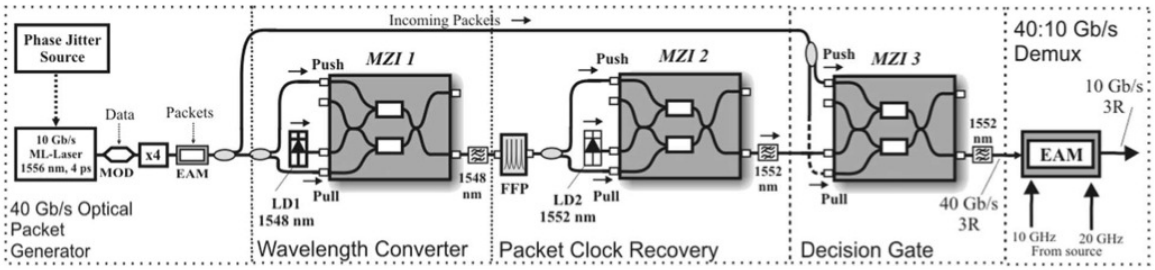

Figure 2.21: Scheme of all-optical 3R regeneration in a MZI-SOA, after [97].

2.7.3 Logic gates

Recently, considerable research has been done for the development of optical one bit memories. High speed all-optical logic gates are crucial devices in all-optical signal processing and in optical networks because they execute essential signal processing functions such as switching, regeneration and header recognition processing in photonic

switching nodes. In particular, all-optical flip-flops are key elements to perform optical signal processing operations in next generation photonic transmission systems, in particular as buffering memories for temporary storage of decisions in optical packet routers [100]. Exploiting non-linear effects in SOAs and MZI-SOAs has enabled the demonstration of integrated optical buffers, making GHz flip-flop operation possible [101]. The MZI-SOA has become an important element to performs a variety of optical logic functions and provides high Extinction Ratio (ER), requires low switching energies to operate and have regenerative capability and compactness [8, 102–104]. An optical logic Exclusive OR (XOR) gate, based on a hybrid integrated MZI-SOA, served has the starting point for the modulation format conversion scheme proposed in Chapter 5.

More recently, an all-optical Random Access Memory (RAM), with true random access read/write functionality has been proposed and demonstrated [105] which will allow the realization of many optical applications such as label recognition, label swapping, buffering and 3R regeneration, and is suitable for asynchronous and variable-length data packet processing functionalities.

2.8 Summary

This chapter has presented a summarized analysis of Optical Modulation Format Conversion Systems (OMFCSs). A form of classification of has been proposed. This classification categorizes the OMFCS according to their purpose and form of analysis of the optical signal. A set of OMFCS currently available in the literature has been presented. Following, we resume the performance of the most relevant technologies and architectures for modulation format conversion in Table 2.1. Most of the technologies may be, or are currently, suitable for integration into small footprints, combining hybrid planar waveguides. The achieved bitrate using MZI-SOA devices is one of the highest, combining advanced modulation formats generation [88].

Finally, Table 2.2 summarizes all-optical format conversions that were described throughout this chapter. From the number of references in each intersection of the double entry table, we verify that a strong research has been undertaken on NRZ to RZ (and vice-versa) format conversion, on ASK signals. Published research papers on all-optical conversion techniques resulting in advanced modulation format (QPSK, 16-QAM and 64-QAM) is still a field with a substantial margin for research studies and experimentation, and the main subject in the following chapters.

Table 2.1: Comparison between different technologies proposed for all-optical modulation format conversion.

Technology	Suitable for Integration?	Bitrate	Power Penalty	Comments
HNLF [35–41,46,47]	no	80 Gbit/s [45,46]	1.6 dB	
CROW	yes	160 Gbit/s [58]	–	Simulation
	yes	50 Gbit/s [57]	1.5 dB	
DI [11,50–52]	no	40 Gbit/s [53]	1.5 dB	
PPLN [62,63]	yes	40 Gbit/s [62]	–	
Si Waveguide	yes	10 Gbit/s [55]	–	Based on XPM
	yes	60 Gbit/s [34]	–	MZM and PLC
GaAs Waveguide	yes	10 Gbit/s [64]	1 dB	
AlGaAs Waveguide	yes	10 Gbit/s [65]	2.7 dB	
SOA	yes	40 Gbit/s [77]	4 dB	
	yes	42.6 Gbit/s [66]	-1.9 dB	XPM and DI
MZI-SOA	yes	85.4 Gbit/s [86]	7.5 dB	110 km fiber
	yes	173 Gbit/s [88]	–	QPSK output

Table 2.2: Summary of all optical format conversion.

From \ To	NRZ-ASK	RZ-ASK	NRZ-DPSK	RZ-DPSK	BPSK	RZ-QPSK	FSK	8PSK	16QAM	64QAM
NRZ-ASK	–	[41,47, 49,51,55, 56,61,63, 64,66– 69,73,80, 86]			[37, 38,53, 58–60, 65,81]	[36,58, 82,87– 89]			[75,78]	
RZ-ASK	[41,57, 74,76,77]	–		[40]	[60,83]					
NRZ-DPSK		[70]	–	[48,63, 71]						
RZ-DPSK			[53]	–						
BPSK					–	[54]				
RZ-QPSK						–		[85]	[44]	[34]
FSK	[75]						–			
8PSK						[45,46]		–		
CSRZ-OOK		[62,63]			[60]					

References

[1] A. Chraplyvy, R. Tkach, A. Gnauck, B. Kasper, and R. Derosier, "8 Gbit/s FSK modulation of DFB lasers with optical demodulation," *Electronics Letters*, vol. 25, no. 5, pp. 319 –321, march 1989.

[2] T. Okoshi, "Recent advances in coherent optical fiber communication systems," *Lightwave Technology, Journal of*, vol. 5, no. 1, pp. 44 – 52, jan 1987.

[3] Y. Yamamoto, "Receiver performance evaluation of various digital optical modulation-demodulation systems in the 0.5-10 μm wavelength region," *Quantum Electronics, IEEE Journal of*, vol. 16, no. 11, pp. 1251 – 1259, nov 1980.

[4] R. Linke and A. Gnauck, "High-capacity coherent lightwave systems," *Lightwave Technology, Journal of*, vol. 6, no. 11, pp. 1750 –1769, nov 1988.

[5] G. Jacobsen, *Noise in Digital Optical Transmission Systems*. Norwood, MA: Artech House, Inc., 1994.

[6] O. Tonguz and R. Wagner, "Equivalence between preamplified direct detection and heterodyne receivers," *Photonics Technology Letters, IEEE*, vol. 3, no. 9, pp. 835 –837, sept. 1991.

[7] H. Phuong and S. Ramesh, "Spectrally efficient coherent optical communication systems," in *Communications, Computers and Signal Processing, 1991., IEEE Pacific Rim Conference on*, may 1991, pp. 91 –94 vol.1.

[8] L. YAN, A. Willner, X. Wu, A. Yi, A. Bogoni, Z. Chen, and H. Jiang, "All-Optical Signal Processing for Ultra-High Speed Optical Systems and Networks," *Lightwave Technology, Journal of*, vol. PP, no. 99, p. 1, 2012.

[9] I. Kang, "High-Speed Photonic Integrated Devices for Advanced Modulation Formats," in *Asia Communications and Photonics Conference and Exhibition*. Optical Society of America, 2009, p. ThT5. [Online]. Available: http://www.opticsinfobase.org/abstract.cfm?URI=ACP-2009-ThT5

[10] E. Lazzeri, A. T. Nguyen, N. Kataoka, N. Wada, A. Bogoni, and L. Potì, "All Optical Add and Drop Multiplexing Node for Hybrid Topology Networks," *J. Lightwave Technol.*, vol. 29, no. 24, pp. 3676–3682, Dec 2011. [Online]. Available: http://jlt.osa.org/abstract.cfm?URI=jlt-29-24-3676

[11] P. Winzer and R.-J. Essiambre, "Advanced Optical Modulation Formats," *Proceedings of the IEEE*, vol. 94, no. 5, pp. 952 –985, may 2006.

[12] D. van den Borne, "Robust optical transmission systems - modulation and equalization," Ph.D. dissertation, Technische Universiteit Eindhoven, March 2008.

[13] F. Xiong, *Digital modulation Techniques*. Norwood, MA: Artech House, Inc., 2000.

[14] J. Zhao, L. Huo, C.-K. Chan, L.-K. Chen, and C. Lin, "Analytical investigation of optimization, performance bound, and chromatic dispersion tolerance of 4-amplitude-shifted-keying format," in *Optical Fiber Communication Conference, 2006 and the 2006 National Fiber Optic Engineers Conference. OFC 2006*, march 2006, p. 3 pp.

[15] I. Djordjevic, L. Xu, and T. Wang, "Beyond 100 Gb/s Optical Transmission Based on Polarization Multiplexed Coded-OFDM With Coherent Detection," *Optical Communications and Networking, IEEE/OSA Journal of*, vol. 1, no. 1, pp. 50 –56, june 2009.

[16] L. Pei-Li and S. Wei-Hua, "Ultrahigh-speed all-optical wavelength conversion and format conversion for polarisation-shift-keying signal based on four-wave mixing in light-holding semiconductor optical amplifier," *Optoelectronics, IET*, vol. 5, no. 2, pp. 72 –76, april 2011.

[17] D. van den Borne, V. Sleiffer, M. S. Alfiad, S. L. Jansen, and T. Wuth, "POLMUX-QPSK modulation and coherent detection: The challenge of long-haul 100G transmission," in *35th European Conference on Optical Communication, ECOC '09.*, 2009, pp. 1–4.

[18] A. Hodzic, B. Konrad, and K. Petermann, "Improvement of system performance in N x 40-Gb/s WDM transmission using alternate polarizations," *Photonics Technology Letters, IEEE*, vol. 15, no. 1, pp. 153 –155, jan. 2003.

[19] "Digital Video Broadcasting (DVB); Measurement guidelines for DVB systems," ETSI, Tech. Rep. TR 101 290, 2001.

[20] H. A. Mahmoud and H. Arslan, "Error vector magnitude to SNR conversion for nondata-aided receivers." *IEEE Transactions on Wireless Communications*, vol. 8, no. 5, pp. 2694–2704, 2009. [Online]. Available: http://dblp.uni-trier.de/db/journals/twc/twc8.html#MahmoudA09

[21] R. A. Shafik, S. Rahman, and A. H. M. R. Islam, "On the Extended Relationships Among EVM, BER and SNR as Performance Metrics," in *International Conference on Electrical and Computer Engineering, ICECE '06.*, 2006, pp. 408–411.

[22] H. Keang-Po and C. Han-Wei, "Generation of arbitrary quadrature signals using one dual-drive modulator," *Lightwave Technology, Journal of*, vol. 23, no. 2, pp. 764–770, 2005.

[23] E. Yamada, Y. Shibata, K. Watanabe, T. Yasui, A. Ohki, H. Mawatari, S. Kanazawa, R. Iga, and H. Ishii, "Demonstration of 50 Gbit/s 16QAM signal generation by novel 16QAM generation method using a dual-drive InP Mach-Zehnder modulator," in *Optical Fiber Communication Conference and Exposition (OFC/NFOEC), 2011 and the National Fiber Optic Engineers Conference*, march 2011, pp. 1 –3.

[24] M. Seimetz, *High-Order Modulation for Optical Fiber Transmission: Phase and Quadrature Amplitude Modulation*, ser. Optical Sciences. New York: Springer, 2009.

[25] M. Seimetz, M. Noelle, and E. Patzak, "Optical systems with high-order DPSK and star QAM modulation based on interferometric direct detection," *Journal of Lightwave Technology*, vol. 25, no. 6, pp. 1515–1530, 2007.

[26] M. Seimetz, "Multi-format transmitters for coherent optical M-PSK and M-QAM transmission," *Proceedings of the 7th International Conference on Transparent Optical Networks*, vol. 2, pp. 225–229, 2005.

[27] ——, "Performance of coherent optical Square-16-QAM-systems based on IQ-transmitters and homodyne receivers with digital phase estimation," *2006 Optical Fiber Communication Conference/National Fiber Optic Engineers Conference, Vols 1-6*, pp. 949–958, 2006.

[28] J. Yu, Z. Dong, X. Tang, W. Jian, Y. Xia, S. Shi, S.-H. Fan, and G.-K. Chang, "Generation of 432Gb/s single-carrier optical signal by format conversion from QPSK to 16QAM," in *Optical Fiber Communication Conference and Exposition (OFC/NFOEC), 2011 and the National Fiber Optic Engineers Conference*, march 2011, pp. 1 –3.

[29] T. Sakamoto, A. Chiba, and T. Kawanishi, "Electro-optic synthesis of 8PSK by quad-parallel Mach-Zehnder modulator," in *Optical Fiber Communication - incudes post deadline papers, 2009. OFC 2009. Conference on*, march 2009, pp. 1 –3.

[30] L. Guo-Wei, T. Sakamoto, A. Chiba, T. Kawanishi, T. Miyazaki, K. Higuma, and J. Ichikawa, "80-Gb/s optical MSK generation using a monolithically integrated quad-mach-zehnder IQ modulator," in *Optical Fiber Communication (OFC), collocated National Fiber Optic Engineers Conference, 2010 Conference on (OFC/NFOEC)*, 2010, pp. 1–3.

[31] M. Secondini, E. Forestieri, and F. Cavaliere, "Novel optical modulation scheme for 16-QAM format with quadrant differential encoding," in *Photonics in Switching, 2009. PS '09. International Conference on*, sept. 2009, pp. 1 –2.

[32] W. Freude, R. Schmogrow, B. Nebendahl, D. Hillerkuss, J. Meyer, M. Dreschmann, M. Huebner, J. Becker, C. Koos, and J. Leuthold, "Software-defined optical transmission," in *Transparent Optical Networks (ICTON), 2011 13th International Conference on*, 2011, pp. 1–4.

[33] T. Sakamoto and A. Chiba, "Coherent Synthesis of Optical Multilevel Signals by Electrooptic Digital-to-Analog Conversion Using Multiparallel Modulator," *Selected Topics in Quantum Electronics, IEEE Journal of*, vol. 16, no. 5, pp. 1140 –1149, sept.-oct. 2010.

[34] H. Yamazaki, T. Yamada, T. Goh, Y. Sakamaki, and A. Kaneko, "64QAM modulator with a hybrid configuration of silica PLCs and LiNbO3 phase modulators for 100-Gb/s applications," in *Optical Communication, 2009. ECOC '09. 35th European Conference on*, sept. 2009, pp. 1 –4.

[35] K. Mishina, S. Kitagawa, and A. Maruta, "All-optical modulation format conversion from on-off-keying to multiple-level phase-shift-keying based on nonlinearity in optical fiber," *Optics Express*, vol. 15, no. 13, pp. 8444–8453, 2007.

[36] S. Kitagawa, S. M. Nissanka, and A. Maruta, "All-Optical Modulation Format Conversion from NRZ-OOK to RZ-M-ary PSK Based on Fiber Nonlinearity," in *Optical Fiber Communication Conference and Exposition and The National Fiber Optic Engineers Conference*. Optical Society of America, 2008, p. OTuD6. [Online]. Available: http://www.opticsinfobase.org/abstract.cfm?URI=OFC-2008-OTuD6

[37] A. Maruta and S. Kitagawa, "All-optical XOR logic gate accompanied with OOK/PSK format conversion by the use of cross phase modulation in optical fiber," in *Photonics Global Conference (PGC), 2010*, dec. 2010, pp. 1 –2.

[38] A. Maruta, "All-optical modulation format conversion using highly nonlinear fibers," in *Photonics Society Summer Topical Meeting Series, 2010 IEEE*, july 2010, pp. 174 –175.

[39] A. Maruta and N. Hashimoto, "Experimental Demonstration of All-Optical Modulation Format Conversion from NRZ-OOK to RZ-8APSK Based on Fiber Nonlinearity," in *Optical Fiber Communication Conference*. Optical Society of America, 2012, p. OM3B.1. [Online]. Available: http://www.opticsinfobase.org/abstract.cfm?URI=OFC-2012-OM3B.1

[40] J. Wang and L. R. Chen, "All-optical OOK-to-DPSK modulation format conversion using XPM in HNLF," in *Optical Communications and Networks (ICOCN 2011), 10th International Conference on*, 5 2011-dec. 7 2011, pp. 1 –2.

[41] L. Wang, Y. Dai, G. Lei, J. Du, and C. Shu, "All-Optical RZ-to-NRZ and NRZ-to-PRZ Format Conversions Based on Delay-Asymmetric Nonlinear Loop Mirror," *Photonics Technology Letters, IEEE*, vol. 23, no. 6, pp. 368 –370, march15, 2011.

[42] A. Bogoni, X. Wu, S. Nuccio, N. Ahmed, and A. Willner, "160 Gb/s all-optical binary-to-quaternary amplitude shift keying format conversion," in *Optical Fiber Communication Conference and Exposition (OFC/NFOEC), 2011 and the National Fiber Optic Engineers Conference*, march 2011, pp. 1 –3.

[43] G. Huang, Y. Miyoshi, A. Maruta, Y. Yoshida, and K. Kitayama, "All-Optical OOK to 16-QAM Modulation Format Conversion Employing Nonlinear Optical Loop Mirror," *Lightwave Technology, Journal of*, vol. 30, no. 9, pp. 1342 –1350, may1, 2012.

[44] X. Wu, J. Wang, H. Huang, and A. Willner, "Experimental optical multiplexing of two 20-Gbit/s QPSK data channels from different wavelengths onto a single 40-Gbit/s star 16-QAM using fiber nonlinearities," in *Lasers and Electro-Optics (CLEO), 2011 Conference on*, may 2011, pp. 1 –2.

[45] G.-W. Lu, E. Tipsuwannakul, C. Lundstrom, M. Karlsson, and P. Andrekson, "Format Conversion From 120-Gb/s RZ-D8PSK to 80-Gb/s RZ-DQPSK Through FWM-Based Optical Phase Erasure," *Photonics Technology Letters, IEEE*, vol. 22, no. 24, pp. 1817 –1819, dec.15, 2010.

[46] G.-W. Lu, E. Tipsuwannakul, T. Miyazaki, C. Lundstrom, M. Karlsson, and P. Andrekson, "Format Conversion of Optical Multilevel Signals Using FWM-Based Optical Phase Erasure," *Lightwave Technology, Journal of*, vol. 29, no. 16, pp. 2460 –2466, aug.15, 2011.

[47] A. Yi, L. Yan, B. Luo, W. Pan, J. Ye, and Z. Chen, "One-to-eleven (11 x 10-Gb/s) all-optical NRZ-to-RZ format conversion and wavelength multicasting using a single pump in a highly nonlinear fiber," in *Optical Fiber Communication Conference and Exposition (OFC/NFOEC), 2011 and the National Fiber Optic Engineers Conference*, march 2011, pp. 1 –3.

[48] G. Lei, Y. Dai, J. Du, and C. Shu, "Wavelength multicasting of DPSK signal with NRZ-to-RZ format conversion," *Electronics Letters*, vol. 47, no. 14, pp. 808 –810, 7 2011.

[49] C. Kwok and C. Lin, "Simultaneous 4 times 10 Gb/s NRZ-to-RZ Modulation Format Conversion in Nonlinear Optical Loop Mirror With a Photonic Crystal Fiber," *Photonics Technology Letters, IEEE*, vol. 19, no. 22, pp. 1825 –1827, nov.15, 2007.

[50] Y. Lu and Y. Su, "Conversions among binary optical modulation formats," *Opt. Express*, vol. 16, no. 6, pp. 3853–3858, Mar 2008. [Online]. Available: http://www.opticsexpress.org/abstract.cfm?URI=oe-16-6-3853

[51] J. Yu, G. K. Chang, J. Barry, and Y. Su, "40 Gbit/s signal format conversion from NRZ to RZ using a Mach-Zehnder delay interferometer," *Optics Communications*, vol. 248, no. 4-6, pp. 419 – 422, 2005. [Online]. Available: http://www.sciencedirect.com/science/article/pii/S0030401804013367

[52] D. Penninckx, H. Bissessur, P. Brindel, E. Gohin, and F. Bakhti, "Optical differential phase shift keying (DPSK) direct detection considered as a duobinary signal," in *Optical Communication, 2001. ECOC '01. 27th European Conference on*, vol. 3, 2001, pp. 456 – 457 vol.3.

[53] P. Groumas, V. Katopodis, C. Kouloumentas, M. Bougioukos, and H. Avramopoulos, "All-Optical RZ-to-NRZ Conversion of Advanced Modulated Signals," *Photonics Technology Letters, IEEE*, vol. 24, no. 3, pp. 179 –181, feb.1, 2012.

[54] H. Kishikawa, P. Seddighian, N. Goto, S. Yanagiya, and L. Chen, "All-optical modulation format conversion from binary to quadrature phase-shift keying using delay line interferometer," in *Photonics Conference (PHO), 2011 IEEE*, oct. 2011, pp. 513 –514.

[55] W. Astar, J. Driscoll, X. Liu, J. Dadap, W. Green, Y. Vlasov, G. Carter, and R. Osgood, "All-Optical Format Conversion of NRZ-OOK to RZ-OOK in a Silicon Nanowire Utilizing Either XPM or FWM and Resulting in a Receiver Sensitivity Gain of 2.5 dB," *Selected Topics in Quantum Electronics, IEEE Journal of*, vol. 16, no. 1, pp. 234 –249, jan.-feb. 2010.

[56] L. Zhou, H. Chen, and A. W. Poon, "On-Chip NRZ-to-PRZ Format Conversion Using Narrow-Band Silicon Microring Resonator-Based Notch Filters," *J. Lightwave Technol.*, vol. 26, no. 13, pp. 1950–1955, Jul 2008. [Online]. Available: http://jlt.osa.org/abstract.cfm?URI=jlt-26-13-1950

[57] Y. Ding, C. Peucheret, M. Pu, B. Zsigri, J. Seoane, L. Liu, J. Xu, H. Ou, X. Zhang, and D. Huang, "RZ-to-NRZ format conversion at 50 Gbit/s based on a silicon microring resonator," in *OptoeElectronics and Communications Conference (OECC), 2010 15th*, july 2010, pp. 862 –863.

[58] Y. Lu, F. Liu, M. Qiu, and Y. Su, "All-optical format conversions from NRZ to BPSK and QPSK based on nonlinear responses in silicon microring resonators," *Opt. Express*, vol. 15, no. 21, pp. 14 275–14 282, Oct 2007. [Online]. Available: http://www.opticsexpress.org/abstract.cfm?URI=oe-15-21-14275

[59] C. Yan, T. Ye, and Y. Su, "All-optical regenerative NRZ-OOK-to-RZ-BPSK format conversion using silicon waveguides," *Opt. Lett.*, vol. 34, no. 1, pp. 58–60, Jan 2009. [Online]. Available: http://ol.osa.org/abstract.cfm?URI=ol-34-1-58

[60] T. Ye, F. Liu, and Y. Su, "Ultrahigh speed OOK-to-PSK conversion using linear filtering in silicon ring resonators," *Chin. Opt. Lett.*, vol. 6, no. 6, pp. 398–400, Jun 2008. [Online]. Available: http://col.osa.org/abstract.cfm?URI=col-6-6-398

[61] T. Ye, C. Yan, Y. Lu, F. Liu, and Y. Su, "All-optical regenerative NRZ-to-RZ format conversion using coupled ring-resonator optical waveguide," *Opt. Express*, vol. 16, no. 20, pp. 15 325–15 331, Sep 2008. [Online]. Available: http://www.opticsexpress.org/abstract.cfm?URI=oe-16-20-15325

[62] J. Wang, J. Sun, X. Zhang, D. Huang, and M. M. Fejer, "Optical phase erasure and its application to format conversion through cascaded second-order processes in periodically poled lithium niobate," *Opt. Lett.*, vol. 33, no. 16, pp. 1804–1806, Aug 2008. [Online]. Available: http://ol.osa.org/abstract.cfm?URI=ol-33-16-1804

[63] J. Wang, J. Sun, X. Zhang, D. Huang, and M. Fejer, "All-Optical Format Conversions Using Periodically Poled Lithium Niobate Waveguides," *Quantum Electronics, IEEE Journal of*, vol. 45, no. 2, pp. 195 –205, feb. 2009.

[64] P. Apiratikul, W. Astar, G. Carter, and T. Murphy, "10-Gb/s Wavelength and Pulse Format Conversion Using Four-Wave Mixing in a GaAs Waveguide," *Photonics Technology Letters, IEEE*, vol. 22, no. 12, pp. 872 –874, june15, 2010.

[65] W. Astar, P. Apiratikul, B. Cannon, T. Mahmood, J. Wathen, J. Hryniewicz, S. Kanakaraju, C. Richardson, T. Murphy, and G. Carter, "Conversion of RZ-OOK to RZ-BPSK by XPM in a Passive AlGaAs Waveguide," *Photonics Technology Letters, IEEE*, vol. 23, no. 19, pp. 1397 –1399, oct.1, 2011.

[66] X. Yang, A. Mishra, R. Manning, R. Webb, and A. Ellis, "All-optical 42.6 Gbit=s NRZ to RZ format conversion by cross-phase modulation in single SOA," *Electronics Letters*, vol. 43, no. 16, pp. 890 –892, 2 2007.

[67] X. Zhao and C. Lou, "Investigation of all-optical nonreturn-to-zero-to-return-to-zero format converter based on a semiconductor optical amplifier and a reconfigurable delayed interferometer," *Appl. Opt.*, vol. 49, no. 7, pp. 1158–1162, Mar 2010. [Online]. Available: http://ao.osa.org/abstract.cfm?URI=ao-49-7-1158

[68] Y. Yu, X. Zhang, J. B. Rosas-Fernández, D. Huang, R. V. Penty, and I. H. White, "Single SOA based 16 DWDM channels all-optical NRZ-to-RZ format conversions with different duty cycles," *Opt. Express*, vol. 16, no. 20, pp. 16 166–16 171, Sep 2008. [Online]. Available: http://www.opticsexpress.org/abstract.cfm?URI=oe-16-20-16166

[69] B. Zou, Y. Yu, W. Wu, and X. Zhang, "Parallel Eight Channels All-Optical NRZ-to-RZ Format Conversions at 40 Gb/s Using a Single SOA," *Photonics Technology Letters, IEEE*, vol. 24, no. 13, pp. 1091 –1093, july1, 2012.

[70] E. Lazzeri, A. T. Nguyen, G. Serafino, N. Kataoka, N. Wada, A. Bogoni, and L. Potì, "All-Optical NRZ-DPSK to RZ-OOK Format Conversion Using Optical Delay Line Interferometer and Semiconductor Optical Amplifier," in *Photonics in Switching*. Optical Society of America, 2010, p. JTuB45. [Online]. Available: http://www.opticsinfobase.org/abstract.cfm?URI=PS-2010-JTuB45

[71] Y. Yu, B. Zou, W. Wu, and X. Zhang, "All-optical parallel NRZ-DPSK to RZ-DPSK format conversion at 40 Gb/s based on XPM effect in a single SOA," *Opt. Express*, vol. 19, no. 15, pp. 14 720–14 725, Jul 2011. [Online]. Available: http://www.opticsexpress.org/abstract.cfm?URI=oe-19-15-14720

[72] W. Hong, D. Huang, X. Zhang, and G. Zhu, "Simulation and analysis of OOK-to-BPSK format conversion based on gain-transparent SOA used as optical phase-modulator," *Opt. Express*, vol. 15, no. 26, pp. 18 357–18 369, Dec 2007. [Online]. Available: http://www.opticsexpress.org/abstract.cfm?URI=oe-15-26-18357

[73] H. N. Tan, M. Matsuura, and N. Kishi, "Transmission performance of a wavelength and NRZ-to-RZ format conversion with pulsewidth tunability by combination of SOA- and fiber-based switches," *Opt. Express*, vol. 16, no. 23, pp. 19 063–19 071, Nov 2008. [Online]. Available: http://www.opticsexpress.org/abstract.cfm?URI=oe-16-23-19063

[74] F. Wang, E. Xu, Y. Yu, and Y. Zhang, "All-optical 40 Gbit/s data format conversion between RZ and NRZ using a fiber delay interferometer and a single SOA," in *Communications and Photonics Conference and Exhibition, 2011. ACP. Asia*, nov. 2011, pp. 1 –6.

[75] S.-K. Hwang and S.-L. Lin, "Optically injected semiconductor lasers for conversion between optical ASK and optical FSK," in *OptoeElectronics and Communications Conference (OECC), 2011 16th*, july 2011, pp. 293 –294.

[76] A. L. Teixeira, G. M. T. Beleffi, T. Silveira, H. Furukawa, and N. Wada, "RZ to NRZ Format Converter Based on a Semiconductor Optical Amplifier with a Saturable Absorber," in *Conference on Lasers and Electro-Optics/Quantum Electronics and Laser Science Conference and Photonic Applications Systems Technologies*. Optical Society of America, 2006, p. CTuD5. [Online]. Available: http://www.opticsinfobase.org/abstract.cfm?URI=CLEO-2006-CTuD5

[77] L. Banchi, M. Presi, A. D'Errico, G. Contestabile, and E. Ciaramella, "All-Optical 10 and 40 Gbit/s RZ-to-NRZ Format and Wavelength Conversion Using Semiconductor Optical Amplifiers," *Lightwave Technology, Journal of*, vol. 28, no. 1, pp. 32 –38, jan.1, 2010.

[78] Y. Lu, C. Yan, Q. Chang, Q. Li, Y. Su, and W. Hu, "An All-Optical Metro-Access Interface for a PON System Based on NRZ to FSK Format Conversion," in *Optical Fiber Communication Conference and Exposition and The National Fiber Optic Engineers Conference*. Optical Society of America, 2008, p. OWH7. [Online]. Available: http://www.opticsinfobase.org/abstract.cfm?URI=OFC-2008-OWH7

[79] A. Marculescu, S. Sygletos, J. Li, D. Karki, D. Hillerkuß, S. Ben-Ezra, S. Tsadka, W. Freude, and J. Leuthold, "RZ to CSRZ Format and Wavelength Conversion with Regenerative Properties," in *Optical Fiber Communication Conference*. Optical Society of America, 2009, p. OThS1. [Online]. Available: http://www.opticsinfobase.org/abstract.cfm?URI=OFC-2009-OThS1

[80] Y. Yu, X. Zhang, F. Wang, and D. Huang, "Multilevel all-optical format conversion from NRZ signal to RZ signal," in *Communications and Photonics Conference and Exhibition (ACP), 2009 Asia*, nov. 2009, pp. 1 –2.

[81] K. Mishina, A. Maruta, S. Mitani, T. Miyahara, K. Ishida, K. Shimizu, T. Hatta, K. Motoshima, and K. Kitayama, "NRZ-OOK-to-RZ-BPSK modulation-format conversion using SOA-MZI wavelength converter," *Lightwave Technology, Journal of*, vol. 24, no. 10, pp. 3751–3758, 2006.

[82] I. Kang, M. Rasras, L. Buhl, M. Dinu, G. Raybon, S. Cabot, M. Cappuzzo, L. Gomez, Y. Chen, S. Patel, A. Piccirilli, J. Jaques, and C. Giles, "High-Speed All-Optical Generation of Advanced Modulation Formats Using Photonic-Integrated All-Optical Format Converter," *Selected Topics in Quantum Electronics, IEEE Journal of*, vol. 18, no. 2, pp. 765 –771, march-april 2012.

[83] F. Fresi, M. Scaffardi, N. Amaya, R. Nejabati, D. Simeonidou, and A. Bogoni, "40-Gb/s NRZ-to-RZ and OOK-to-BPSK Format and Wavelength Conversion on a Single SOA-MZI for Gridless Networking Operations," *Photonics Technology Letters, IEEE*, vol. 24, no. 4, pp. 279 –281, feb.15, 2012.

[84] J. M. Dailey, R. P. Webb, and R. J. Manning, "All-optical technique for modulation format conversion from on-off-keying to alternate-mark-inversion," *Opt. Express*, vol. 18, no. 21, pp. 21 873–21 882, Oct 2010. [Online]. Available: http://www.opticsexpress.org/abstract.cfm?URI=oe-18-21-21873

[85] J. M. Dailey, R. Webb, and B. Manning, "Generation of 21.3 Gbaud 8PSK Signal Using an SOA-Based All-Optical Phase Modulator," in *37th European Conference and Exposition on Optical Communications*. Optical Society of America, 2011, p. Mo.1.LeSaleve.6. [Online]. Available: http://www.opticsinfobase.org/abstract.cfm?URI=ECOC-2011-Mo.1.LeSaleve.6

[86] M. Irfan Anis, N. Amaya, G. Zervas, R. Nejabati, D. Simeonidou, M. Scaffardi, A. Bogoni, S. Pinna, and F. Fresi, "Defragmentation and grooming on 85.4 Gb/s by simultaneous format and wavelength conversion in an integrated quad SOA-MZI," in *Optical Network Design and Modeling (ONDM), 2012 16th International Conference on*, april 2012, pp. 1 –6.

[87] K. Mishina, S. M. Nissanka, A. Maruta, S. Mitani, K. Ishida, K. Shimizu, T. Hatta, and K. I. Kitayama, "All-optical modulation format conversion from NRZ-OOK to RZ-QPSK using parallel SOA-MZI OOK/BPSK converters," *Optics Express*, vol. 15, no. 12, pp. 7774–7785, 2007.

[88] I. Kang, M. Rasras, L. Buhl, M. Dinu, S. Cabot, M. Cappuzzo, L. Gomez, Y. Chen, S. Patel, N. Dutta, A. Piccirilli, J. Jaques, and C. Giles, "Generation of 173-Gbits/s single-polarization QPSK signals by all-optical format conversion using a photonic integrated device," in *Optical Communication, 2009. ECOC '09. 35th European Conference on*, sept. 2009, pp. 1 –2.

[89] S. M. Nissanka, A. Maruta, S. Mitani, K. Shimizu, T. Miyahara, T. Aoyagi, T. Hatta, A. Sugitatsu, and K. i. Kitayama, "All-optical modulation format conversion from NRZ-OOK to RZ-QPSK using integrated SOA Three-Arm-MZI wavelength converter," in *OFC 2009*, 2009, pp. 1–3.

[90] E. Ciaramella, "Wavelength conversion and all-optical regeneration: Achievements and open issues," *J. Lightwave Technol.*, vol. 30, no. 4, pp. 572–582, Feb 2012. [Online]. Available: http://jlt.osa.org/abstract.cfm?URI=jlt-30-4-572

[91] M.-F. Huang, J. Yu, Y.-K. Huang, E. Ip, and G.-K. Chang, "Wavelength Converter for Polarization-Multiplexed 100-G Transmission With Multilevel Modulation Using a Bismuth Oxide-Based Nonlinear Fiber," *Photonics Technology Letters, IEEE*, vol. 22, no. 24, pp. 1832 – 1834, dec.15, 2010.

[92] G. Contestabile, A. Maruta, S. Sekiguchi, K. Morito, M. Sugawara, and K. Kitayama, "160 gb/s cross gain modulation in quantum dot soa at 1550 nm," in *Optical Communication, 2009. ECOC '09. 35th European Conference on*, vol. 2009-Supplement, sept. 2009, pp. 1 –2.

[93] M. Spyropoulou, M. Bougioukos, G. Giannoulis, C. Kouloumentas, D. Kalavrouziotis, A. Maziotis, P. Bakopoulos, R. Harmon, D. Rogers, J. Harrison, A. Poustie, G. Maxwell, and H. Avramopoulos, "Large-scale photonic integrated circuit for multi-format regeneration and wavelength conversion," in *Optical Fiber Communication Conference and Exposition (OFC/NFOEC), 2011 and the National Fiber Optic Engineers Conference*, march 2011, pp. 1 –3.

[94] D. Apostolopoulos, D. Klonidis, P. Zakynthinos, K. Vyrsokinos, N. Pleros, I. Tomkos, and H. Avramopoulos, "Demonstration of 8 Error-free Cascades of 2R NRZ SOA-MZI Wavelength Converter," *Ofc: 2009 Conference on Optical Fiber Communication, Vols 1-5*, pp. 1710–1712 3161, 2009.

[95] D. Petrantonakis, D. Apostolopoulos, M. Spyropoulou, N. Pleros, K. Vyrsokinos, and H. Avramopoulos, "40 Gb/s NRZ Wavelength Conversion with Enhanced 2R Regeneration Characteristics using a Differentially-biased SOA-MZI switch," *2009 Ieee Leos Annual Meeting Conference Proceedings, Vols 1and 2*, pp. 781–782 844, 2009.

[96] J. F. Pina, H. J. A. da Silva, P. N. Monteiro, J. Wang, W. Freude, and J. Leuthold, "Cross-Gain Modulation-based 2R Regenerator Using Quantum-Dot Semiconductor Optical Amplifiers at 160 Gbit/s," in *Transparent Optical Networks, 2007. ICTON '07. 9th International Conference on*, vol. 1, 2007, pp. 106–109.

[97] G. T. Kanellos, D. Petrantonakis, D. Tsiokos, P. Bakopoulos, P. Zakynthinos, N. Pleros, D. Apostolopoulos, G. Maxwell, A. Poustie, and H. Avramopoulos, "All-Optical 3R Burst-Mode Reception at 40 Gb/s Using Four Integrated MZI Switches," *J. Lightwave Technol.*, vol. 25, no. 1, pp. 184–192, Jan 2007. [Online]. Available: http://jlt.osa.org/abstract.cfm?URI=jlt-25-1-184

[98] P. Velanas, A. Bogris, and D. Syvridis, "Polarization-Insensitive 2R-Regenerator based on Two-Pump Fiber Optical Parametric Amplifier," *2009 Ieee/Leos Winter Topicals Meeting Series (Wtm 2009)*, pp. 193–194 271, 2009.

[99] H. Simos, A. Bogris, and D. Syvridis, "Investigation of a 2R all-optical regenerator based on four-wave mixing in a semiconductor optical amplifier," *Journal of Lightwave Technology*, vol. 22, no. 2, pp. 595–604, 2004.

[100] K. Huybrechts, G. Morthier, and R. Baets, "Fast all-optical flip-flop based on a single distributed feedback laser diode," *Opt. Express*, vol. 16, no. 15, pp. 11 405–11 410, Jul 2008. [Online]. Available: http://www.opticsexpress.org/abstract.cfm?URI=oe-16-15-11405

[101] R. C. Galindo, "Flip-Flops Ópticos basados en Interferómetros Mach-Zehnder Activos con Realimentación," Ph.D. dissertation, Universidad Politecnica de Valencia, May 2007.

[102] C. Reis, A. Maziotis, C. Kouloumentas, C. Stamatiadis, M. Bougioukos, N. Calabretta, P. André, R. Dionisio, B. Neto, H. J. S. Dorren, H. Avramopoulos, and A. Teixeira, "All-optical clocked D flip-flop memory using a hybrid integrated S-R latch," *Microwave and Optical Technology Letters*, vol. 53, no. 6, pp. 1201–1204, 2011.

[103] C. Reis, P. Andre, R. Dionisio, B. Neto, A. Teixeira, A. Maziotis, C. Kouloumentas, C. Stamatiadis, M. Bougioukos, H. Avramopoulos, N. Calabretta, and H. J. S. Dorren, "Experimental evaluation of all-optical asynchronous and synchronous memories," in *Computer Engineering Conference (ICENCO), 2010 International*, 2010, pp. 26–28.

[104] C. Reis, A. Maziotis, C. Kouloumentas, C. Stamatiadis, M. Bougioukos, N. Calabretta, P. Andre, R. Dionisio, B. Neto, H. J. S. Dorren, H. Avramopoulos, and A. Teixeira, "All-optical synchronous S-R flip-flop based on active interferometric devices," *Electronics Letters*, vol. 46, no. 10, pp. 709–710, 2010.

[105] N. Pleros, D. Apostolopoulos, D. Petrantonakis, C. Stamatiadis, and H. Avramopoulos, "Optical static ram cell," *Photonics Technology Letters, IEEE*, vol. 21, no. 2, pp. 73 –75, jan.15, 2009.

Chapter 3

MZI-SOA Characterization

This chapter is dedicated to the static and dynamic characterization of the MZI-SOA. These functionalities of the MZI-SOA will be studied experimentally, in a device manufactured by the Centre for Integrated Photonics (CIP) [1]. The device is a commercial hybrid-integrated device consisting of a passive, planar silica balanced MZI with nonlinear SOAs and Phase Shifters (PSs) assembled in each interferometer arm. Section 3.1 describe the characterization of active and passive components of a MZI-SOA, in static operational conditions. The methodology uses only power measurements to extract operative parameters. Then, in section 3.2, an investigation of the dynamic properties of the MZI-SOA, as an optical gate and binary phase modulator, will be performed. At the end, overall conclusions about this topic are presented.

3.1 Static Characterization

MZI-SOAs are compact devices with a vast potential for application in several optical domains. They can be used in logical gates [2], digital phase modulation [3], switching and wavelength conversion [4], all-optical processing and signal regeneration [5], among others. In all these applications, the MZI-SOA must be previously biased to set an operational state in terms of output power and power/phase change as a function of the available inputs, and depending on the application in hands. However most of these biasing points require very long and difficult initial setup phase, which varies from device to device, due to its internal fabrication yields.

A picture of the packaged MZI-SOA device used in this work is shown in Figure 3.1. The package contains a chip with two MZI-SOA structures [6]. The MZI-SOA is hybridly integrated with the following parts: a silica motherboard that contains the optical waveguides such as the couplers and the Y junctions; a silicon daughterboard where the SOAs are fitted and which is used to be passively assembled in the motherboard; the active elements, i.e. the SOAs, that are assembled in the daughterboard; and a V-groove to ease fibre pigtailing of the motherboard [7]. Hybridly integrated MZI-SOA result in more flexibility but increased yields, where each passive and active elements has its own tolerances and asymmetries (e.g. the couplers are not exactly 50 % splitting ratio). These issues have some implications in many MZI-SOA functionalities, for example on the maximization of ER between the interferometer output ports. Figure 3.2 shows a picture of a prototype box that included temperature control and SOA current and phase shifter voltage electronics. The MZI-SOA chip temperature is measured by a thermistor and a proportional, integral, and differential (PID) control loop actuates on the Peltier cell to keep the chip

temperature stable at the desired value. All measurements were done at a temperature setting of 25 ° C.

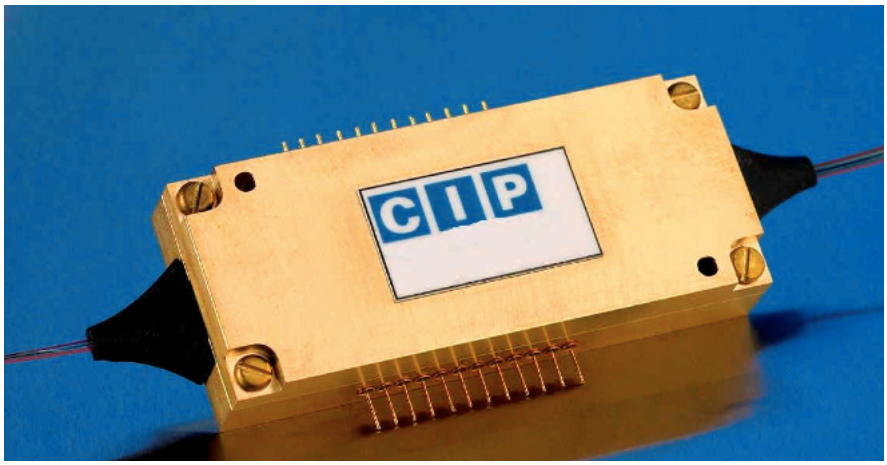

Figure 3.1: Dual MZI-SOA device used to obtain experimental results. A ribbon of 8 fibers enters the MZI-SOAs on the right (4 fibers per MZI-SOA, 2 control and 2 interferometric inputs), and a ribbon of 4 fibre exits on the left (2 fibers per MZI-SOA, all interferometric outputs).

Figure 3.2: MZI-SOA driving box. The box includes a dual MZI-SOA, a temperature control, SOA bias and phase shifter bias electronics board and a power supply unit. The front plate contains the interface knob, numerical display, and the input (8) and output (4) fiber connectors.

Due to the interferometric structure of the device, the power distribution along the device will affect the output interference depth and its potential optimization. Therefore, it is critical to first have a passive parts characterization. In order to carry out the analysis on MZI-SOA asymmetry properties, we used a 6 ports hybrid device, as shown in Figure 3.3. Each arm of the MZI incorporates one SOA and one PS. In order to assess each input-output path, two sets of switches are used, as seen in Figure 3.3. Two sets of measurements were performed. The gain of one of the arms with the other arm blocked by a switched off SOA, and the SOA gain dependence on the biasing current. A Distributed Feed-Back (DFB) laser with wavelength 1546.12 nm is used as the input signal and will be kept fixed in all upcoming

experimental tests (The wavelength was chosen according to the MZI-SOA manufacturer specifications). All power measurements were obtained through a Power Meter (PM).

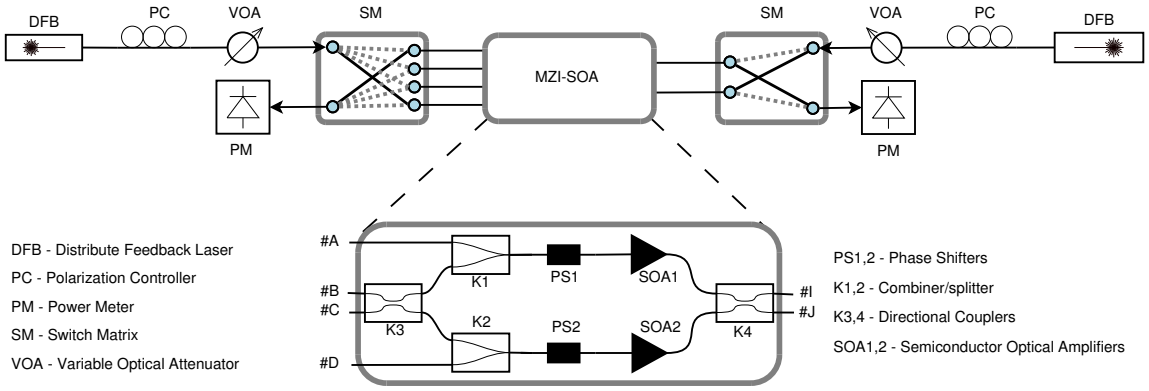

Figure 3.3: Experimental setup used to characterize the MZI-SOA with power measurements.

3.1.1 Internal couplers

Due to the interferometric structure of the device, the power distribution along the device will affect the output interference depth and its potential optimization. Therefore, it is critical to characterize all couplers. In order to carry out the analysis on MZI-SOA asymmetry properties, each input-output path is analyzed independently, switching on one SOA at time, accordingly to the path.

For all coupling factor measurements, CW laser input power is 3 dBm. When simply biased, the SOAs current was by default 200 mA. PS1 and PS2 are switched off (voltage source = 0 V), since a phase shifter has little impact on couplers characterization because only one SOAs is biased at each measurement. Phase shifters characterization is described in the next sub-section.

Coupling factor of coupler K1 is characterized using the setup depicted in Figure 3.4. SOA1 is biased at 200 mA and SOA2 is switched off, i.e. with 0 mA current. Port #I is used as the input, but port #J could also be used as well. Power measurements must be carried out at ports #A, #B and #C, with a PM. Coupling factor α_1 is obtained as

$$\alpha_1 = \frac{P_{\#A}}{(P_{\#A} + P_{\#B} + P_{\#C})} \tag{3.1}$$

using power values in a linear scale.

Coupling factor of K2 is measured with SOA2 biased at 200 mA and SOA1 unbiased (0 mA). As can be seen in Figure 3.5, light is injected through MZI-SOA port #J and optical power measurements are made at ports #B, #C and #D. Coupling factor α_2 is computed as

$$\alpha_2 = \frac{P_{\#D}}{(P_{\#B} + P_{\#C} + P_{\#D})} \tag{3.2}$$

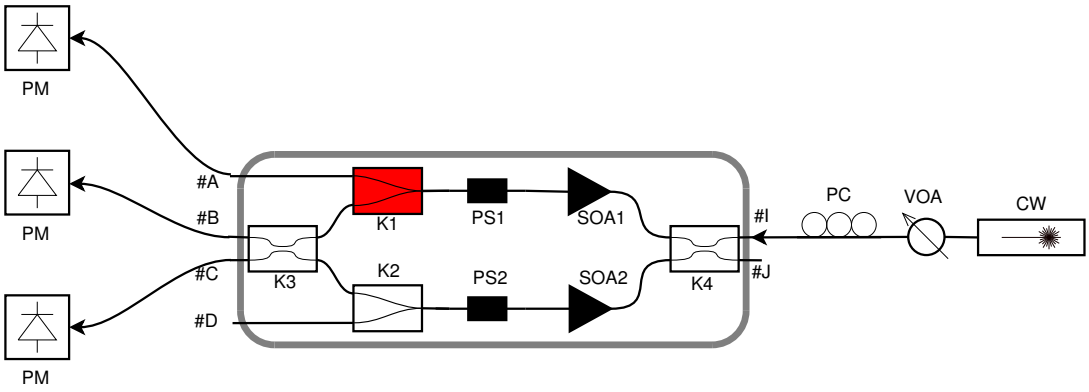

Figure 3.4: Setup for the characterization of K1 coupling factor.

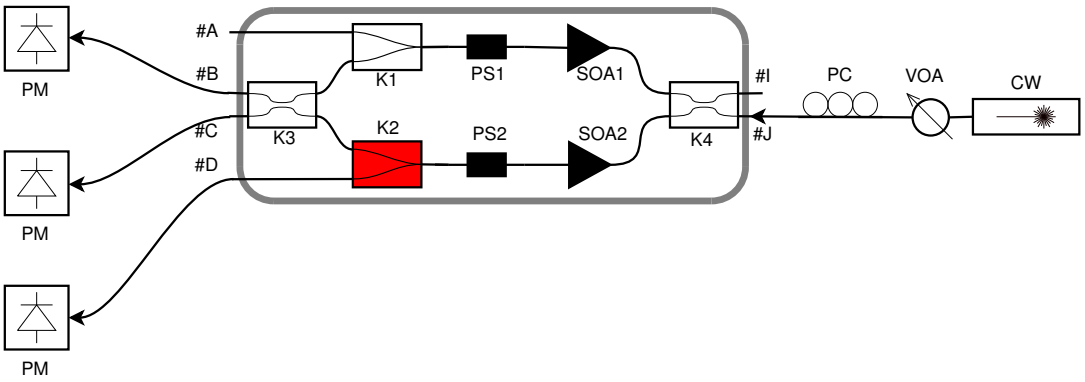

Figure 3.5: Setup for the characterization of K2 coupling factor.

For coupler K3 characterization, only two power measurements are necessary, at port #B and port #C, as depicted in Figure 3.6. In this case, either SOA1 or SOA2 could be biased at 200 mA, however one SOA must be switched off. Input power can be injected from port #I or port #J. Coupling factor α_3 is obtained through the following expression,

$$\alpha_3 = \frac{P_{\#B}}{(P_{\#B} + P_{\#C})} \tag{3.3}$$

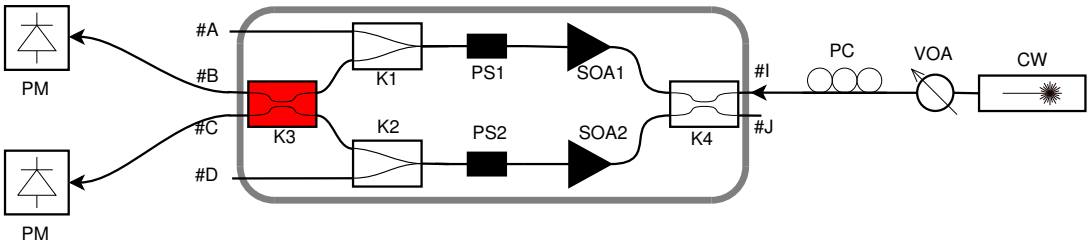

Figure 3.6: Setup for the characterization of K3 coupling factor.

Finally, coupling factor calculation of coupler K4 uses the setup from Figure 3.7. If port #A receives the input optical power, then SOA1 should be biased, while SOA2 remains unbiased. If the input choice goes to port #D, then SOA2 should be biased and SOA1 switched off. If ports #B or #C are used as inputs, one of the two SOAs can be biased. Power measurement is taken at ports #I and #J. Coupling factor α_4 is given by,

$$\alpha_4 = \frac{P_{\#I}}{(P_{\#I} + P_{\#J})} \tag{3.4}$$

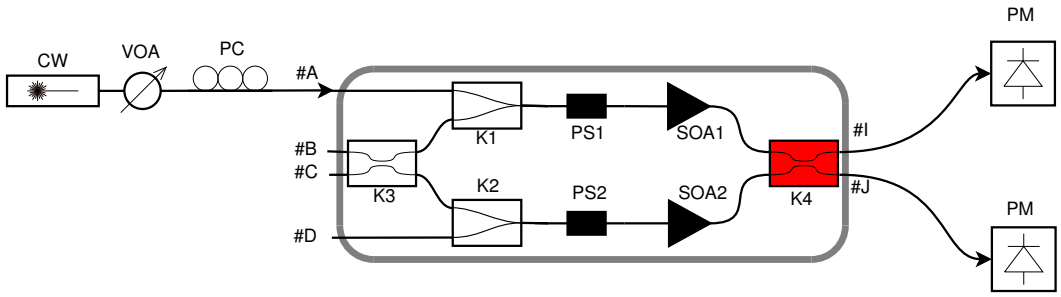

Figure 3.7: Setup for the characterization of K4 coupling factor.

The measurements performed are summarized in Table 3.1. We can observe that couplers are not 50 % - 50 % as ideally would be expected in an interferometric structure and their splitting factors are all different. This induces an asymmetric power distribution along the interferometer arms which in any operational point will cause second order effects like the different saturation of the SOAs in each interferometer arms. From here, we can observe the coupling factor of all passive couplers inside the interferometric structure, and compute the overall asymmetry on the power distribution along the interferometer arms. Coupling factors values $\alpha_{1,2,3,4}$ will be used to improve the results from MZI-SOA model, described in Chapter 4.

Table 3.1: Procedure for measurements and calculations

Coupler	CW port	PM port	I_{SOA1}	I_{SOA2}	Formulation	Value
K1	#I	#A, #B, #C	200 mA	0 mA	$\alpha_1 = \frac{P_{\#A}}{(P_{\#A}+P_{\#B}+P_{\#C})}$	52%
K2	#J	#B, #C, #D	0 mA	200 mA	$\alpha_2 = \frac{P_{\#D}}{(P_{\#B}+P_{\#C}+P_{\#D})}$	42%
K3	#I	#B, #C	200 mA	0 mA	$\alpha_3 = \frac{P_{\#B}}{(P_{\#B}+P_{\#C})}$	52%
K4	#A	#I, #J	200 mA	0 mA	$\alpha_4 = \frac{P_{\#I}}{(P_{\#I}+P_{\#J})}$	60%

3.1.2 Phase shifters

Phase shifters are designed as a set of electrodes astride one waveguide. When voltages are applied, electric fields are created across the waveguide. The phase shifts are proportional to the voltages applied. To characterize phase shifter PS1, we proceed with the setup depicted in Figure 3.8. The laser source must be connected at port #B or #C. Both SOAs must be biased with the same current used for coupler characterization, in order to keep the conditions for which the couplers have been characterized. As an example, we could use 200 mA to bias both SOAs, but different values can also be considered. Phase shifter PS2 must be disabled, i.e., unbiased (0 V). Following the electrodes, the optical beams in the waveguides are recombined via coupler K4, converting the phase difference between both arms of the interferometer into a power variation on ports #I and #J.

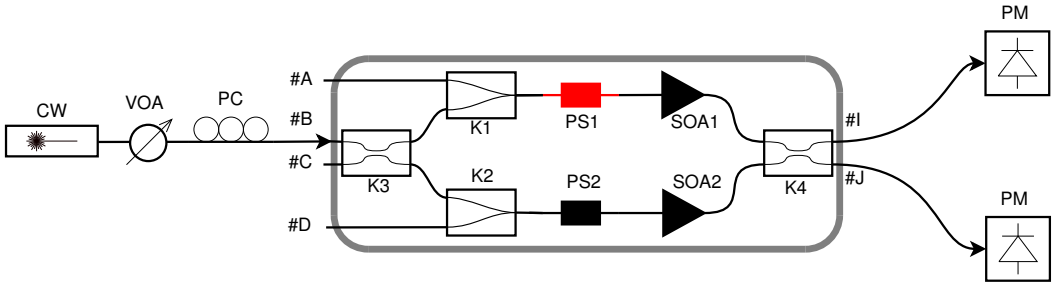

Figure 3.8: Setup for the characterization of phase shifter PS1.

The voltage of PS1 is swept with a fixed step from minimum to maximum values, i.e., from 0 V to 10 V, according to the manufacturer specifications. For each step, we took note on the power measurements at ports #I and #J, and we obtained four graphs as represented in Figure 3.9.

From each curve, we took note on the voltages at which the power reaches a minimum ($V\pi$ when $\Delta\phi = \pi$) and a maximum (V_0 when $\Delta\phi = 0$). We repeat the same process to characterize PS2, using the setup depicted in Figure 3.10. Now PS1 should be deactivated (no voltage on electrodes) and PS2 voltage swept between 0 V and 10 V.

Ideally, the pair of curves from PS1 characterization should be the same as the ones obtained with PS2. The differences are due to unequal power balance in both arms of the MZI-SOA, because of the coupling factor of couplers K1 and K4 is not 50 %. Since more power is injected into one of the SOA, this will increase the phase shift in the SOA due to XPM, and the combination of signals coming from both arms will show phase unbalance is not the same from the lower and the upper arm. However, despited the unbalance between both arms of the interferometer, the transmitted light is periodic in phase difference (and therefore voltage) and is proportional to η [8,9],

$$\eta = \left[cos\left(\frac{\Delta\phi}{2}\right)\right]^2 \tag{3.5}$$

where $\Delta\phi$ is the phase difference experienced by the light between both arms of the

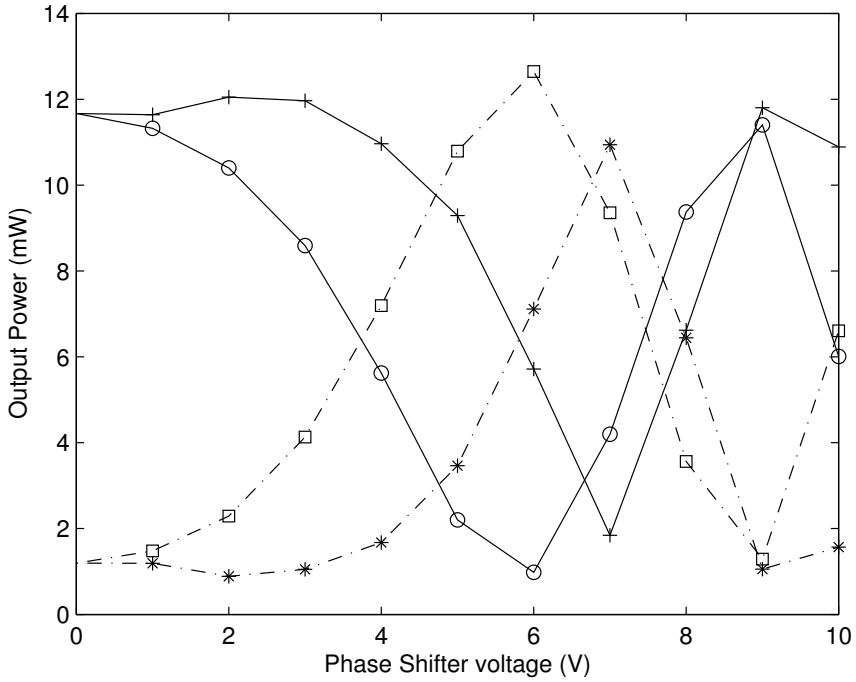

Figure 3.9: MZI-SOA output power at port #I (full line) and #J (dashed line), as a function of PS1 (asterisks, plus signs) and PS2 (square and circle symbols) bias voltage, respectively. Both SOAs bias current is equal to 200 mA. The lines are guides for the eyes.

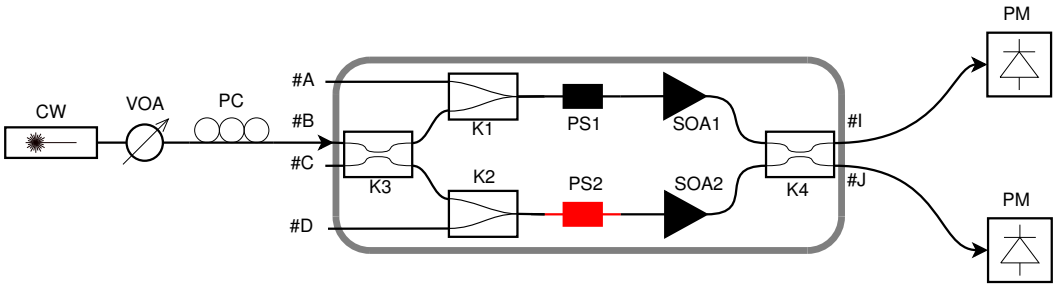

Figure 3.10: Setup for the characterization of phase shifter PS2.

interferometer.

An extensive measurement campaign has been conducted to characterize PS1 and PS2, for SOA bias currents between 150 mA and 400 mA. The results are not presented here, but will be used to adjust the parameters of the MZI-SOA model in Chapter 4.

3.1.3 Semiconductor optical amplifiers

Having all the passive paths characterized, it is now critical to have the active devices characterized. So, the next step of our analysis was the evaluation of SOA output power as function of input power and SOA current. These measurements were made, again considering the two arm separately, using forward propagation, from input #A to output #I, with SOA2 disabled, and, similarly, from input #B to output #J, with SOA1 disabled, as depicted in Figure 3.11 and Figure 3.12, respectively. It is worth noting that this characterization is referred to the overall path on which the signal propagates, so it takes into account losses and any other kind of asymmetry of the MZI-SOA device.

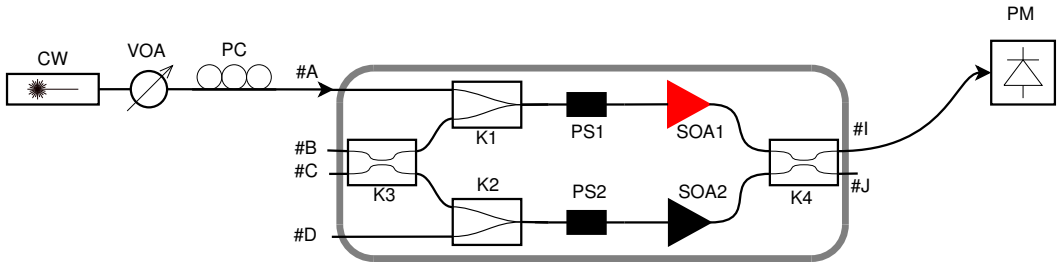

Figure 3.11: Setup for the characterization of SOA1.

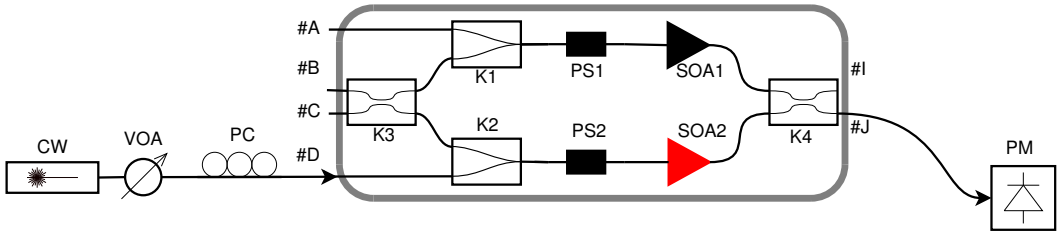

Figure 3.12: Setup for the characterization of SOA2.

To evaluate the dependence of the SOA from the bias current, the input power is set initially at a low value and the bias current is varied from 150 mA to 400 mA. Output powers are measured and stored. The input power is increased to a higher value (always below the maximum allowable power from the manufacturer specifications), and the previous process and measurements are repeated. The trends of the SOA output power vs. SOA current are shown in Figure 3.13a.

To characterize the influence of the input power on the SOA gain, the bias current is kept constant. The input power is gradually increased from 0.1 mW to 10 mW, and the measured output power is recorded. The trends of the SOA output power vs. input power are found and resulting curves are shown in Figure 3.13b, for both SOAs and for several bias currents. From this curves, we obtain the necessary input power from which SOA gain begin to saturate.

Both setups in Figure 3.11 and Figure 3.12 considers a single input laser source from

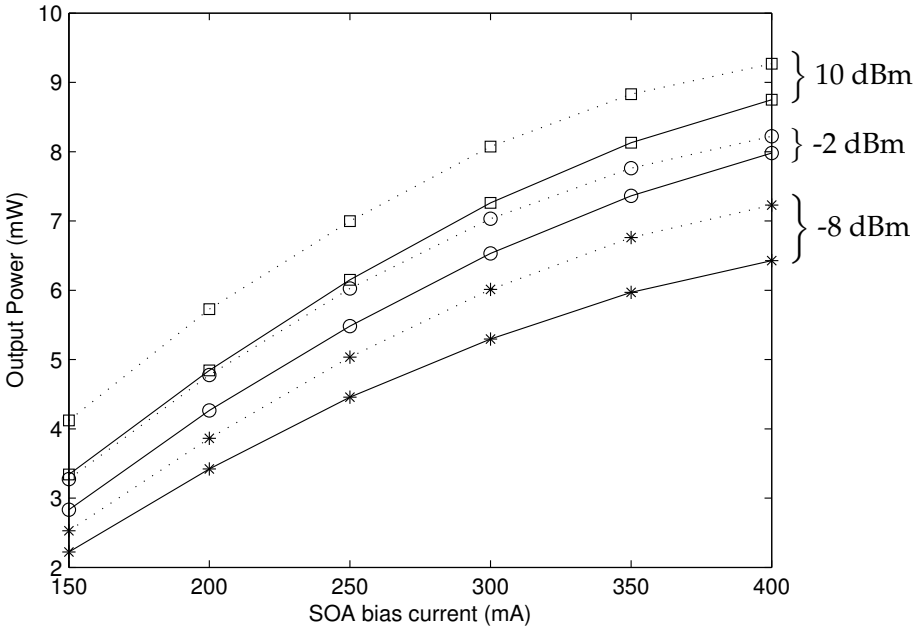

(a)

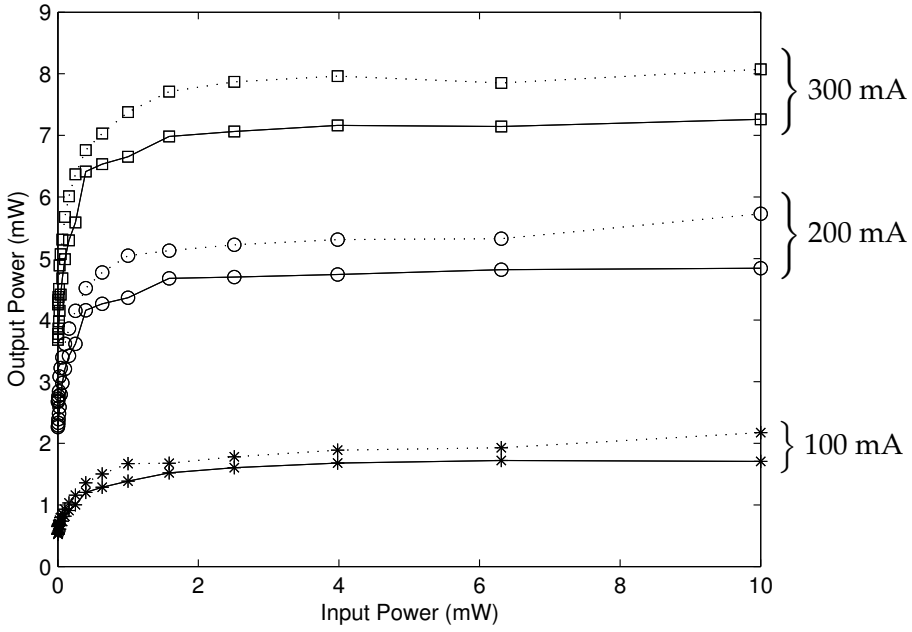

(b)

Figure 3.13: SOA static characterization: (a) MZI-SOA output power at port #I (full line) and #J (dashed line), as a function of SOA1 and SOA2 bias current, respectively. Input power equal to -8, -2 and 10 dBm (asterisks, circles and squares, respectively). (b) MZI-SOA output power at port #I (full line) and #J (dashed line), as a function of input power at ports #A and #D, respectively. Input SOA currents equal to 100, 200 and 300 mA (asterisks, circles and squares, respectively). The lines are guides for the eyes.

arms #A or #D, respectively, and the results are supported on this configuration. However, the input signal could be connected to port #B or #C, or a combination of several inputs simultaneously. This is the case when the MZI-SOA is used as the central element for phase modulation in the following Chapters. To extrapolate this characterization, we can adjust the static SOA characterization considering all the MZI-SOA inputs contributing to the overall power at the SOA input. Therefore, depending on the input(s) used to feed the SOA with a signal, the optical power at the SOA input is computed using a straightforward combination, according to the coupler (e.g. coupling factor) in the signal's path. Thus, the power at the input of SOA1 and SOA2 are given by:

$$P_{inSOA_1} = P_{inA}(1-\alpha_1) + (1-\alpha_3)\alpha_1 P_{inB} + (1-\alpha_1)(1-\alpha_3)P_{inC} \tag{3.6}$$

$$P_{inSOA_2} = P_{inD}(1-\alpha_2) + \alpha_2(1-\alpha_3)P_{inC} + \alpha_2\alpha_3 P_{inB} \tag{3.7}$$

where all the powers in (3.6) and (3.7) are given in Watt and α_1, α_2 and α_3 are the coupling factors of couplers K1, K2 and K3, respectively.

The SOA Amplifier Spontaneous Emission (ASE) profile has also been measured as function of the bias current and the wavelength, for the C band (between 1530 and 1560 nm) and part of the L band (between 1560 and 1600 nm). These measurements are presented in Figure 3.14, and they provide a good indication on the spectral capabilities of the gain of the SOAs. It can be observed that the -3 dB bandwidth of the ASE is 34 nm, on average. We can observe that this value may be considered independent of the bias current. For operation in the C band, the SOA gain should be maximum near the band centre so that the gain difference between the maximum and minimum gain within the C band is minimized.

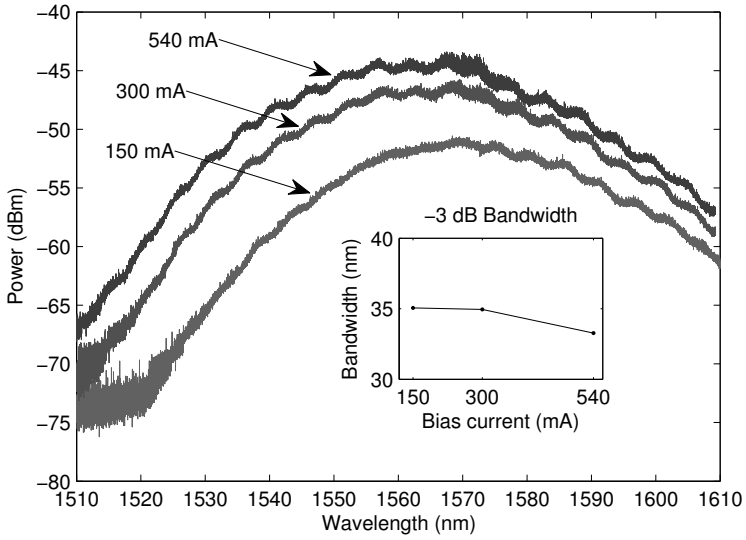

Figure 3.14: Optical spectra of SOA generated ASE and -3 dB bandwidth (inset), as a function of SOA bias current (150, 300 and 540 mA).

3.1.4 Extinction ratio

The power at the output of the MZI-SOAs (at ports #I and #J) is a result of an interference process occurring in coupler K4. The electromagnetic fields at the two inputs of coupler K4 will define the conditions for the outputs measured. So, specifically, when used as an amplitude modulator, one important factor to take into consideration is the ER of the output signal. The ER is the ratio of the optical power levels present at output ports #I and #J,

$$ER = 10log\left(\frac{P_J}{P_I}\right) \tag{3.8}$$

where ER is given in dB.

For example, through SOAs current variation, the power distribution on the MZI-SOA arms can be further changed, leading to the consequent variation of the interference conditions on output couplers. To observe the dependence of ER on bias currents, we use the setup depicted in Figure 3.15. A CW signal is injected into port #B, with both phase shifters voltage with 0 V. In Figure 3.16, we observe the dynamic of both the constructive and destructive interference respectively at the output port #J and #I, by gradually increasing SOA1 bias current, with SOA2 current constant at a reference value (200 mA).

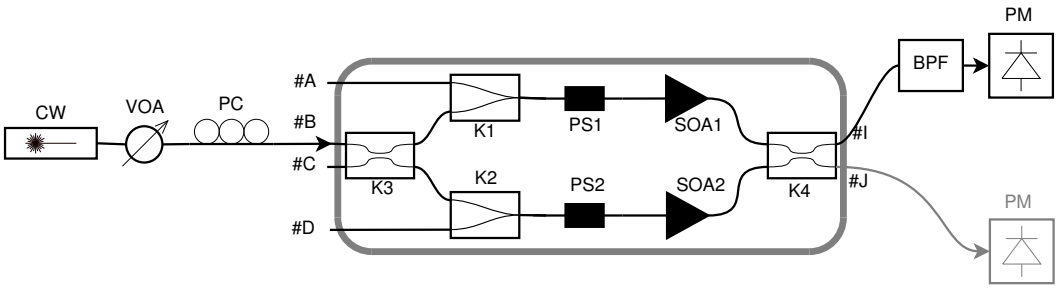

Figure 3.15: Setup for the characterization of ER dependence on bias current.

This procedure is repeated with SOA1 bias current constant at 200 mA, and SOA2 current variable, with a CW laser beam connected at input port #B. Using this methodology and after measuring the power output, we see in Figure 3.16 that there is a misalignment between #I and #J minimum and maximum power levels. This is a result of the gain change in the SOA with the changing current and also to both the unbalanced coupling factors and phase shift of the couplers. The best operational point, without phase shifters adjustment, is found searching SOA1 bias current for the highest ER. We present a model in the next chapter to find the best operational parameters to maximize the ER, but also applicable for any other condition. The formulation allows to predict the achievable ER and to adjust operational conditions in order to optimize the balancing of MZI-SOA for phase and amplitude modulation, a subject discussed in more detail in the following chapters. The process of balancing an MZI-SOA is described in Appendix B.

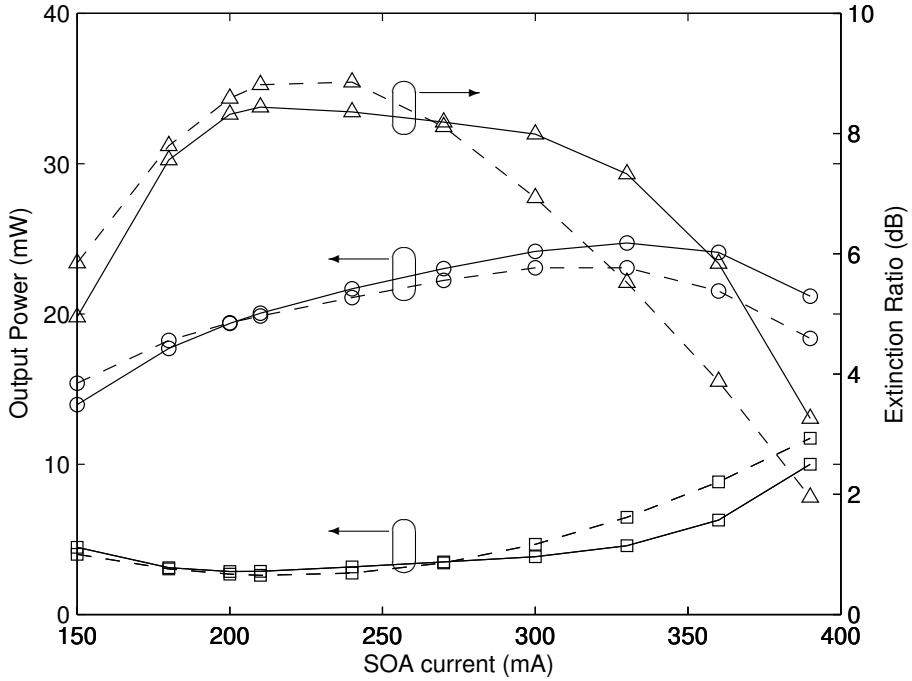

Figure 3.16: MZI-SOA output power at port #I (squares) and port #J (circles) and Extinction Ratio (triangles), as a function of SOA1 (dashed line) and SOA2 (full line) bias current. Input power is injected at port #B. The lines are guides for the eyes.

3.2 Dynamic characterization

After the static characterization, this section investigates the dynamic properties of the MZI-SOA. This study is focused on the properties of the MZI-SOA as an optical gate and as a binary phase modulator. In the past few years, the data volume of communication networks increased dramatically, so there is a need for finding fast optical gating, switching and transmission techniques, along with equipment with low power consumption and integration facilities. Among those techniques, optical phase modulation is an option that allow greater transmission distances in both digital and analog transmission systems [10].

3.2.1 All-optical XOR gate

Figure 3.17 illustrates the experimental setup to study the dynamic properties of the MZI-SOA, based on a wavelength conversion architecture proposed in [11] in a co-propagation scheme, where an all-optical XOR gate is implemented using an integrated MZI-SOA. In the MZI, both data signals are launched into the SOAs where their carrier densities and thereby the refractive index are modulated. This causes a phase modulation of the CW probe signal propagating through the SOAs according to the intensity variations of the input control signals, by XPM. By properly setting the input optical powers and controlling

the SOA parameters, the control signal from the two SOAs interferes either constructively or destructively at the output of the interferometer in order to provide the logical XOR operation of the two control sequences on the probe signal. According to the XOR operation (Table 3.2), when both control signals (ports #A and #D) are time synchronized, no pulses are obtained on the probe signal at the MZI-SOA output (port #I). Conversely, as the data signals give up time overlapping, some pulses with increasing energy will appear on the probe signal, at the MZI-SOA output.

Table 3.2: XOR symbolic truth table

Input #A	input #D	Output #J
0	0	0
0	1	1
1	0	1
1	1	0

Experimental setup

The experimental setup consists of an external cavity laser peaking at 1549.32 nm (λ_1), followed by a Polarization Controller (PC) and an external MZM. The NRZ data signal generated by a serial Bit Error Rate Tester (BERT) (Agilent N4901B) is a Pseudo Random Bit Sequence (PRBS) sequence at 10 Gbit/s, optically amplified by an EDFA (IPG-EAD-500-C3-W) and split into two equal parts using a 3 dB coupler (COUPLER1). Both signals are time synchronized using Optical Delay Lines (ODLs). Polarization controllers are included at ports #A and #D of a MZI-SOA (CIP 40G-2R2-ORP), in order to optimize the destructive output signal at port #J. Different data patterns may be obtained by delaying signals at port #A and port #D.

The probe signal, a CW light beam with 0 dBm and lasing at 1546.12 nm (λ_2), is launched into port #B of the MZI-SOA in a co-propagating direction with the data control signals. Finally, the probe signal is recovered at port #J, using a filter with a 40 GHz bandwidth (X-tract Net Test). We use two measurement instruments to analyze the output signal: a sampling oscilloscope (Agilent 86100A), connected through a PIN photodiode (HP-11982A), and an Optical Complex Spectrum Analyzer (OCSA) (APEX AP 2441A) to gather phase and power information of the output signal, for time domain characterization. Details of the OCSA connections and synchronization are presented in Appendix A.

The counter-propagation scheme presented in Figure 3.18 uses the same probe signal, but now launched into port #I. The output signal is recovered at port #B (constructive output). For this setup, an isolator is placed at ports #A, #D and #I of the MZI-SOA, to protect all laser

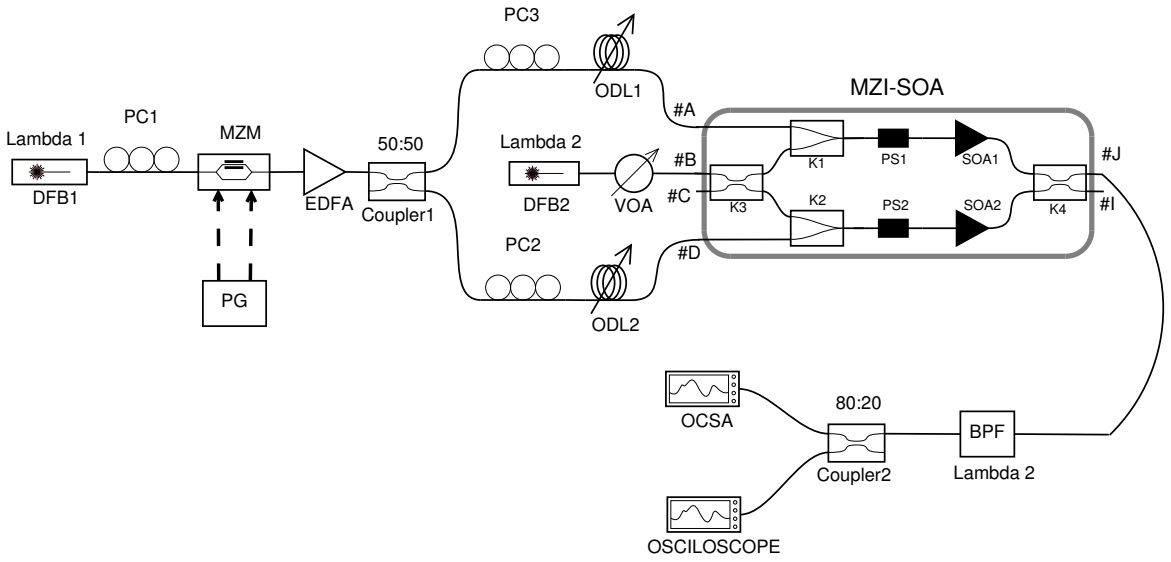

Figure 3.17: All-optical XOR gate setup, based on a MZI-SOA, in a co-propagation scheme.

sources.

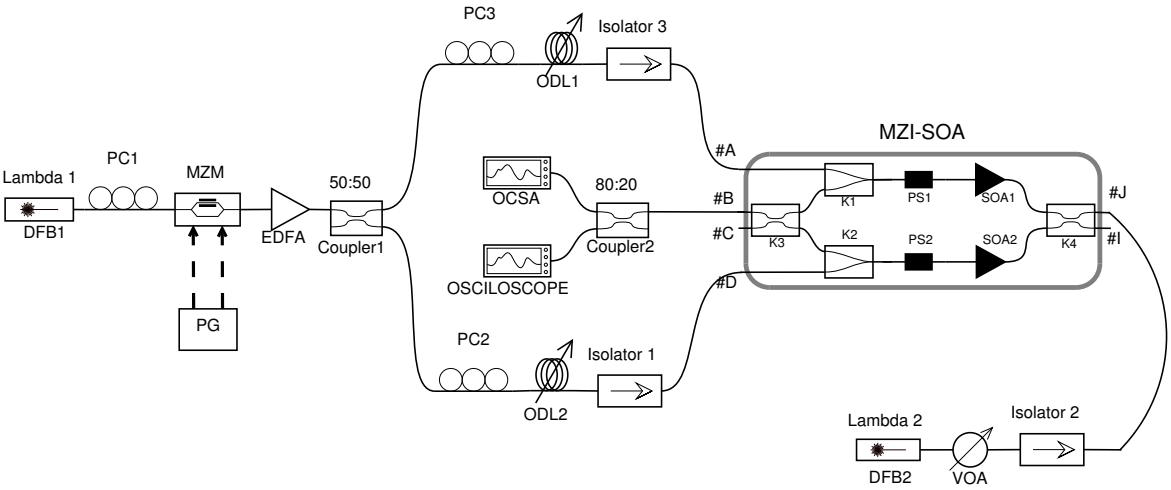

Figure 3.18: Wavelength and format conversion setup in counter propagation scheme.

Operating the MZI-SOA device requires a number of optimizations in several operational parameters such as SOA bias current, phase shifters voltage, polarization, input powers of the control and probe signals. A detailed explanation on the experimental procedure to balance the output power of an MZI-SOA is presented in Appendix B.

Experimental results and discussion

As an example, Figure 3.19 illustrates the data input signals (λ_1) injected into the arms #A and #D of the MZI-SOA, each with 2 dBm mean power, and the corresponding XOR gate output (λ_2), at 10 Gbit/s at port #J, in a co-propagating scheme. The results obtained experimentally are in agreement with the principle of operation of an XOR gate: the logical XOR gate output presents the value 0 if both of the operands have the same value, and 1 otherwise.

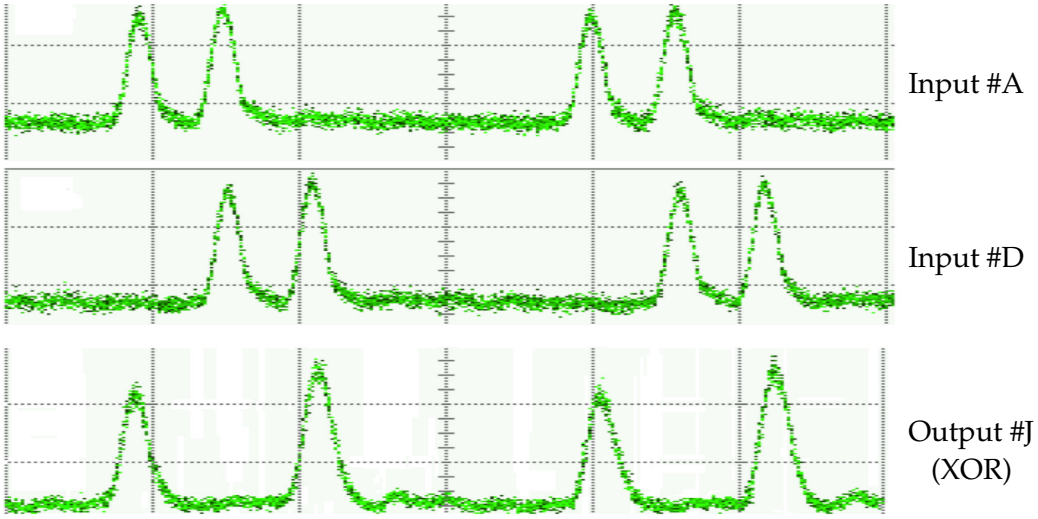

Figure 3.19: Input optical data sequences at ports #A and #D (first two sequences from top) and resulting XOR output at port #J (bottom sequence). Vertical scale is arbitrary and horizontal scale is 500 ps/div.

Figure 3.20 presents the ER of the output signal with the variation of the input power of the NRZ control signals, from 0 to 4 dBm, maintaining the power of the CW probe signal constant at 0 dBm. For both co and counter-propagation scheme, the performance of the all-optical XOR gate is almost independent of the input power, since the power variation of the two data signals involved in the comparison is the same. However, the counter-propagation scheme shows a better performance, with an improvement on the ER ranging from 0.72 dB to 1.64 dB. These results are in agreement with other experimental studies [12].

3.2.2 Binary phase modulation

Phase modulation generates signals of 0 and 1 by changing the phase of light, while allowing it to be in the ON position (See Chapter 2 for a detailed description of phase modulation). As opposed to intensity modulation, phase modulation has superior bandwidth efficiency and is not easily affected by signal distortions caused by transmission fibers and relay nodes. Several optical techniques have already been proposed to implement optical phase modulators, based on frequency shifters [13], LN waveguide [14], gain-transparent SOA [15], or using HNLF as the optical medium to phase modulate a CW laser [16].

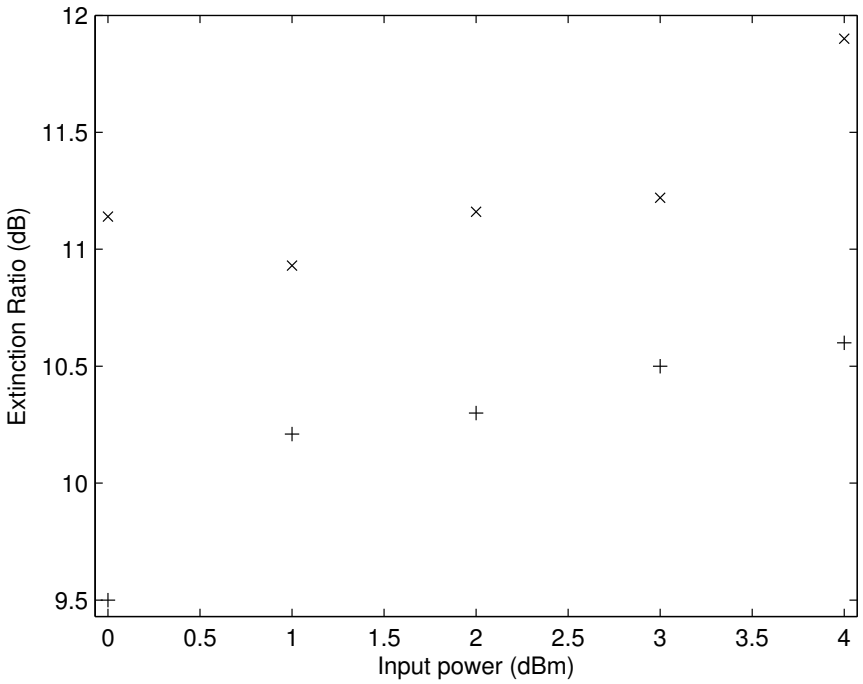

Figure 3.20: Experimental measurements of the ER of the output signal, as a function of the input power for co-propagation (+ sign) and counter-propagation (x sign) schemes.

Principle of Operation

Following the experimental results with the XOR gate [2], the next step is to characterize the phase modulation properties of a MZI-SOA, using both interferometric arms, in co and counter-propagation schemes. The setup is the same as the XOR, with MZI-SOA operational parameters tuned to set port #I has the destructive output. If both data control signals are time synchronized, the CW light from the two SOAs interferes destructively. According to the XOR operation in Figure 3.21, no pulse amplitude variation is observed at the output port #I of the interferometer [17]. However, the phase ϕ of $\lambda_{c_{XOR}}$ will vary in accordance to the input pattern, as depicted in Figure 3.21 [18].

Experimental Results and Discussion

The phase modulation performance will now be investigated for different bit rates. In the following experimental results, the input power and the operational parameters were optimized on the basis of the phase eye diagram opening (also called phase span in the following paragraphs), since BER measurements were not performed, due to setup limitations imposed by the coherent receiver used (the OCSA limits the size of the data sequence length, thereby BER measurements are not possible). A picture of the experimental setup is shown in Figure 3.22.

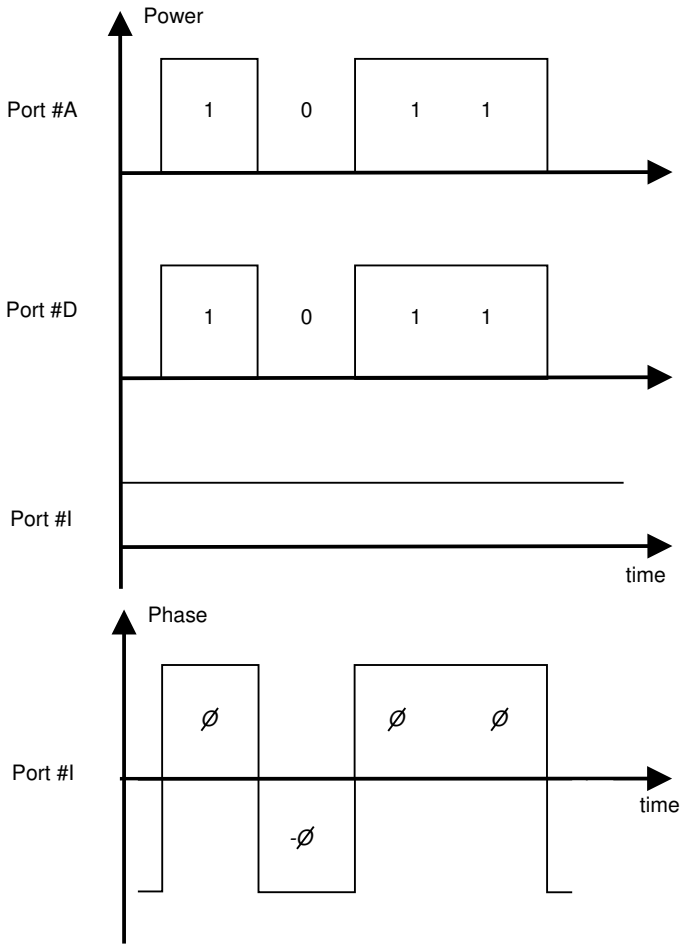

Figure 3.21: Principle of operation diagram.

In order to validate the feasibility of the MZI-SOA based phase modulator, experiments at 2.5 and 10 Gbps were carried out. An average ER of 11.3 dB and a mean power of 2.5 dBm were measured for data signals launched into ports #A and #D of the MZI-SOA. The bias current (I_{SOA}) of both SOAs were varied simultaneously, from 150 to 300 mA for 2.5 Gbps and from 150 to 400 mA for 10 Gbps. For each bias current, the mean power of the control signal (P_{CW}) was increased from -6 to 2 dBm. The voltage applied to the PSs was adjusted in order to maximize the destructive interference at output port #I.

Due to limitations imposed by the OCSA, the length's sequence at 2.5 Gbps was restricted to 4 bits [19]. Figure 3.23a shows the bit pattern launched at the interferometric ports (#A and #D) of the MZI-SOA. Figure 3.23b illustrate the output signal at port #I for bias current at 250 mA and control signal at -4 dBm. The phase shift related to different logic levels is well defined but inverted when compared with the data signal. In Figure 3.24a, phase span is plotted as a function of P_{CW} for several bias currents. The results show that they increase as the bias current is raised. Mean values vary between 35° and 50°. It can be observed in Figure 3.24b that the mean output power is also proportional to the increase of I_{SOA} and

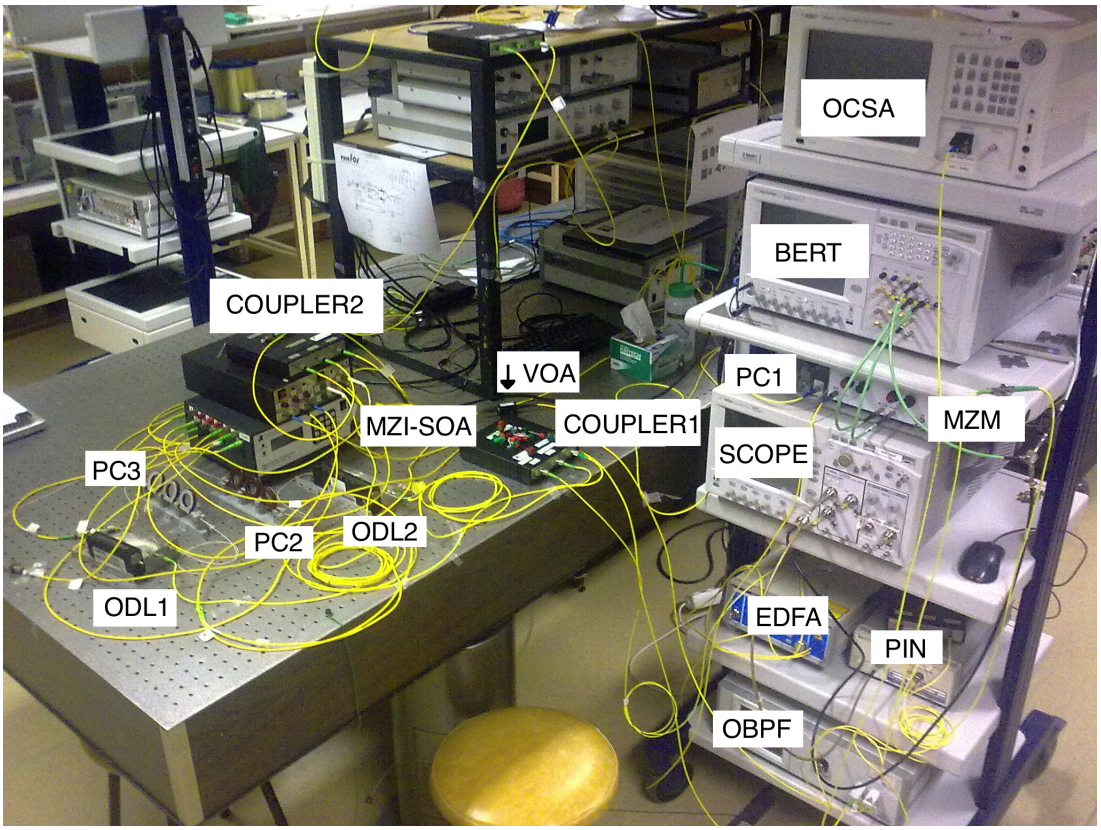

Figure 3.22: Picture of the experimental setup to perform all-optical logic gate and phase modulation experiments with an MZI-SOA. OBPF: Optical band pass filter; PC: Polarization controller; VOA: Variable optical attenuator; ODL: Optical delay line; MZM: Mach-Zehnder modulator; OCSA: Optical complex spectrum analyzer; SCOPE: Oscilloscope; BERT: Bite error Tester (Pattern generator); PIN: Optical receiver; EDFA: Optical amplifier. The laser source for the probe and control signals aren't visible from the figure.

P_{CW} since the SOAs gain is not saturated.

The proposed optical phase modulator was also evaluated at 10 Gbps. The tests were performed using data sequences with 16 bits [19]. Figure 3.26a shows the bit pattern coupled at the input ports (#A and #D) of the MZI-SOA. The resulting output signal with bias current at 150 mA and control signal at 0 dBm is depicted in Figure 3.26b. Output power fluctuations are mainly due to noise. As with 2.5 Gbps experiments, phase shifts are inverted when compared with data signal logic levels. However, due to the dynamics of the SOA and the carrier recovery time, output phase levels are less pronounced at 10 Gbps when fast variations occurs at the MZI-SOA data inputs. Phase constellations diagrams in Figure 3.27 shows that phase logic levels are evenly defined when the bias current is increased. As it can be seen in Figure 3.25a and Figure 3.25b, we obtain higher values of phase span and output mean power, respectively, by increasing the bias current. For P_{CW} ranging from -6 to 0 dBm, SOAs are in linear amplification regime. In this case, the mean values of the phase span vary

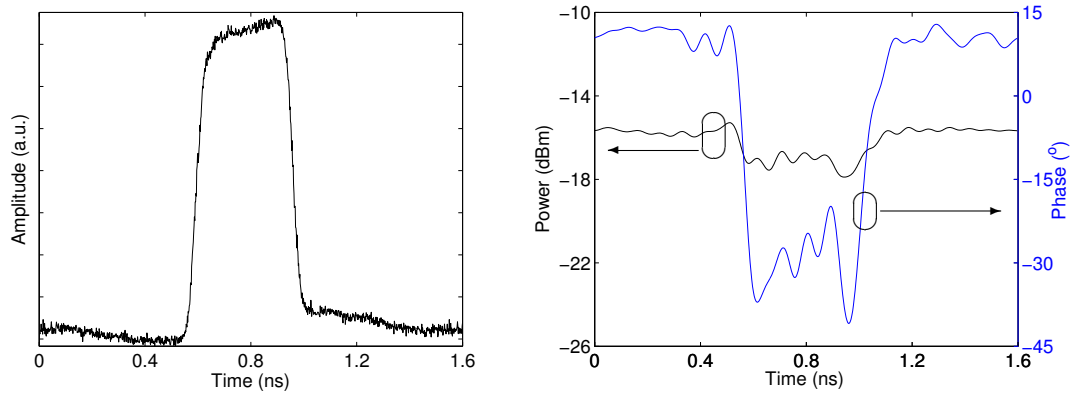

(a) (b)

Figure 3.23: (a) – Input sequence "0100" and (b) – Phase and power output, with SOA input current I_{SOA} equal to 250 mA and input laser power P_{CW} equal to -4 dBm.

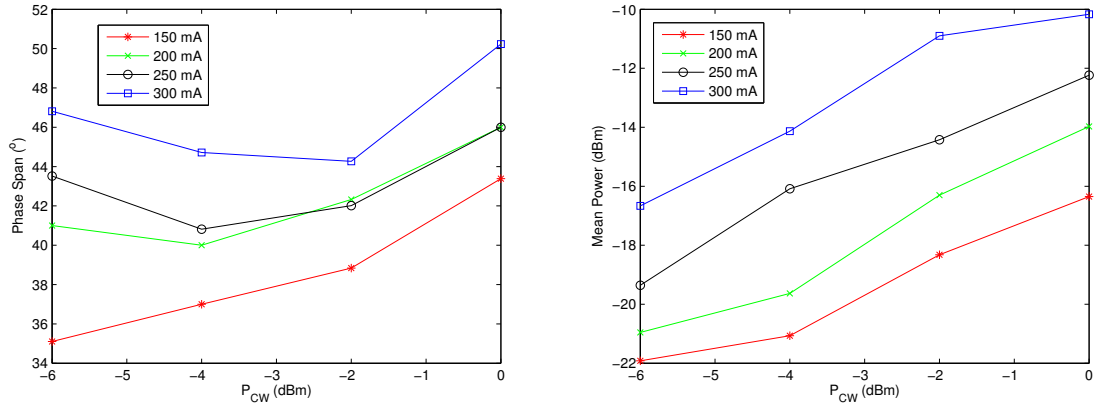

(a) (b)

Figure 3.24: (a) – Phase span and (b) – Mean power. Input SOA currents equal to 150, 200, 250 and 300 mA (asterisks, crosses, circles and squares respectively). The lines are guides for the eyes.

between 70° and 170°. For P_{CW} above 0 dBm, the SOAs saturates, which reduces phase span values and output mean powers.

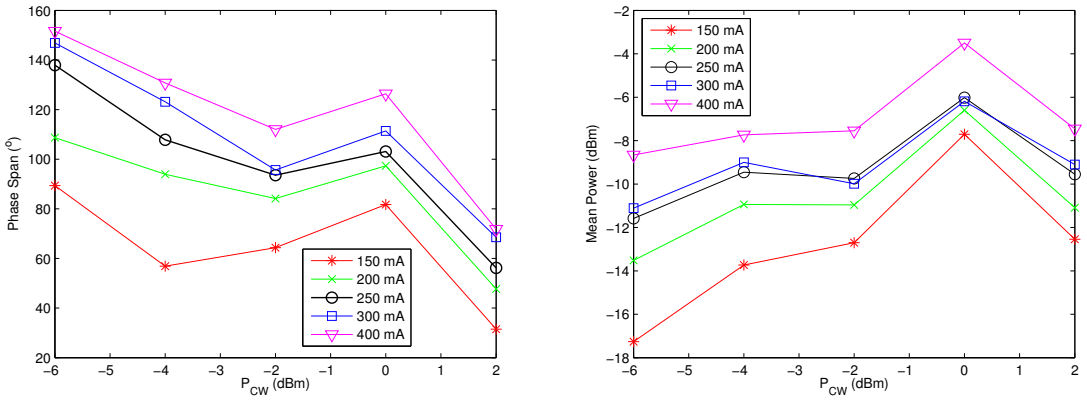

(a) (b)

Figure 3.25: (a) – Phase span and (b) – Mean power. Input SOA currents equal to 150, 200, 250, 300 and 400 mA (asterisks, crosses, circles, squares and triangles, respectively). The lines are guides for the eyes.

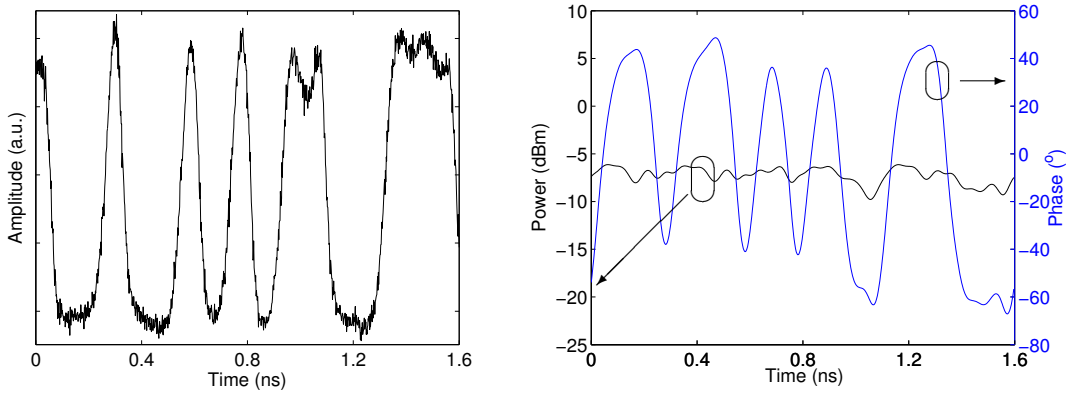

(a) (b)

Figure 3.26: (a) – Input sequence "1110010010101100" and (b) – Phase and power output, with input SOA current I_{SOA} equal to 150 mA and input laser power P_{CW} equal to 0 dBm.

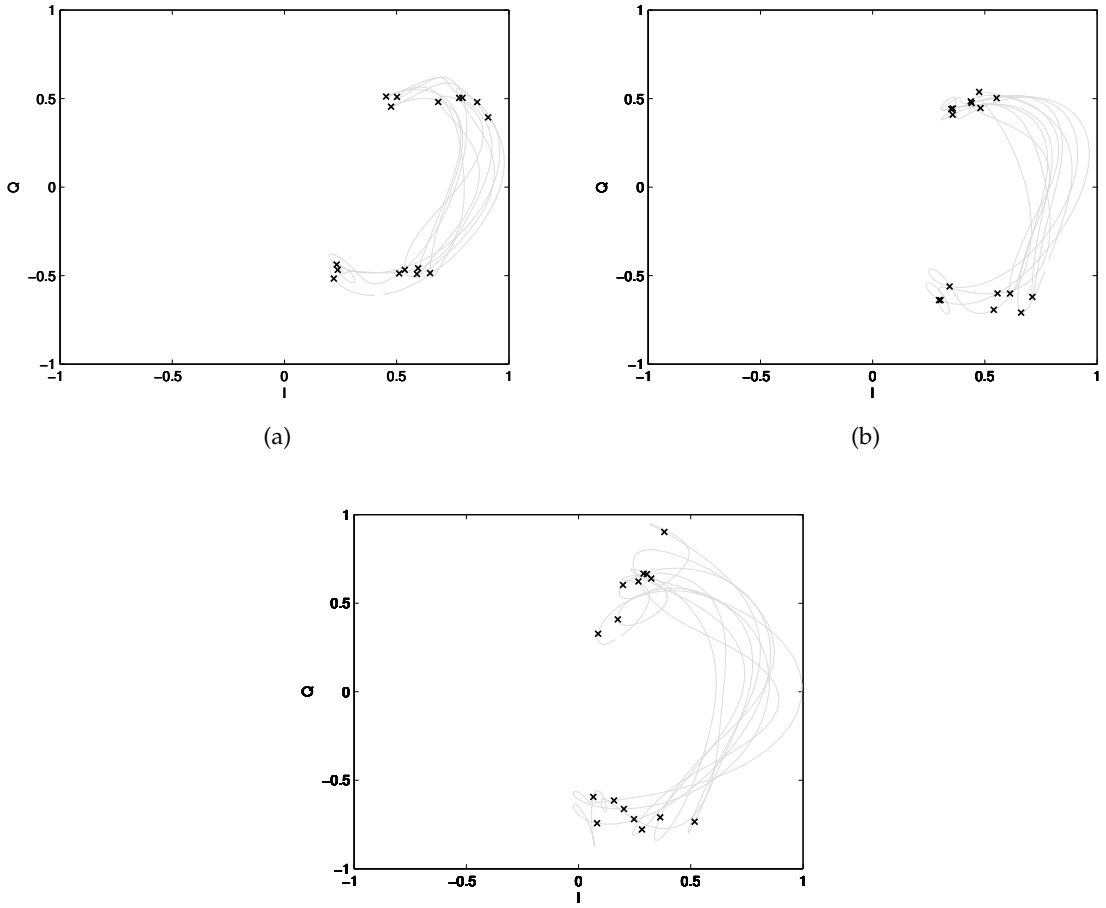

(a)

(b)

(c)

Figure 3.27: Measured signal constellation, with path lines (grey color) and sampled symbols (black crosses). input laser power P_{CW} equal to 0 dBm and input SOA current I_{SOA} equal to (a) 150 mA, (b) 200 mA and (c) 400 mA. Input control signals at 10 Gbit/s.

3.3 Conclusions

In this chapter, we conduct static and dynamic characterization of a integrated MZI-SOA. All active and passive components of the MZI-SOA were characterize to assess the properties of the device for phase modulation experiments. This process allow extracting the coupling factors and relevant gain functions which contribute for the determination of the MZI-SOA behavior, having in mind that most of these parameters are hidden, since they are masked in the output power which are normally a sum or difference of internal fields with amplitude and phase variations.

A novel method to perform optical phase modulation has been presented, based on an all-optical XOR gate configuration. We assess the impact of SOAs bias current and input CW power on the phase of the destructive output of a MZI-SOA. We observed that an increase of the bias current produces higher values of phase spans and output mean powers. However, SOAs gain saturation has an opposite effect on the output signal. The experimental results demonstrate the feasibility of a MZI-SOA device as an optical phase modulator.

Summarizing, having in mind next generation optical networks, which are meant to be as flexible and transparent as possible, this chapter has characterized the operating conditions of the MZI-SOA working as an optical gate and phase modulator, which results will be useful for the next chapters, dealing with advanced modulation format conversion techniques.

References

[1] "CIP Technologies," July 2012. [Online]. Available: http://www.ciphotonics.com/

[2] C. Reis, R. P. Dionisio, B. Neto, A. Teixeira, and P. Andre, "All-optical XOR based on integrated MZI-SOA with co- and counter-propagation scheme," in *ICTON Mediterranean Winter Conference,2009. ICTON-MW 2009. 3rd*, 2009, pp. 1–4.

[3] R. Dionisio, C. Reis, P. Andre, R. Nogueira, and A. Teixeira, "Experimental study of a phase modulator using an active interferometric device," in *MELECON 2010*, 2010, pp. 1142–1146.

[4] N. Yan, J. del Val Puente, T. G. Silveira, A. Teixeira, A. P. S. Ferreira, E. Tangdiongga, P. Monteiro, and A. M. J. Koonen, "Simulation and Experimental Characterization of SOA-MZI-Based Multiwavelength Conversion," *J. Lightwave Technol.*, vol. 27, no. 2, pp. 117–127, 2009.

[5] Y. Xingwen, Y. Runxiang, J. Kurumida, and S. J. B. Yoo, "A Theoretical and Experimental Study on Modulation-Format-Independent Wavelength Conversion," *Lightwave Technology, Journal of*, vol. 28, no. 4, pp. 587–595, 2010.

[6] G. Maxwell, A. Poustie, C. Ford, M. Harlow, P. Townley, M. Nield, I. Lealman, S. Oliver, L. Rivers, and R. Waller, "Hybrid integration of monolithic semiconductor optical amplifier arrays using passive assembly," *55th Electronic Components & Technology Conference, Vols 1 and 2, 2005 Proceedings*, pp. 1349–1352, 2005.

[7] G. Maxwell, B. Manning, M. Nield, M. Hariow, C. Ford, M. Clements, S. Lucas, P. Townley, R. McDougall, S. Oliver, R. Cecil, L. Johnston, A. Poustie, R. Webb, I. Lealman, L. Rivers, J. King, S. Perrin, R. Moore, I. Reid, and D. Scrase, "Very low coupling loss, hybrid-integrated all-optical regenerator with passive assembly," in *Optical Communication, 2002. ECOC 2002. 28th European Conference on*, vol. 5, sept. 2002, pp. 1 –2.

[8] M. Bass and E. Stryland, *Fiber optic handbook – fiber, devices and system for optical communication*. McGraw-Hill, 2002.

[9] A. Perez-Pardo, T. T. Ng, P. Petropoulos, S. Sales, and D. J. Richardson, "Analysis of the dynamic responses of soa wavelength converters using linear frequency resolved gating technique," *Photonics Technology Letters, IEEE*, vol. 20, no. 13, pp. 1079–1081, 2008.

[10] M. N. Sysak, L. A. Johansson, J. Klamkin, L. A. Coldren, and J. E. Bowers, "Characterization of third order distortion in InGaAsP optical phase modulator monolithically integrated with balanced UTC photodetector," *2006 Ieee Leos Annual Meeting Conference Proceedings, Vols 1 and 2*, pp. 338–339, 2006.

[11] T. Fjelde, D. Wolfson, A. Kloch, B. Dagens, A. Coquelin, I. Guillemot, F. Gaborit, F. Poingt, and M. Renaud, "Demonstration of 20 Gbit/s all-optical logic XOR in integrated SOA-based interferometric wavelength converter," *Electronics Letters*, vol. 36, no. 22, pp. 1863–1864, 2000.

[12] M. Hattori, K. Nishimura, R. Inohara, and M. Usami, "Bidirectional Data Injection Operation of Hybrid Integrated SOA-MZI All-Optical Wavelength Converter," *Journal of Lightwave Technology*, vol. 25, no. 2, pp. 512 –519, Feb 2007.

[13] B. Qi, L.-L. Huang, H.-K. Lo, and L. Qian, "Polarization insensitive phase modulator for quantum cryptosystems," *Opt. Express*, vol. 14, no. 10, pp. 4264–4269, 2006.

[14] C. Langrock, E. Diamanti, R. V. Roussev, Y. Yamamoto, M. M. Fejer, and H. Takesue, "Highly efficient single-photon detection at communication wavelengths by use of upconversion in reverse-proton-exchanged periodically poled LiNbO3 waveguides," *Opt. Lett.*, vol. 30, no. 13, pp. 1725–1727, 2005.

[15] W. Hong, D. Huang, X. Zhang, and G. Zhu, "Simulation and analysis of gain-transparent SOA used as optical phase-modulator in DPSK applications," Y. Nakano, Ed., vol. 6782. Wuhan, China: SPIE, 2007, pp. 67 822L–12.

[16] V. Marembert, C. Schubert, C. Weinert, H. G. Weber, K. Schulze, F. Futami, and S. Watanabe, "Investigations of fiber Kerr switch: nonlinear phase shift measurements and optical time-division demultiplexing of 320 Gbit/s DPSK signals," in *Lasers and Electro-Optics, 2005. (CLEO). Conference on*, vol. 2, 2005, pp. 1432–1434 Vol. 2.

[17] R. Vilar, J. M. Martinez, F. Ramos, and J. Marti, "All-optical DGD monitor for packet-switched networks based on an integrated active Mach-Zehnder interferometer operating as logic XOR gate," *Optics Communications*, vol. 281, no. 21, pp. 5330–5334, 2008.

[18] S. C. Cao and J. C. Cartledge, "Measurement-based method for characterizing the intensity and phase modulation properties of SOA-MZI wavelength converters," *Photonics Technology Letters, IEEE*, vol. 14, no. 11, pp. 1578–1580, 2002.

[19] "APEX Optical Spectrum Analyzer AP2041B," November 2009.

Chapter 4

MZI-SOA Static Model

4.1 Introduction

THe MZI-SOA is a well known device with potential in a variety of applications. However, integrated MZI-SOAs with hybrid technology encompasses several components (couplers, waveguides, phase shifters and SOAs), all with their own tolerances and asymmetries. These issues lead to very long and difficult initial setup phase [1], which varies from device to device due to fabrication and integration yields. However, MZI-SOA working characteristics are well described with a static model, through which we can carry out the operational parameters optimization and the determination of operational limits.

This chapter starts with the description of a static model of a MZI-SOA, based on the interferometric structure of the MZI, and power measurements following the procedure described in the previous Chapter (See section 3.1 for more details). MOGA is exploited for operational parameter extraction of the model.

4.2 Structure and electric field analysis

From the MZI-SOA interferometric structure presented in Figure 4.1, and considering that the output ports are #I and #J, the electric fields E_I and E_J of the optical signal are, respectively:

$$\begin{aligned} E_I &= \sqrt{P_1}e^{j\varphi_1}\sqrt{1-\alpha_4} + \sqrt{P_2}e^{j\varphi_2}j\sqrt{\alpha_4} \\ &= \sqrt{P_1}e^{j\varphi_1}\sqrt{1-\alpha_4} + \sqrt{P_2}e^{j\left(\varphi_2+\frac{\pi}{2}\right)}\sqrt{\alpha_4} \end{aligned} \tag{4.1}$$

$$\begin{aligned} E_J &= \sqrt{P_1}e^{j\varphi_1}j\sqrt{\alpha_4} + \sqrt{P_2}e^{j\varphi_2}\sqrt{1-\alpha_4} \\ &= \sqrt{P_1}e^{j\left(\varphi_1+\frac{\pi}{2}\right)}\sqrt{\alpha_4} + \sqrt{P_2}e^{j\varphi_2}\sqrt{1-\alpha_4} \end{aligned} \tag{4.2}$$

The scalar notation is used for both E_I and E_J after assuming that the two fields are identically polarized. P_1 and P_2 are the output powers of SOA1 and SOA2, respectively. The constant α_4 is the coupling factor of coupler K4. The variable φ is a phase contribution from the SOA. Using Euler's equation,

$$e^{j\varphi_x} = cos(\varphi_x) + jsin(\varphi_x), \qquad x = 1, 2$$

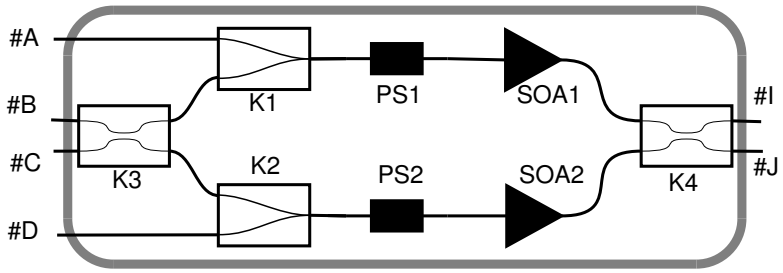

Figure 4.1: MZI-SOA representation. K1 and K2 are combiners; K3 and K4 are couplers; SOA1 and SOA2 are semiconductor optical amplifiers; PS1 and PS2 are phase shifters; #A, #B, #C, #D, #I, and #J are bidirectional optical ports.

the output fields E_I is described in a cartesian notation as,

$$\begin{aligned} E_I &= \sqrt{P_1}\left(cos\left(\varphi_1\right) + jsin\left(\varphi_1\right)\right)\sqrt{1-\alpha_4} \\ &\quad + \sqrt{P_2}\left(cos\left(\varphi_2+\frac{\pi}{2}\right) + jsin\left(\varphi_2+\frac{\pi}{2}\right)\right)\sqrt{\alpha_4} \\ &= \left[\sqrt{P_1}cos\left(\varphi_1\right)\sqrt{1-\alpha_4} + \sqrt{P_2}cos\left(\varphi_2+\frac{\pi}{2}\right)\sqrt{\alpha_4}\right] \\ &\quad + j\left[\sqrt{P_1}sin\left(\varphi_1\right)\sqrt{1-\alpha_4} + \sqrt{P_2}sin\left(\varphi_2+\frac{\pi}{2}\right)\sqrt{\alpha_4}\right] \\ &= \mathrm{Re}\left(E_I\right) + j\mathrm{Im}\left(E_I\right) \end{aligned} \tag{4.3}$$

and for E_J field as,

$$\begin{aligned} E_J &= \sqrt{P_1}\left(cos\left(\varphi_1+\frac{\pi}{2}\right) + jsin\left(\varphi_1+\frac{\pi}{2}\right)\right)\sqrt{\alpha_4} \\ &\quad + \sqrt{P_2}\left(cos\left(\varphi_2\right) + jsin\left(\varphi_2\right)\right)\sqrt{1-\alpha_4} \\ &= \left[\sqrt{P_1}cos\left(\varphi_1+\frac{\pi}{2}\right)\sqrt{\alpha_4} + \sqrt{P_2}cos\left(\varphi_2\right)\sqrt{1-\alpha_4}\right] \\ &\quad + j\left[\sqrt{P_1}sin\left(\varphi_1+\frac{\pi}{2}\right)\sqrt{\alpha_4} + \sqrt{P_2}sin\left(\varphi_2\right)\sqrt{1-\alpha_4}\right] \\ &= \mathrm{Re}\left(E_J\right) + j\mathrm{Im}\left(E_J\right) \end{aligned} \tag{4.4}$$

4.3 MZI-SOA output power

The output power P_I is taken from the absolute value of (4.3),

$$P_I = |E_I|^2 = \mathrm{Re}^2\left(E_I\right) + \mathrm{Im}^2\left(E_I\right) \tag{4.5}$$

where

$$\begin{aligned}\mathrm{Re}^2\left(E_I\right) = P_1\left[cos\left(\varphi_1\right)\right]^2\left(1-\alpha_4\right) + P_2\left[cos\left(\varphi_2+\frac{\pi}{2}\right)\right]^2\alpha_4 \\ + 2\sqrt{P_1P_2\left(1-\alpha_4\right)\alpha_4}cos\left(\varphi_1\right)cos\left(\varphi_2+\frac{\pi}{2}\right)\end{aligned} \tag{4.6}$$

and

$$\begin{aligned}\mathrm{Im}^2\left(E_I\right) = P_1\left[sin\left(\varphi_1\right)\right]^2\left(1-\alpha_4\right) + P_2\left[sin\left(\varphi_2+\frac{\pi}{2}\right)\right]^2\alpha_4 \\ + 2\sqrt{P_1P_2\left(1-\alpha_4\right)\alpha_4}sin\left(\varphi_1\right)sin\left(\varphi_2+\frac{\pi}{2}\right)\end{aligned} \tag{4.7}$$

Combining results of (4.6) and (4.7) into (4.4), we can write

$$\begin{aligned}P_I = P_1\left(1-\alpha_4\right)\left[cos^2\left(\varphi_1\right)+sin^2\left(\varphi_1\right)\right] \\ + P_2\alpha_4\left[cos^2\left(\varphi_2+\frac{\pi}{2}\right)+sin^2\left(\varphi_2+\frac{\pi}{2}\right)\right] \\ + 2\sqrt{P_1P_2\left(1-\alpha_4\right)\alpha_4}\left[sin\left(\varphi_2+\frac{\pi}{2}\right)sin\left(\varphi_1\right)+cos\left(\varphi_2+\frac{\pi}{2}\right)cos\left(\varphi_1\right)\right]\end{aligned} \tag{4.8}$$

Using trigonometric equalities $sin(A)sin(B)+cos(A)cos(B) = cos(A-B)$ and $sin^2(A)+cos^2(B) = 1$, (4.8) simplifies to,

$$P_I = P_1\left(1-\alpha_4\right) + P_2\alpha_4 + 2\sqrt{P_1P_2\left(1-\alpha_4\right)\alpha_4}cos\left(\varphi_2-\varphi_1+\frac{\pi}{2}\right) \tag{4.9}$$

The argument of the cosine function can be written as a phase difference,

$$\Delta\phi = \varphi_2 - \varphi_1 \tag{4.10}$$

so,

$$P_I = P_1\left(1-\alpha_4\right) + P_2\alpha_4 + 2\sqrt{P_1P_2\left(1-\alpha_4\right)\alpha_4}cos\left(\Delta\phi+\frac{\pi}{2}\right) \tag{4.11}$$

We simplify the cosine argument, to give,

$$P_I = P_1\left(1-\alpha_4\right) + P_2\alpha_4 - 2\sqrt{P_1P_2\left(1-\alpha_4\right)\alpha_4}sin\left(\Delta\phi+\delta_1\right) \tag{4.12}$$

Additional term δ_1 in the sine argument represent a phase mismatch on paths or coupler crossing factors.

The same analysis for output power P_J gives:

$$P_J = P_1\alpha_4 + P_2\left(1-\alpha_4\right) + 2\sqrt{P_1P_2\left(1-\alpha_4\right)\alpha_4}sin\left(\Delta\phi+\delta_2\right) \tag{4.13}$$

where δ_2 is different from δ_1.

P_1, P_2 and $\Delta\phi$ behavior depend only on operational variables (SOA bias current I_{SOA}, MZI-SOA input power P_{in} and phase shifter voltage V_{PS}), and their parameters will be obtained based on a fitting process between this model and experimental measurements.

4.4 SOA gain model

We assume that the output power of the SOA is proportional to its gain and the input power,

$$P_1 = G_1P_{inSOA_1} \tag{4.14}$$

$$P_2 = G_2P_{inSOA_2} \tag{4.15}$$

The gain is dependent of two operational parameters, bias current and input power of the SOA,

$$G_1 = f\left(I_{SOA_1}, P_{inSOA_1}\right) \tag{4.16}$$

$$G_2 = f\left(I_{SOA_2}, P_{inSOA_2}\right) \tag{4.17}$$

The large signal amplifier gain is given by the following relation [2]:

$$G = G_0e^{\left(-\frac{G-1}{G}\frac{P_{out}}{P_s}\right)} \tag{4.18}$$

The quantity P_s is known as the saturation power of the gain medium. G_0 is the unsaturated gain of the amplifier, i.e., the gain for $P_{in} \ll P_s$. Using a Taylor series expansion of the gain exponential term, up to the second order, we express a linear relation between the output power and the gain of the SOA,

$$G \simeq G_0\left(1-\frac{G-1}{G}\frac{P_{out}}{P_s}\right) \tag{4.19}$$

After a algebraic simplification of the equation, and using the relation $G = P_{out}/P_{inSOA}$, the gain becomes,

$$G\left(P_{inSOA}\right) \simeq \frac{G_0P_s + P_{inSOA}G_0}{P_s + P_{inSOA}G_0} \tag{4.20}$$

We also consider a linear relation between SOA gain and bias current,

$$G\left(I_{SOA}\right) = pI_{SOA} \tag{4.21}$$

Combining both (4.20) and (4.21) gives the following expression to model SOA gain:

$$G\left(P_{inSOA}, I_{SOA}\right) \simeq \frac{G_0 P_s + P_{inSOA} G_0}{P_s + P_{inSOA} G_0} \left(pI_{SOA}\right) \tag{4.22}$$

4.5 MZI-SOA output phase model

From (4.10), $\Delta\phi$ is a phase term that is physically originated by the combination of two electric fields in coupler K4, from both arms of the MZI-SOA. $\Delta\phi$ depends on three operational parameters: SOAs bias current (I_{SOA}), input power (P_{in}) and phase shifter voltage (V_{PS}). The dependence of $\Delta\phi$ on SOA bias current and input power is [2]:

$$\begin{aligned}
&\Delta\phi\left(I_{SOA_1}, I_{SOA_2}, P_{inSOA_1}, P_{inSOA_2}\right) \\
&\quad = -\frac{\alpha}{2}\left(ln\left(G_1\left(I_{SOA_1}, P_{inSOA_1}\right)\right) - ln\left(G_2\left(I_{SOA_2}, P_{inSOA_2}\right)\right)\right) \\
&\quad = -\frac{\alpha}{2} ln\left(\frac{G_1\left(I_{SOA_1}, P_{inSOA_1}\right)}{G_2\left(I_{SOA_2}, P_{inSOA_2}\right)}\right) \\
&\quad = -\frac{\alpha}{2} ln\left(\frac{G_1}{G_2}\right)
\end{aligned} \tag{4.23}$$

where α is the linewidth enhancement factor [2]. The phase difference dependence with bias current and input power, comes directly from (4.22). From a Taylor series approximation of the natural logarithm up to the second term, and removing the variables dependence form the expression, for simplicity, we get,

$$\begin{aligned}
\Delta\phi &= -\frac{\alpha}{2} ln\left(\frac{G_1}{G_2}\right) \\
&\simeq -\frac{\alpha}{2}\left(\frac{G_1}{G_2} - 1\right) \\
&= -\frac{\alpha}{2}\left(\frac{G_1 - G_2}{G_2}\right)
\end{aligned} \tag{4.24}$$

The influence of the phase shifter voltage on $\Delta\phi$ is modeled using a quadratic expression (simulation results, not presented here, have shown that a linear, cubic or higher order approximation is not appropriate to fit experimental measurements, due to large errors produced):

$$\Delta\phi\left(V_{PS}\right) = aV_{PS}^2 + bV_{PS} + c \tag{4.25}$$

Combining (4.24) and (4.25), we obtain,

$$\begin{aligned}\Delta\phi\left(I_{SOA_1}, I_{SOA_2}, P_{inSOA_1}, P_{inSOA_2}, V_{PS1}, V_{PS2}\right) \simeq \\ -\frac{\alpha}{2}\left(\frac{G_1\left(I_{SOA_1}, P_{inSOA_1}\right) - G_2\left(I_{SOA_2}, P_{inSOA_2}\right)}{G_2\left(I_{SOA_2}, P_{inSOA_2}\right)}\right) \\ +\sum_{i=1}^{2}\left(a_i V_{PS}^2 + b_i V_{PS} + c_i\right)\end{aligned} \tag{4.26}$$

Since (4.12) and (4.13) already have a constant term for the sine argument (δ_1 and δ_2), the constant term c_i from the previous equation is not necessary and therefore not considered. Without loss of generality, we also consider that one of the phase shifters inside the MZI-SOA structure is always deactivated, i.e, $V_{PS} = 0$ V, and that the other phase shifter influence is enough to invert the output power (and phase) values of the interferometer structure, when swept from minimum to maximum voltage. Therefore, the output phase model is simplified and becomes,

$$\begin{aligned}\Delta\phi\left(I_{SOA_1}, I_{SOA_2}, P_{inSOA_1}, P_{inSOA_2}, V_{PS}\right) \simeq \\ -\frac{\alpha}{2}\left(\frac{G_1\left(I_{SOA_1}, P_{inSOA_1}\right) - G_2\left(I_{SOA_2}, P_{inSOA_2}\right)}{G_2\left(I_{SOA_2}, P_{inSOA_2}\right)}\right) \\ +aV_{PS}^2 + bV_{PS}\end{aligned} \tag{4.27}$$

where V_{PS} is either the voltage applied to PS1 or PS2.

4.6 Genetic algorithm

Genetic Algorithms (GAs) [3, 4] are optimization algorithms based on the mechanics of natural selection and natural genetics, where stronger individuals are the likely winners in a competitive environment. They represent a class of iterative optimization algorithms that simulate the evolution of species. GAs presume that a potential solution to any problem is an individual represented by a set of parameters. These parameters are regarded as genes and can be structured on a string or chromosome. A fitness function is defined in order to estimate the goodness of an individual. Initially, the population is usually generated randomly. Every individual in the population is an encoded version of a possible solution. At each step, individuals are selected to form the parents, following a selection paradigm in which individuals with better fitness are selected with a higher probability. Then, they are evolved by means of genetic operators, such as reproduction, crossover, and mutation, to generate new offsprings (the next generation) that is hoped to fit better than the previous one. Finally, a replacement scheme is applied to determinate which individuals of the population will survive from the offsprings and the parents. This process is repeated until a stopping criterion is fulfilled.

The reproduction operator creates a literal copy of selected individuals from the parent population in the descendant generation. The crossover operator is applied to pairs of individuals in order to interchange their genetic material. To generate good offspring, a good mechanism for selecting parents is necessary. Roulette wheel selection is one of the most common techniques [5]. When using this method, the probability of selecting an individual is proportional to its health. In this way, good properties should propagate down the generations. On the other hand, the mutation operator makes a random change in the genetic material of a single individual, allowing the GA to explore new corners of the search space and hence avoiding the risk of being trapped in a local optimum. The evolution process is repeated a predefined number of iterations or until another criterion is met. Since individuals from the population become fitter throughout the generations, it is hoped that the final population will contain an optimal or near optimal solution.

4.6.1 Multi-objective genetic algorithm

The problem considered in this study is to establish a vector, or set, of best-fit parameters (a, b, δ_1, δ_2 and α), to minimize simultaneously the error between two sets of measured and estimated values. To satisfy two objectives simultaneously, two main approaches are used to overcome this problem in the literature. The first one consists in the combination of the different objectives into a single one, and then use one of the techniques for single objective optimization [6,7]. In such cases, the compromise between the objectives is a priori determined through the choice of the combination rule. The main criticism addressed to this approach is the difficulty to choose a priori the compromise.

Another method is to postpone this choice after having several candidate solutions. This is the goal of the Pareto-based method using the notion of dominance between candidate solutions: Given a set of objectives, a solution is said to Pareto dominate another if the first is not inferior to the second in all objectives, and, additionally, there is at least one objective where it is better [8]. In this case, the goal of the search algorithm becomes the identification of a set of solutions which are non-dominated by any others, which is the main concept behind MOGA [5].

MOGA uses a controlled elitist genetic algorithm [9], which favors individuals with better fitness value but also individuals that can help increase the diversity of the population, even if they have a lower fitness value. It is important to maintain the diversity of the population, i.e. the proximity measure between two population members [5], for the process to converge to an optimal Pareto front. This is done by controlling the number of individuals in the Pareto front (and therefore the elite members) as the algorithm runs, and by favoring individuals that are relatively far away from the front. We set the fraction of individuals in the Pareto front to 35 % of the population size.

For the computation of the unknown parameters of (4.12) and (4.13), two objective functions, F_{P_I} and F_{P_J}, must be minimized simultaneously. Each function is the Root Mean Squared Error (RMSE) between all the point from the computed (P^c) and the measured powers (P^m) for one output port (port #I or port #J). These functions are given by the following equations:

$$F_{P_I} = \sqrt{\frac{1}{N}\sum_{k=1}^{N}\left(\left[P_I^m(k) - P_I^c(k)\right]^2\right)} \tag{4.28}$$

$$F_{P_J} = \sqrt{\frac{1}{N}\sum_{k=1}^{N}\left(\left[P_J^m(k) - P_J^c(k)\right]^2\right)} \tag{4.29}$$

Where N is the number of measured data points used in the fitting process.

From the Pareto front and the corresponding candidate solutions, we perform discrimination of the optimized sets error-wise, and then finally select one that has the lowest error from the rest of the characterizations, i.e., a single solution is chosen from the Pareto front, as the lower mean value between F_{P_I} and F_{P_J},

$$F_P = min\left\{\frac{F_{P_I} + F_{P_J}}{2}\right\} \tag{4.30}$$

An initial set of values may be used to initiate the population (parameters). In that case, all individuals of the initial population are randomly generated from a seed individual, composed by a set of non-random parameters selected by the user. Upper and lower boundaries may be also defined and used to set a range to each parameter, according to their physical limits or other valid criteria.

4.7 Experimental validation

The work reported in this section validates the the static MZI-SOA model and the genetic algorithm optimization process described above.

As already described in the previous Chapter, an important feature to properly design a MZI-SOA based phase modulation system is the evaluation of the optical power and the ER at the output ports. For the proposed phase modulation scheme presented in Chapter 3, based on the all-optical XOR gate, one output should be set with maximum output power (constructive output port) and the other with minimum output power (the destructive output port). Therefore, one should set optimal operational parameters for the MZI-SOA to produce maximum ER between output ports.

4.7.1 SOA gain

From the SOA model in (4.22), the unknown parameters P_s, G_0 and p are computed by fitting the model to measurements made from a single arm of the MZI-SOA, and for each SOAs, as a function of bias current (I_{SOA}) and SOA input power (P_{inSOA}). The measurement are originated from the static characterization described in section 3.1.3, using

the experimental setup of Figure 3.11 and 3.12. Input power for both SOAs depends on the input power from the MZI-SOA input port and the coupling factor of coupler K1, K2 and K3, depending on the input that is used. Having experimentally estimated the coupling factors using the process described in section 3.1.1 (the coupling factor values are listed in Table 3.1), the expression for the power at the SOA input are given in Table 4.1.

Table 4.1: SOA input power formulation

Input port	Formulation
#A	$P_{inSOA1} = \alpha_1 P_{inA}$
#B	$P_{inSOA1} = (1-\alpha_3)(1-\alpha_1) P_{inB}$
	$P_{inSOA2} = \alpha_3 (1-\alpha_2) P_{inB}$
#C	$P_{inSOA1} = \alpha_3 (1-\alpha_1) P_{inC}$
	$P_{inSOA2} = (1-\alpha_3)(1-\alpha_2) P_{inC}$
#D	$P_{inSOA2} = \alpha_2 P_{inD}$
#I	$P_{inSOA1} = (1-\alpha_4) P_{inI}$
	$P_{inSOA2} = \alpha_4 P_{inI}$
#J	$P_{inSOA1} = \alpha_4 P_{inJ}$
	$P_{inSOA2} = (1-\alpha_4) P_{inJ}$

Matlab© was the tool used to fit the SOA model to experimental measurements. Since the SOA model in (4.22) is a single nonlinear equation, we've made use of a nonlinear regression method from the surface fitting Toolbox (we use MOGA fitting technique with the MZI-SOA model only). The results are presented in Table 4.2.

Table 4.2: SOA gain model coefficients obtained after nonlinear regression

Device	G_0	P_s	p	Goodness of fit (r^2)
SOA1	472.2	0.00757	3.666	0.9871
SOA2	417.7	0.008968	3.585	0.9834

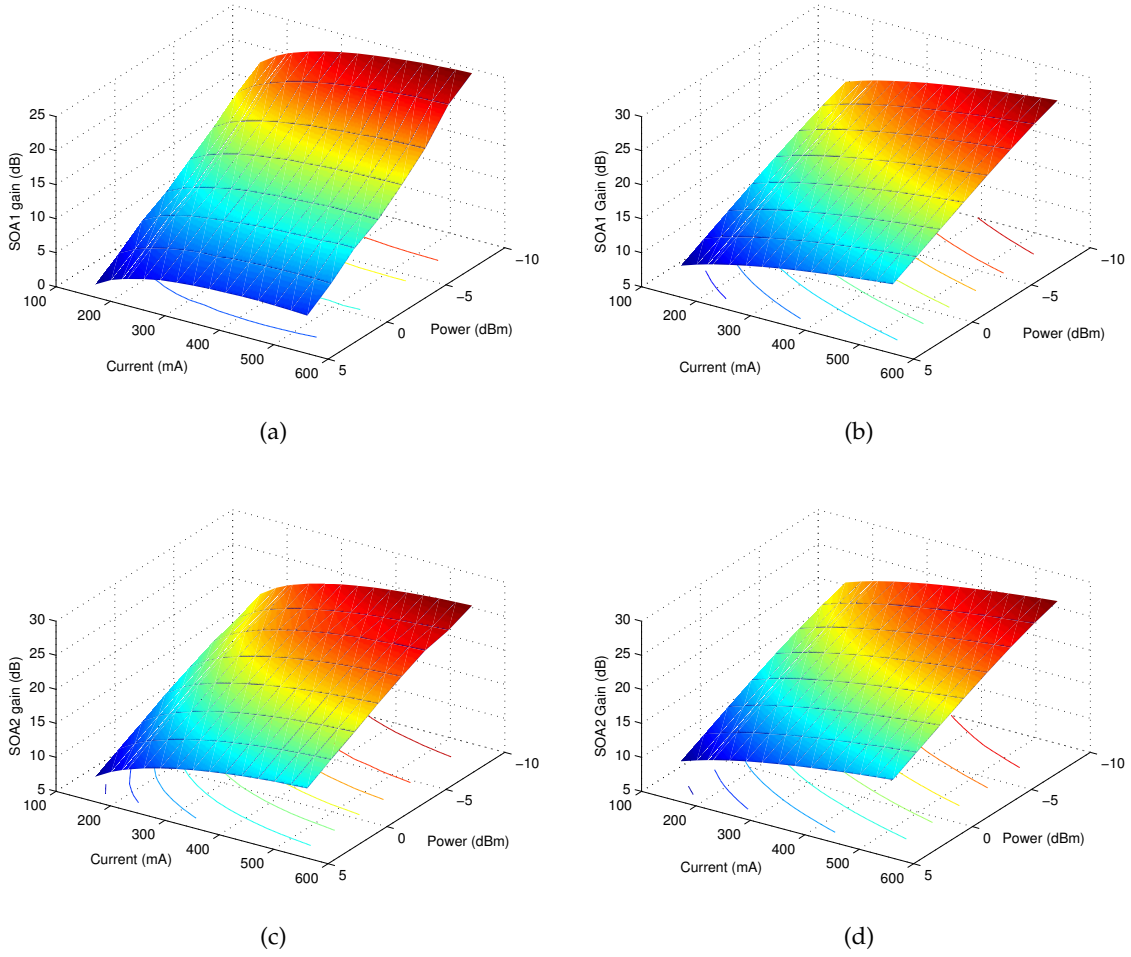

(a) (b)

(c) (d)

Figure 4.2: SOAs gain and modeling characterization: (a) and (c) are experimental measurements for SOA1 and SOA2, respectively; (b) and (d) are modeled data for SOA1 and SOA2, respectively. MZI-SOA input power is between -10 and 4 dBm and bias current varies between 100 and 540 mA.

The results shows that the SOA model is accurate ($r^2 = 0.9871$ for SOA1 and $r^2 = 0.9834$ for SOA2) and may be used to predict similar values has the ones extracted from experimental measurements. The fitting results are represented in Figure 4.2.

This model, together with the estimated parameters of Table 4.2, will be subsequently used to simulate both SOAs behavior inside the MZI-SOA model.

4.7.2 MZI-SOA output

The approach to find the unknown coefficients for $\Delta\phi$, and ultimately a solution for the MZI-SOA model, is to use a method that includes equations (4.12) and (4.13) simultaneously in the fitting process, since all the parameters are common in both equation, except δ_1 and δ_2. GAs, and specially MOGA, are a suitable choice to find a solution.

Concerning the optimization of the MZI-SOA model parameters with MOGA, three different scenarios are envisaged to fit the model to the experimental power measurements. The first one uses only one variable operational parameter (I_{SOA}), the second uses two variable operational parameters (I_{SOA} and P_{inSOA}), and the third scenario three variable operational parameters (I_{SOA}, P_{inSOA} and V_{PS}). For all scenarios, MOGA runs for 3000 iterations with an initial population of 100 individuals, i.e., parameters sets, randomly regenerated from a seed individual. The simulation was carried out in a Matlab© environment, with genetic algorithm and optimization library functions.

One variable operational parameter: I_{SOA}

To fit the unknown parameters of the MZI-SOA model, extra power measurements were performed with the setup of Figure 3.11. A CW signal was coupled into input port #B, with 3 dBm. We observe the dynamic of both the constructive and destructive interference respectively at the output port #I and #J, changing the current of SOA1, and fixing the SOA2 current at a reference value of 200 mA. Both phase shifters voltage were set to 0 V, so the only unknown parameters of the model are α, δ_1 and δ_2.

Results of the fitting process with MOGA are presented in Table 4.3. Figure 4.3 also shows experimental data compared with values estimated through (4.12) and (4.13). In both cases, we observe a misalignment between #I and #J minimum and maximum power levels. This is a clear result of the gain change in the SOA with the changing current and also to both the unbalanced splitting factors and phase shift of the couplers. Moreover, the minimum of the #I output power does not reach the zero, impacting the maximum achievable ER.

Table 4.3: Parameters obtained after MOGA fitting methodology with one variable operational parameter (I_{SOA1}).

Parameter	Lower Bound	Upper Bound	Seed	MOGA Result	Units
δ_1	0	2π	0	4.49×10^{-2}	rad
δ_2	0	2π	0	1.57×10^{-1}	rad
α	0	10	3 [10]	5.4682	-

From the analysis of Figure 4.3, it is clear that the model prescribed, even considering the approximations made, e.g., linear gain dependence of the SOA with the current, gives out a very precise fitting of the output power values. This is very important, since, from here one can capture the reasoning behind the major performance limitations of these structures, and based on this optimization of the behavior having in mind the application target can be made. As an example, it can be said that the best operational point, without phase shifters adjustments, for maximum ER, would most probably be achieved if the SOA1 would be

biased at 250 mA.

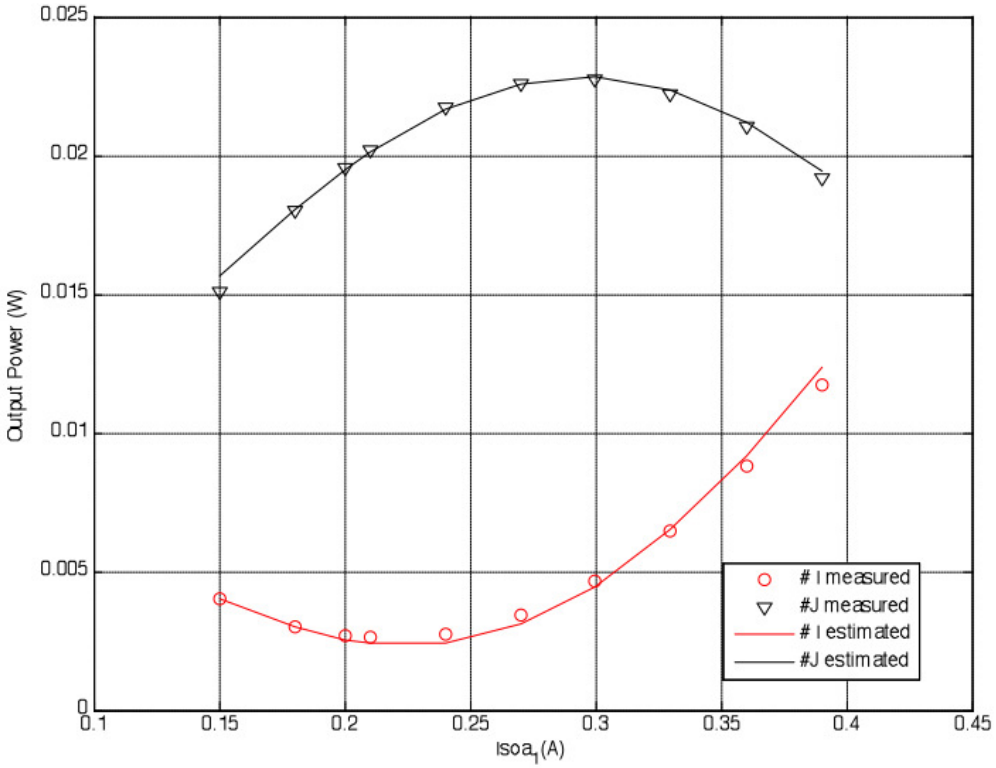

Figure 4.3: Measured (discrete symbols) and estimated (full lines) power levels on #I (red), #J (black) output ports with 3 dBm optical input power at #B.

Two variable operational parameters: I_{SOA} and P_{inSOA}

With only one variable operational parameter, we saw a good agreement between the model and experimental measurements. Now, we allow two operational parameters to change, I_{SOA} and P_{inSOA}. In this scenario, both phase shifter are once again considered inactive ($V_{PS1} = V_{PS2} = 0$ V). The unknown parameters of the model are α, δ_1 and δ_2. Initial seed of the genetic algorithm, along with upper and lower boundaries (according to their physical limits) are defined in Table 4.4.

From all the solutions from the Pareto front (Figure 4.4a), one was chosen with the lower mean value between objectives F_{P_I} and F_{P_J} (Figure 4.4b), and the best set of parameters that minimizes mean RMSE are given in Table 4.4, in the column "MOGA Result". The value for parameter α is consistent with typical values found in SOAs [10] (from 3 to 10). δ_1 and δ_2 are phase values, not associated with any physical parameter.

From the best set of parameters that MOGA delivered, we compute the output powers from the MZI-SOA model. With SOAs bias current between 0 and 540 mA and MZI-SOA input power at port #B between -10 and 4 dBm, we create in Figure 4.5, a surface plot of

Table 4.4: Parameters used with MOGA methodology with two variable operational parameter (I_{SOA1} and P_{inSOA}) and values obtained after the fitting process.

Parameter	Lower Bound	Upper Bound	Seed	MOGA Result	Units
δ_1	0	2π	0	1.7125	rad
δ_2	0	2π	0	0.4340	rad
α	0	10	3 [10]	5.1819	-

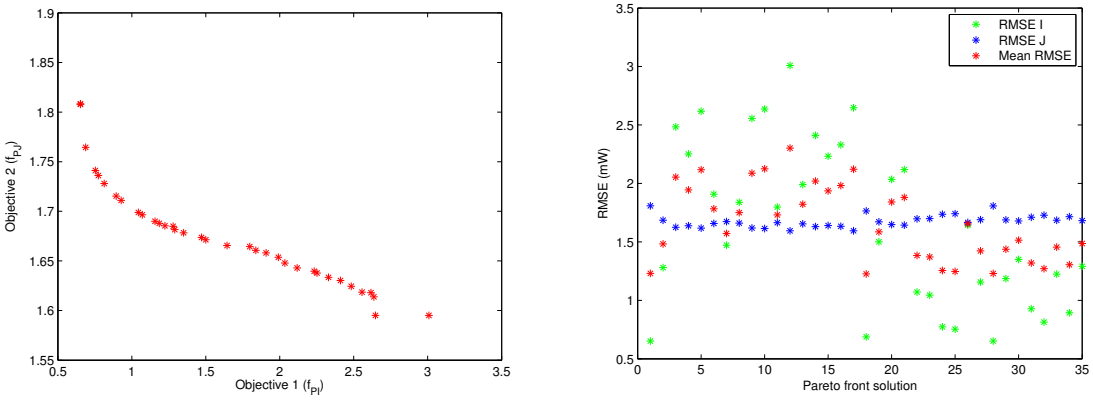

(a) (b)

Figure 4.4: MOGA results on the MZI-SOA model: (a) Pareto front (red stars); (b) RMSE of the two objectives function (F_{P_I}: green stars; F_{P_J}: red stars), and their mean value (F_P: blue stars), for each solution of the Pareto front.

the optical power at port #I and #J. Both simulated and measured output powers are in agreement. The same conclusion was also verified comparing the ER from the model and from measurements (Figure 4.6).

Three variable operational parameters: I_{SOA}, P_{inSOA} and V_{PS}

In the third fitting scenario, phase shifters voltage V_{PS} is also an input parameter of the MZI-SOA model. Power measurements are taken at the output ports #I and #J. Input signal is a CW laser at input port #B. Both SOAs are biased with the same current ($I_{SOA1} = I_{SOA2}$). Only one phase shifter will be active at a time.

From the experimental setup of Figure 3.10, we first measure the output power of the MZI-SOA with the phase shifter on the upper arm turned off ($V_{PS1} = 0$ V). On the lower arm, the phase shifter voltage (V_{PS2}) was swept between 0 V and 10 V (1 V step). Then, we

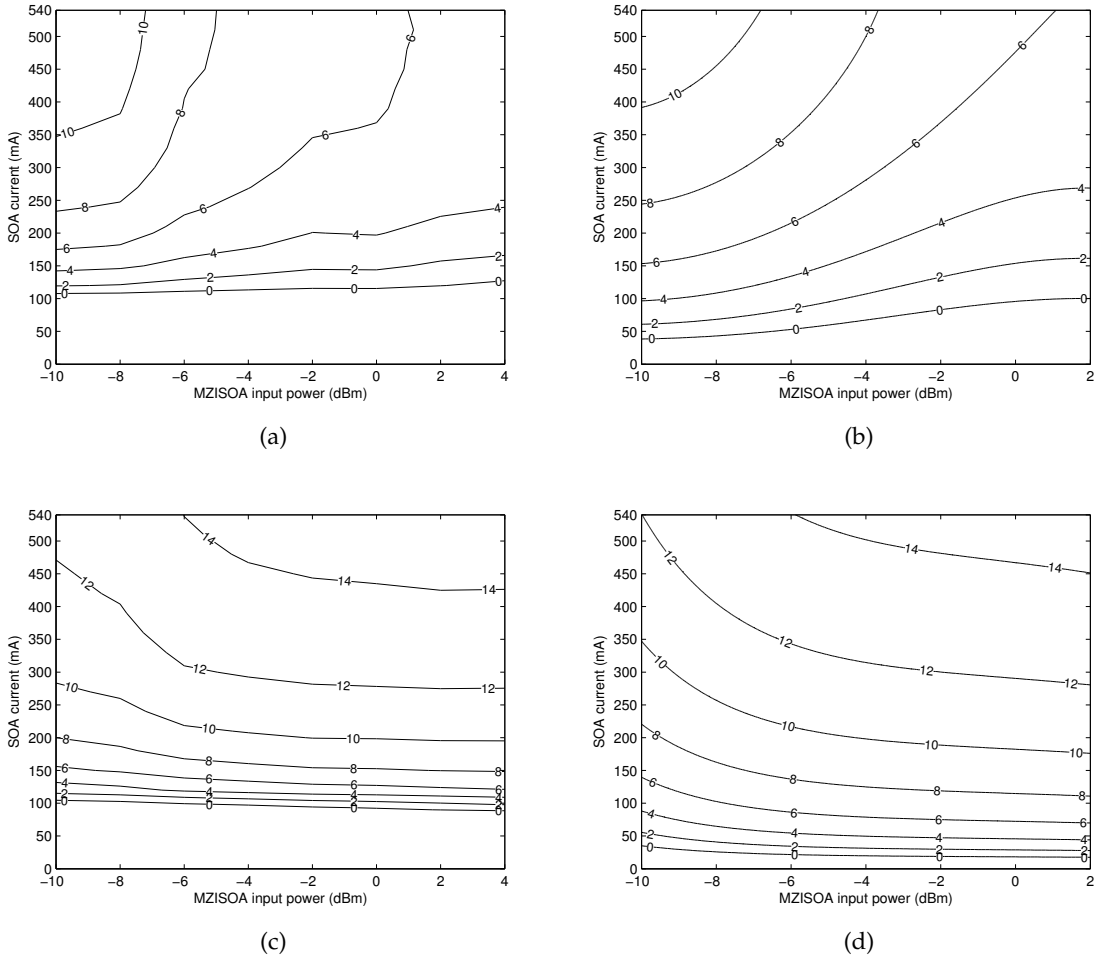

Figure 4.5: MZI-SOA output power, in dBm, as a function of bias current and input power: (a) and (c) are experimental measurements for output ports #I and #J, respectively; (b) and (d) are results with the corresponding model using MOGA, for output ports #I and #J, respectively. MZI-SOA input power is between -10 and 4 dBm and bias current varies between 0 and 540 mA.

switch the measurement process by turning off V_{PS2} and sweeping V_{PS1} also between 0 V and 10 V with 1 V step (Figure 3.8). For each voltage value, the bias current of both SOAs was swept simultaneously from 0 to 540 mA (30 mA step), and input power from -10 to 2 dBm (2 dB step).

Initial population seed for the model coefficients are given in Table 4.5, along with upper and lower constraints. After running MOGA, and from all the solutions from the Pareto front (Figure 4.7), one was chosen with the lower mean value, according to (4.30), and the resulting set of parameters, for $V_{PS1} = 0$ or $V_{PS2} = 0$, presented also in Table 4.5.

As an example of the goodness of the fitting process, we choose to compare the experimental measurement and the model outputs, for a single input power (3 dBm),

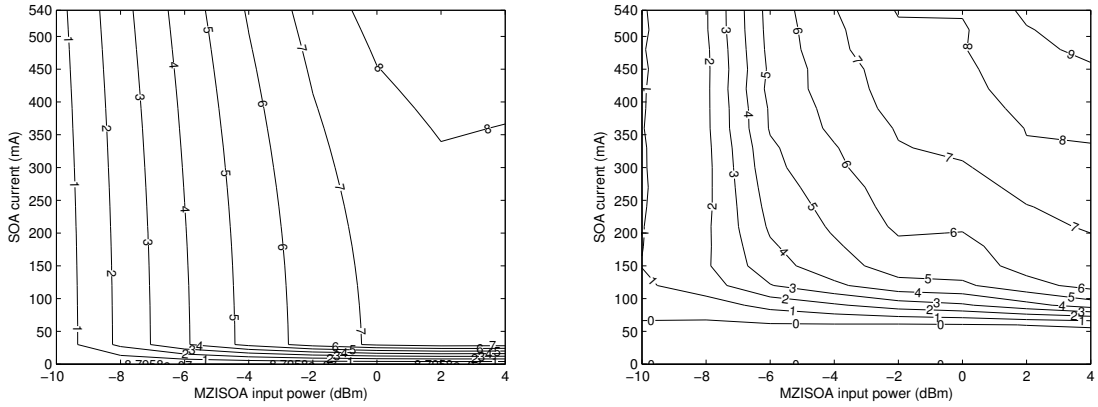

(a) (b)

Figure 4.6: ER, in dB, between MZI-SOA output ports, as a function of bias current and input power: (a) experimental measurements; (b) modeled data using MOGA. MZI-SOA input power is between -10 and 4 dBm and SOAs bias current varies between 0 and 540 mA.

Table 4.5: Model parameters obtained after MOGA, using three variable operational parameter.

Parameter	Lower Bound	Upper Bound	Seed	MOGA Result		Units
				$(V_{PS1} = 0)$	$(V_{PS2} = 0)$	
δ_1	0	2π	0	1.0186	0.3085	rad
δ_2	0	2π	0	0.7991	0.2765	rad
α	0	10	3 [10]	5.0595	5.2341	-
a	$-\infty$	$+\infty$	0	0.1267	-0.099	radV^{-2}
b	$-\infty$	$+\infty$	0	0.0656	0.0863	radV^{-1}

sweeping I_{SOA1} from 0 to 540 mA and V_{PS} from 0 to 10 V (one Phase shifter active at a time). The results presented in Figure 4.8 are quite satisfactory, since in both situations, when $V_{PS1} = 0$ or when $V_{PS2} = 0$, the model follows the behavior of the measured powers at port #I and #J. Not only the behavior is similar, but the values encountered are also in agreement.

The computed ER between output port is also consistent with measurement, as depicted in Figure 4.9.

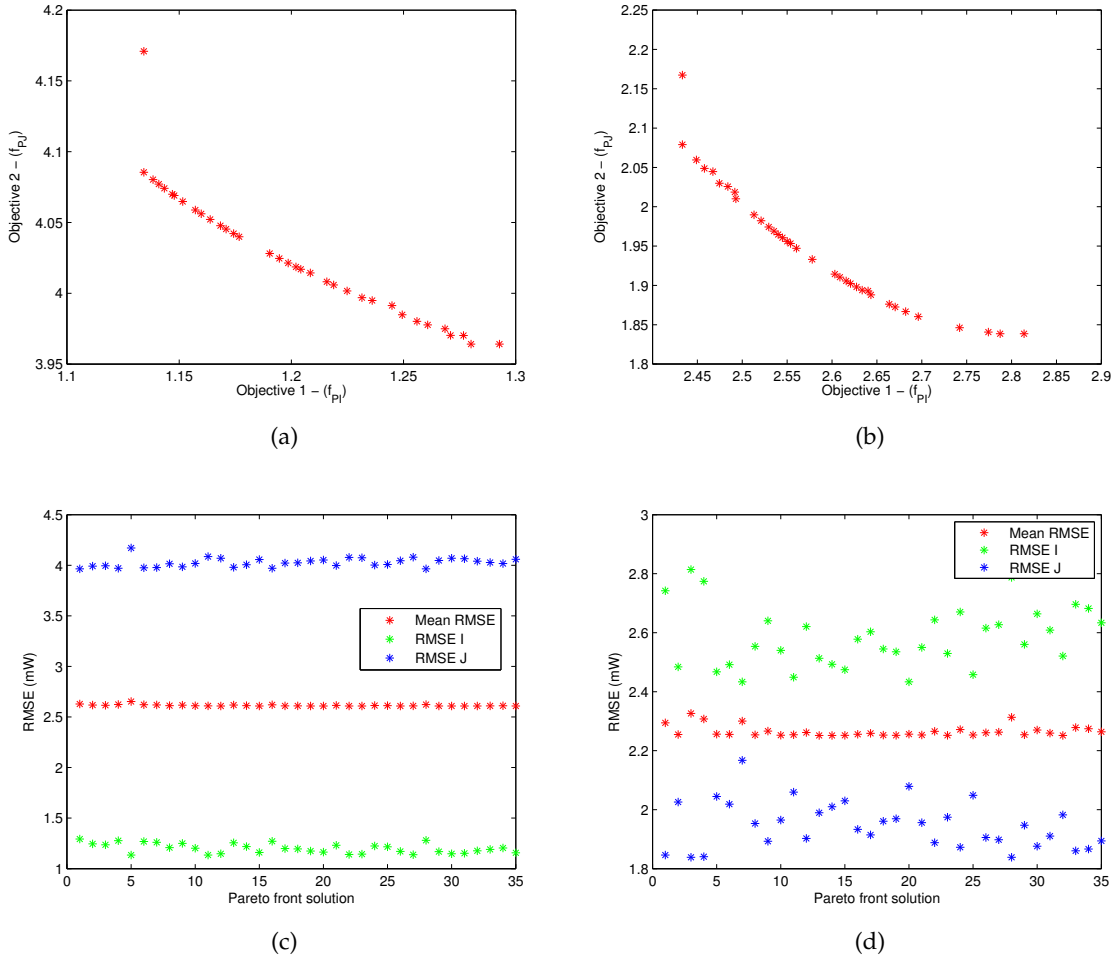

Figure 4.7: Pareto front and RMSE after MOGA application: (a) Pareto front with phase shifter 1 (PS1) active and resulting RMSE in (c); (b) Pareto front with phase shifter 2 (PS2) active and resulting RMSE in (d).

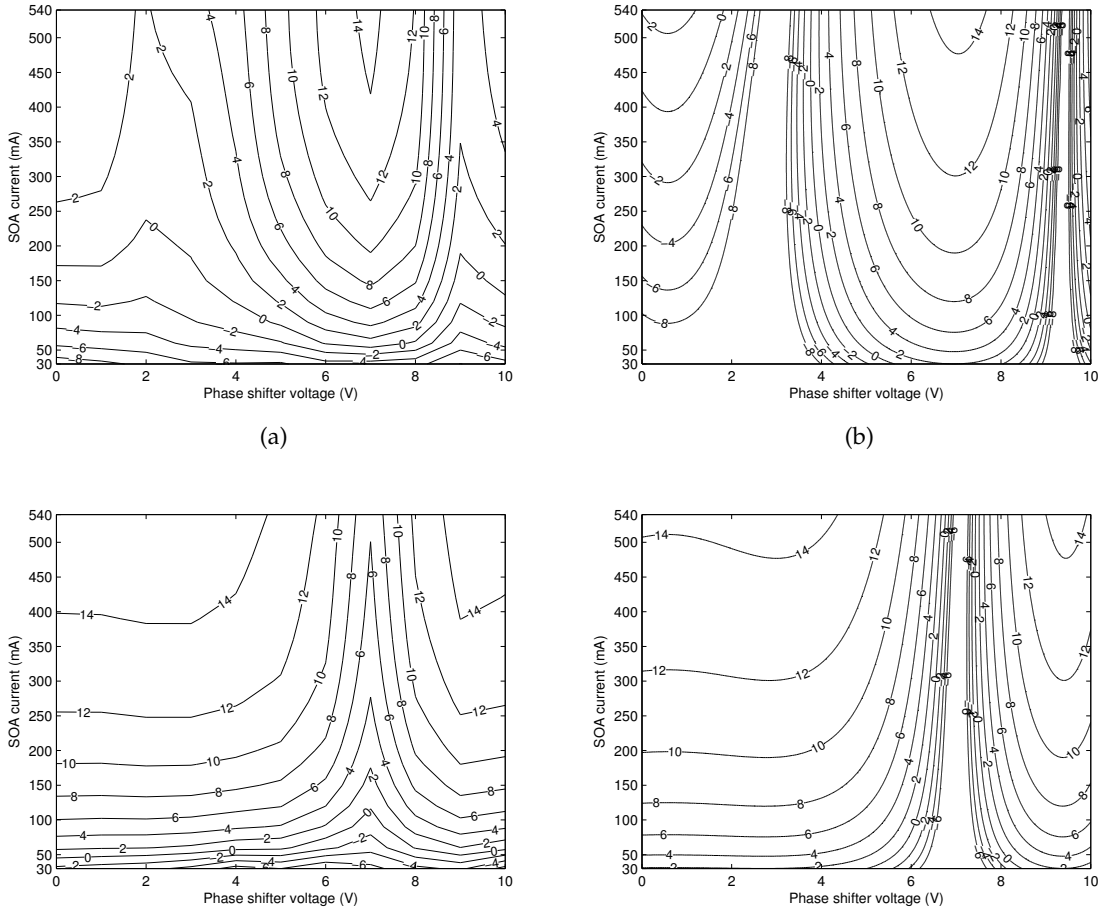

Figure 4.8: MZI-SOA output power, in dBm, as a function of bias current and phase shifter voltage: (a) and (c) are experimental measurements for output ports #I and #J, respectively; (b) and (d) are the corresponding modeled data using MOGA for output ports #I and #J, respectively. Each phase shifter voltage varies between 0 and 10 V and bias current between 0 and 540 mA.

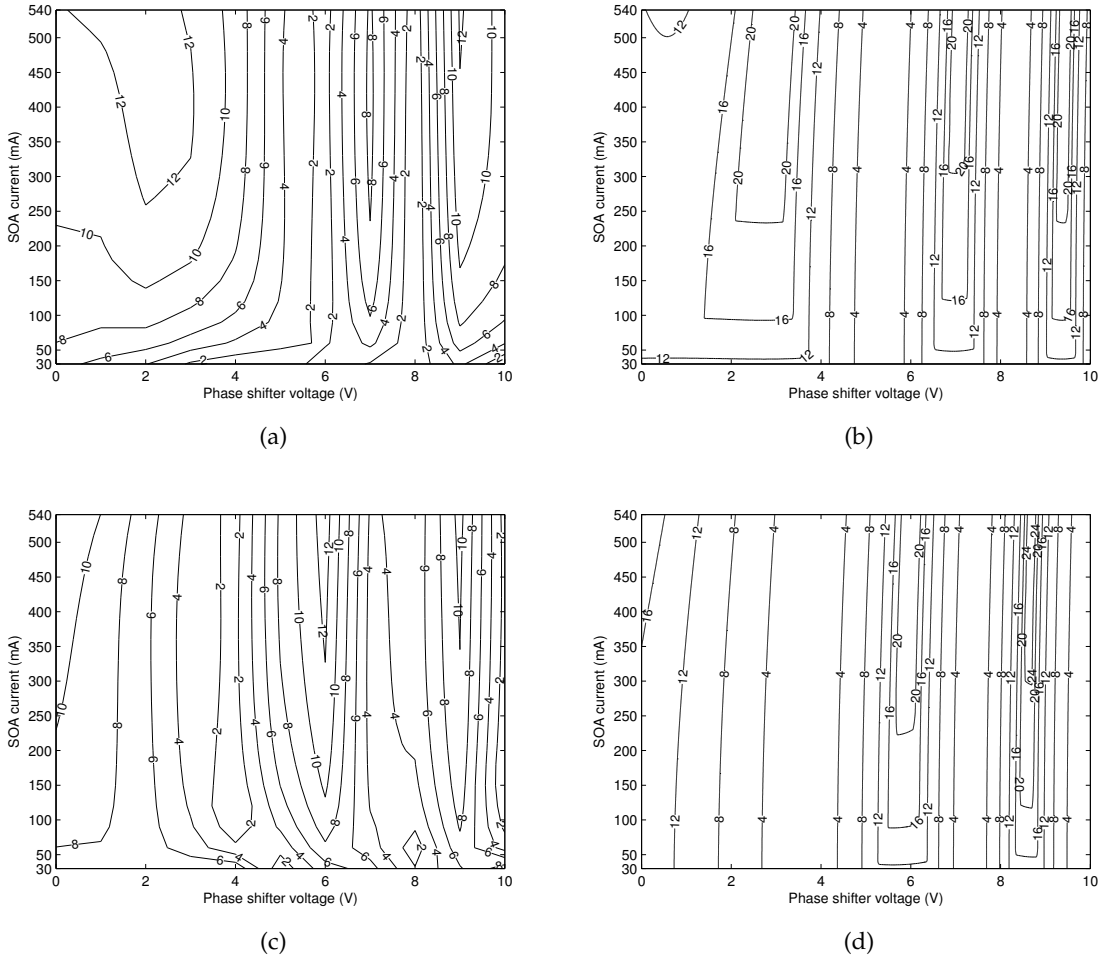

Figure 4.9: ER, in dB, between MZI-SOA output ports, as a function of bias current and phase shifters voltage: (a) and (c) are experimental measurements when varying V_{PS1} and V_{PS2}, respectively; (b) and (d) are the corresponding modeled data using MOGA when varying V_{PS1} and V_{PS2}, respectively. Phase shifters voltage varies between 0 and 10 V and SOAs bias current varies between 0 and 540 mA.

4.8 Conclusions

This chapter has presented a black box static model of a MZI-SOA, based on a set of functions and a methodology for evaluating the MZI-SOA relevant factors, based on external power measurements only (See Chapter 3) with a single CW laser. Optimization of performance and determination of operational limits are enabled by the proposed methodology and good agreement was obtained between simulated and experimental results using MOGA. The proposed process allows the user to quickly and effectively find the optimal operating point for maximal ER between output ports, or any other specific target.

This model may reduce the time need to setup the operational parameters of an MZI-SOA, since most of these biasing points require very long and difficult initial setup phase, which varies from device to device, due to their internal fabrication yields.

References

[1] J. P. Wang, B. S. Robinson, S. J. Savage, S. A. Hamilton, E. P. Ippen, R. Mu, H. Wang, J. Sarathy, and B. B. Stefanov, "Efficient performance optimization of SOA-MZI devices," *Opt. Express*, vol. 16, no. 5, pp. 3288–3292, Mar 2008. [Online]. Available: http://www.opticsexpress.org/abstract.cfm?URI=oe-16-5-3288

[2] N. K. Dutta and Q. Wang, *Semiconductor Optical Amplifier*. Singapore: World Scientific Publishing, 2006.

[3] D. E. Goldberg, *Genetic Algorithms in Search, Optimization and Machine Learning*, 1st ed. Boston, MA, USA: Addison-Wesley Longman Publishing Co., Inc., 1989.

[4] K. F. Man, K. S. Tang, and S. Kwong, *Genetic Algorithms: Concepts and Designs with Disk*, 2nd ed., M. Johnson and M. Grimble, Eds. Secaucus, NJ, USA: Springer-Verlag New York, Inc., 1999.

[5] C. Coello, G. Lamont, and D. Van Veldhuisen, *Evolutionary Algorithms for Solving Multi-Objective Problems*, ser. Genetic and Evolutionary Computation Series. Springer, 2007. [Online]. Available: http://books.google.pt/books?id=rXIuAMw3lGAC

[6] S. Luke, *Essentials of Metaheuristics*. Lulu, 2009. [Online]. Available: http://cs.gmu.edu/$\sim$sean/book/metaheuristics/

[7] L. Ingber, "Simulated annealing: Practice versus theory," *Mathematical and Computer Modelling*, vol. 18, no. 11, pp. 29–57, 1993.

[8] R. Poli, W. B. Langdon, and N. F. McPhee, *A field guide to genetic programming (1st ed.)*, March 2008. [Online]. Available: http://www.gp-field-guide.org.uk

[9] K. Deb, A. Pratap, S. Agarwal, and T. Meyarivan, "A fast and elitist multiobjective genetic algorithm: Nsga-ii," *Evolutionary Computation, IEEE Transactions on*, vol. 6, no. 2, pp. 182–197, Apr 2002.

[10] J. M. Dailey and T. L. Koch, "Simple Rules for Optimizing Asymmetries in SOA-Based Mach-Zehnder Wavelength Converters," *Lightwave Technology, Journal of*, vol. 27, no. 11, pp. 1480–1488, 2009.

Chapter 5

All-Optical Format Conversion Techniques

5.1 Introduction

Nowadays, advanced modulation formats are required to increase the capacity of optical channels through increased spectral efficiency. Also important is to maintain the traffic in the optical domain, when passing through a switch or router. All-optical signal processing is a promising technique to avoid optical-to-electrical and electrical-to-optical converters. For all-optical networks to become viable, there will be a need for other all-optical signal processing techniques such as wavelength conversion, optical label processing and modulation format conversion.

This Chapter present two different techniques to convert NRZ-OOK signal into more advanced modulation format, where the phase and the amplitude of the signal are both taking part of the modulation process. The first techniques will explain and present an all-optical modulation format conversion system, from OOK to Quasi-CPM QPSK, based on two MZI-SOA in a serial configuration. Furthermore, we will show the feasibility of the conversion from NRZ-OOK to Quasi-CPM experimentally, and discuss the limitations and future evolution of the proposed scheme [1].

The second part will study and present a study of a setup using MZI-SOA in a parallel configuration, for all-optical conversion of signals from OOK into QPSK and m-QAM. Several impairments will be numerically evaluated and the setup will be experimentally demonstrated.

5.2 Format Conversion from OOK to Continuous Phase QPSK Modulation

So far, several methods for all-optical format conversion have been investigated using MZI-SOAs: They are compact devices, with low-power consumptions and capable of 3R-regeneration. All-optical conversion from NRZ-OOK to RZ-BPSK [2] and more recently Return-to-Zero Quadrature Phase Shift Keying (RZ-QPSK) [3, 4] were proposed and experimentally demonstrated, by using MZI-SOAs with different architectures. However, a linear modulation like QPSK does not transmit at constant intensity. On symbol transitions of 180°, the signal crosses through nearly zero intensity. The RZ pulse carving function ensures that all symbol transitions go through the amplitude null. The resulting fluctuations in intensity leads to SPM and XPM in single and multiple channel fibre transmission, respectively, and limit the allowed transmit power of RZ-QPSK systems.

Continuous Phase Modulation (CPM) is a format with constant amplitude and continuous phase. Gaussian Minimum Shift Keying (GMSK) is a special case of CPM that as been used in practical wireless communication systems. Recently, 80 Gb/s optical MSK generation was experimentally demonstrated in [5]. With proper choice of pulse shapes and other parameters, CPM schemes may achieve higher bandwidth efficiency than QPSK and higher order M-ary Phase Shift Keying (M-PSK) schemes [6]. Recent studies and simulations have quantified the potential benefits of CPM over QPSK for optical fibre transmissions [7].

5.2.1 Principle of OOK to Quasi-CPM conversion

Figure 5.1 presents the diagram of the proposed modulation format conversion. The central element is a MZI-SOA configured as an XOR gate. NRZ-OOK sequence_{AD} (signal I) with wavelength λ_0 is launched simultaneously into ports #A and #D, and a CW signal at wavelength λ_1 is launched in port #B. In both SOAs, the carrier density is changed according to the amplitude of the data sequence, and the phase and amplitude of the CW signal λ_1 after passing both SOAs are changed due to XPM and XGM, respectively. By properly setting the input optical powers, phase shifters voltage and controlling the SOA bias currents, signal λ_1 from the two SOAs interferes constructively in one port and destructively in the other, according to the XOR operation. From the destructive output, signal λ_1 presents minimal power variations and has a phase of 0° or 180° corresponding to 0 or 1 of the NRZ-OOK sequence_{AD}, as we have experimentally verified in Chapter 3 [8]. The second stage of the modulator is similar to the first, but now the signal coming from MZI-SOA1 is launched into MZI-SOA2 with an assist CW signal λ_2. NRZ-OOK sequence_{EH} (signal Q) with wavelength λ_0 is launched simultaneously into port #E and #H. Operational parameters of MZI-SOA2 are adjusted to produce on signal λ_1 an additional phase shift of 0° or 90°, corresponding to 0 or 1 of the NRZ-OOK sequence_{EH}. After passing MZI-SOA2 destructive output and bandpass filter, the phase of signal λ_1 is continuously modulated between four different values (0°, 90°, 180° and 270°), depending on the combination of NRZ-OOK sequence_{AD} and sequence_{EH}, combined with reduced power variations. Therefore, NRZ-OOK signals can be converted to a Quasi-CPM (below 360°) signal. Table 5.1 show the truth table of the conversion system, considering sequence_{AD} and sequence_{EH} input binary data.

Table 5.1: Phase value at output port #L as a function of sequence_{AD} and sequence_{EH} logical values combination.

sequence_{AD}	0	1	0	1
sequence_{EH}	0	0	1	1
Output Phase	0°	180°	270°	90°

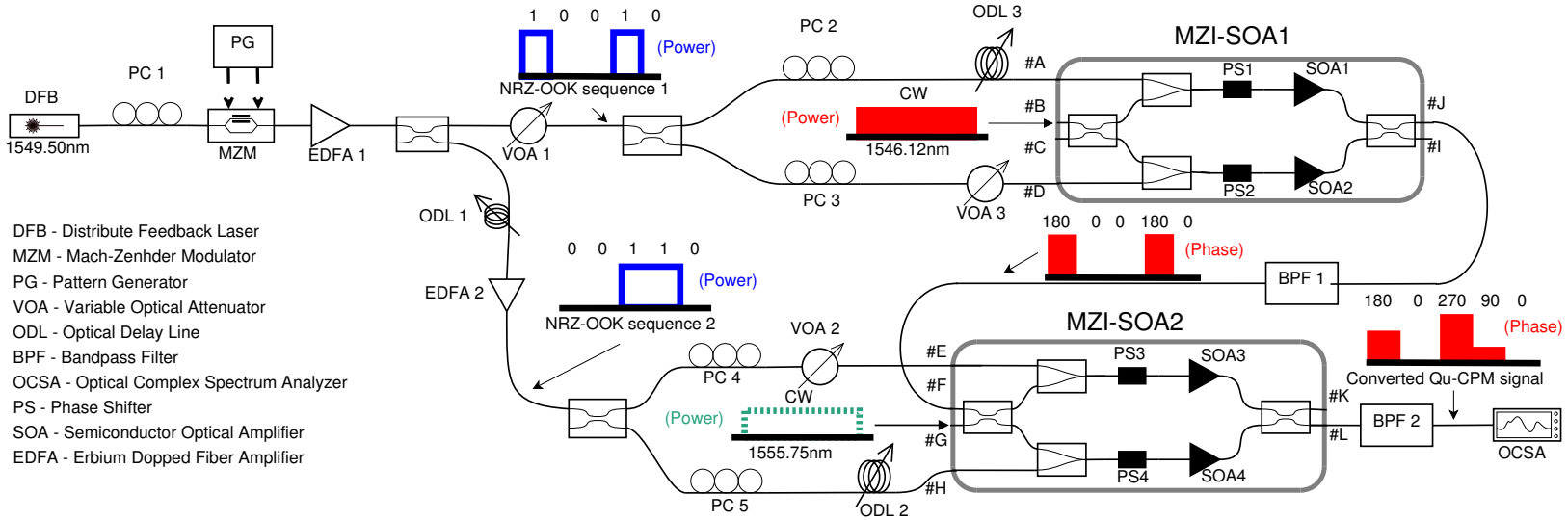

Figure 5.1: Experimental setup and examples of optical signals along the modulator.

5.2.2 Experiments and results

From the experimental setup depicted in Figure 5.1, a CW laser at 1546.12 nm (λ_1) is applied at the input #B of MZI-SOA1 with an average power of -1 dBm. A 10 Gb/s NRZ-OOK signal is generated at wavelength 1549.50 nm (λ_2). Due to functional limitations imposed by the OCSA used as a coherent receiver, the length's data sequence is restricted to 16 bits (See Appendix A for further details on the OCSA operation). NRZ-OOK signal is first amplified by an EDFA (EDFA1) then split by two 50 % couplers on four signals. The first two NRZ-OOK signals are applied to MZI-SOA1 arms #A and #D, and the next two NRZ-OOK signals are first synchronized with the filtered output signal of MZI-SOA1, and then applied to MZI-SOA2 arms #E and #H. The time delay inside MZI-SOA1 (between inputs #A/#D and output #J) was measured and is equal to 32 ps. considering additional delays imposed by the fiber patch cords and BPF1, the delay between input #E (#H) and input #F of MZI-SOA2 was set to 3 bits (300 ps) using ODL1. Both pairs of NRZ-OOK signals, before launch on MZI-SOA input arms, are firstly synchronized between them by ODLs (ODL3 and ODL2), adjusted by Variable Optical Attenuators (VOAs) (VOA3 and VOA2) to the appropriate average power to maintain the SOAs saturated, and their polarization optimized by PCs. According to the values obtained with MZI-SOA static model presented in Chapter 4, mean power is set to 1.5 dBm at inputs #A and #D, 1.0 dBm at input #H and 1.8 dBm at input #E, for optimum ER at the output ports of both MZI-SOAs. An assist CW light at 1555.75 nm (λ_3) is launched into port #F with 10 dBm to suppress the rapid change of carriers in SOA3 and SOA4, which induces frequency chirp and amplitude fluctuations [2]. The signal after both MZI-SOAs is filtered with narrow optical band-pass filters (BPF1 and BPF2), centered at λ_1, to eliminate the optical channel used for NRZ-OOK signal generation (λ_2) and the assist wavelength (λ_3).

Operational parameters values for each MZI-SOA (Phase shifter voltage, SOA bias current) are also set after the MZI-SOA static model described in Chapter 4. SOAs bias currents are: $I_{SOA1} = 200$ mA, $I_{SOA2} = 242$ mA, $I_{SOA3} = 280$ mA and $I_{SOA4} = 200$ mA. For the phase shifters, the voltage are set to $V_{PS1} = 0.0$ V, $V_{PS2} = 9.7$ V, $V_{PS3} = 6.2$ V and $V_{PS4} = 0.0$ V.

As an example, we start to analyze the behavior of the conversion system, by using a simple 16 input sequence, '0000100100000000'. Table 5.2 present the expected output phase sequence.

Table 5.2: Phase value at output port #L as a function of the combination of sequence$_{AD}$ '0000100100000000' and a replica delayed by 3 bits (sequence$_{EH}$).

seq.$_{AD}$	0	0	0	0	1	0	0	1	0	0	0	0	0	0	0	0
seq.$_{EH}$	0	0	0	0	0	0	0	1	0	0	1	0	0	0	0	0
Phase	0°	0°	0°	0°	180°	0°	0°	90°	0°	0°	270°	0°	0°	0°	0°	0°

Table 5.3: SOA parameters for the dynamic simulation of the MZI-SOA

Name	Value	Unit
Section Length	2.53×10^{-4}	m
Section Width	1.5×10^{-6}	m
Section Thickness	100×10^{-9}	m
Group Effective Index	3.7	-
Internal Loss	4000	$1/\mathrm{m}$
Confinement Factor	0.3	-
Facet Reflectivity	0.001	-
Linear Recombination	5.0×10^{7}	$1/\mathrm{s}$
Bimolecular Recombination	1.0×10^{-16}	m^3/s
Auger Recombination	7.5×10^{-41}	m^6/s
Initial Carrier Density	1.0×10^{-12}	$1/\mathrm{m}^3$
Gain Coefficient Linear	13.5×10^{-20}	m^2
Carrier Density at Transparency	1.5×10^{-12}	$1/\mathrm{m}^3$
Linewidth Factor	3.0	-
Differential Index	-1.0×10^{-26}	m^3

Experimental analysis is provided in back-to-back to measure the feasibility of phase modulation after each MZI-SOA. We start by analyzing each MZI-SOA individually, with a similar setup as the one described in Chapter 3 and depicted in Figure 3.17. VPI Transmission Maker program (from now on called simply VPI) [9] is the software tool used for simulation of the dynamic process involved in the format conversion conversion setup. VPI uses a transmission line model of a SOA from which we create a MZI-SOA interferometer. SOA parameters were based on the ones used by Sun *et al* [10] and they are illustrated in Table 5.3.

Figure 5.2 shows the signals along the setup with MZI-SOA1. The phase (Figure 5.2f) and power (Figure 5.2d) at port #J follows the variations of the input NRZ-OOK signal (Figure 5.2b), and the constellation clearly identifies a binary phase modulation process with 180°

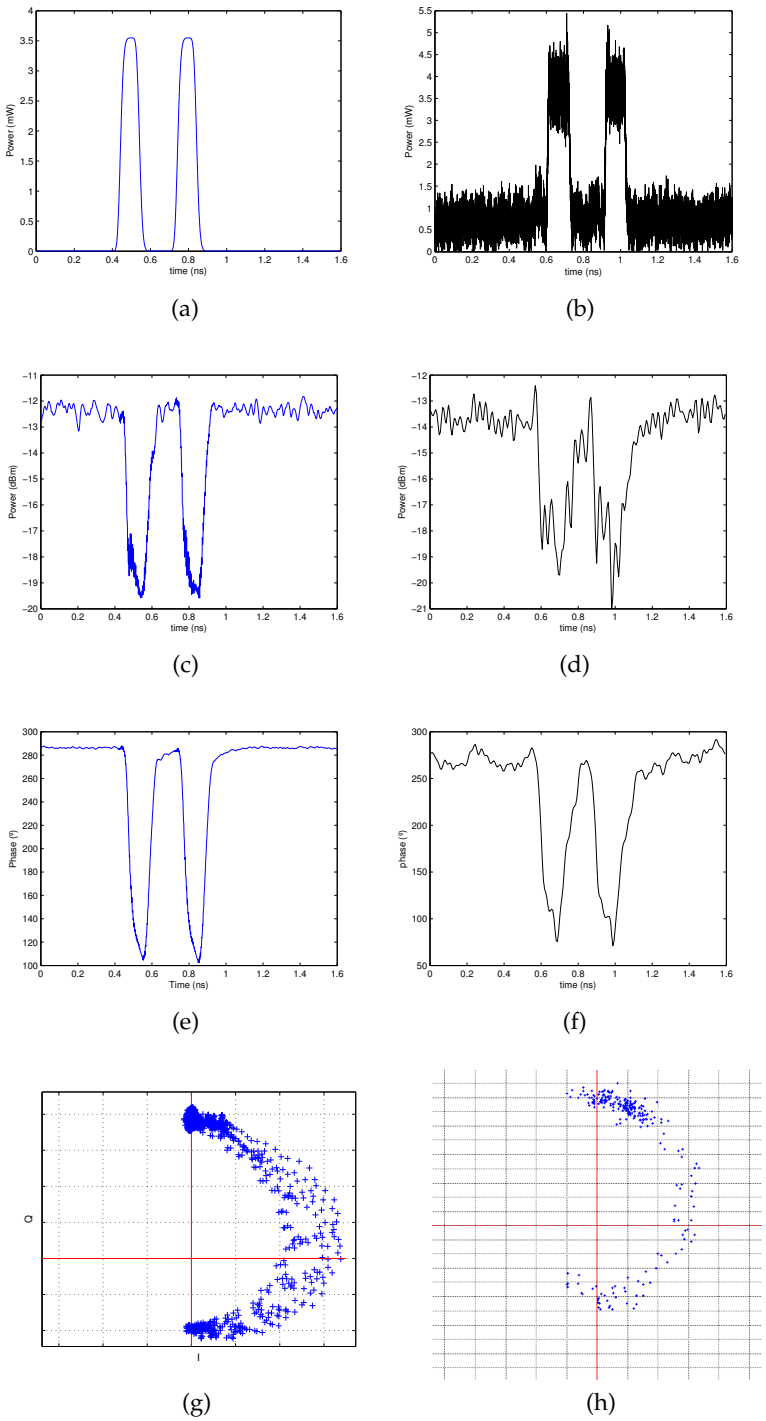

Figure 5.2: MZI-SOA1 output signal. Left column: Simulations results using VPI; Right column: Experimental measurements. (a), (b): input sequence; (c), (d): Output power; (e), (f): Output phase; (g), (h): constellation diagram.

shift (Figure 5.2h) between logical 1 and 0. We also observe a good agreement between simulated and experimental results in all stages on the conversion process. A similar analysis follows when we study the behavior of the phase conversion using MZI-SOA2. According to the experimental results, the phase (Figure 5.3d) of the output signal at port #L, follows the variations of the input signal (the same signal represented in Figure 5.2b but not shown here) with 90° phase shift between logical values. Output power (Figure 5.3b) remains relatively low since port #L is configured as the destructive output. Also here, simulation and experimental results are in agreement.

When combining both MZI-SOA according to the setup of Figure 5.1, the experimental measurements at the output port are presented in Figure 5.4.

Twelve different NRZ-OOK sequences each with 16 bits were used and appropriately chosen to produce an even number of phase's symbols at the Quasi-CPM signal. Since the optical measurement device allows only 16 bits length sequences, we need to choose appropriate sequences, that combined with a replica delayed by 3 bit, should produce an experimental constellation diagram with an equal distribution of constellation points. The Matlab code used to find those sequeces is presented in Appendix C.

Figure 5.5a shows the phase eye diagram with a clear opening and 180° span, and Figure 5.5b the spectra for converted signal from MZI-SOA1 output. Mean power of MZI-SOA1 output is 0.096 mW (-10 dBm) with standard deviation between 0.048 mW and 0.082 mW.

Figure 5.6a shows the phase eye pattern from MZI-SOA2 output, where 4 distinct phases are distinguishable and Figure 5.6b the optical spectrum of the converted signal. Due to non-optimal settings for MZI-SOA operational parameters, spectrum is asymmetrical and phase levels are not evenly spaced by 90°, closing the eye between 90° and 180°. Mean power for all 12 sequences is 0.43 mW (-3.61 dBm) with standard deviation between 0.1 mW and 0.15 mW.

The constellation diagram in Figure 5.7 is impaired by I-Q imbalance (uneven axial distance between symbols) and quadrature errors (different radial distances between symbols and constellation centre), due to non-optimal settings. However, CPM behavior is evident from the signal path generated, and validates the proposed setup.

As a summary for this section, we have proposed, numerically and experimentally evaluated an all-optical format conversion from NRZ-OOK to Quasi-CPM using cascaded MZI-SOAs. We have observed an eye opening of the converted signal with four distinct phase levels at 10 Gbaud, with good agreement between simulation and measurements.

5.3 Format Conversion from OOK to QPSK and QAM Modulation

Traditional intensity modulated with direct detection formats show reduced spectral efficiency and are inadequate for high capacity WDM applications. To transmit data at 100 Gb/s/channel and beyond, even more advanced modulation formats, such as coherently detected, polarization multiplexed QPSK [11], multilevel QAM [12], and OFDM [13] are required. The use of advanced modulation formats allows increasing the bit rate of each channel without increasing significantly the spectral width of the transmitted signal.

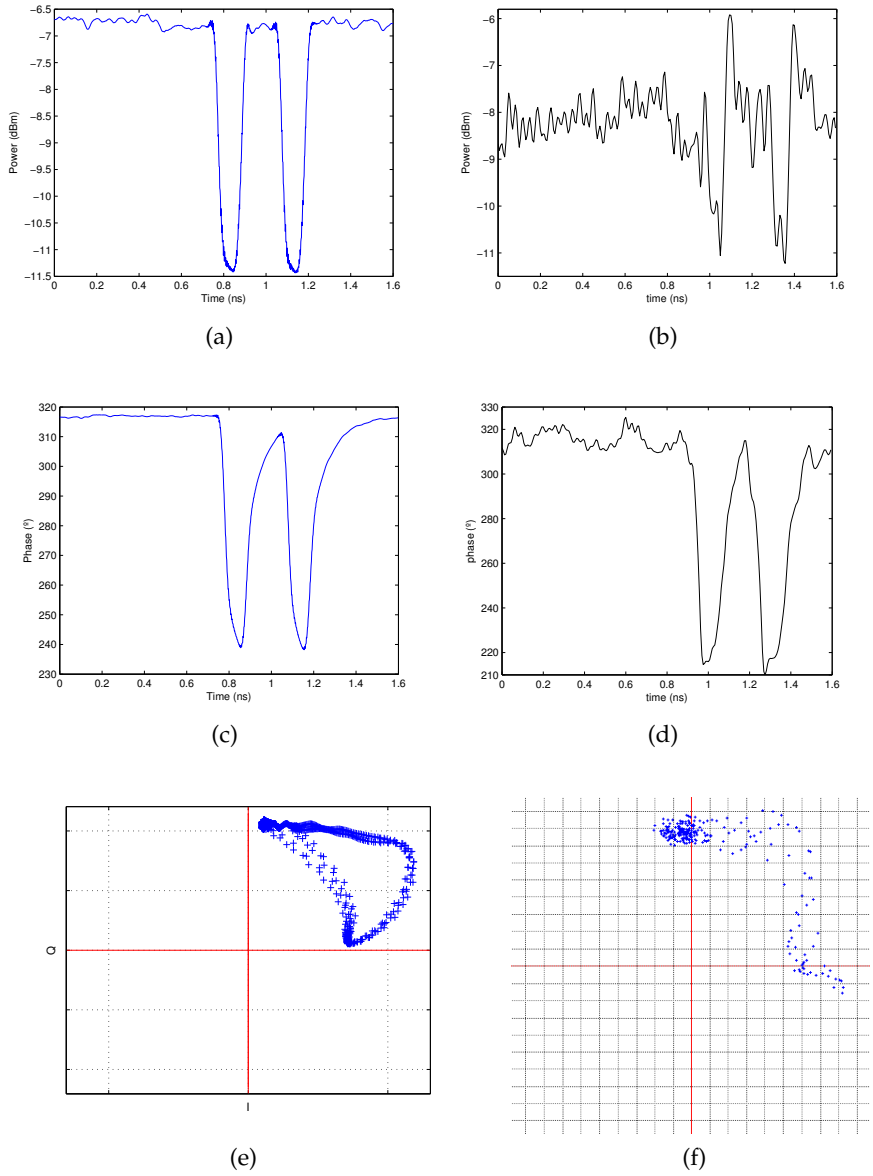

Figure 5.3: Standalone MZI-SOA2 output signal. Left column shows simulations results and right column experimental measurements. (a), (b): power; (c), (d): phase; (e), (f): constellation.

.

This allows using tight channel spacing and, consequently, increasing the capacity of a link. By using coherent detection, the amplitude, phase and state of polarization of the received signal are assessable. Thus, a much "smarter" receiver may be implemented using an advanced digital signal processing, thus overcoming many of the transmission impairments.

Both PSK and QAM offers comparable theoretical bandwidth efficiencies for a small number of symbols ($M \leq 8$) [14]. However, as M increases, QAM is less vulnerable to

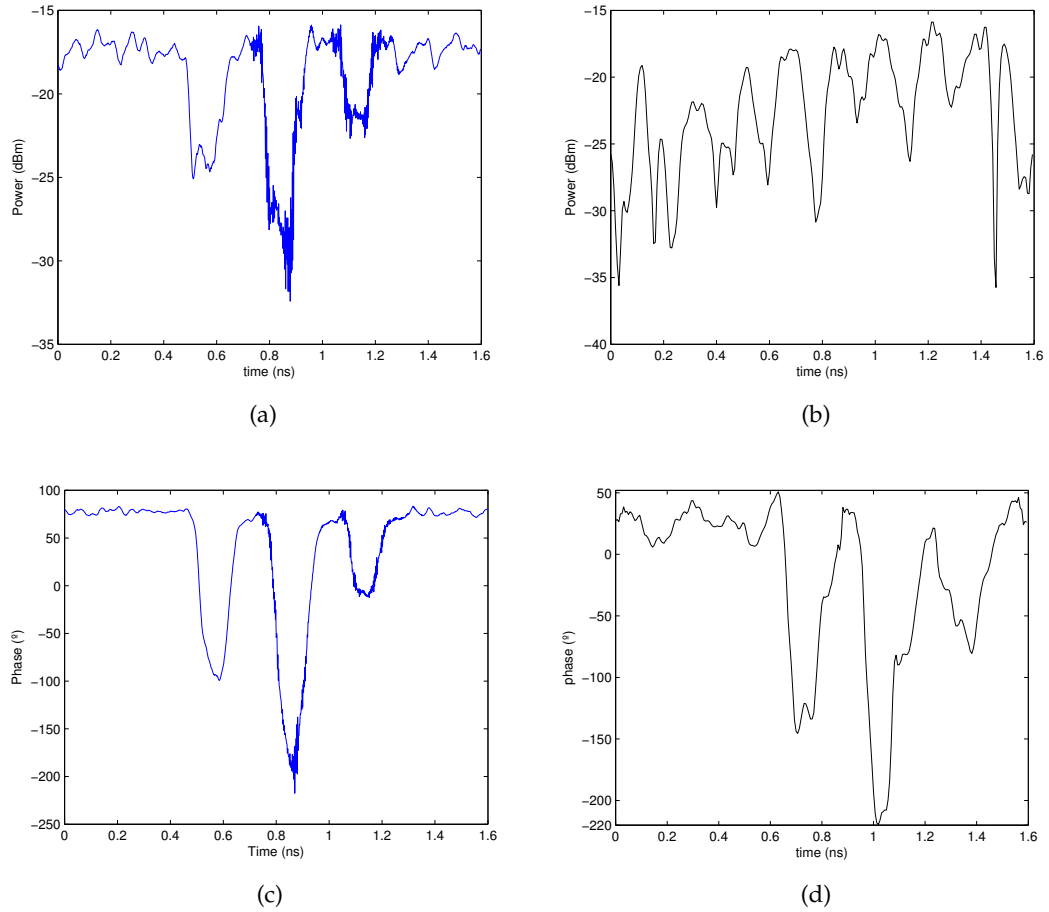

Figure 5.4: Cascaded MZI-SOA1 and MZI-SOA2 output signal. Left column shows simulations results and right column experimental measurements. (a), (b): power; (c), (d): phase.

.

channel impairments like amplitude and phase distortion. This is fundamentally related to the larger Euclidean distance d between points in the QAM signal constellation, for the same alphabet. Several generation schemes for multilevel QAM were proposed in [12], adjusting the number of modulation levels by adding an extra MZM or PMod in serial or parallel configurations. However, complex electrical control of this generation schemes is requested.

In the past two decades, particularly with the development of digital signal processing, several post-detection techniques have been able to overcome these obstacles, through the use of coherent detection systems. Once this receiver maps both amplitude and phase of the optical electric field in the electrical domain, it is possible, using appropriate subsystems and algorithms incorporated in the receiver, to compensate several imperfections associated to transmission [15].

In this section, we investigate the feasibility to generate 16-QAM and 64-QAM signals, using an all-optical method with reduced electrical complexity. We describe the structure

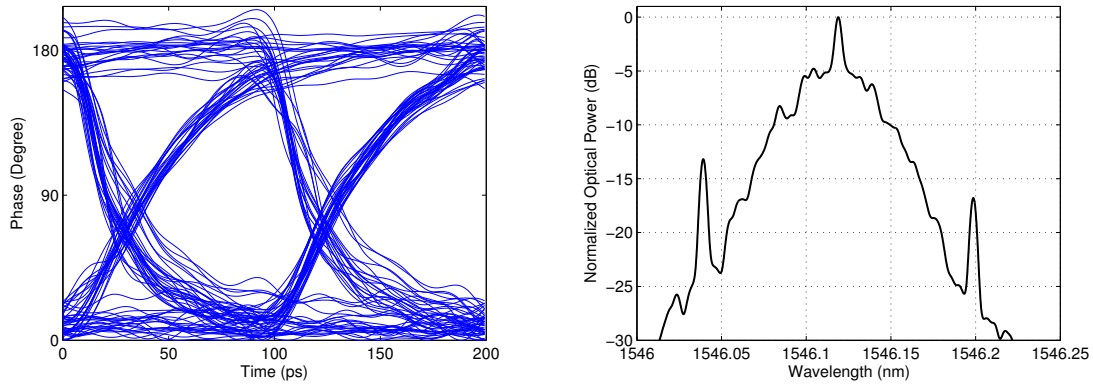

(a) (b)

Figure 5.5: MZI-SOA1 output signal measurements: (a) Phase eye diagram and (b) power spectrum.

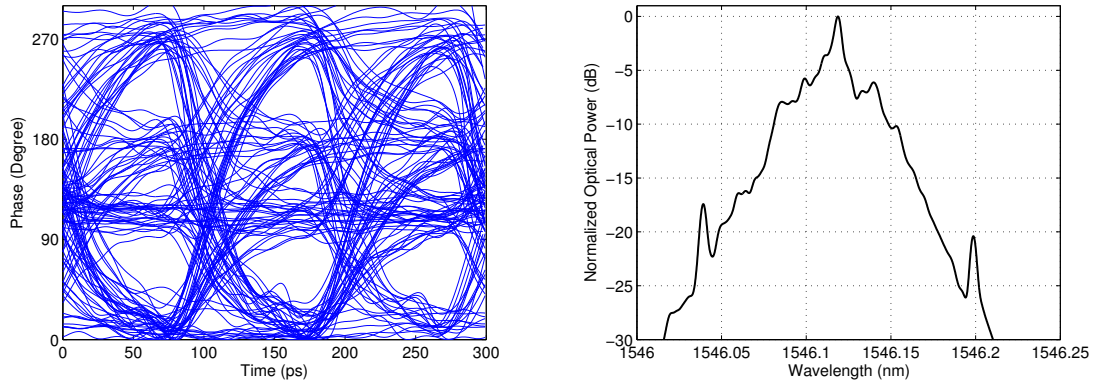

(a) (b)

Figure 5.6: MZI-SOA2 output signal measurements: (a) Phase eye diagram and (b) power spectrum.

of the system and the principle of operation. We continue with the simulation setup, the analysis and discussion on the influence of operational parameters mismatch on the overall performance of the system. We also present the experimental results attained with QPSK generation.

5.3.1 Principle of OOK to QAM and QPSK Conversion

The modulation format converter follows the structure proposed in [3]. The configuration consists of an interferometric structure, with one MZI-SOA in each arm. Figure 5.8 shows the corresponding diagram. A group of N NRZ-OOK data sequences, with wavelengths $\lambda_1 - \lambda_N$, are first multiplexed and injected into port #A of MZI-SOA1. A similar operation is carried out in the lower arm, where Z different NRZ-OOK data

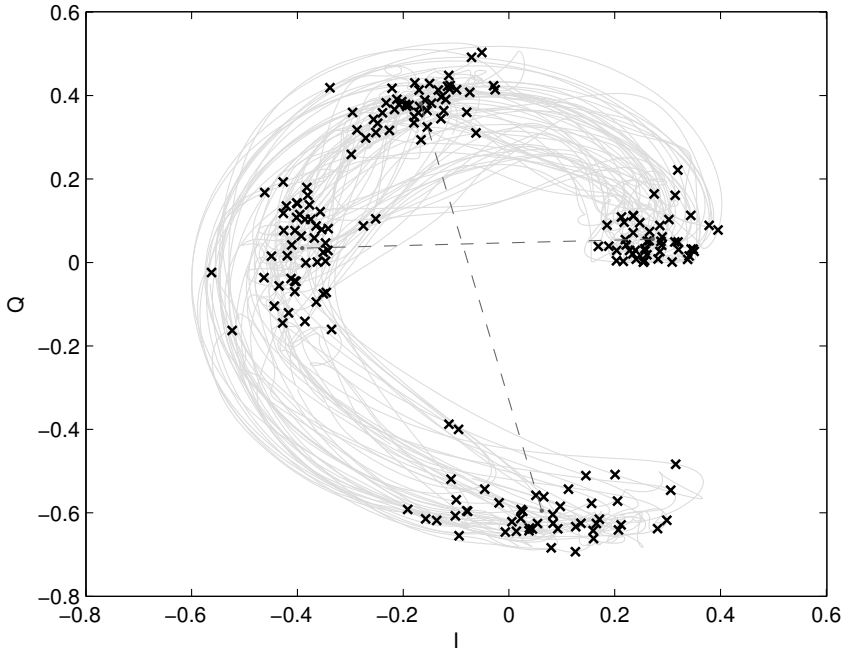

Figure 5.7: Measured Quasi-CPM signal constellation, with path lines and sampled symbols (black crosses). Dashed lines shows quadrature imbalance of the constellation.

sequences ($Z \leq N$) are multiplexed and injected in port #D of MZI-SOA2. Both MZI-SOA1 and MZI-SOA2 are also fed with a CW laser source with wavelength λ_0, at ports #B and #C, respectively. Through XPM in SOAs [16], each MZI-SOA converts the multiplexed signal at the input, to a multi-level multi-phase signal with wavelength λ_0 at the output. Inside COUPLER2, both signals are rotated by $\pi/2$ against each other and combined to produce a multi-level multi-phase signal (QPSK or QAM). The number of symbols of the output signal is proportional to the number of NRZ-OOK data sequences at the input,

$$M = 2^{N+Z} \tag{5.1}$$

An Optical BPF, centered in λ_0, removes all unwanted wavelength from COUPLER2 output. Finally, both I and Q components of the signal are recovered with a coherent receiver. Due to its importance, the coherent receiver is described in more detail in the following section.

Coherent receiver

The resulting signals from the all-optical conversion system are analyzed with a OCSA for spectral analysis, and a coherent receiver. A diagram of the coherent receiver is shown in Figure 5.9. The received optical signal, having an arbitrary state of polarization, is separated into two linear polarizations by a Polarization Beam Splitter (PBS). Through a 90° Optical

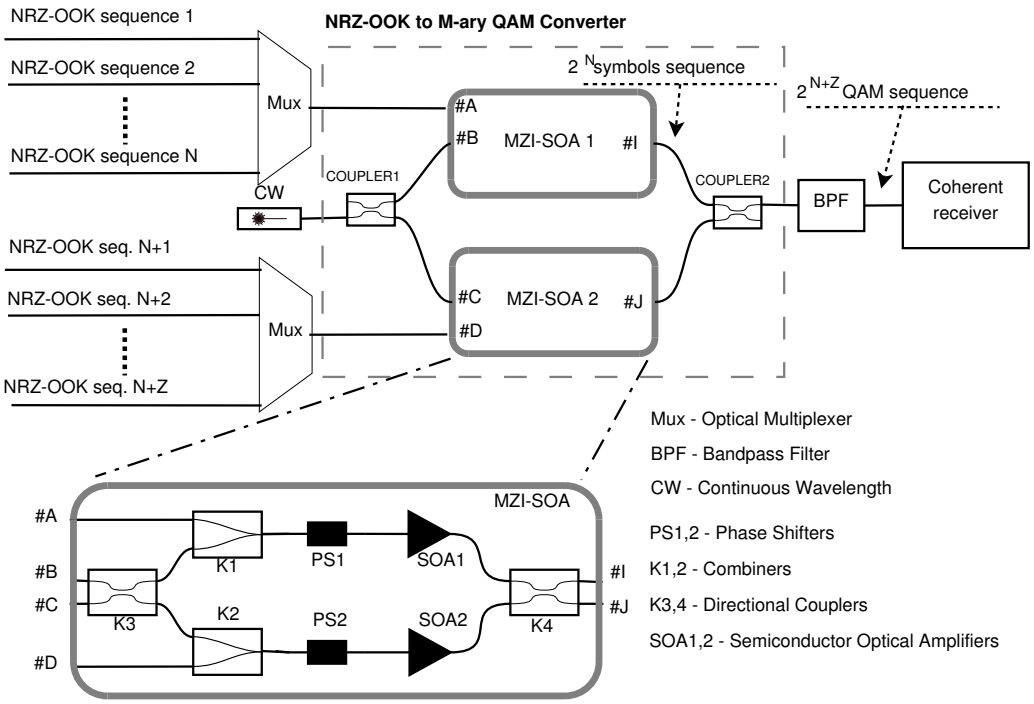

Figure 5.8: Setup diagram of the format converter. The MZI-SOA internal structure is also shown.

Hybrid, the signal is mixed with the local oscillator, giving rise to the components:

$$E_{1,2} = \frac{1}{2}\left(E_{SX} + \frac{1}{\sqrt{2}}E_{LO}\right) \tag{5.2}$$

$$E_{3,4} = \frac{1}{2}\left(E_{SX} + \frac{j}{\sqrt{2}}E_{LO}\right) \tag{5.3}$$

$$E_{5,6} = \frac{1}{2}\left(E_{SY} + \frac{1}{\sqrt{2}}E_{LO}\right) \tag{5.4}$$

$$E_{7,8} = \frac{1}{2}\left(E_{SY} + \frac{j}{\sqrt{2}}E_{LO}\right) \tag{5.5}$$

where E_{SX} and E_{SY} are the two orthogonal received electric fields (divided by PBS), corresponding to X and Y polarization, respectively, and E_{LO} is the electric field of the local oscillator. The output photocurrents are:

$$I_{PD_1}(t) = R\sqrt{\frac{k_r P_r P_{LO}}{2}} cos\left(\theta_r(t) - \theta_{LO}(t) + \delta\right) \tag{5.6}$$

$$I_{PD_2}(t) = R\sqrt{\frac{k_r P_r P_{LO}}{2}} sin\left(\theta_r(t) - \theta_{LO}(t) + \delta\right) \tag{5.7}$$

$$I_{PD_3}(t) = R\sqrt{\frac{(1-k_r) P_r P_{LO}}{2}} cos\left(\theta_r(t) - \theta_{LO}(t)\right) \tag{5.8}$$

$$I_{PD_4}(t) = R\sqrt{\frac{(1-k_r) P_r P_{LO}}{2}} sin\left(\theta_r(t) - \theta_{LO}(t)\right) \tag{5.9}$$

where R is the responsivity of the photodiode, k_r is the power ratio between the two polarization components and δ is the difference between their phases. It is easy to conclude that the receiver can measure separately the complex amplitudes of the two polarization defined by [15]:

$$I_X(t) = I_{PD_1}(t) + jI_{PD_2}(t) \tag{5.10}$$

$$I_Y(t) = I_{PD_3}(t) + jI_{PD_4}(t) \tag{5.11}$$

The block diagram of the receiver system is shown in Figure 5.10. After the coherent detection, all four signals detected by the receiver ((5.6) to (5.9)) are directly connected to the oscilloscope, which in this system works only as an Analog to Digital Conversion (ADC) system, i.e., it only digitizes the signal with a specific sampling rate and sends the data to a computer through an ethernet communication for post processing. An application developed with Matlab [17] controls the oscilloscope settings, such as the sampling rate, the record length or channel settings. From a DSP point of view, the application also performs five tasks on the received signal:

- Filter: low-pass or band-pass filter: Butterworth, Bessel or Chebyshev. The filter order and the cut frequency can be selected.
- Normalization, Orthogonalization and Resampling: In this block a signal conditioning is realized. Resampling is only used to adjust the sampling rate of the oscilloscope to the data rate of the consecutive digital signal processing algorithms [15]. Before the signal equalization, the sampling frequency (when it is high) may be reduced up to 1.5 samples per symbol, limit imposed to a correct equalization [18]. In order to recover the original signal using a receiver with a suboptimal hybrid, it is also used the GramÐ Schmidt orthogonalization algorithm described in [15].

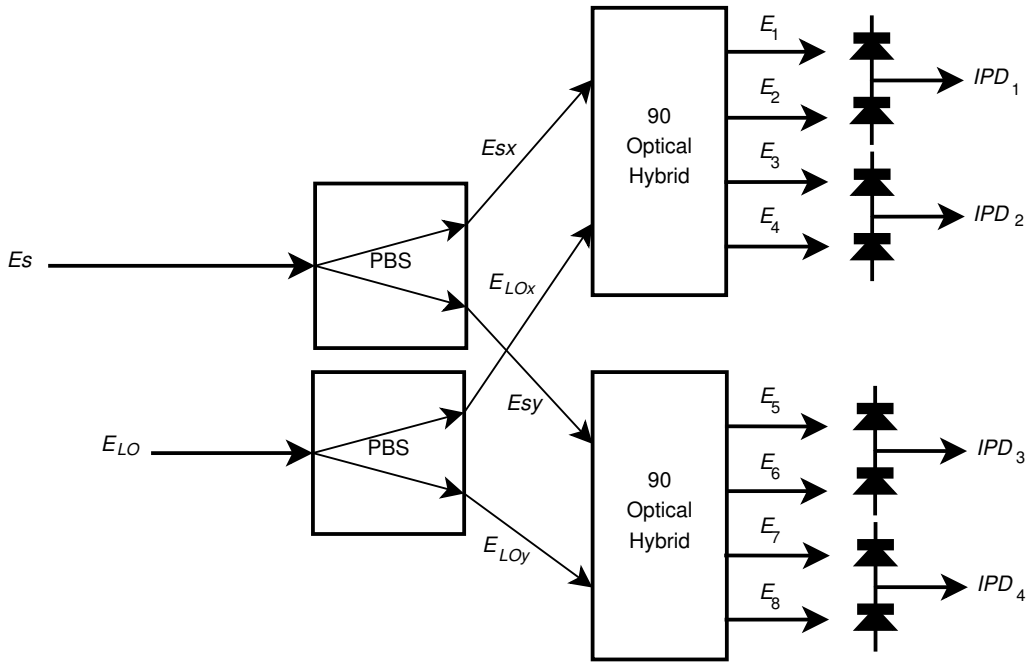

Figure 5.9: Coherent receiver with phase and polarization diversity.

- Equalization: The equalization of the signal consists of chromatic dispersion compensation, in particular by Time Domain or Frequency Domain Equalizer method (described respectively in [19] and [20]), and the Constant Modulus Algorithm equalizer, which reduce Inter Symbol Interference (ISI). The description of this algorithm can be seen in [15, 21].
- Phase Recovery: This block performs phase recovery using a Viterbi and Viterbi algorithm with phase unwrapping, described in [15]. This algorithm can compensate some frequency shift occurred between the received signal and the local oscillator (often due to poor control in frequency of lasers) and laser phase noise variation over the time. Maximum performance in this algorithm is important to avoid signal transitions. To discard the transitions, the signal is resampled, detecting the clock of the received signal through a signal's derivative. The signal resampling is done in the middle of the symbol's time slot.
- Measurements: This module performs several performance measures and analyzes the signal, such as EVM, BER, Quadrature Skew or Eye Diagram measurements.

5.3.2 Simulation Setup

Description

VPI TransmissionMaker 8.5 software tool was used to simulate the proposed system, and to verify the feasibility of all-optical modulation format conversion from NRZ-OOK

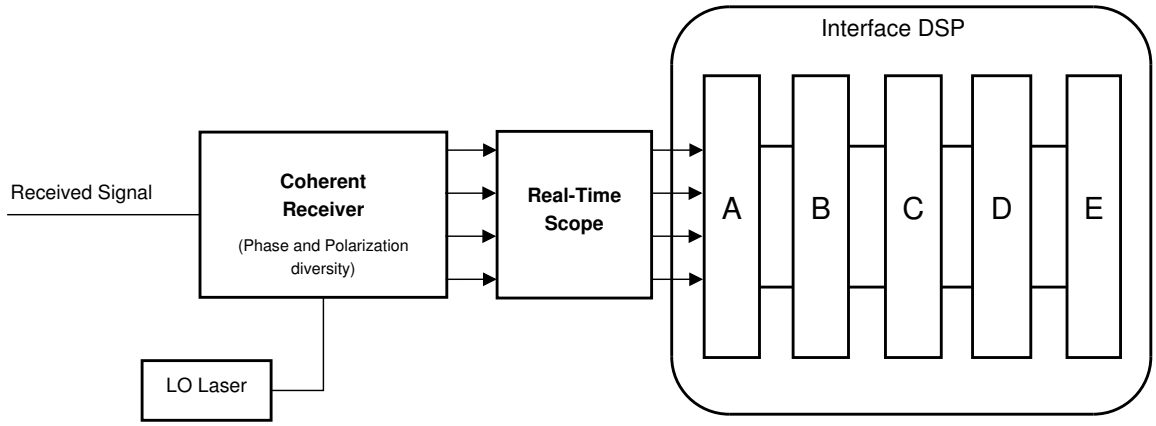

Figure 5.10: Coherent receiver and analyzer. A: Filter; B: Normalization, Orthogonalization and Resampling; C: Equalization (CD and PMD); D: Phase recovery; E: Measurements.

to QPSK, 16-QAM and 64-QAM signals.

From 5.1, four data sequences are required to generate 16-QAM signals ($N = Z = 2$). Each optical sequence is produced using a laser source and a MZM at 40 Gbps. For 64-QAM generation, an additional wavelength is used in each MZI-SOA input ($N = Z = 3$). With only one data sequence in each MZI-SOA input ($N = Z = 1$), the setup is similar to the one found in [3] for QPSK generation. SOA model physical parameters are based on a commercial device [22], with fast recovery time. Table 5.3 shows the values of the SOA parameters used in the simulation. COUPLER1, COUPLER2, and all MZI-SOAs internal couplers (K3 and K4) and combiners (K1 and K2) have coupling factor set to 0.5. BPF optical bandwidth is 120 GHz. A hybrid 90°, two pairs of balanced photodiodes for Optical to Electrical (O-E) conversion, a DC block and a sampling block (at symbol rate of 40 Gsample/s) compose the coherent receiver.

Operational Parameters Computation and Optimization

From an operational point of view, the proposed conversion system is controlled though a limited set of parameters: Laser power (P_{CW}, $P_{1,\ldots,N+Z}$) and ER ($ER_{1,\ldots,N+Z}$) are related with the optical input signals (NRZ-OOK sequences or CW laser); SOA bias current ($I_{bias_{1,2}}$) and phase shifter voltage ($V_{PS_{1,2}}$) are associated with MZI-SOA operational setup.

The methodology for the extraction of the operational parameters that satisfy a best-fit criterion is based on MOGA [1], a method already used in Chapter 4. Now, the problem considered is to minimize EVM between an ideal constellation diagram, and a simulated constellation diagram (both previously normalized). The goal is to use an efficient and accurate method capable to extract a set of operational parameters that satisfy, at the same time, the ideal constellation point for each and every modulation formats analyzed (QPSK and QAM). The variables (operational parameters of the system) considered for optimization are P_{CW}, $P_{1,\ldots,N+Z}$, $ER_{1,\ldots,N+Z}$, $I_{bias_{1,2}}$ and $V_{PS_{1,2}}$. All SOAs bias currents ($I_{bias_{1,2}}$) were set with the same value. The same criterion was also applied to the voltage ($V_{PS_{1,2}}$) of all phase

shifters.

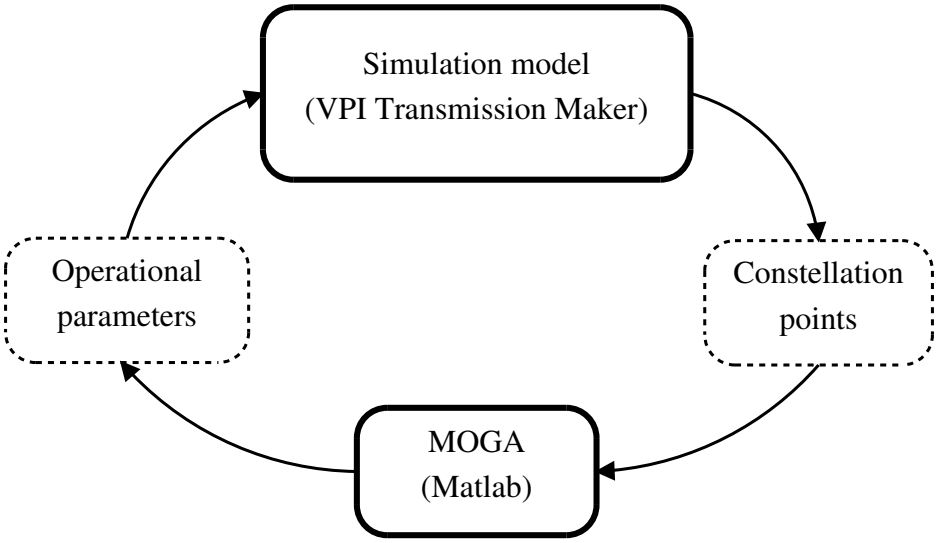

Figure 5.11: Simulation cycle to optimize the operational parameters of the all-optical conversion system.

The first iteration process starts with a initial set of operational parameters, that *VPI Transmission Maker* uses to run a simulation of the model, and returns a constellation diagram. The resulting constellation points are sent to *Matlab*. Then, MOGA is run for 50 generations, as a compromise between accuracy and simulation time [23]. MOGA run with an initial population of 200 individuals, i.e. 200 different parameter's sets. All members of the initial population are randomly generated from a seed individual, composed by a set of non-random operational parameters selected by the user (or the last computed set of operational parameters selected from the previous iteration). Upper and lower boundaries are also used, according to the physical limits of each operational parameter. Two objectives functions, F_I (5.12) and F_Q (5.13), must be minimized simultaneously to produces the best set of operational parameters and reduce the EVM between the simulated and the ideal constellation points. Each function is the RMSE between the ideal I^i (Q^i) and the simulated I^s (Q^s) cartesian coordinates of the constellation points,

$$F_I = \sqrt{\frac{1}{N_p}\sum_{k=1}^{N_p}\left(\left[I^i(k) - I^s(k)\right]^2\right)} \tag{5.12}$$

$$F_Q = \sqrt{\frac{1}{N_p}\sum_{k=1}^{N_p}\left(\left[Q^i(k) - Q^s(k)\right]^2\right)} \tag{5.13}$$

Where N_p is the number of data points used in the fitting process. From the resulting Pareto

front and the corresponding candidate solutions, the best solution is chosen by finding, between all candidate solutions, the one with the lower mean value between F_I and F_Q,

$$F_P = min\left\{\frac{F_I + F_Q}{2}\right\} \tag{5.14}$$

From the result of (5.14), the best operational parameters set is sent back to *VPI Transmission Maker*, and the process is repeated in the next iteration. The simulation cycle stops when a minimum EVM between the output constellation and the ideal constellation is attained.

Simulation Results

Table 5.4 presents the values found using the co-simulation process described in the previous section. The results shows that the power and ER of each new added input sequence should follow a linear increase, compared to the previous one. For each MZI-SOA , starting from an input sequence with -10 dBm power and 7 dB ER, each new input sequence added should have input power increased by 4 dB and ER by 3 dB.

Figure 5.12 present the normalized constellation diagram of the generated QPSK, 16-QAM and 64-QAM signals. The discrete points in the constellation diagram reflect the correct behavior of the format conversion system. Computed EVM between ideal and simulated constellation, using (2.8), are 1.4 % for QPSK, 2.1 % for 16-QAM and 3.7 % for 64-QAM. The distortion of the signals, which are visible as minor deformations in the constellation diagram, are caused by several physical factors, such as the limited recovery time of the SOA, nonlinear characteristics of the MZI-SOA during the wavelength conversion process, and residual chirp effect.

5.3.3 Impairment Analysis and Results

From the computational process of the previous section, we may infer that operational parameters deviation from an optimal solution have a direct influence on the generated signal and may influence it characteristics. To quantify their influence, each operational parameter is swept individually around the optimal values presented in Table 5.4, and the effect on the constellation diagram analyzed. During simulations of the system represented in Figure 5.8, all sources of noise are limited or switched off, such as SOAs internal noise and lasers linewidth, to avoid masking the impact of operational parameter's deviation on the output signal. This analysis will be necessary on the following subsection, to understand the source of impairments on the output signal, due to operational parameter's mismatch or imbalance, that normally occurs during an experimental setup.

CW Laser

This section present the analysis of the transmitter output, when the CW laser power (probe signal) is deviated from the optimal value. Figures 5.13b to 5.13g shows the results for QPSK, 16-QAM and 64-QAM output constellations. It can be observed that for all cases,

Table 5.4: Optimal operational parameters obtained with MOGA

Name	Symbol	Value	Unit
SOAs bias current	$I_{bias_{1,2}}$	0.5	A
MZI-SOAs phase shifters voltage	$V_{PS_{1,2}}$	0.0	V
CW laser power	P_{CW}	11.5	dBm
NRZ-OOK sequence 1 power	P_1	-10.0	dBm
NRZ-OOK sequence $N+1$ power	P_{N+1}	-10.0	dBm
NRZ-OOK sequence $2,\ldots,N$ power	$P_{2,\ldots,N}$	$P_1 + 4\,(N-1)$	dBm
NRZ-OOK seq. $N+2,\ldots,N+Z$ power	$P_{N+2,\ldots,N+Z}$	$P_{N+1} + 4\,(Z-1)$	dBm
NRZ-OOK sequence 1 ER	ER_1	7	dB
NRZ-OOK sequence $N+1$ ER	ER_{N+1}	7	dB
NRZ-OOK sequence $2,\ldots,N$ ER	$ER_{2,\ldots,N}$	$ER_1 + 3\,(N-1)$	dB
NRZ-OOK seq. $N+2,\ldots,N+Z$ ER	$ER_{N+2,\ldots,N+Z}$	$ER_{N+1} + 3\,(Z-1)$	dB

there is a phase rotation and amplitude variation of the symbols. Furthermore, the effect is deeper on the outer symbols of the constellation diagram. This effect is only visible for 16-QAM and 64-QAM modulations, and it is associated to the distortion caused by the combination of higher power control signals present on the MZI-SOA input ports, which are used to generate QAM signals (Figures 5.13c-5.13d and 5.13f-5.13g). EVM is plotted against CW power variation in Figure 5.13a (lines are linear regression based on the simulated data). The results shows that EVM increases with an increase on the standard deviation of the probe laser power, with a slope of 1.5 % / mW, in all simulated signals, with more impact on the 64-QAM signal.

Input NRZ-OOK Sequences

In order to measure the influence of the input signals on the constellation diagram, we modified the optical power and the ER of each NRZ-OOK sequence independently. Without loss of generality, we bound the variations to MZI-SOA1 inputs only, and maintained MZI-SOA2 inputs to their optimal values (In case we choose to vary the input signals of MZI-SOA2 or in both MZI-SOAs, the constellation points would be following a similar trend). Laser power and ER are swept from their optimal values with a standard deviation between

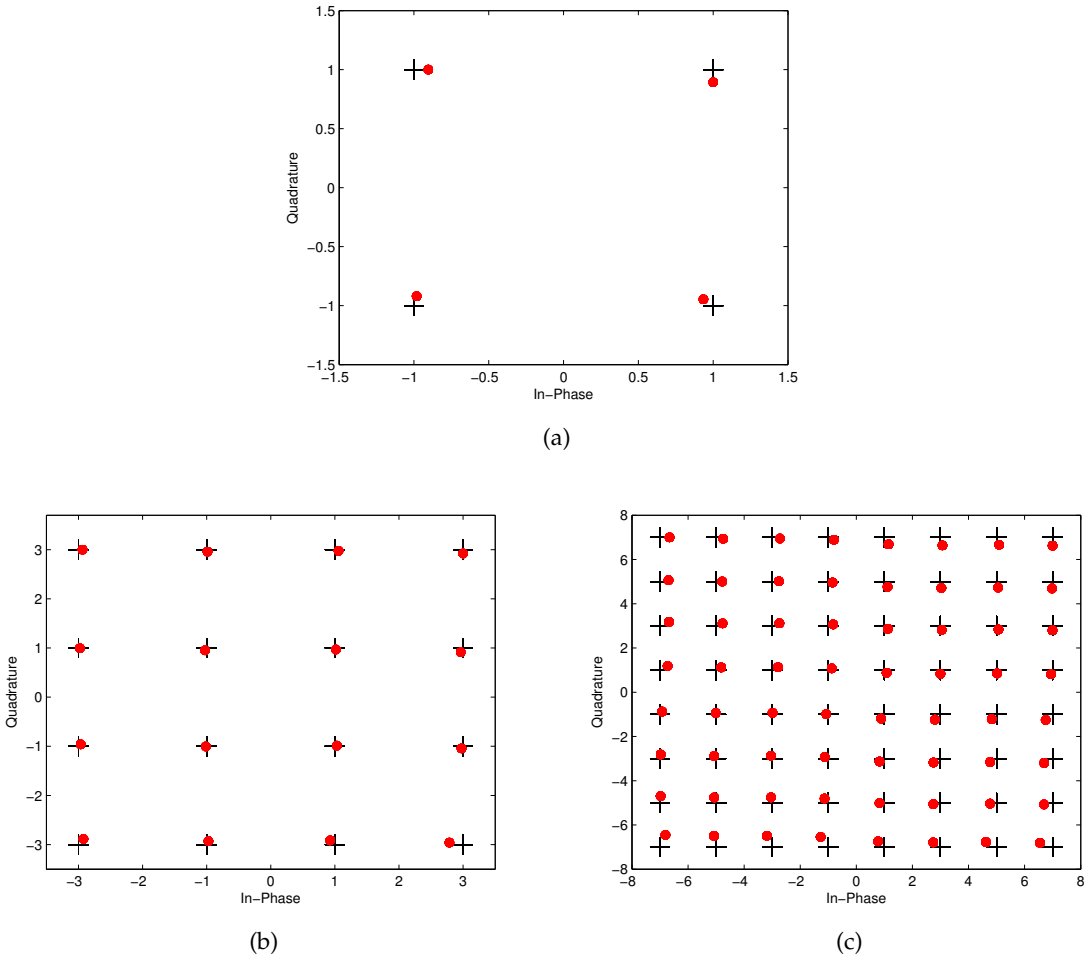

(a)

(b)

(c)

Figure 5.12: Output constellations: (a) QPSK, (b) 16-QAM and (c) 64-QAM. Black crosses are ideal values and red points are output results from the simulation and optimization process.

1 μW and 0.1 mW for the laser power, and between 0 dB and 3 dB for the ER. Figure 5.14 and 5.15 shows the results. Both impairments on the NRZ-OOK sequences disperse the constellation points away from the center of the decision boundaries in a random way, and with similar intensity in all constellation points (Figures 5.14b-5.14g and 5.15b-5.15g). In order to provide further insight into the results, we have presented the EVM in Figure 5.14a and 5.15a. It can be observed that non optimal laser power (in W) increases EVM with an exponential growth, whereas EVM due non optimal ER (in dB) tend to increases linearly, then maintains an almost constant value. 64-QAM signal are the most affected by non optimal ER of the input sequences.

External couplers

COUPLER1 and COUPLER2 are the external couplers of the conversion system represented in Figure 5.8. To assess their influence on the conversion process, we proceed

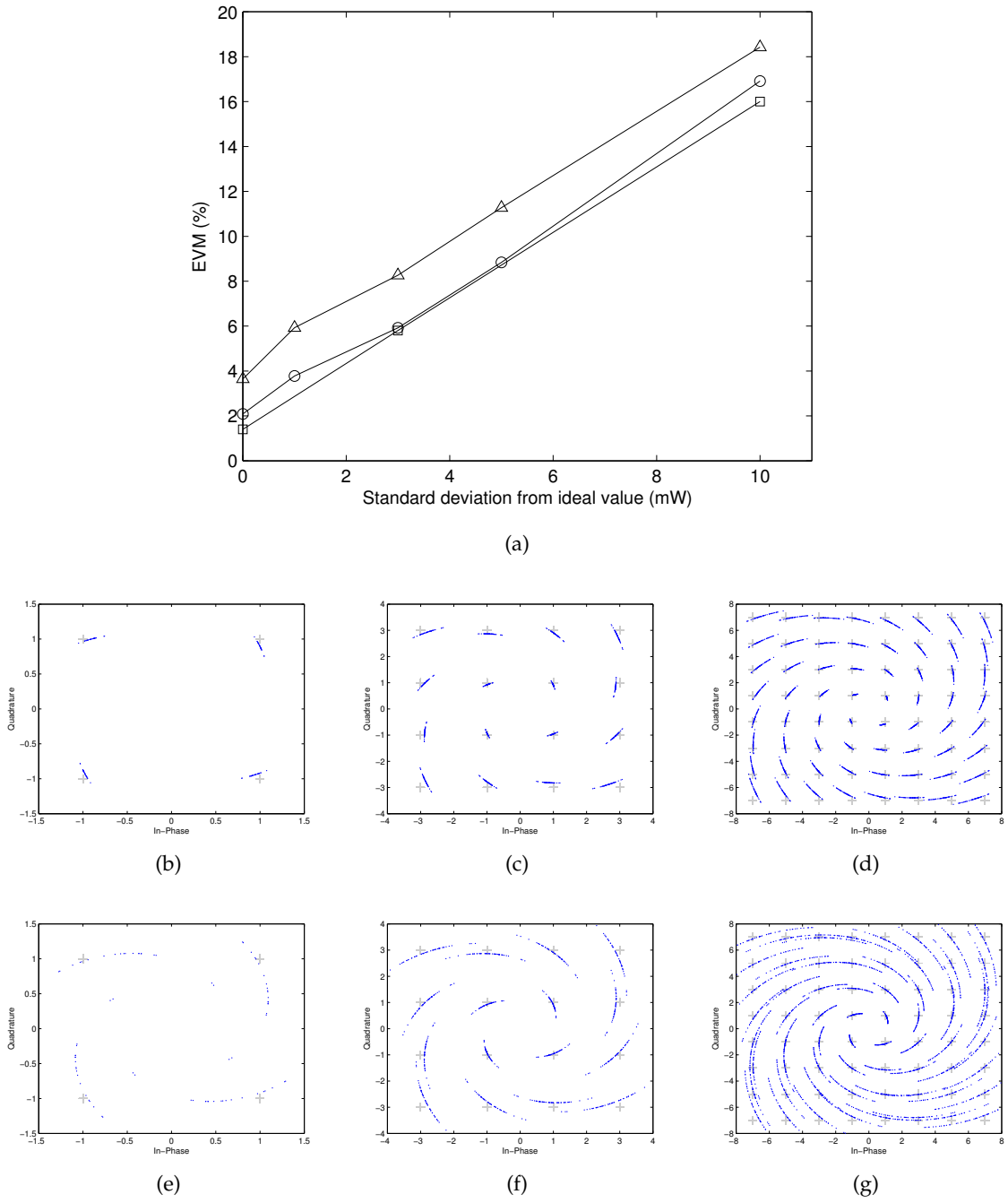

(a) (b) (c) (d) (e) (f) (g)

Figure 5.13: Constellation distortion caused by probe optical input power deviation from ideal values (in mW). EVM diagram is drawn in (a): QPSK (squares), 16-QAM (circles) and 64-QAM (triangles). The lines are guide for the eyes. Constellation diagrams for 3 mW standard deviation from ideal power for (b) QPSK, (c) 16-QAM and (d) 64-QAM; for 50 mW standard deviation: (e) QPSK, (f) 16-QAM and (g) 64-QAM (Greyed crosses represent ideal constellation points).

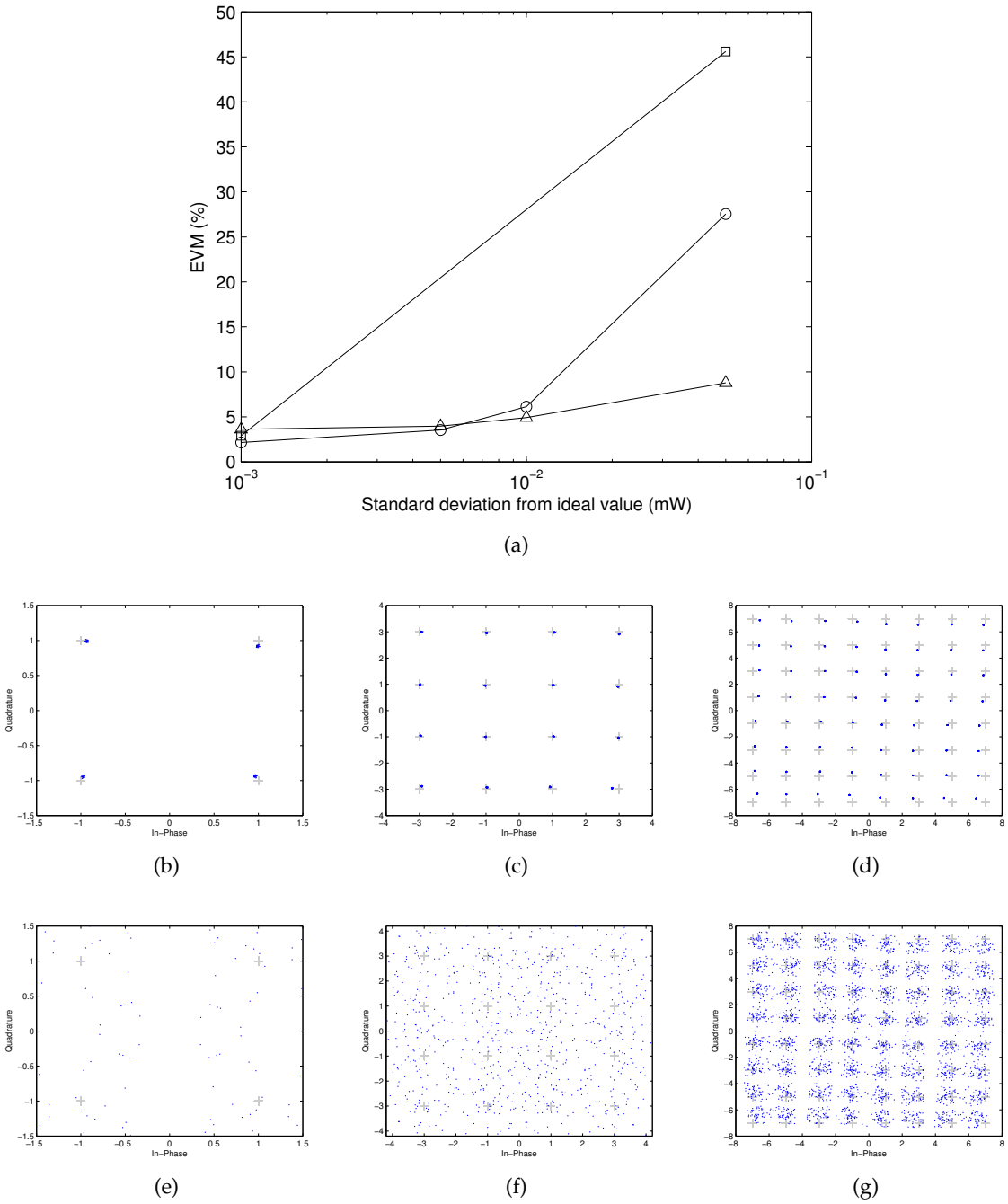

(a) (b) (c) (d) (e) (f) (g)

Figure 5.14: Constellation distortion caused by NRZ-OOK optical input power deviation from ideal values. EVM diagram is drawn in (a): QPSK (squares), 16-QAM (circles) and 64-QAM (triangles). The lines are guide for the eyes. Constellation diagrams for 1 μW deviation from ideal value for (b) QPSK, (c) 16-QAM and (d) 64-QAM; for 50 μW (e) QPSK, (f) 16-QAM and (g) 64-QAM (Greyed crosses represent ideal constellation points).

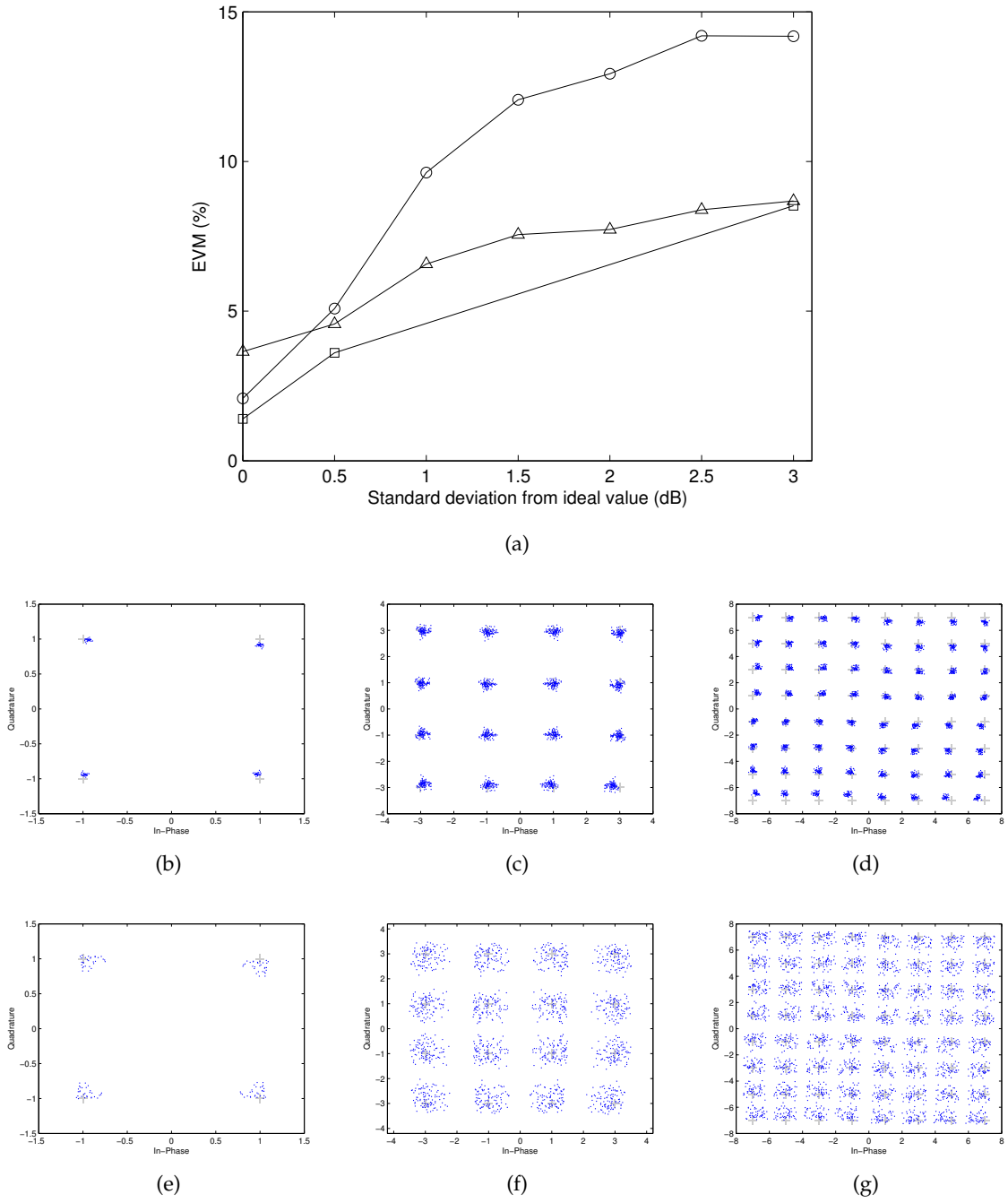

(a) (b) (c) (d) (e) (f) (g)

Figure 5.15: Constellation distortion caused by NRZ-OOK extinction ratio signal deviation from ideal values. EVM diagram is drawn in (a): QPSK (squares), 16-QAM (circles) and 64-QAM (triangles). The lines are guide for the eyes. Constellation diagrams for 0.5 dB deviation from ideal value for (b) QPSK, (c) 16-QAM and (d) 64-QAM; for 3 dB (e) QPSK, (f) 16-QAM and (g) 64-QAM (Greyed crosses represent ideal constellation points).

with a set of simulation, where the coupling factor α is deviated from the ideal value (0.5), with a standard deviation ranging from 0 to 0.05. EVM results are presented in Figure 5.16a. COUPLER1 has more influence on the performance of the conversion system, since It is directly connected to the P_{CW} laser with high power (11.5 dBm). A small deviation on the coupling factor of COUPLER1 will unbalance the power splitting of the probe signal P_{CW}, influencing the wavelength conversion process and the power balance inside each MZI-SOA. As an example with 64-QAM signals, for a standard deviation of 0.05 from the optimal coupling factor value, EVM stays below 7 % when COUPLER2 is unbalanced, but goes up to 28 % in the case of COUPLER1. These and other results for QPSK and 16-QAM are represented in Figures 5.16b - 5.16g. In the same way as in the probe signal analysis, the outer symbols of 16-QAM and 64-QAM constellation diagram are more affected due the interaction of the probe signal with higher power input signals inside the MZI-SOA, in the wavelength conversion process.

SOA bias current

Figure 5.17 shows the impact of SOA bias currents mismatch from the optimal value. During the simulation, all four SOAs (two from MZI-SOA1 and two from MZI-SOA2) are affected with non optimal bias current. The spreading of the constellation points increases with non optimal SOA bias currents, denoting a deeper phase rotation in the outer points of the 16-QAM and 64-QAM constellations (Figure 5.17b to 5.17g). Figure 5.17a shows calculated EVM values caused by non optimal bias currents, with standard deviation up to 100-mA. EVM increases linearly with a 0.22 % / mA slope for 16-QAM and 64-QAM modulation.

MZI-SOA Phase Shifters Voltage

Each MZI-SOA was modeled with two phase-shifters, one in each arm (PS1 and PS2). To measure the impact of unbalanced phase settings from optimal values, and without loss of generality, only PS2 angle value is modified, and defined as a gaussian variable with 0 rad mean value and standard deviation varying between 0 and 2π rad, for both MZI-SOA1 and MZI-SOA2. EVM results are depicted in Figure 5.18a and 5.18b for 16-QAM and 64-QAM respectively. The worst EVM results are originated by a π shift combination on both PS2 phase shifters, in each MZI-SOA. This combination result in a phase inversion of the signal in one arm of each MZI-SOA, leading to the worst unbalanced combination at the output ports, and consequently to undesired signals with incorrect phase and power.

BER analisys

The BER is computed for each impairment, using (2.11). To manage and include all BER results in the same figure, the standard deviation for each operational parameter is normalized according to the ideal values, i.e., 0 stands for ideal value (no deviation) and 1 means that the standard deviation has the same magnitude as the ideal value. This approach allows to compare the influence of each operational parameter mismatch on the proposed

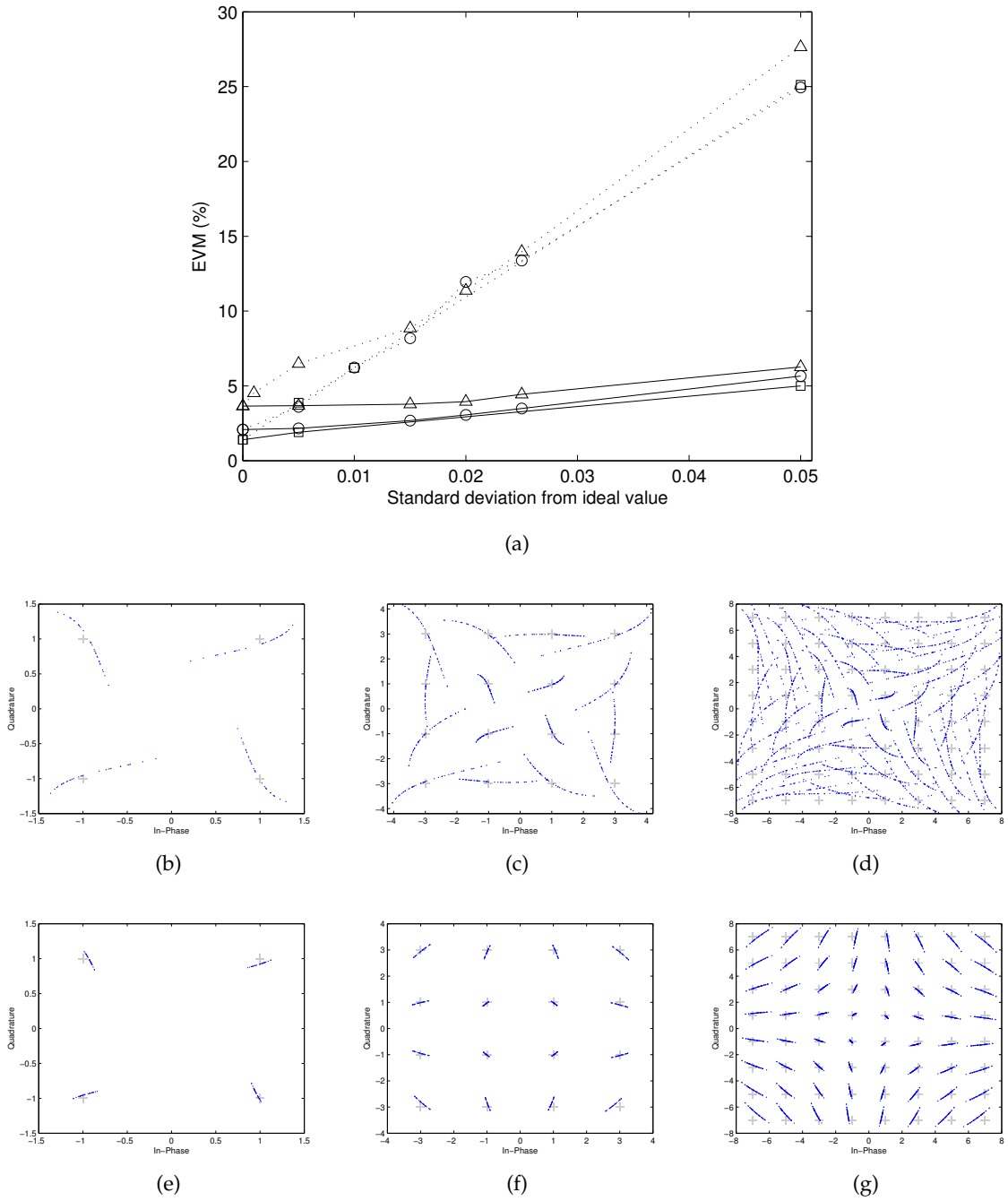

(a)

(b) (c) (d)

(e) (f) (g)

Figure 5.16: Constellation distortion caused by coupling factor deviation from ideal values. EVM diagram is drawn in (a): QPSK (squares), 16-QAM (circles) and 64-QAM (triangles); Dashed lines for COUPLER1 and full lines for COUPLER2 (The lines are guide for the eyes). Constellation diagrams for 0.05 deviation from ideal value for COUPLER1: (b) QPSK, (c) 16-QAM and (d) 64-QAM; for COUPLER2: (e) QPSK, (f) 16-QAM and (g) 64-QAM (Greyed crosses represent ideal constellation points).

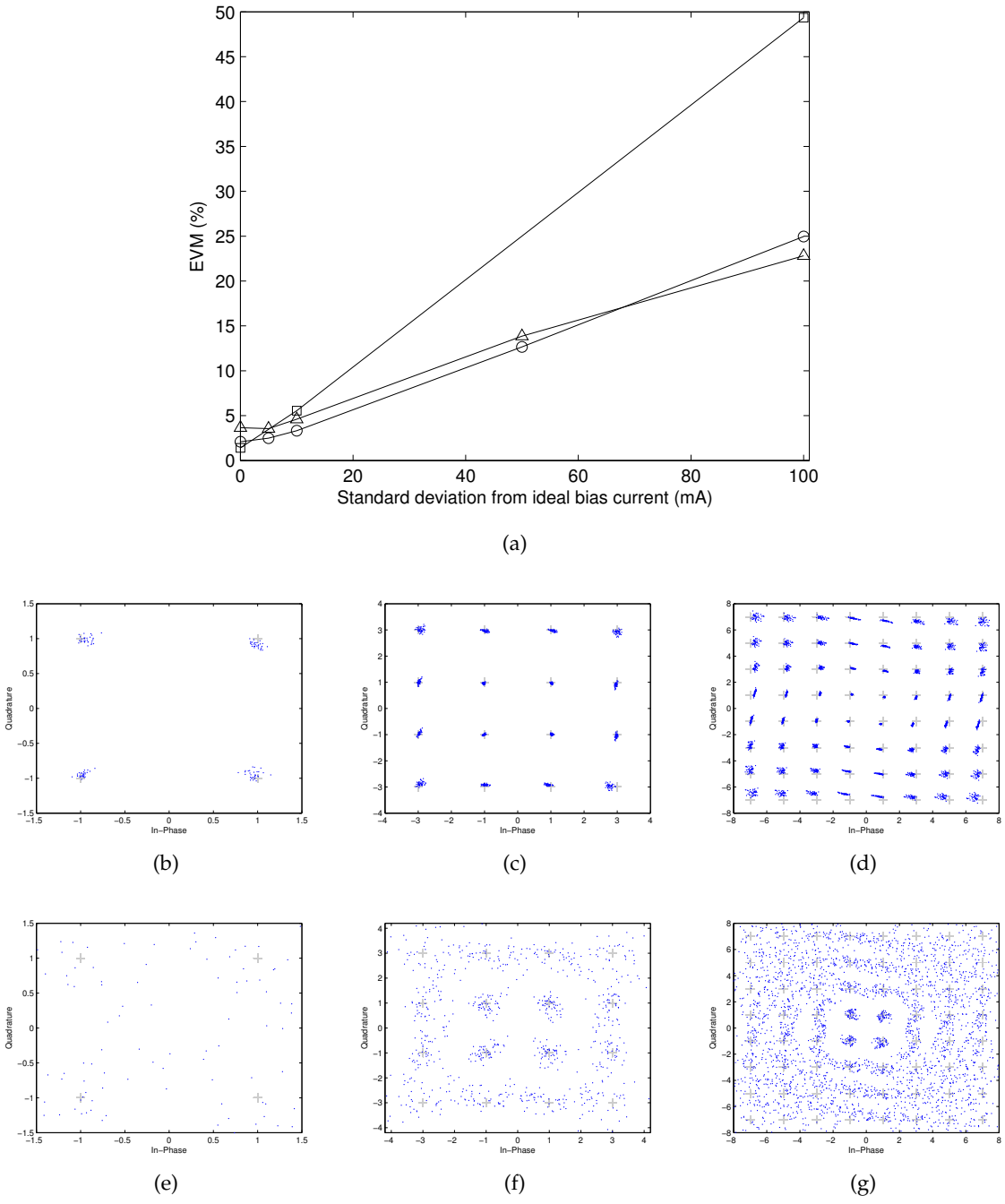

(a) (b) (c) (d) (e) (f) (g)

Figure 5.17: Constellation distortion caused by MZI-SOA bias current deviation from ideal values. EVM diagram is drawn in (a): QPSK (squares), 16-QAM (circles) and 64-QAM (triangles). The lines are guide for the eyes. Constellation diagrams for 10 mA deviation from ideal value for (b) QPSK, (c) 16-QAM and (d) 64-QAM; for 100 mA (e) QPSK, (f) 16-QAM and (g) 64-QAM (Greyed crosses represent ideal constellation points).

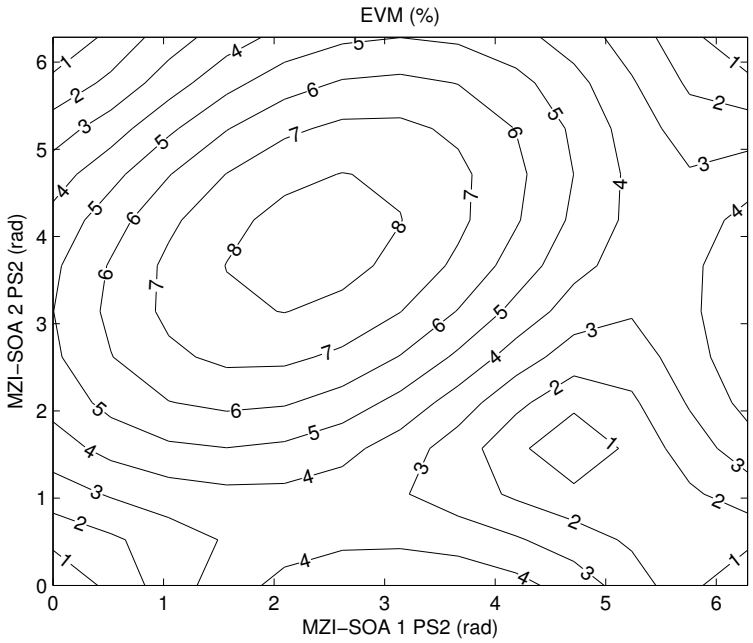

(a)

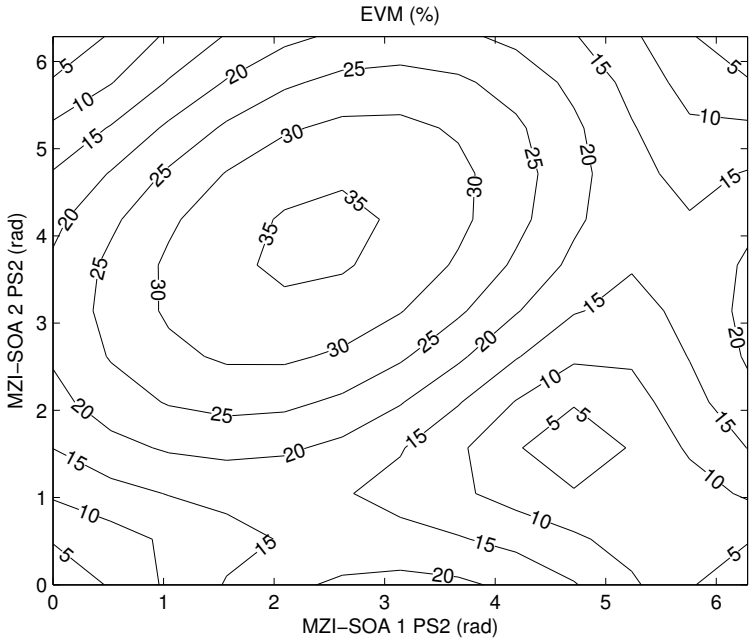

(b)

Figure 5.18: EVM caused by MZI-SOA phase shifter (PS2) voltage deviation from optimal values: (a) for 16-QAM and (b) for 64-QAM.

system. BER results are represented on Figure 5.19a for 16-QAM and Figure 5.19b for 64-QAM. The most critical parameters for both 16-QAM and 64-QAM output signals are the

probe optical input power (P_{CW}), and the coupling factor α from the coupler connected directly to the probe signal (COUPLER1). Indeed, the wavelength conversion process occurring inside SOAs strongly depends on the power of the input probe signal. Small variations have influence on the XPM and XGM processes inside the SOA, and consequently on the phase and power of the output signal.

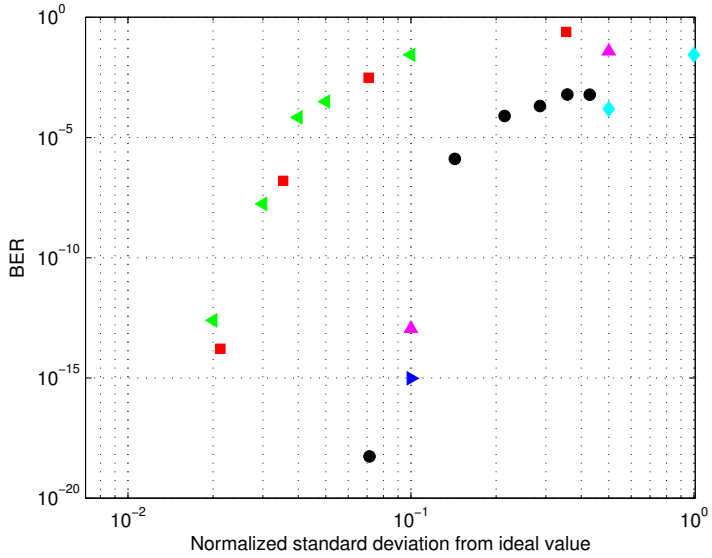

(a)

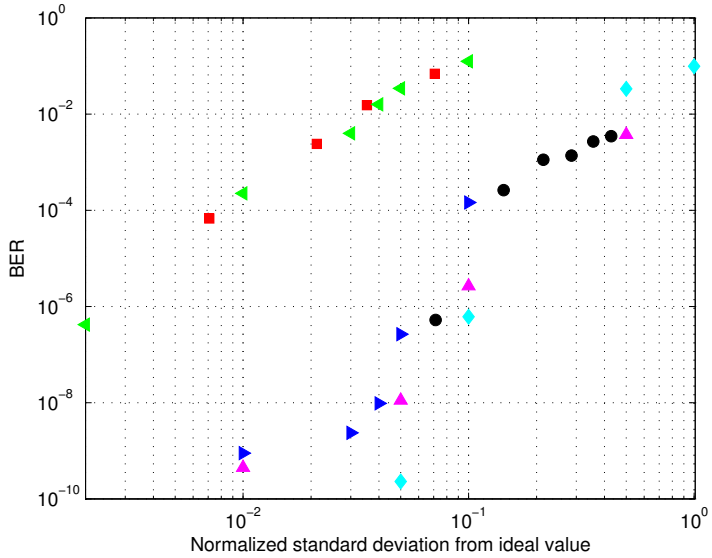

(b)

Figure 5.19: BER results for each operational parameter impairments for (a) 16-QAM and (b) 64-QAM output signals: COUPLER1 (left-pointing triangle), COUPLER2 (right-pointing triangle), Bias current (diamond), probe input power (squares), control signal input power (upward-pointing triangle), control signal extinction ratio (circles).

On the other hand, the high input power used for the probe signal will significantly unbalance the system if the coupler directly connected to it is not equally dividing the probe signal power for the two MZI-SOAs following COUPLER1.

5.3.4 Experimental setup

This section describes the experimental setup for QPSK and 16-QAM signals generation. 64-QAM was not experimentally tested due to the insufficient number of optical components, necessary to build such a testbed in the Laboratory. A picture of the overall experimental setup is presented in Figure 5.20.

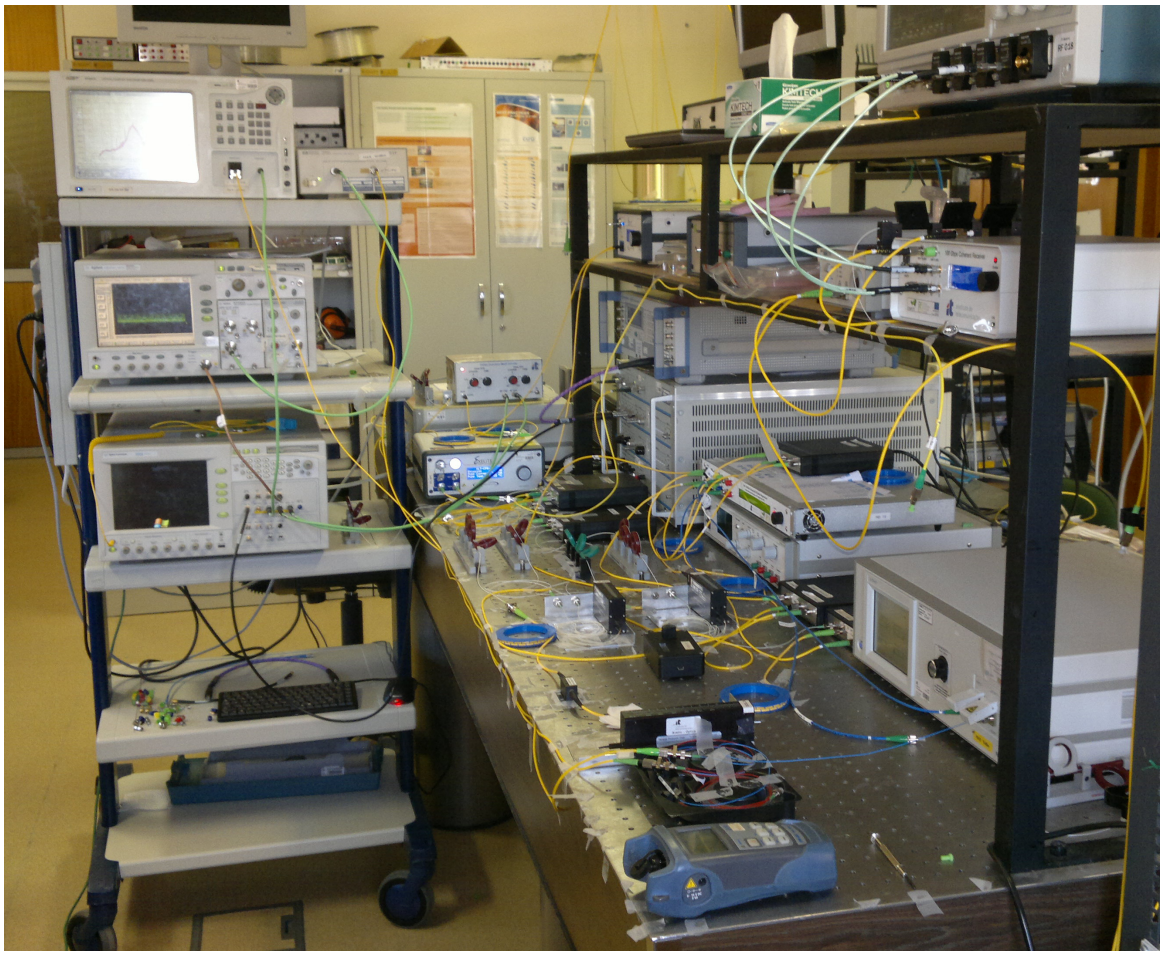

Figure 5.20: Testbed of the experimental setup for QPSK and QAM signals generation.

QPSK

As depicted in Figure 5.22, the experimental setup for NRZ-OOK to QPSK format conversion starts with two $2^{12} - 1$ PRBS, 10 Gb/s optical intensity modulated NRZ

transmitters. A single clock is used to synchronise both pattern generators and the OCSA (This last connection is not shown in the diagram). One of the transmitters (TX1) is formed by an External Cavity laser (ECL) laser at 1540 nm (λ_1) followed by an external dual drive MZM and an Agilent BER tester (N4901B) as the pattern generator, and connects to input port #E (0.8 dBm) of MZI-SOA2. The other optical transmitter (TX2) is composed by an ECL laser with wavelength 1554.94 nm (λ_2) and a SHF optical BER tester (10000B) connected to port #A (0 dBm) of MZI-SOA1. Figure 5.21 shows the generated signal from TX2. For each transmitter, an EDFA (Exelite XLT-CFA 19) boosts the optical signal power before reaching the control port of the MZI-SOAs. A VOA is included to control the input power, and a PC is also present for polarization adjustments. TX2 is followed by an ODL to adjust the bit alignment between TX1 and TX2 PRBS sequences. The probe CW signal (Figure 5.23) is generated with a tunable laser with 100 kHz line width peaking at 1550 nm (λ_3), connected to a PC and followed by an optical splitter (50:50) to port #B (-5.8 dBm) and port #F (-5.53 dBm) of the MZI-SOAs.

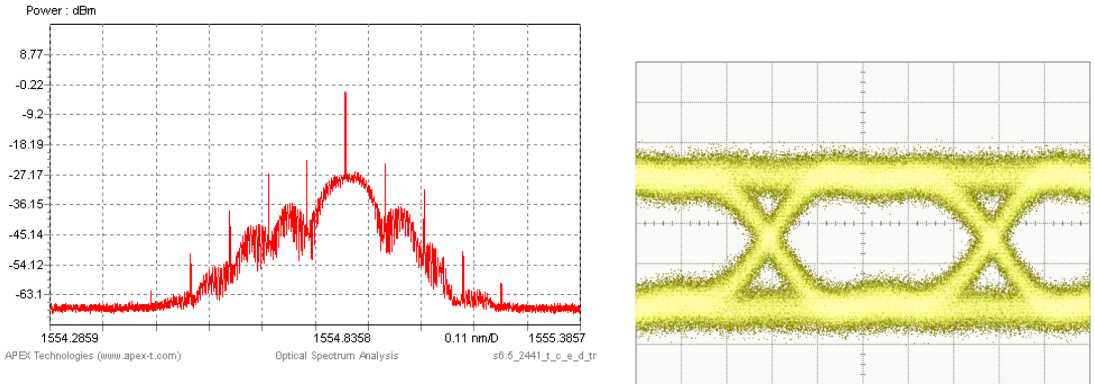

(a) (b)

Figure 5.21: NRZ-OOK control signal of transmitter TX2: (a) power spectrum (Wavelength resolution is 0.16 pm) and (b) eye diagram (Horizontal scale is 20 ps/division).

The bias current of MZI-SOA1 andMZI-SOA2 were set to 450 mA. Phase shifter voltage were set to 0.0 V (PS1) and 0.69 V (PS2) for MZI-SOA1, and 0.0 V (PS1) and 0.25 V (PS2) for MZI-SOA2, after the results from the static model (Chapter 4) and minor adjustment with a balancing procedure to maximize eye opening of the output signal at ports #J and #K (see Appendix B). The wavelength converted signals from ports #J and #K are then combined with a (50:50) coupler, and the resulting signal is optically filtered to remove unwanted signals (λ_1 and λ_2) and ASE noise (FINISAR 4000 filter). An ODL is included at port #K for bit alignment with the signal at port #J. The resulting QPSK signal is then passed through a State of Polarization (SOP) locker (THORLABS PL100S) and analyzed with an OCSA and a coherent receiver (Hybrid 90°and Tektronics DPO72004B oscilloscope). The local oscillator on the coherent receiver is the same laser used as a probe at MZI-SOAs input ports #B and #F.

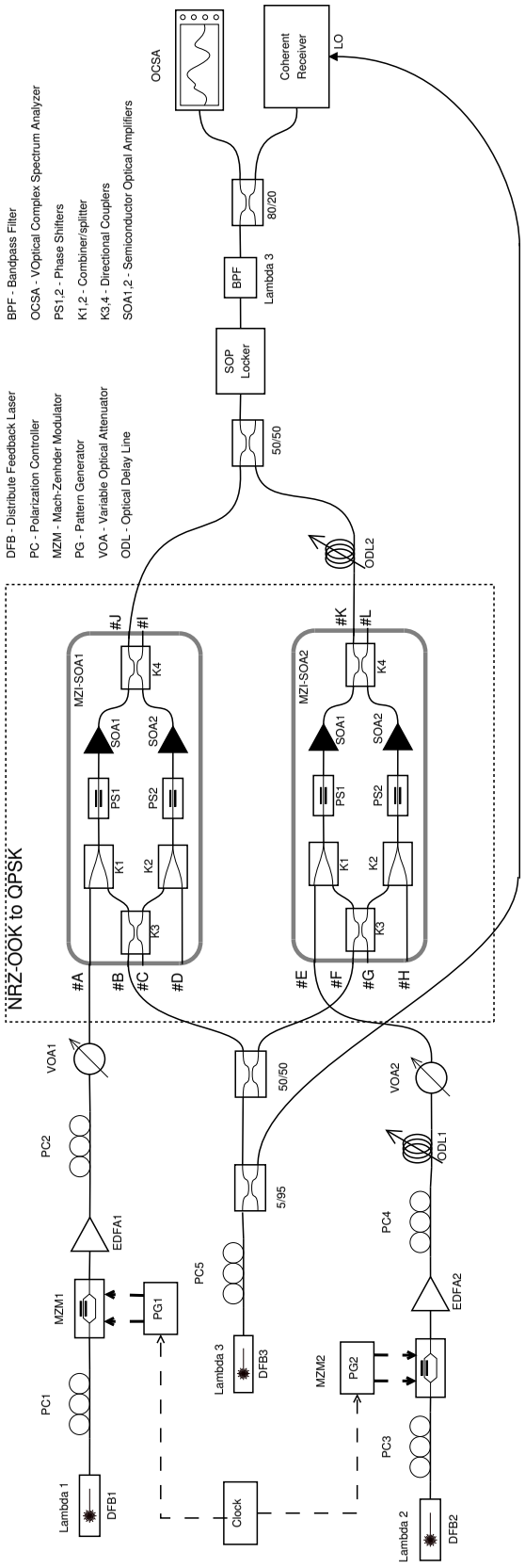

Figure 5.22: Experimental setup layout for NRZ-OOK to QPSK all-optical format conversion.

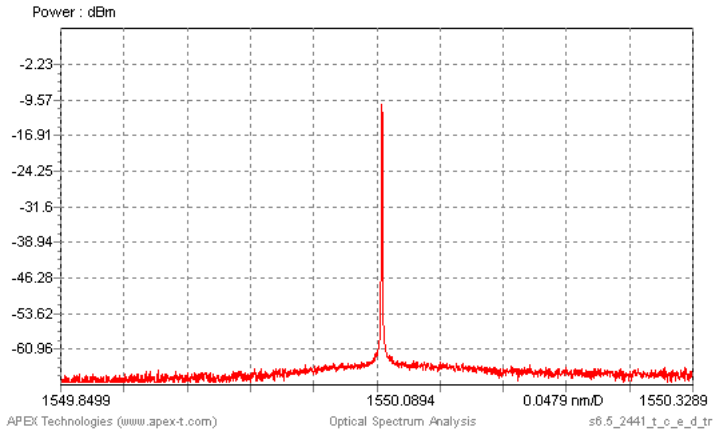

Figure 5.23: Power spectrum of the laser used as a probe signal. Wavelength resolution is 0.16 pm.

16-QAM

The setup used for NRZ-OOK to 16-QAM conversion, depicted in 5.25, is similar to the one used for QPSK. But here, two NRZ-OOK optical signals are previously combined using a Optical Add-Drop Multiplexer (OADM), to produce a four level ASK control signal (Figure 5.24), for each input (ports #A and #E). Since the available OADMs central wavelength is not tunable, we had to change the wavelength of the laser sources in order to use them: The new set of wavelength sources are centered in 1549.32 nm for λ_1, 1549.82 nm for λ_2 and 1554.94 nm for λ_3. An additional ODL (ODL2) is used for bit alignment between optical sequences, and also to produce uncorrelated signals for input #A and #E, which are using the same PRBS signals sources. Measured optical power levels are 0.65 dBm (port #A), -11.11 dBm (port #B), -3.54 dBm (port #E) and -10.73 dBm (port #F).

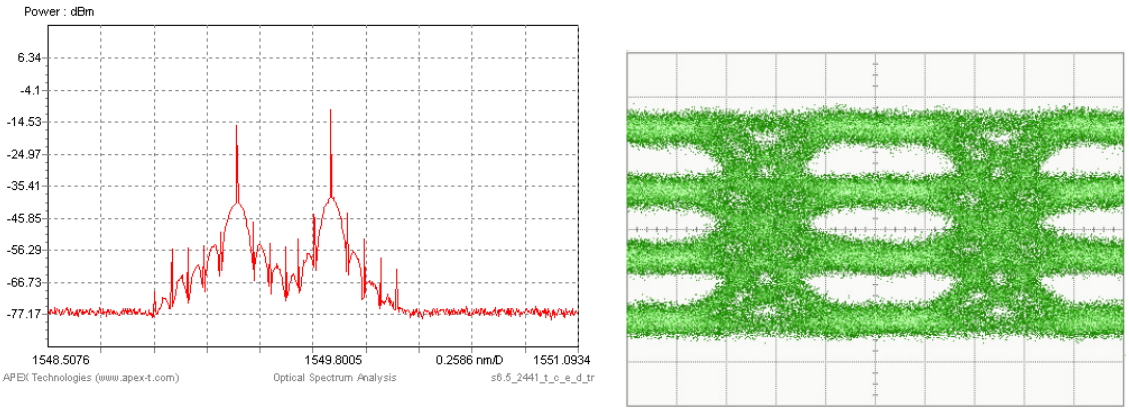

(a)

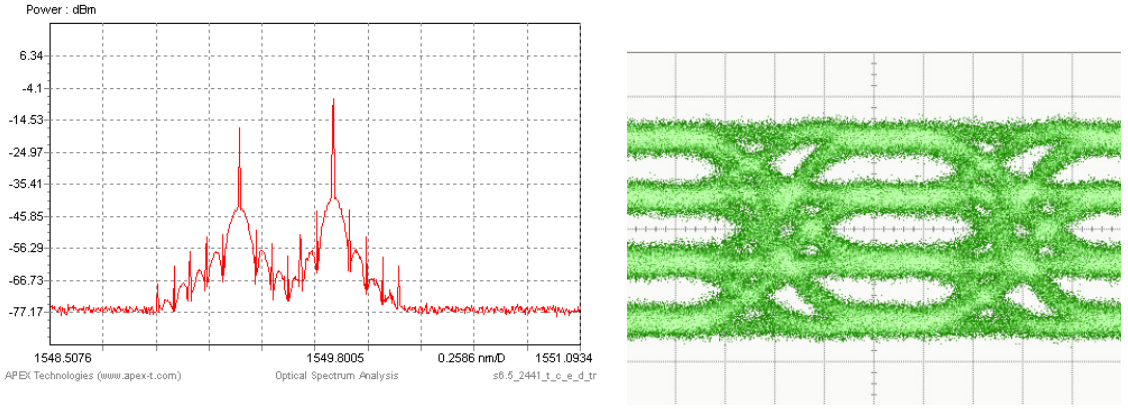

(b)

Figure 5.24: Control signals at (a) input port #A and (b) input port #E of MZI-SOAs. Power spectrum: Wavelength resolution is 0.16 pm. Eye diagram: Horizontal scale is 20 ps/division and vertical scale is 19 mV/division.

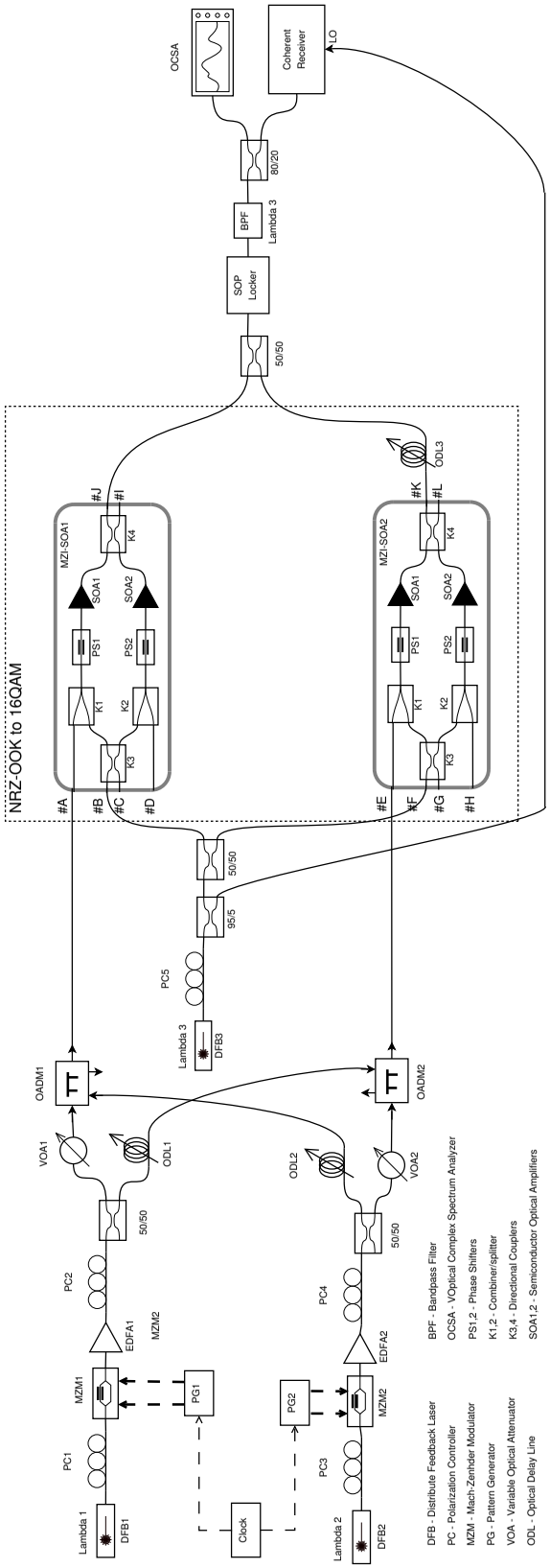

Figure 5.25: Experimental setup layout for NRZ-OOK to 16-QAM all-optical format conversion.

5.3.5 Experimental results

All the results in this section refers to a back-to-back configuration, without transmission.

QPSK

We first analyze the signals generated by each MZI-SOAs individually. We opened the optical path at ports #J and #K and filtered each output signals for time and spectral analysis using an sampling oscilloscope and an OCSA. The data sequence at the input is 1111100001100010 with equal number of 1s and 0s. The results for output signal at port #J are shown in Figure 5.26.

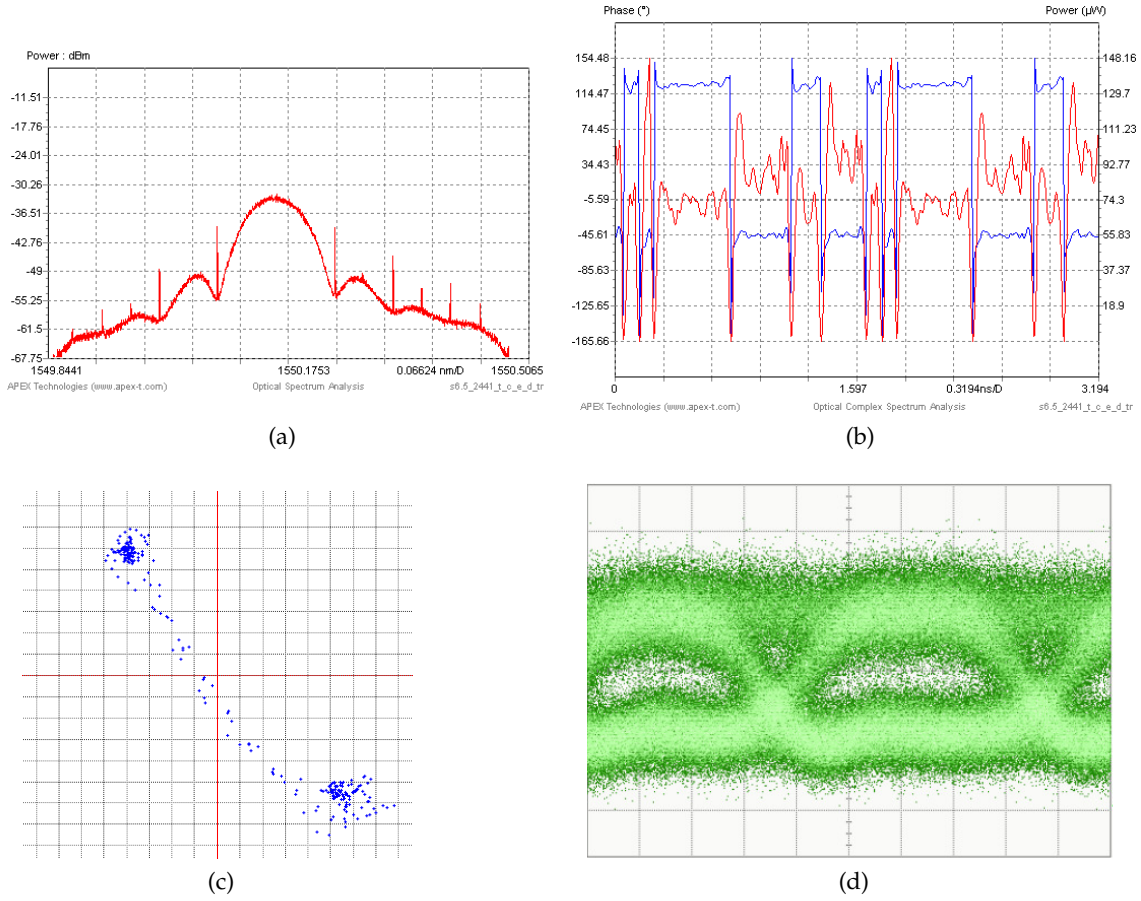

(a) (b)

(c) (d)

Figure 5.26: BPSK signal at port #J (after filtering): (a) Optical spectra; (b) Time profile of optical power (red line) and phase (blue line); (c) signal constellation; (d) eye diagram. The eye diagram is obtained with a 65 GHz electrical bandwidth oscilloscope. horizontal scale is 20 ps/division and vertical scale is 1.8 mV/division. The spectral resolution is 0.16 pm.

It can be seen that the incoming NRZ-OOK signal (Figure 5.21) is successfully wavelength and format converted to a BPSK signal. The phase profile follows the data sequence and present a π shift between logical values (Figure 5.26b). The optical spectrum

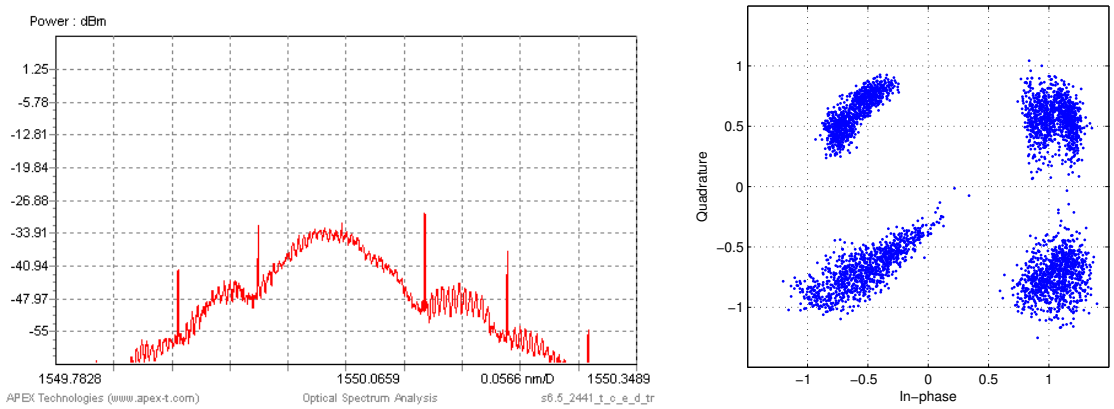

(a) (b)

Figure 5.27: QPSK signal: (a) Power spectrum; (b) Normalized Experimental QPSK after DSP processing (Viterbi algorithm). The spectral resolution is 0.16 pm.

shows that the signal is carrier suppressed with 10 GHz optical bandwidth (Figure 5.26a). The constellation diagram shows a clear separation between two distinct aggregated points in opposite quadrants (Figure 5.26c). The converted signal eye diagram shows some patterning effects in the "one" level, due to the slow recovery time of the SOAs and the large duty cycle (50%) of the incoming NRZ-OOK signal (Figure 5.26d). Although not shown, the output signal at port #K follows a similar trend.

The individual analysis of each MZI-SOA output is an important step, that allows to fine tune and optimize the spectral and temporal characteristics of each signal. Having done this operation, the setup in once again closed as depicted in Figure 5.22. The results of the conversion from BPSK to QPSK are presented in Figure 5.27. The spectrum bandwidth of the resulting signal is 10 GHz and maintain the suppressed carrier characteristic of the BPSK signals (Figure 5.27a). The constellation in Figure 5.27b was obtained with a $2^{16} - 1$ bit PRBS sequence at the input, using a coherent receiver (Hibrid 90° and realtime oscilloscope), since the previous 16 bit sequence and the OCSA receiver were unable to produce an acceptable diagram. Despite the visible impairments on the measured constellation, caused mainly by unperfected MZI-SOA balancing and operational parameters optimization (e.g. see section 5.3.3 for a detailed analysis), the result diagram shows four distinct aggregate in each quadrant, with a computed EVM of 12.3 %.

16-QAM

The experimental verification for NRZ-OOK to 16-QAM format conversion proved to be a more difficult task. With the signals of Figure 5.24 at the input ports #A and #E, the results of the wavelength conversion and format conversion within each MZI-SOA are shown in Figure 5.28. As described in the principle of operation (see section 5.3.1), each MZI-SOA must generate a 4-ASK phase modulated signal, where phase should span from 0 to 270°.

Figure 5.28e and 5.28e shows that, despite the effort to reach that goal, the phase varies only between 0 and 240°for output #J and between 0 and 183° at output port #K, respectively, with unequal phase span between logical values. When combining both signals with a coupler, the results were inconclusive.

As a summary, we have proposed and numerically evaluated an all-optical format conversion system from 10 Gbps NRZ-OOK to 20 Gbps QPSK, 40 Gbps 16-QAM and 160 Gbps 64-QAM, using parallel MZI-SOAs. A MOGA was used to compute the optimal operational parameters of the proposed setup. This concept has the advantages to combine seamless optical networking between different modulation formats together with the generation of m-ary QAM or QPSK signals from OOK signals. Higher order QAM signals may be theoretically generated, increasing the number of NRZ-OOK sequences at the input. A detailed analysis of the operational parameters influence on the output signal was conducted. CW laser power and COUPLER1 coupling factor are the most sensitive parameters that influence the BER of the converted signal. The conducted studies from this paper were followed by experimental demonstration. Te results shows that QPSK generation is feasible, which validates the proposed method. The experimental generation of signals with a higher number of symbols (e.g. 16-QAM) was inconclusive, and only integration and miniaturization of the overall system, combined with closed loop control to continuously adjust the operational parameters of the system, may lead to acceptable results.

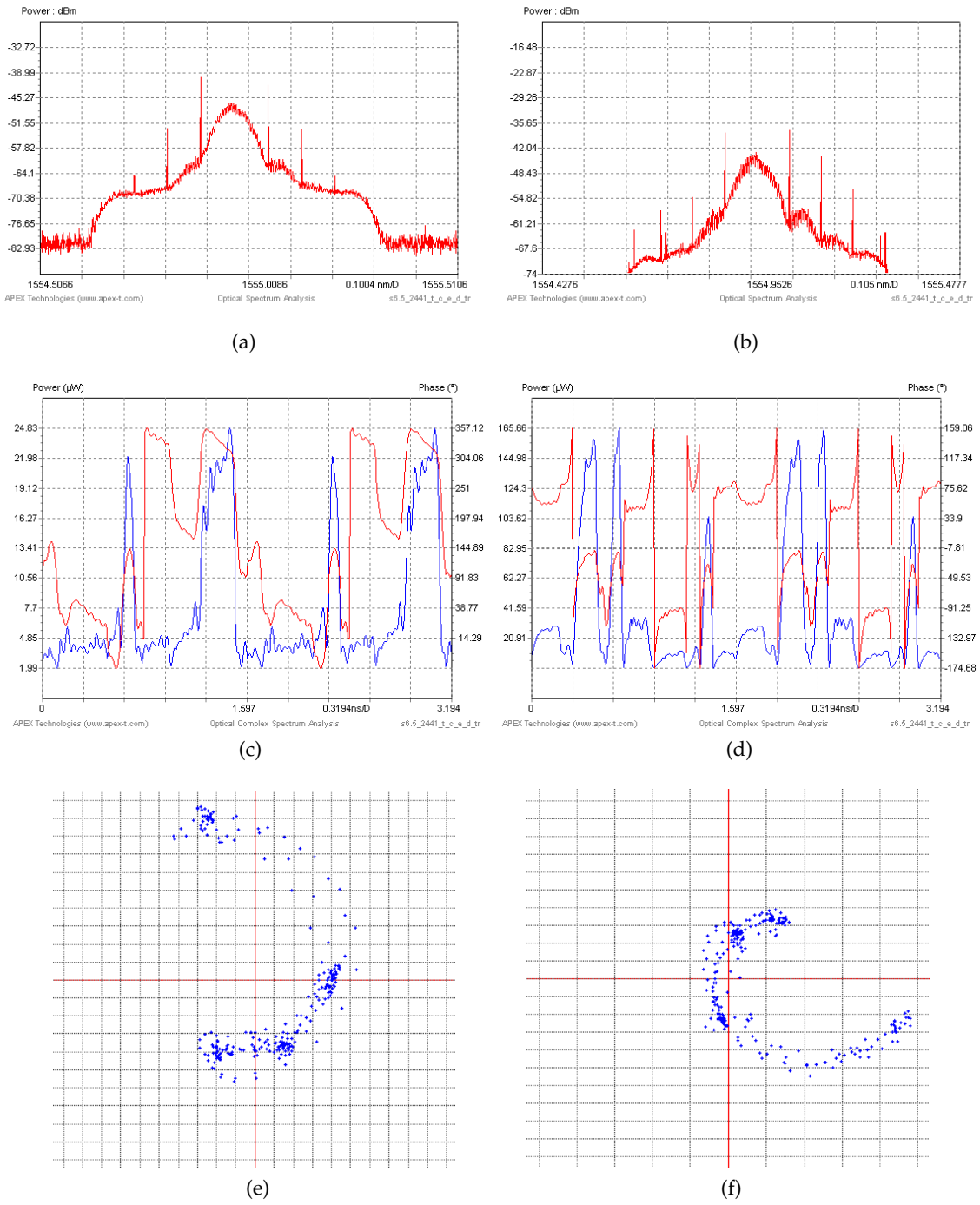

(a) (b)

(c) (d)

(e) (f)

Figure 5.28: : Signal at port #J (Left column) and at port #K (Right column). 5.28a, 5.28b: Power spectrum; 5.28c, 5.28d: Time profile (power and phase); 5.28e, 5.28f: Constellation. The spectral resolution is 0.16 pm.

5.4 Conclusions

In this section, we have proposed, numerically and experimentally evaluated all-optical format conversion from NRZ-OOK to advanced modulation format, using two different configurations: cascaded and parallel MZI-SOAs.

With the cascade configuration, we gave successfully generated a Quasi-CPM from two NRZ-OOK optical signals with an all-optical technique. We have observed an eye opening of the converted signal with four distinct phase levels at 10 Gbaud, with good agreement between simulation and measurements. More studies on the dependence of Quasi-CPM signal characteristics with MZI-SOAs operational parameters are necessary to optimize the performance of the method, for this or other phase coding.

With the parallel MZI-SOAs configuration, we have experimentally evaluated an all-optical format conversion from 10 Gbps NRZ-OOK to 10 Gbaud QPSK signal. System impairments analysis caused by non optimal operational parameters was numerically conducted for 20 Gbps QPSK, 40 Gbps 16-QAM and 160 Gbps 64-QAM. CW laser power and the coupling factor of optical coupler connected to it are the most sensitive operational parameter. Impairments from other components of the system, such as fiber lengths mismatch between the interferometer arms, will also influence the overall performance, and should be subject of further investigation.

Polarization effect of the MZI-SOA or inside fiber may have limited the success of the experiments.

As a wrap up of this chapter, we may conclude that both conversion systems have the advantages to combine seamless optical networking between different modulation formats (OOK, CPM, QPSK and QAM) together with the generation of advanced modulation format signals from OOK signals. Higher order signals (m-QAM or CPM m-PSK) may be theoretically generated, increasing the number of NRZ-OOK sequences at the input of the conversion system. However, closed loop control is required to continuously adjust the correct balance between operational parameters, and to avoid distortion of the output signal. Nevertheless, the all-optical nature of the process reduces electrical control complexity of the transmitter, compared to other techniques where input sequences are combined in the electrical domain [12], and allow for direct conversion of signal in the optical domain, avoiding the electrical bottleneck of legacy systems.

References

[1] R. P. Dionisio, G. Parca, C. Reis, and A. L. Teixeira, "Operational parameter optimisation of MZI-SOA using multi-objective genetic algorithms," *Electronics Letters*, vol. 47, no. 9, pp. 561–562, 2011.

[2] K. Mishina, A. Maruta, S. Mitani, T. Miyahara, K. Ishida, K. Shimizu, T. Hatta, K. Motoshima, and K. Kitayama, "NRZ-OOK-to-RZ-BPSK modulation-format conversion using SOA-MZI wavelength converter," *Lightwave Technology, Journal of*, vol. 24, no. 10, pp. 3751–3758, 2006.

[3] K. Mishina, S. M. Nissanka, A. Maruta, S. Mitani, K. Ishida, K. Shimizu, T. Hatta, and K. I. Kitayama, "All-optical modulation format conversion from NRZ-OOK to RZ-QPSK using parallel SOA-MZI OOK/BPSK converters," *Optics Express*, vol. 15, no. 12, pp. 7774–7785, 2007.

[4] S. M. Nissanka, A. Maruta, S. Mitani, K. Shimizu, T. Miyahara, T. Aoyagi, T. Hatta, A. Sugitatsu, and K. i. Kitayama, "All-optical modulation format conversion from NRZ-OOK to RZ-QPSK using integrated SOA Three-Arm-MZI wavelength converter," in *OFC 2009*, 2009, pp. 1–3.

[5] L. Guo-Wei, T. Sakamoto, A. Chiba, T. Kawanishi, T. Miyazaki, K. Higuma, and J. Ichikawa, "80-Gb/s optical MSK generation using a monolithically integrated quad-mach-zehnder IQ modulator," in *Optical Fiber Communication (OFC), collocated National Fiber Optic Engineers Conference, 2010 Conference on (OFC/NFOEC)*, 2010, pp. 1–3.

[6] F. Xiong, *Digital modulation Techniques*. Norwood, MA: Artech House, Inc., 2000.

[7] T. F. Detwiler, S. M. Searcy, B. E. Basch, and S. E. Ralph, "Continuous phase modulation as an alternative to QPSK for 100 Gb/s optical links," in *OFC 2010*, 2010, pp. 1–3.

[8] R. Dionisio, C. Reis, P. Andre, R. Nogueira, and A. Teixeira, "Experimental study of a phase modulator using an active interferometric device," in *MELECON 2010*, 2010, pp. 1142–1146.

[9] "Vpi photonics," March 2013. [Online]. Available: http://www.vpiphotonics.com

[10] S. Jinying, G. Morthier, and R. Baets, "Numerical and theoretical study of the crosstalk in gain clamped semiconductor optical amplifiers," *Selected Topics in Quantum Electronics, IEEE Journal of*, vol. 3, no. 5, pp. 1162–1167, 1997.

[11] D. van den Borne, V. Sleiffer, M. S. Alfiad, S. L. Jansen, and T. Wuth, "POLMUX-QPSK modulation and coherent detection: The challenge of long-haul 100G transmission," in *35th European Conference on Optical Communication, ECOC '09.*, 2009, pp. 1–4.

[12] M. Seimetz, "Multi-format transmitters for coherent optical M-PSK and M-QAM transmission," *Proceedings of the 7th International Conference on Transparent Optical Networks*, vol. 2, pp. 225–229, 2005.

[13] S. L. Jansen, I. Morita, T. C. W. Schenk, and H. Tanaka, "121.9-Gb/s PDM-OFDM Transmission With 2-b/s/Hz Spectral Efficiency Over 1000 km of SSMF," *Journal of Lightwave Technology*, vol. 27, no. 3, pp. 177–188, 2009.

[14] B. Pattan, *Robust Modulation Methods & Smart Antennas in Wireless Communications*. Upper Saddle River, NJ: Prentice Hall PTR, 2000.

[15] S. Savory, "Digital coherent optical receivers: Algorithms and subsystems," *Selected Topics in Quantum Electronics, IEEE Journal of*, vol. 16, no. 5, pp. 1164 –1179, sept.-oct. 2010.

[16] N. K. Dutta and Q. Wang, *Semiconductor Optical Amplifier*. Singapore: World Scientific Publishing, 2006.

[17] R. M. Ferreira, A. Shahpari, M. Lima, and A. L. Teixeira, "Coherent Fiber Communications Analyzer," in *10th Symposium on Enabling Optical Networks and Sensors - SEON*, June 2012.

[18] E. Ip and J. Kahn, "Digital equalization of chromatic dispersion and polarization mode dispersion," *Lightwave Technology, Journal of*, vol. 25, no. 8, pp. 2033 –2043, aug. 2007.

[19] S. Tsukamoto, K. Katoh, and K. Kikuchi, "Unrepeated transmission of 20-gb/s optical quadrature phase-shift-keying signal over 200-km standard single-mode fiber based on digital processing of homodyne-detected signal for group-velocity dispersion compensation," *Photonics Technology Letters, IEEE*, vol. 18, no. 9, pp. 1016 –1018, 1, 2006.

[20] T. Xu, G. Jacobsen, and S. Popov, "Frequency-Domain Chromatic Dispersion Equalization Using Overlap-Add Methods in Coherent Optical System." *Journal of Optical Communications*, vol. 32, no. 2, pp. 131–135, June 2011.

[21] Y. Fan, X. Chen, W. Zhou, X. Zhou, and H. Zhu, "The comparison of cma and lms equalization algorithms in optical coherent receivers," in *Wireless Communications Networking and Mobile Computing (WiCOM), 2010 6th International Conference on*, sept. 2010, pp. 1 –4.

[22] "CIP Technologies," July 2012. [Online]. Available: http://www.ciphotonics.com/

[23] C. Coello, G. Lamont, and D. Van Veldhuisen, *Evolutionary Algorithms for Solving Multi-Objective Problems*, ser. Genetic and Evolutionary Computation Series. Springer, 2007. [Online]. Available: http://books.google.pt/books?id=rXIuAMw3lGAC

Chapter 6

Conclusions

THe aim of this chapter is to conclude the studies of the all-optical format conversion and phase modulation techniques carried out in the frame of this thesis. Additionally, an outlook on the future work will be given. In doing so, this section is divided in two sections. The first section summarizes the results presented in this thesis and afterwards, the projected future work will be outlined.

6.1 Conclusions

This section overviews the work presented in this thesis and summarizes its main conclusions. The motivation for the work was presented in Chapter 1, which arises from the wish to avoid the electronic bottleneck affecting opaque optical network nodes. A possible vehicle for solving this problem is the MZI-SOA, a compact semiconductor device capable of performing many different functions for all-optical modulations format conversion and signal generation.

First, in Chapter 2, the state of the art of optical modulation format conversion was reviewed. This chapter has presented a summarized analysis of Optical Modulation Format Conversion Systems (OMFCS). A form of classification has been proposed. This classification categorizes the OMFCS according to their purpose and form of analysis of the optical signal. A set of OMFCS currently available in the literature has been presented. We also resumed the performance of the most relevant technologies and architectures for modulation format conversion.

In Chapter 3, an MZI-SOA sample device was experimentally evaluated and a study of the MZI-SOA as a building block of phase modulation is presented. In particular, all active and passive components of the MZI-SOA were characterize to assess the properties of the device for phase modulation experiments. This process allows extracting the coupling factors and relevant gain functions which contribute for the determination of the MZI-SOA behavior, knowing that most of these parameters are hidden since they are masked in the output power which are normally a sum or difference of internal fields with amplitude and phase variations. A novel method to perform optical phase modulation has also been presented, based on an all-optical XOR gate configuration. We access the impact of SOAs bias current and input CW power on the phase of the destructive output of a MZI-SOA. We observed that an increase of the bias current produces higher values of phase spans (eye diagram opening) and output mean powers. However, SOAs gain saturation has an opposite effect on the output signal. The experimental results demonstrate the feasibility of a MZI-SOA device as an optical phase modulator.

From Chapter 4, a black box simulation model for such devices is presented, with a view to analyze the device performance in system applications in the most effective way. Optimization of performance and determination of operational limits are enabled by the proposed methodology and good agreement was obtained between simulated and experimental results using MOGA. The proposed process allows the user to quickly and effectively find the optimal operating point for maximal ER between output ports, or any other specific target.

Finally, Chapter 5 presents two different techniques to convert NRZ-OOK signals into advanced modulation format using all-optical techniques. The first techniques proposed and experimentally verified is an all-optical modulation format conversion system, from OOK to Quasi-CPM QPSK, based on two MZI-SOAs in a serial configuration. We have observed an eye opening of the converted signal with four distinct phase levels at 10 Gbaud. The second techniques uses a setup with two MZI-SOAs in a parallel configuration, for all-optical conversion from OOK to QPSK and m-QAM signals. Several impairments on the signal constellation were numerically evaluated. It was shown that the most critical parameters for both 16-QAM and 64-QAM signals are the probe optical input power and the coupling factor from the coupler connected to the probe signal. The high input power used for the probe signal will significantly unbalance the system if the coupler directly connected to it is not equally dividing the probe signal power. additionally, we have successfully verified the all-optical conversion system in the laboratory, by combining two NRZ-OOK sequences into one QPSK signal at 10 Gbaud with an experimental testbed.

6.2 Directions for future work

The research topics presented in this thesis are important and the results relevant, and lead the way to additional research on this domain. Some future research topics are now enumerated.

1. Regarding the topic of a MZI-SOA simulation using a static model, our attention was focused on numerical or semi-analitical method to facilitate the initial setup, when implementing an experimental setup with an MZI-SOA. However, the same model could also provide additional information, if an extension of the model could be developed to compute the phase of the outgoing signals, and predict the location of the constellation points in a phase modulated signal, avoiding the use of complex and computationally demanding dynamic rate equation for the SOAs.

2. Although the work of this thesis used an optimization strategy based on MOGA to perform the fitting of the MZI-SOA model with experimental measurements, other heuristics or combination of heuristics could be approached, namely particle swarm optimization or ant colony among others.

3. Further numerical investigation should be made with the all-optical conversion system from OOK to m-QAM, to investigate the impact of other components of the system

on the constellation diagram BER, such as fiber lengths mismatch or polarization stochastic variation of the PC.

4. Following the experimental validation of the all-optical conversion from NRZ-OOK to QPSK, we verify that external factors, such as temperature fluctuations or air movements, have influence on the experimental setup and the produced signal. Thus, a closed loop control system, using information from the constellation output, could be implemented and used to adjust the correct balance between operational parameters, such as bias current, phase shifters voltage or laser power.

5. The experimental evaluation of the parallel MZI-SOA configuration for all-optical conversion from NRZ-OOK to 16-QAM was simulated, but not undertaken in laboratory. Several issues related with fiber length mismatch have disabled the possibility to test this setup in smaller timescales. However, a conclusive and positive result may be achieved with the integration of the parallel MZI-SOA configuration in a single wafer, with hybrid integration.

6. Another important work could be to study the polarization effect on the converted signals, and adapt the proposed all-optical techniques to generate polarization multiplexed signals.

7. Finally, as compared with actual coherent system (e.g. Dual Polarization Quadrature Phase Shift Keying (DP-QPSK)), the proposed techniques may decrease the power consumption. It may be relevant to evaluate such techniques in the energy consumption plane, since green communications are currently one of the target for a low carbon economy.

Appendix A

Optical Complex Spectrum Analyzer for phase and power measurements

THe objective of this section is to explain how to use an OCSA to correctly measure the phase and power of an optical signal. It describes what the equipment is able to measure and what the limitations are. The section continues with a detailed description of the hardware connections (both optical and electrical), the sequence of parameters that a user must set from the software menu and an explanation on how to read and save the results, such as phase, power or constellation diagram.

A.1 Why do we need an optical complex spectrum analyzer?

Usually, an Optical Spectrum Analyzer (OSA) can only measure power and wavelength of a light beam. An OCSA, as an instrument capable of measuring the optical phase as well, allows for a broader and deeper analysis. Some of the functionalities of an OCSA are:

- High resolution spectrum analyzer
- Optical phase analyzer
- Time resolved chirp, intensity and alpha parameter measurements
- Short pulse measurement
- Low linewidth tunable lasers evaluation
- High-order modulation format analysis
- Constellation diagrams
- Phase and intensity eye diagram

A.2 Measurement principle

An OCSA uses a heterodyne technique to measure spectral phase and intensity [1]. Knowing the amplitude and the phase of each spectral component and using a method based upon a spectral analysis of the optical field, the temporal variations of the amplitude and the phase can be calculated by Fourier transform, giving the intensity, chirp, phase and alpha factor as a function of time. Moreover, no particular polarization requirements

are necessary, due to an internal configuration with polarization diversity, which make the device polarization independent.

As depicted in Figure A.1, an external clock, usually coming from a pattern generator and synchronized with the data sequence, interact with the signal under test, giving beatings on the receiver section. Then these beatings are filtered on the electrical domain. Moreover, due to the principle of operation, OCSA can only be used to characterize periodic modulation signals with discrete spectra. The constant frequency gap between spectral components is equal to the pattern repetition rate F_r, given by,

$$F_r = \frac{R_b}{P_l} \tag{A.1}$$

where R_b is the transmission bit rate (bits/second) of the data sequence, F_r is the pattern repetition frequency (Hz) and P_l is the pattern length (bits). F_r is one of the technical specifications of the OCSA, and usually two values are specified: F_{r_1} and F_{r_2}.

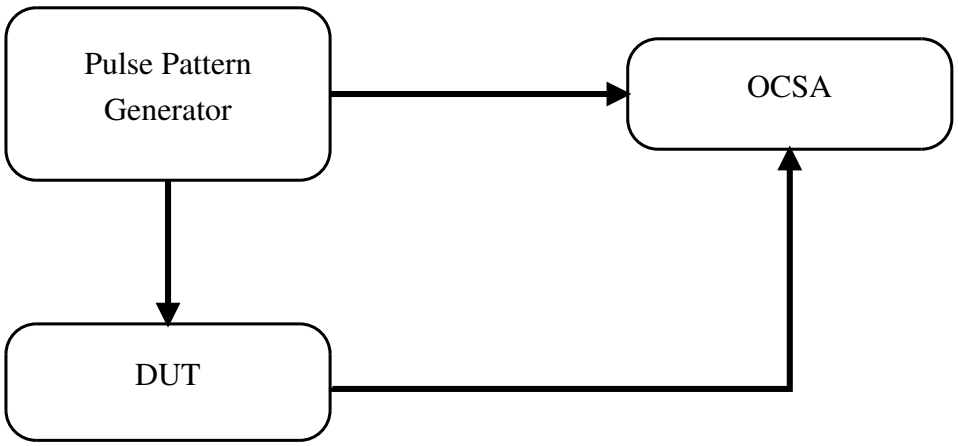

Figure A.1: Measurement configuration

In order to measure high transmission rates, it is required to increase the pattern length to obtain frequency components suitable for the OCSA.

A.3 Frequency-domain measurement technique: Advantages and limitations

Any transmission rate can be measured with an OCSA, because the bandwidth limit can be higher than 1 THz (proportional to the wavelength span), assuring that equation A.1 is applicable. However, and since frequency-domain method are dependent on repetitive waveforms, they are limited as an evaluation tool for longer patterns, intermittent signals, and for detecting rare events, such as bit errors, where time-domain methods are more tailored. Table A.1 gives more details on other important specifications and identifies the main differences between time and frequency techniques. Limitations on the real-time

approach, using a Real-Time Scope (RTS), are that the entire spectrum of a band is not captured at once (unlike with an OSA), but instead requires tuning of the Local Oscillator (LO) or reference laser [2].

Table A.1: Comparison between frequency-domain and time-domain measurement techniques.

Specifications	Frequency-domain [2] [3]	Time-domain [4]
	OCSA	RTS + Optical Front-end
Display update rate	10 nm/s	50 nm/s
Dynamic range	80 dB	< 40 dB
Wavelength resolution	< 0.16 pm	> 1 pm
Spectral span	80 pm – 82 pm	LO frequency $\pm$ 30 GHz
Wavelength range	C band	C or L band
Pattern length	Thousand of bits	Millions of bits (burst mode)

A.4 Measurement procedure

The measurement procedure for a complex spectrum measurement must start with an adequate spectral width and carrier selection. If the instrument has an "Auto" function, the spectral width and carrier selection are automatically set depending on the signal under test.

In case of a signal using optical amplification, the automatic span search can be wrong due to the spontaneous emission generated by the optical amplifier. Moreover, if the spectral width is not wide enough for the signal under analysis, the measurement will be wrong due to the lack of spectral components. This will induce a distortion in the calculated chirp, pulse shape and phase parameters.

The carrier can also be selected manually. A wrong carrier choice influences chirp and phase calculation, but there is no difference in pulse shape. The chirp is given by the difference between carrier and instantaneous optical frequency,

$$C(t) = f(t) - f_0 \tag{A.2}$$

If an adjacent frequency is taken instead of the real carrier (at 625 MHz from the carrier for example), then $c(t)$ is translated by 625 MHz. The phase is given by,

$$\varphi(t) = \int_0^t C(t)dt \tag{A.3}$$

Therefore, if the carrier is moved by a constant frequency F, the measured phase will be,

$$\varphi'(t) = \varphi(t) + Ft \tag{A.4}$$

explaining why phase measurement can be totally different with two different carrier selection.

A.5 Application example: Phase modulator characterization

An example will be given to further illustrate the measurement process using an OCSA. The experimental setup shown in Figure is meant to characterize a Device Under Test (DUT) that converts a signal from NRZ-OOK to BPSK format [5]. The equipment used is listed below:

- BERT
- OCSA
- Sampling oscilloscope

For sake of simplicity, other passive or active optical components also used in the experimental setup but not relevant for the description of the measurement process, are not identified.

In order to validate the feasibility of the DUT as a phase modulators, experiments at 10 Gbps were carried out. The OCSA is set with a repetition frequency of 625 MHz. From equation A.1, it is necessary to generate a 16 bits pattern. Figure A.2 left inset shows the NRZ signal generated with pattern 1110010010101100, and right inset shows power and phase measurements along with the constellation diagram taken with an OCSA at the DUT output.

In this particular example, the DUT needs all data and clock outputs from the pattern generator to work properly. The clock signal feeding the OCSA comes from the trigger output.

When clock signal ports are not enough to simultaneously connect several measuring instruments, a power splitter can be used to divide the signal. As shown in Figure A.3, two instruments share the same output, allowing simultaneous display of spectra and time signals.

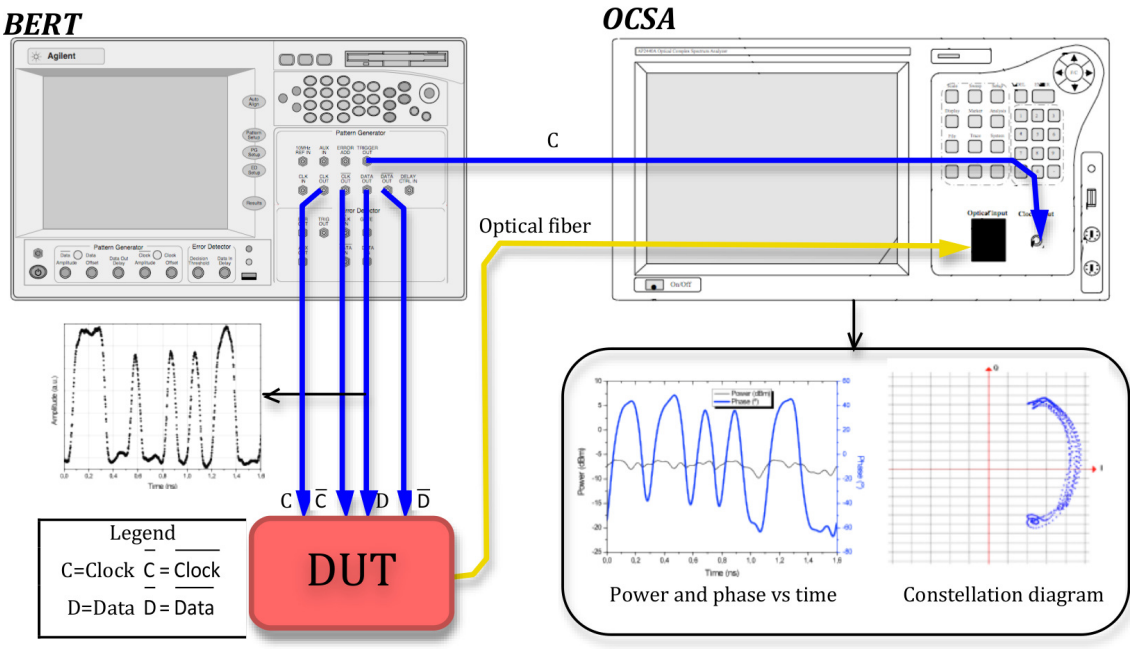

Figure A.2: Experimental setup with measured signals

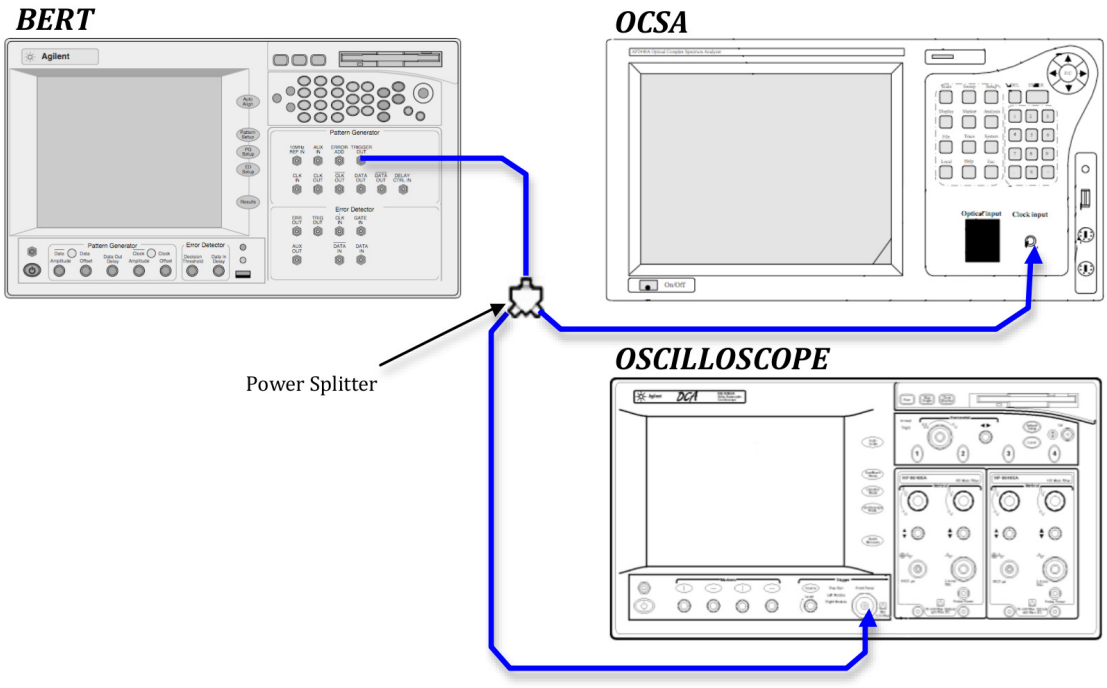

Figure A.3: Power splitter used to feed two instruments with the same clock signal

References

[1] D. A. Reid, S. G. Murdoch, and L. P. Barry, "Stepped-heterodyne optical complex spectrum analyzer," *Opt. Express*, vol. 18, no. 19, pp. 19 724–19 731, 2010.

[2] D. van der Weide, "Measuring complex optical modulation in fiber," *Lightwave Magazine*, pp. 23–27, February 2010. [Online]. Available: http://www.lightwaveonline.com/

[3] "ARAGON BOSA PHASE," February 2010. [Online]. Available: http://www.aragonphotonics.com/

[4] "OPTAMETRA OM4106B coherent lightwave signal analyzer," February 2010. [Online]. Available: http://www.optametra.com/2009/documents/OM4106B_Tek.pdf

[5] R. Dionisio, C. Reis, P. Andre, R. Nogueira, and A. Teixeira, "Experimental study of a phase modulator using an active interferometric device," in *MELECON 2010*, 2010, pp. 1142–1146.

Appendix B

Balancing a Mach-Zehnder Interferometer with Semiconductor Optical Amplifiers

THe objective of this section is to describe how to balance a MZI-SOA. Due to very small changes in motherboard fabrication of photonic hybrid integrated devices [1], there is a very small effective path length difference in each arm of the MZI, which causes a small phase change and slightly unbalance the MZI. Similar effects are also seen in the SOAs contained in each arm of the MZI. Therefore, it is very important to firstly balance the interferometer to get it to work properly. The MZI-SOA is balanced when a maximum ER between the interferometer output ports is achieved.

B.1 Balancing with a probe signal

For the balancing process of the MZI-SOA. Connect a CW probe signal, followed by a PC, into port #B (or #C) of the device, as depicted in the experimental setup of Figure B.1. Set the CW power to a typical value, for example 1 dBm, and choose a wavelength within the SOA gain bandwidth. Output power at port #I and #J can be monitored with two power meters or by using, simultaneously, an optical switch with one power meter. It is advisable to use an optical filter to recover the CW signal at the output ports.

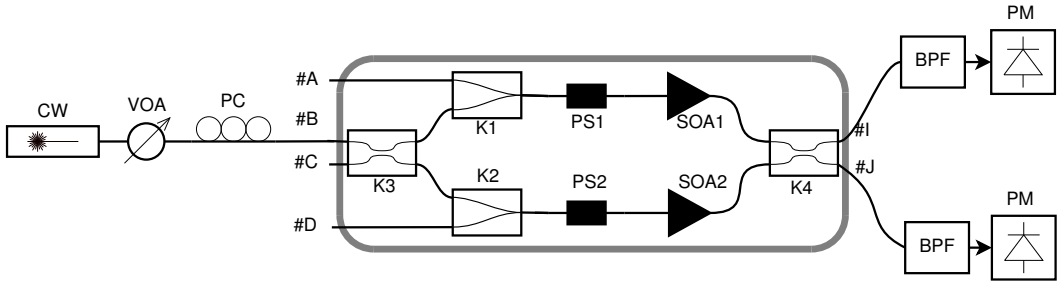

Figure B.1: Experimental setup to balance the MZI-SOA.

The device can be used in co and counter-propagation schemes, since it is optically symmetric. Therefore, the CW signal can be also coupled to one of the following MZI-SOA ports #I or #J, and power meters to ports #B and #C.

Assuming that the Peltier controller is powered on, so the temperature of the device is stabilized, the bias current of both SOAs must be set to an equal value. Higher data rates normally require higher bias currents. Adjust the input CW polarization and apply a voltage

to one or both phase shifters. A phase shift of π radians can be achieved with only one phase shifter. Monitor the power at the output ports to obtain a minimum value on one port (destructive output) and a maximum value on the other port (constructive output). At this step, a small detuning on the SOA bias current may also improve the ER. At every change, the voltage of the phase shifters and the CW input polarization should be re-adjusted. This process results in the maximum ER between output ports.

B.2 Adding control signals

The control pulses may be input in a co or counter propagating manner with respect to the pros signal, although better performance at high data rates is usually achieve in the co-propagating scheme (i.e. for probe input into #B or #C port, the control pulses should be introduced into #A and #D port). An example of the experimental set-up for this scheme is depicted in Figure B.2. It is important when setting up this experiment that the lengths of the push and pull arms are kept the same (to within a few cm). The following list gives some tips to effectively set-up the switching of the interferometer:

1. Disconnect the ”pull” pulses and adjust the push-pulse power to a low value (for example below -5 dBm). Monitor the output port (selecting the output filter to pass λCW) that was set-up as the destructive output when the interferometer was balanced using a fast sampling scope (for example a 30 GHz or faster PIN diode and 30 GHz or faster electrical input).

2. Slowly turn up the power of the push pulses until you see pulses starting to occur on the scope (these should begin to occur at switching power levels less than +2 dBm). Mark the peak pulse position in time with a horizontal (time base) marker.

3. Disconnect the push pulses and reconnect the pull pulses. Follow the same procedure for these pulses and adjust the time delay to get the λCW carved pulse later in time than the waveform from the push pulse (denoted by the previous marker) (for example by 12.5ps for 40 Gb/s data rates). Initially set the pull pulse power to a value less than the push pulse (for example 3 dB less).

4. Introduce back the push pulses and adjust the control pulse powers, polarizations and relative timing to obtain good window closure. When optimizing the control pulses it may be necessary to finely adjust the interferometer balance condition (i.e. SOA bias currents, λCW polarization and phase shifter voltage).

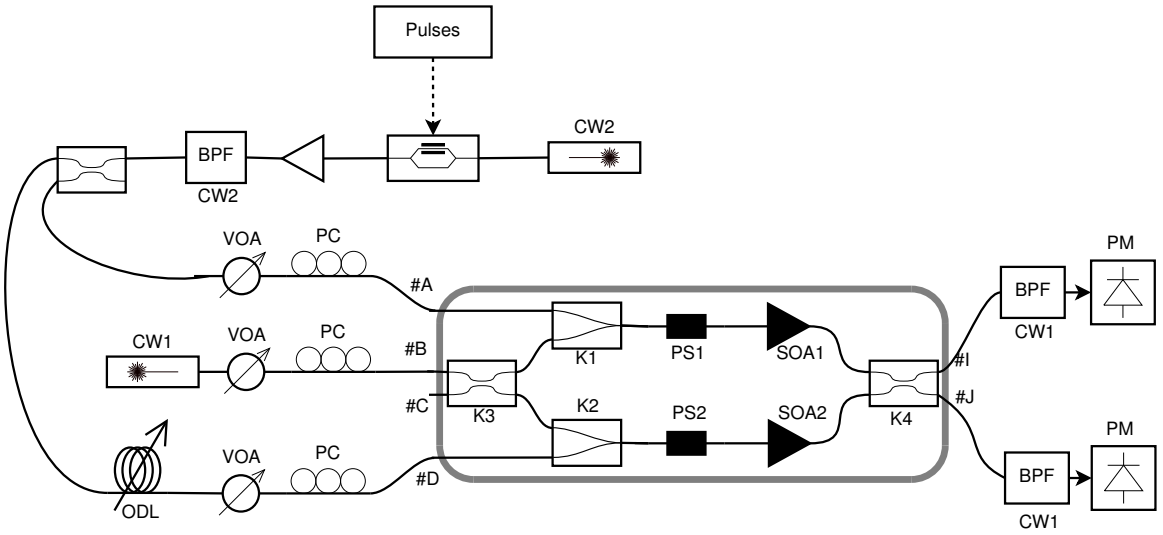

Figure B.2: Experimental setup with control signals. ODL: Optical Delay Line; PC: Polarization Controller; VOA: Variable Optical Attenuator.

References

[1] "CIP Technologies," July 2012. [Online]. Available: http://www.ciphotonics.com/

Appendix C

Matlab Code

THe following Matlab code can be used to compute all combination of two identical sequences with 16 bits length and delayed 3 bits with each other, that will result in a 16 symbols QPSK signal with equal symbol distribution.

```
siz=2^16-1;% Number of possible sequences with 16 bits length
counter=1;
for k=1:siz
    seq1=dec2bin(k,16); % Sequence 1 in binary format
    seq2=[seq1(14:16) seq1(1:13)];% 3 bits delay between sequences
    sum=seq1+seq2-96; % 0->A 2->B
    differ=seq1-seq2; % -1->C 1->D
    A=length(find(sum==0));
    B=length(find(sum==2));
    C=length(find(differ==-1));
    D=length(find(differ==1));
    sum2=seq1+seq1-96;
    E=length(find(sum2==2));
    vect=[A B C D];
    metrics=(max(vect)-min(vect));
    if(metrics==0)
        if(E==8)
            res(counter)=k;
            counter=counter+1;
        end
    end
end
dec2bin(res,16) % Results listed in binary format
```